

2014

Experimental and Theoretical Study of CO Oxidation on Metal Atoms with Oxygen Allotropes

Angela Nicole Smith
Lehigh University

Follow this and additional works at: <http://preserve.lehigh.edu/etd>

 Part of the [Chemistry Commons](#)

Recommended Citation

Smith, Angela Nicole, "Experimental and Theoretical Study of CO Oxidation on Metal Atoms with Oxygen Allotropes" (2014). *Theses and Dissertations*. Paper 1632.

This Dissertation is brought to you for free and open access by Lehigh Preserve. It has been accepted for inclusion in Theses and Dissertations by an authorized administrator of Lehigh Preserve. For more information, please contact preserve@lehigh.edu.

Experimental and Theoretical Study of CO Oxidation on Metal Atoms with Oxygen
Allotropes

by

Angela Nicole Smith

A Dissertation

Presented to the Graduate and Research Committee

of Lehigh University

in Candidacy for the Degree of

Doctor of Philosophy

in

Department of Chemistry

Lehigh University

August 31, 2014

© 2014 Copyright
Angela N. Smith

Approved and recommended for acceptance as a dissertation in partial fulfillment of the requirements for the degree of Doctor of Philosophy

Angela Nicole Smith
Experimental and Theoretical Study of CO Oxidation on Metal Atoms with Oxygen Allotropes

May 30, 2014

Defense Date

July 29, 2014

Approved Date

Dr. David T. Moore
Dissertation Director

Committee Members:

Dr. Gregory S. Ferguson

Dr. David A. Vivic

Dr. Christopher J. Kiely

ACKNOWLEDGMENTS

I would like to thank my advisor first and foremost, Dr. David T. Moore, for his guidance, advice, and assistance throughout my graduate career and my development as a professional chemist. I would like to thank my graduate committee members, Dr. Gregory Ferguson, Dr. David Vicic and Dr. Christopher Kiely for their help. I also thank my colleagues, both former and current, Rebekah Klimas, Alex Hunter, Nina Jarrah, Ryan Ludwig and Michael Goodrich, who have been great co-workers and are always willing to help. I also want to thank the chemistry department for financial support during my graduate career at Lehigh University.

I would like to further thank Dr. Moore, Dr. Ferguson, Dr. Jim Roberts, Dr. Becky Miller, Dr. Kelley Caflin, and Dr. Michael Barrett for career advice and insight into solving the “two-body” problem of post-graduate life and career. I also want to thank my running buddies, Dr. Caflin and Katherine Kressler, who have ran, listened and offered advice and encouragement. I also want to acknowledge my family, especially my parents Mary Lou and Daniel, for their ever-present support throughout my academic career and understanding when I would forget to call or visit for long periods of time. Finally, I would like to thank my fiancé, Andrew Henry, for assistance in writing scripts to gather data from calculations and building a Faraday cage, and his support of my decisions during my graduate career. I could not have completed this journey without everyone’s support and assistance throughout these five years.

NON-TECHNICAL ABSTRACT

The motivation for this work is to answer fundamental questions about a potential energy surface (PES), where the PES describes how the energy of a complex, or a set of molecules, changes with alterations in the structure of the complex. The PES can be thought of as a mountain range, in which one will observe peaks (maxima) and valleys (minima) of varying heights and depths. The valleys represent reactants, intermediates and products of a reaction, while the peaks represent transition states between the valleys, e.g., between reactants and products. To move from one valley (reactants) to another valley (products), there are many possible pathways that may be considered. If a hiker had a topographic map of the mountain range, he may identify a pathway that is the shortest distance “as the crow flies,” but would require climbing a huge mountain that is 6,200 feet, similar to Mt. Washington in New Hampshire. Similar to the mountain, some reactions proceed over a large energy barrier between reactants and products. Instead of going over the huge mountain, the hiker identifies a path with some smaller peaks and valleys and a rock wall; in this case, the hiker may need to use additional techniques and tools, such as ropes to climb the rock wall, to circumvent that mountain. To a great extent, efforts have been made to circumvent large energy barriers in experiments, and one way involves the use of a catalyst to lower the activation energy, similar to using ropes to climb a sheer rock wall. A catalyst is a substance that is added into a reaction and increases the rate of a reaction, but is chemically unchanged at the end of the reaction. In analogy to hiking, catalysis, the increase in the rate of reaction, is similar to finding a different way around that huge mountain, but typically involves the use of an

additional substance, or tool, like the “rock-climbing pathway.” In this pathway, when the hiker used the ropes, he did not physically change those ropes, but the ropes provided a “quicker” or easier route for the hiker to traverse; therefore, the ropes were a catalyst in the hiker’s journey. In our experiments and calculations, we are working to understand the probable pathways, or mechanisms, of specific catalytic reactions and determine the peaks (maxima) and valleys (minima) along these pathways. By studying probable pathways with different structures (and their related energies) from reactants to products, we are building the potential energy surfaces, similar to developing topographical map of a mountain range. We are looking at one specific reaction, the oxidation of carbon monoxide to carbon dioxide, which is necessary to purify hydrogen gas to be used as an alternative energy source.

Table of Contents

ACKNOWLEDGMENTS	iv
NON-TECHNICAL ABSTRACT	v
LIST OF FIGURES	xi
LIST OF TABLES	xvii
ABSTRACT	1
Chapter 1. Catalysis of CO Oxidation with Gold (Au) Nanoparticles	4
1.1 Motivation and Introduction	4
1.2 Project Goals	12
1.3 References	13
Chapter 2. Computational Background and Methods and Experimental Methods	15
2.1 Computational Methods	15
2.1.1 Moller-Plosset Perturbation Theory	17
2.1.2 Density Functional Theory	17
2.1.3 Mixed Double Hybrid DFT	20
2.1.4 Using Computational Methods to Investigate Minima on a Potential Energy Surface	20
2.1.5 Gaussian Program	22
2.1.6 Basis Sets	22
2.1.7 Types of Calculations and Their Applications:	24
2.2 Experimental Methods	31
2.2.1 Gas-aggregation Nanoclusters Source System	31
2.2.2 Gas Rack and Ozone-Generation System	35
2.2.3 Ozone Generation for Use in Reactant and Matrix Gas Mix	37
2.2.4 Ozone Mix Deposition	38
2.3 References	39
Chapter 3. Charge-dependent Trends in Structures and Vibrational Frequencies of [CO-Au-O ₂] ^q (q=-1,0,+1) Complexes: Evidence for Cooperative Interactions	41
3.1 Abstract	41
3.2 Introduction	41
3.3 Computational Methods	46
3.4 Results and Discussion	46

3.4.1 Structures, Relative Energies and Vibrational Frequencies	46
3.4.2 Charge Dependent Trends	69
3.4.3 Molecular Orbitals	77
3.5 Conclusions	80
3.6 References	82
Chapter 4. DFT-calculated CO Oxidation Pathways for Au Atoms and Anions with O ₂ : Observation of Possibly De-activating Carbonate Species	85
4.1 Abstract	85
4.2 Introduction	85
4.3 Results	87
4.3.1 Neutral Pathway Description	90
4.3.2 Anionic Singlet Pathways Description	99
4.3.3 <i>Ab initio</i> Molecular Dynamics (AIMD/ADMP)	102
4.4 Discussion	107
4.4.1 Neutral Pathways	107
4.4.2 Anionic Singlet Pathways	108
4.5 Computational Methods	109
4.6 References	111
Chapter 5. Calculations of Two CO Oxidative Pathways with Au ^q (q=+1, 0, -1) and Ozone: Direct O ₃ Oxidation of CO Catalyzed by Au ^q Atoms or “Secondary” Oxidation of CO by (O ₂)AuO ^q	113
5.1 Abstract	113
5.2 Introduction	113
5.3 Results	114
5.3.1 O ₃ Oxidation Pathway	115
5.3.2 AuO Oxidation Pathway	119
5.4 Discussion	132
5.4.1 O ₃ Oxidation Pathway	132
5.4.2 AuO Oxidation Pathway	132
5.4.3 Similarities of O-TS & G-TS	133
5.4.4 Comparison of O ₂ and O ₃ Systems	135
5.5 Conclusions	137
5.6 Computational Methods	138
5.7 References	139

Chapter 6. DFT Investigations of CO Oxidation Pathways with Two Oxygen Species (O ₂ and O ₃) and Cu ^q Atoms (q= +1, 0, -1): Observation of CuO and O ₃ Oxidation Pathways for Oxygen Allotropes.....	141
6.1 Abstract.....	141
6.2 Introduction	141
6.3 Results	143
6.3.1 O ₂ , Cu ^q , CO Complexes and Pathways	144
6.3.2 O ₂ Pathways.....	154
6.3.3 Ozone, Cu, and CO Interactions.....	167
6.4 Discussion.....	182
6.4.1 O ₂ Pathways.....	182
6.4.2 Ozone Pathways	183
6.4.3 Comparison of O ₂ and O ₃ Systems.....	186
6.4.4 Comparisons to Au Systems.....	187
6.5 Conclusions	190
6.6 Computational Methods	191
6.7 References	192
Chapter 7. Matrix Isolation Experiments on the Interactions of Ozone (O ₃), Carbon Monoxide (CO), Copper Ions (Cu ⁻) and Counter-cations of Ar ⁺	194
7.1 Abstract.....	194
7.2 Introduction:	194
7.3 Results:	194
7.3.1 O ₃ in Ar Experiments	195
7.3.2 O ₃ :CO Experiments.....	196
7.3.3 Cu:O ₃ Experiments.....	199
7.3.4 Cu:O ₃ :CO Experiments	204
7.3.5 Peak Comparisons with Cu Computational Work.....	208
7.4 Discussion.....	210
7.4.1 O ₃ , CO	210
7.4.2 Cu, O ₃	210
7.4.3 Cu, O ₃ , CO.....	213
7.4.4 Peak Comparisons with Cu Computational Work.....	215
7.4.5 CO ₂ Contamination	216
7.5 Conclusions	217

7.6 Experimental Methods.....	217
7.7 References	219
Chapter 8. Efforts toward Expanding the Size of Clusters Studied in DFT Calculations: Au ₂ ^q with CO and O ₂ (or O ₃) (q= +1, 0, -1) and Future Work.....	220
8.1 Au ₂ Introduction	220
8.2 Results	220
8.2.1 Binary Complexes: Au ₂ CO, Au ₂ O ₂ , and Au ₂ O ₃	220
8.2.2 Ternary Complexes	227
8.2.3 O ₃ Pathway	237
8.3 Discussion.....	237
8.3.1 O ₂ Systems.....	237
8.3.2 O ₃ Systems.....	238
8.4 Future Work.....	239
8.4.1 Computational Work	239
8.4.2 Experimental Work	241
8.5 References	244
Appendices	245
A2. Appendix to Chapter 2.....	245
A2.1 Gaussian Keywords	245
A2.2 Input File Examples.....	247
A3. Appendix to Chapter 3.....	253
A3.1 Tables and Figures in Support of Text.	253
A3.2 Comparison of B3LYP, mPW1PW91, B3PW91:	260
A4. Appendix to Chapter 4.....	272
A5. Appendix to Chapter 5.....	287
A6. Appendix to Chapter 6.....	304
A7. Appendix to Chapter 7.....	312
Vitae	328

LIST OF FIGURES

Figure 2.1 Solidworks rendering of internal components for nanocluster experimental system (courtesy of Alex Hunter).....	33
Figure 2.2 Simple schematic, not to scale, of the gas rack, mixing rack and deposition lines (shown with blue lines) and the ozone generation, storage and deposition systems (shown with black lines). The ozone generation system is shown in the purple box with the glass tube and copper wire wrap attached to a Tesla coil. Red circled Xs represent valves, green R rectangles are regulators, orange P circles are pressure gauges, blue bars are flow controllers, the orange rectangle is the vacuum pump, and the ozone bottle is the gray cylinder.	36
Figure 3.1 Geometry and structural characteristics of cationic, neutral and anionic binary complexes, $[\text{AuCO}]^q$ and $[\text{AuO}_2]^q$ calculated with B3LYP/SDD/6-311+G(3df).	48
Figure 3.2 Structural details of the OAUO^q species shown as cartoons ($q=0,-1$).	57
Figure 3.3 Geometry and structural characteristics of cationic, neutral and anionic ternary complexes, $[\text{O}_2\text{AuCO}]^q$ and $[\text{Au}(\text{CO})\text{O}_2]^q$, which can be described as separated (A-D), pre-reactive (E & F). <i>Italicized</i> numbers correspond to angles (in degrees) and bold numbers correspond to bond lengths (in angstroms).	61
Figure 3.4 Geometry and structural characteristics of the neutral and anionic long range ternary complexes, labeled A-D, and pre-reactive rotamers, labeled E & F. Numbers in bold correspond to bond lengths in Angstroms and numbers in italics are bond angles in degrees.	67
Figure 3.5 Electrostatic potential mapped on the total electron density isosurfaces (density =0.0004) for binary complexes calculated at B3LYP-SDD/6-311+G(3df). The color map spans a range of 0.1 in each case, with red (blue) as most negative (positive). The charges for anions are mapped over -0.21 to -0.11; neutrals, -0.05 to +0.05, and cationic, +0.13 to +0.23. Note that the color intensities are also mapped to the values, such that colors near the ends of the range appear brightest, while those in the center appear transparent.	72
Figure 3.6 Electrostatic potential mapped on the total electron density isosurfaces (density =0.0004) for ternary complexes calculated at B3LYP-SDD/6-311+G(3df). The color map spans a range of 0.1 in each case, with red (blue) as most negative (positive). The charges for anions are mapped over -0.21 to -0.11; neutrals, -0.05 to +0.05, and cationic, +0.13 to +0.23. Note that the color intensities are also mapped to the values, such that colors near the ends of the range appear brightest, while those in the center appear transparent.	73
Figure 3.7 Selected molecular orbitals showing Au-CO σ -donation and π -backbonding character for binary $[\text{AuCO}]^q$ and ternary $[\text{O}_2\text{AuCO}]^q$ complexes, $q=+1,0,-1$	78

- Figure 3.8** Five highest occupied molecular orbitals and LUMO of “pre-reactive complexes,” Au(CO)O₂ (Fig. 3.3 C) and [Au(CO)O₂]⁻ singlet (Fig. 3.3 F). Au(CO)O₂ β-spinorbitals are not shown, but are similar to the (shown) α-spinorbitals, except that the LUMO-β is the same structure as HOMO-2α (shown in figure). Note that for both series, all orbitals feature a node in the “breaking” bond (O-O), and a bonding interaction in the “forming” bond (2nd C-O bond). 79
- Figure 3.9** Comparison of the orbital HOMO-2(α) and spin density for the Au(CO)O₂ doublet ternary species (Figure 3.3 E) calculated with B3LYP-SDD/6-311+G(3df). 79
- Figure 4.1** Reaction pathways of [O₂+Au+CO]⁰ (doublet) towards CO oxidation with the relative energies (in kcal/mol) of the stable points. The In-TS pathway is represented by the blue and purple solid (and blue dotted) lines; the Out-TS pathway is represented with the solid red line. The main minima and transition states that are described above in the text are in bold. The blue dotted line indicates transition states that can be “skipped”, where barriers are lower than the reactant asymptote. 88
- Figure 4.2** Reaction pathways of [O₂+Au+CO]⁻ (singlet) towards CO oxidation with the relative energies (in kcal/mol) of the stable points. The In-TS pathway is represented by the blue solid lines; the Out-TS pathway is represented with the solid red line. The main minima and transition states that are described above in the text are in bold. 88
- Figure 4.3** The reaction pathway(s) for the neutral doublet state is shown for [O₂+Au+CO]⁰, where each position is now represented by the respective electrostatic potential (ESP) mapped on to the total electron density isosurface (density = 0.0004). The color map spans a range of 0.1 with red (blue) as most negative (positive) from -0.05 to +0.05. 91
- Figure 4.4** The reaction pathway(s) for the anionic singlet state is shown for [O₂+Au+CO]⁻, where each position is now represented by the respective electrostatic potential (ESP) mapped on to the total electron density isosurface (density = 0.0004). The color map spans a range of 0.1 with red (blue) as most negative (positive) from -0.20 to -0.10. 91
- Figure 4.5** Snapshots of MD simulations starting from the neutral (doublet) pre-reactive (in, Pre₁) structure with a fictitious electron mass of 0.1 amu, time step of 0.05 fs, and nuclear kinetic energy of 30 kcal/mol. 103
- Figure 4.6** Snapshots of MD simulations starting from the anionic singlet pre-reactive (in, Pre₁) structure with a fictitious electron mass of 0.1 amu, time step of 0.05 fs, and nuclear kinetic energy of 30 kcal/mol. 103
- Figure 4.7** Snapshots of MD simulations starting from the neutral (doublet) pre-reactive (out, Pre₂) structure with a fictitious electron mass of 0.1 amu, time step of 0.05 fs, and nuclear kinetic energy of 50 kcal/mol. 104
- Figure 4.8** Snapshots of MD simulations starting from the anionic singlet pre-reactive (out, Pre₂) structure with a fictitious electron mass of 0.1 amu, time step of 0.05 fs, and nuclear kinetic energy of 50 kcal/mol. 104

Figure 4.9 Five highest occupied molecular orbitals and LUMO of the “In” and “Out” transition states of the neutral and anionic (singlet) charge states, where a) and b) are neutral In-TS and Out-TS and c) and d) are anionic singlet In-TS and Out-TS, respectively.	105
Figure 4.10 Five highest occupied molecular orbitals and LUMO of the carbonate-like product, Pro ₁ (AuCO ₃), of the neutral and anionic (singlet) charge states, where a and b are neutral and anionic charge states, respectively.	106
Figure 4.11 Five highest occupied molecular orbitals and LUMO of the carbon dioxide product, Pro ₂ (OAuCO ₂), of the neutral and anionic (singlet) charge states, where a and b are neutral and anionic charge states, respectively.	106
Figure 5.1 The reactant-side complexes (BR) for all charge and spin states (cationic, neutral (doublet) and anionic; singlet and triplet) with the bond lengths (in bold, Å) and angles (in italics, °) shown in the structures, calculated at B3LYP-SDD/6-311+G(3df).	116
Figure 5.2 a) The neutral doublet reaction pathway(s) for [O ₃ +Au+CO] along the “O ₃ oxidation” pathway is shown with relative energies for calculated stable points. The main minima and transition states, described in the text, are in bold. The solid blue line shows the O ₃ oxidation process; the dashed blue line indicates the possible, shorter pathway from ² O-TS ⁰ to structure ² PRO ⁰ . b) The neutral doublet reaction pathway(s) for [O ₃ +Au+CO] along the “AuO oxidation” pathway is shown with relative energies for calculated stable points. The dashed blue line shows the AuO oxidation process over one transition state(² G-TS ⁰); the dashed red line indicates the possible, shorter pathway from ² G-TS ⁰ to structure ² PRO ⁰	120
Figure 5.3 The reaction pathway(s) for the neutral doublet state is shown for Au atom, CO and O ₃ , where each position is now represented by the respective electrostatic potential (ESP) mapped on to the total electron density isosurface (density = 0.0004). The color map spans a range of 0.1 with red (blue) as most negative (positive) from -0.05 to +0.05.	122
Figure 5.4 The reaction pathways for the cationic singlet state for Au ⁺ , CO and O ₃ are shown, where the blue and purple lines represent the two O ₃ oxidation pathways, ¹ O-TS ₁ ⁺ & ¹ O-TS ₂ ⁺ and red line represents the AuO oxidation pathway, ¹ G-TS ⁺	127
Figure 5.5 The reaction pathways for the cationic triplet states are shown, where ³ G-TS ⁺ (red line) represents the AuO pathway and ³ O-TS ⁺ (blue line) represents the O ₃ pathway and both pathways start from the “O ₃ in” minimum (³ BR ₁ ⁺). The dotted purple line shows the reactants with triplet ozone and indicates the instability of that ozone species.	127
Figure 5.6 The reaction pathway(s) for the anionic singlet state is shown for Au atoms, CO and O ₃ , where both pathways originate with the C _{2v} “O ₃ in” minimum (¹ BR ₁ ⁻). The blue line shows the O ₃ oxidation pathway and the red line represents the AuO pathway.	128

Figure 5.7	The reaction pathways for the anionic triplet system for Au ⁻ , CO and O ₃ are displayed with the related structures and energies per minima and transition state. The dotted purple line shows the reactants with triplet O ₃ and indicates its instability. The blue line indicates the O ₃ pathway; the solid red line indicates the AuO oxidation pathway and the purple pathway shows the alternate post-reactive pathway that can continue over ³ LB ₄ ⁻ to structure ³ AR ₃ ⁻ (red line).	128
Figure 6.1	B3LYP predicted structures, bond lengths (Å), and angles (°) for [CuCO] ^q and [CuO ₂] ^q (q=+1, 0, -1) binary complexes.	146
Figure 6.2	B3LYP predicted structures, bond lengths (Å), and angles (°) for [O ₂ CuCO] ^q and [Cu(CO)O ₂] ^q (q=+1,0,-1) ternary complexes, with designated structural types as “separated” or “pre-reactive” as described in the text.	149
Figure 6.3	The reaction pathway(s) for the anionic singlet state is shown for Cu atoms, CO and O ₂ , where all pathways originate with the C _{2v} separated minimum (Sep). The red line shows the O ₂ “in” oxidation pathway and the blue line represents the CuO pathway. The purple pathway represents the “Out” pathway.	155
Figure 6.4	The reaction pathway(s) for the neutral doublet state is shown for Cu atoms, CO and O ₂ , where all pathways originate with the C _{2v} separated minimum (Sep). The red line shows the O ₂ out oxidation pathway. The purple pathway shows the second “Out” pathway that leads to formation of CuCO ₃ . The blue line represents the CuO pathway.	155
Figure 6.5	The reaction pathway(s) for the anionic triplet state is shown for Cu ⁻ , CO and O ₂ , where all pathways originate with the separated minimum (Sep). The red line shows the O ₂ out oxidation pathway. The purple pathway moves from In-TS to form the lower energy product complex, PRO ₁ . The blue line shows the formation of PRO ₂ from TS ₁	156
Figure 6.6	The reaction pathway(s) for the anionic singlet [O ₂ +Cu+CO] ⁻ is shown for, where each position is now represented by the respective electrostatic potential (ESP) mapped on to the total electron density isosurface (density = 0.0004). The color map spans a range of 0.1 with red (blue) as most negative (positive) from -0.20 to -0.10.	160
Figure 6.7	The reactant-side complexes (BR) for all charge and spin states (cationic, neutral (doublet) and anionic; singlet and triplet) with the bond lengths (in bold, Å) and angles (in italics, °) shown in the structures, calculated at B3LYP-SDD/6-311+G(3df).	169
Figure 6.8	The reaction pathway(s) for the neutral doublet state is shown for Cu atom, CO and O ₃ ; both O ₃ and CuO oxidation pathways originate from the “O ₃ in” minimum (² BR ₁ ⁰). The solid red line shows the O ₃ oxidation process and the solid blue line represents the CuO pathway ..	175
Figure 6.9	The reaction pathway(s) for the anionic singlet state is shown for Cu ⁻ , CO and O ₃ , where both pathways originate with the C _{2v} “O ₃ in” minimum (¹ BR ₁ ⁻). The red line shows the O ₃ oxidation pathway and the blue line represents the CuO pathway.	175

- Figure 6.10** The reaction pathway(s) for the neutral doublet state is shown for Cu atom, CO and O₃, where each position is now represented by the respective electrostatic potential (ESP) mapped on to the total electron density isosurface (density = 0.0004). The color map spans a range of 0.1 with red (blue) as most negative (positive) from -0.05 to +0.05. The solid red line shows the O₃ oxidation process and the solid blue line represents the CuO pathway. 176
- Figure 6.11** Anionic singlet reaction profiles are shown with electrostatic potentials mapped on B3LYP total electron density isosurfaces (density=0.0004) for each complex on the O₃ oxidation (red line) and CuO oxidation (blue line) pathways. The color map spans a range of 0.1 in each case with red (blue) as most negative (positive). The charges for cationic complexes are mapped over -0.20 to -0.10. Note that color intensities are also mapped to the values, such that colors near the ends of the range appear brightest, while those in the center appear transparent..... 176
- Figure 7.1** a) FTIR spectrum (650-4000 cm⁻¹) taken at 10K after deposition of a 0.05% O₃ in Ar mixture at 20K for 2 hours. b) Focus on the O₃ anti-symmetric peak (doublet) at 1039.4 and 1041.1 cm⁻¹. c) Focus on the 2100-2400 cm⁻¹ region. Note that the spectrum in c) is on a different scale than those in a) and b). 197
- Figure 7.2** Note that all spectra (a-d) are on different wavenumber and absorbance scales. a)FTIR spectrum (650-4000 cm⁻¹) taken at 10K for deposition of a 0.06% O₃ and 0.14% CO in Ar mixture at 20K deposition for 2 hours at ~5 sccm (resolution of 0.5 cm⁻¹). b) Focus on O₃ region (1020-1060 cm⁻¹) of the high resolution (0.125 cm⁻¹) spectrum. c) Focus on the CO region around 2140 cm⁻¹. d) Focus on CO₂ anti-symmetric peak region (2325-2375 cm⁻¹). 198
- Figure 7.3** a) FTIR spectrum (650-4000 cm⁻¹) taken at 10K for co-deposition of Cu⁻ and Ar⁺ (30eV) with 0.5% O₃ in Ar mixture at 10K (and ~2.5 sccm) for 2 hours (resolution of 0.5 cm⁻¹). b) Focus on the 700-900 cm⁻¹ region. c) Focus on the 1100-1350 cm⁻¹ region. Note that all spectra are on different wavenumber and absorbance scales. 201
- Figure 7.4** Difference spectra to identify changes during 5K annealing steps and photo-exposure steps for the data shown in Figure 7.3. a) Region between 650-1000 cm⁻¹ to look for changes in the CuO₃ peak. b) Region of 1100-1600 cm⁻¹ to look for changes in the trans-O₄⁺ complex. 201
- Figure 7.5** a) FTIR spectrum (650-4000 cm⁻¹) for Cu⁻ and Ar⁺ (30eV) co-deposited with 0.5% O₃ in Ar mixture at ~5 sccm at 10K for 2 hours (resolution of 0.5 cm⁻¹). b) Focus on the 700-1000 cm⁻¹ region. c) Focus on the 1100-1350 cm⁻¹; the high frequency, low amplitude sine wave is etaloning due to the matrix. Note that all spectra are on different wavenumber and absorbance scales. 202
- Figure 7.6** a) Recorded and b) difference spectra of the 2K annealing steps for Cu⁻, Ar⁺ (70eV), and 0.2% O₃ in Ar deposited at 10K and 10 sccm for 4 hours. The system is annealed from the 10K deposited spectrum up

	to 20K by 2K and then dropped back to 10K (post annealing). In b), the top (navy) line shows the differences observed between the deposited 10K and post-annealing 10K spectra.	203
Figure 7.7	a) Recorded and b) difference spectra of the photo-exposure steps for Cu^- , Ar^+ (70eV), 0.2% O_3 in Ar deposited at 10K and 10 sccm for 4 hours. The sine wave in the baseline of a) is matrix etaloning. c) Zoom in on the 470nm-10K difference spectrum to better observe the changes in peaks as a function of light the sample with 470 nm. Note that the scales are different in a) and b).	203
Figure 7.8	a) Recorded spectrum taken at 10K for deposition of Cu^- , Ar^+ (30eV), 0.05% O_3 and 0.15% CO in Ar at 20K for 2 hours and b) difference spectra of the 5K annealing and photo-exposure steps. All photo-exposures were completed at 10K. Note that the scales are different in a) and b).	206
Figure 7.9	a) Region of 700-1000 cm^{-1} of FTIR spectrum after deposition at 10K of Cu^- , Ar^+ (30eV), 0.5% O_3 and 0.3% CO in Ar for 2 hours; b) region of 1050-1400 cm^{-1} ; c) region of 1600-2100 cm^{-1} , and d) zoom in on region of 1650-1800 cm^{-1} to observe the peaks on top of the broad 1734 cm^{-1} feature. Note that the scales are different in a)-d).	206
Figure 7.10	a) Region of 700-1000 cm^{-1} in post-deposition FTIR spectrum after deposition of Cu^- , Ar^+ (30eV), 0.2% O_3 and 0.2% CO in Ar at 20K for 2 hours; b) region of 1050-1400 cm^{-1} ; c) region of 1650-2100 cm^{-1} . Note that the scales are different in a)-c).	207
Figure 8.1	B3LYP predicted binary $[\text{Au}_2\text{CO}]^q$ and $[\text{Au}_2\text{O}_2]^q$ ($q=+1, 0, -1$) complexes with bond length (\AA) and angles ($^\circ$).	222
Figure 8.2	B3LYP predicted structures for the binary $[\text{Au}_2\text{O}_3]^q$ complexes with bond lengths (\AA) and angles ($^\circ$), where structures A-C are the cationic (doublet) structures; D-F, neutral singlet; G-I, neutral triplet, and J-M are anionic (doublet) structures.	222
Figure 8.3	B3LYP predicted ternary $[\text{O}_2\text{Au}_2\text{CO}]^q$ ($q=+1, 0, -1$) complexes with bond length (\AA) and angles ($^\circ$).	224
Figure 8.4	B3LYP predicted ternary $[\text{O}_3\text{Au}_2\text{CO}]^q$ ($q=+1, 0, -1$) complexes with bond length (\AA) and angles ($^\circ$), where A-G are separated complexes, H is a “pre-reactive in” (or peroxy carbonyl) complex and I-K are O_3 “insertion” complexes.	230
Figure 8.5	Possible oxidation pathway for neutral (singlet) $\text{O}_3\text{Au}_2\text{CO}$ with concerted O_3 molecule. The “reactant-side” minima is 8.3 B, the global minimum for the “separated” $\text{O}_3\text{Au}_2\text{CO}$ (singlet) complexes.	236
Figure 8.6	Selected higher lying orbitals showing σ -donation and π -backbonding character for binary and ternary complexes: A) $[\text{Au}_2\text{CO}]^+$ (Au_2CO singlet is similar); B) Au_2CO triplet; c) $[\text{Au}_2\text{CO}]^-$; D) $\text{O}_2\text{Au}_2\text{CO}$ singlet (Figure 8.2 B); E) $\text{O}_2\text{Au}_2\text{CO}$ triplet (Figure 8.2 C); F) $[\text{O}_2\text{Au}_2\text{CO}]^-$. For open spin species (B, C, E, F), only the α -spinorbitals are shown.	236

LIST OF TABLES

Table 3.1 Calculated stretching vibrational frequencies in cm^{-1} and intensities (in parentheses) of optimized binary and ternary complexes ^{a,b} for B3LYP-SDD/6-311+G(3df).	49
Table 3.2 ZPE and BSSE corrected binding energies ^a for cationic, neutral and anionic binary and ternary complexes ^{b,c} calculated with the B3LYP-SDD/6-311+G(3df) in kcal/mol and cooperative binding evaluated as a function of like charges.	52
Table 3.3 Calculated bond lengths (in Å) for binary and ternary complexes ^{a,b} with B3LYP-SDD/6-311+G(3df).	53
Table 3.4 Calculated shifts in vibrational frequencies (in cm^{-1}) of optimized binary and ternary complexes ^{a,b} in B3LYP-SDD/6-311+G(3df).	54
Table 3.5 Hirshfeld charges per fragment ^a calculated from the Hirshfeld population analysis for cationic, neutral and anionic binary and ternary complexes ^{b,c} calculated with B3LYP-SDD/6-311+G(3df).	74
Table 4.1 Calculated bond lengths (in Å) for reactant-side transition state complexes ^a with B3LYP-SDD/6-311+G(3df).	92
Table 4.2 Calculated stretching vibrational frequencies (in cm^{-1}) of the reactant-side transition states ^a for B3LYP-SDD/6-311+G(3df).	93
Table 4.3 Calculated bond lengths (in Å) for “major” transition state complexes ^a with B3LYP-SDD/6-311+G(3df).	93
Table 4.4 Calculated stretching vibrational frequencies (in cm^{-1}) of the “major” transition states ^a for B3LYP-SDD/6-311+G(3df).	96
Table 4.5 Calculated bond lengths (in Å) for ternary low barrier and post-reactive transition state complexes ^a with B3LYP-SDD/6-311+G(3df).	96
Table 4.6 Calculated stretching vibrational frequencies (in cm^{-1}) of ternary low barrier and post-reactive transition state complexes ^a for B3LYP-SDD/6-311+G(3df).	96
Table 4.7 Calculated bond lengths (in Å) for post-reactive and product complexes ^a with B3LYP-SDD/6-311+G(3df).	97
Table 4.8 Calculated stretching vibrational frequencies (in cm^{-1}) of ternary post-reactive and product complexes ^a for B3LYP-SDD/6-311+G(3df).	97
Table 5.1 Bond lengths (in Å) for ternary, reactant-side $[\text{O}_3\text{AuCO}]^q$ ^a complexes, $q=(+1,0,-1)$, calculated with B3LYP-SDD/6-311+G(3df).	117
Table 5.2 Vibrational frequencies (in cm^{-1}) of ternary ^a (reactant side) $[\text{O}_3\text{AuCO}]^q$ ($q=-1,0,+1$) complexes calculated with B3LYP-SDD/6-311+G(3df).	117
Table 5.3 Bond lengths (in Å) for O_3 oxidation transition state (O-TS) complexes ^a , $\{\text{AuCOO}_3\}^q$ $q=(+1,0,-1)$, calculated with B3LYP-SDD/6-311+G(3df).	123
Table 5.4 Vibrational frequencies (in cm^{-1}) for O_3 oxidation transition state (O-TS) complexes, $\{\text{AuCOO}_3\}^q$ $q=(+1,0,-1)$, calculated with B3LYP-SDD/6-311+G(3df).	123

Table 5.5 Bond lengths (in Å) for AuO oxidation, $\{\text{O}_2(\text{O})\text{AuCO}\}^q$ transition state complexes, $q=(+1,0,-1)$, calculated with B3LYP-SDD/6-311+G(3df).	124
Table 5.6 Vibrational frequencies (in cm^{-1}) for AuO oxidation, $\{\text{O}_2\text{OAuCO}\}^q$ transition state complexes, $q=(+1,0,-1)$, calculated with B3LYP-SDD/6-311+G(3df).	124
Tables 5.7 Bond lengths (in Å) for the post-reactive minima, $[\text{O}_2\text{AuOCO}]^q$ or $[\text{AuO}_2\text{CO}_2]^q$, complexes, $q=(+1,0,-1)$, calculated with B3LYP-SDD/6-311+G(3df).	129
Table 5.8 Bond lengths (in Å) for the post-reactive minima, $[\text{O}_2\text{AuOCO}]^q$ or $[\text{AuO}_2\text{CO}_2]^q$, complexes, $q=(+1,0,-1)$, calculated with B3LYP-SDD/6-311+G(3df).	129
Table 5.9 Bond lengths (in Å) for the product, $[\text{O}_2\text{AuCO}_2]^q$, complexes, $q=(+1,0,-1)$, calculated with B3LYP-SDD/6-311+G(3df).	130
Table 5.10 Vibrational frequencies (in cm^{-1}) of the products, $[\text{O}_2\text{AuCO}_2]^q$ ($q=+1,0,-1$), calculated with B3LYP-SDD/6-311+G(3df).	130
Table 6.1 B3LYP predicted stretching vibrational frequencies (in cm^{-1}) of optimized binary, $[\text{CuCO}]^q$ and $[\text{CuO}_2]^q$ and ternary, $[\text{O}_2\text{CuCO}]^q$ and $[\text{CuCOO}_2]^q$ complexes ($q=, +1, 0, -1$).	145
Table 6.2 B3LYP predicted bond lengths (in Å) of optimized binary, $[\text{CuCO}]^q$ and $[\text{CuO}_2]^q$ and ternary, $[\text{O}_2\text{CuCO}]^q$ and $[\text{CuCOO}_2]^q$ complexes ($q=, +1, 0, -1$).	146
Table 6.3 ZPE and BSSE corrected binding energies ^a (kcal/mol) of $[\text{CuCO}]^q$ and $[\text{CuO}_2]^q$ and ternary, $[\text{O}_2\text{CuCO}]^q$ and $[\text{CuCOO}_2]^q$ complexes ($q=, +1, 0, -1$) and cooperative binding evaluated for similarly charged complex groups predicted with B3LYP.	150
Table 6.4 Bond lengths (in Å) of reactant-side transition state complexes, $q=(+1,0,-1)$, calculated with B3LYP-SDD/6-311+G(3df).	156
Tables 6.5 Vibrational frequencies (in cm^{-1}) of the reactant-side transition state of $[\text{O}_2+\text{Cu}+\text{CO}]q^a$ complexes, $q=(+1,0,-1)$, calculated with B3LYP-SDD/6-311+G(3df).	162
Table 6.6 Bond lengths (in Å) for CuO oxidation and O_2 oxidation transition state complexes, $\{\text{CuCOO}_3\}^q$ $q=(+1,0,-1)$, calculated with B3LYP-SDD/6-311+G(3df).	162
Table 6.7 Vibrational frequencies (in cm^{-1}) for CuO oxidation and O_2 oxidation transition state complexes (from pre-reactive complexes), $\{\text{CuCOO}_3\}^q$ $q=(+1,0,-1)$, calculated with B3LYP-SDD/6-311+G(3df).	163
Table 6.8 Bond lengths (in Å) for post-reactive transition state, $\{\text{OCuO-CO}\}^q$, complexes, $q=(+1,0,-1)$, calculated with B3LYP-SDD/6-311+G(3df).	163
Table 6.9 Vibrational frequencies (in cm^{-1}) for post-reactive transition states, $\{\text{O}_2\text{OCuCO}\}^q$, $q=(+1,0,-1)$, calculated with B3LYP-SDD/6-311+G(3df).	164
Table 6.10 Bond lengths (in Å) for the product, $[\text{CuCO}_3]q$ or $[\text{OCuCO}_2]^q$, complexes, $q=(+1,0,-1)$, calculated with B3LYP-SDD/6-311+G(3df).	164
Table 6.11 Vibrational frequencies (in cm^{-1}) of the products, $[\text{O}_2\text{AuCO}_2]^q$ ($q=+1,0,-1$), calculated with B3LYP-SDD/6-311+G(3df).	165

Table 6.12 Bond lengths (in Å) for ternary, reactant-side $[\text{O}_3\text{CuCO}]^q$ complexes, $q=(+1,0,-1)$, calculated with B3LYP-SDD/6-311+G(3df).	170
Table 6.13 Vibrational frequencies (in cm^{-1}) of ternary ^a (reactant side) $[\text{O}_3\text{CuCO}]^q$ ($q=-1,0,+1$) complexes calculated with B3LYP-SDD/6-311+G(3df).	171
Table 6.14 Bond lengths (in Å) for O_3 oxidation transition state (O-TS) complexes ^a , $\{\text{CuCOO}_3\}^q$ $q=(+1,0,-1)$, calculated with B3LYP-SDD/6-311+G(3df).	177
Table 6.15 Vibrational frequencies (in cm^{-1}) for O_3 oxidation transition state (O-TS) complexes, $\{\text{CuCOO}_3\}^q$ $q=(+1,0,-1)$, calculated with B3LYP-SDD/6-311+G(3df).	177
Table 6.16 Bond lengths (in Å) for CuO (G-TS) oxidation, $\{\text{O}_2(\text{O})\text{CuCO}\}^q$ transition state complexes, $q=(+1,0,-1)$, calculated with B3LYP-SDD/6-311+G(3df).	178
Table 6.17 Vibrational frequencies (in cm^{-1}) for CuO oxidation, $\{\text{O}_2\text{OCuCO}\}^q$ transition state complexes, $q=(+1,0,-1)$, calculated with B3LYP-SDD/6-311+G(3df).	178
Table 6.18 Bond lengths (in Å) for the product, $[\text{O}_2\text{CuCO}_2]^q$ complexes, $q=(+1,0,-1)$, calculated with B3LYP-SDD/6-311+G(3df).	179
Table 6.19 Vibrational frequencies (in cm^{-1}) of the products, $[\text{O}_2\text{AuCO}_2]^q$ ($q=+1,0,-1$), calculated with B3LYP-SDD/6-311+G(3df).	179
Table 7.1 Peak assignments of main absorption frequencies (cm^{-1}) of ozone in argon for spectra taken at 10K. Resolution is 0.5 cm^{-1} for all peaks. Assignments were made based on previous assignments in the literature. ³⁴	197
Table 8.1 B3LYP predicted bond lengths (in Å) for binary $[\text{Au}_2\text{CO}]^q$ and $[\text{Au}_2\text{O}_2]^q$ and ternary $[\text{O}_2\text{Au}_2\text{CO}]^q$ or $[\text{Au}_2\text{COO}_2]^q$ complexes ($q=+1, 0, -1$).	223
Table 8.2 B3LYP predicted stretching vibrational frequencies in, cm^{-1} , and intensities (in parenthesis) for binary $[\text{Au}_2\text{CO}]^q$ and $[\text{Au}_2\text{O}_2]^q$ and ternary $[\text{O}_2\text{Au}_2\text{CO}]^q$ or $[\text{Au}_2\text{COO}_2]^q$. Labels A-F correspond to the structures shown in Figure 8.3.	223
Table 8.3 ZPE and BSSE corrected binding energies ^a (kcal/mol) for binary $[\text{Au}_2\text{CO}]^q$ and $[\text{Au}_2\text{O}_2]^q$ and ternary $[\text{O}_2\text{Au}_2\text{CO}]^q$ or $[\text{Au}_2\text{COO}_2]^q$ complexes ($q=+1, 0, -1$) and cooperative binding evaluated for similarly charged complex groups.	224
Table 8.4 B3PLYP predicted bond lengths (in Å) for binary $[\text{Au}_2\text{CO}]^q$ and $[\text{Au}_2\text{O}_2]^q$ and ternary $[\text{O}_2\text{Au}_2\text{CO}]^q$ or $[\text{Au}_2\text{COO}_2]^q$ complexes ($q=+1, 0, -1$).	231
Table 8.5 ZPE and BSSE corrected binding energies ^a (kcal/mol) for binary $[\text{Au}_2\text{CO}]^q$ and $[\text{Au}_2\text{O}_3]^q$ and ternary $[\text{O}_3\text{Au}_2\text{CO}]^q$ complexes ($q=+1, 0, -1$) and cooperative binding evaluated for similarly charged complex groups.	232
Table 8.6 B3LYP predicted stretching vibrational frequencies in cm^{-1} for binary $[\text{Au}_2\text{O}_3]^q$ and ternary $[\text{O}_3\text{Au}_2\text{CO}]^q$. Labels A-I correspond to Figure 8.4.	233

ABSTRACT

This dissertation is focused on the calculations of potential energy surfaces for carbon monoxide (CO) oxidation mechanisms with oxygen allotropes (O₂ and ozone, O₃) on monoatomic and diatomic metals. Density functional theory (DFT) calculations have been completed on the interactions of CO and oxygen allotropes with monoatomic and diatomic copper and gold species with charges of +1, 0, and -1 at the B3LYP-SDD/6-311+G(3df) level of theory. Major conclusions, structures and pathways were verified with double-hybrid DFT methods. Trends were also investigated for different DFT functionals and basis sets and the results were in general agreement with the B3LYP result. The computational work is an effort to build a comprehensive set of complexes for aforementioned charge and size, calculated at the same level of theory.

Calculations for monoatomic Au showed cooperative binding in the interactions of [O₂AuCO]^q and [O₃AuCO]^q (q=+1, 0, -1) along with identification of new minima and transition states along the CO-oxidation pathway(s). The reaction pathways were verified with intrinsic reaction coordinate (IRC) calculations to verify the transition states and minima connected along the potential energy surface. *Ab initio* molecular dynamics (AIMD) calculations were completed for the [O₂+Au+CO]^q pathways to determine if the reaction pathways would be (approximately) followed. Both O₂ and O₃ systems show similarities in the minima and transition states of pathways across charge and spin states; there are also similarities between structures in the two oxygen allotrope systems, where a number of the O₃ structures look very similar to the O₂ structures with an additional O atom. The ozone pathways show an ozone-concerted mechanism as favorable to singlet and doublet spin states, while triplet states show preference for stepwise Au oxidation by

O₃ and subsequent AuO oxidation of CO. Calculations of [CuCO]^q, [CuO₂]^q, [O₂CuCO]^q, [O₃CuCO]^q and [CuO₃]^q complexes and reaction pathways have shown very similar complexes and reaction pathways to the atomic Au systems. However, there are some differences with respect to the energetically favorable pathways and minima between the two elements.

The complexes of O₂ (O₃), CO and diatomic Au^q has also been calculated to further understand the affect of size and charge on the interactions of CO and O₂ (O₃) and to look for trends in the structures and energies of the calculated complexes. Similar complexes were observed in the atom and dimer systems; the [O₃+Au₂+CO] reaction pathway also shows a pathway that is reminiscent of the Au atomic pathway.

Observation of like complexes and pathway for mono- and diatomic gold suggests that trends in the CO oxidation mechanism as a function of size exist. Anti-cooperativity of binding was calculated for all [O₂Au₂CO]^q complexes, where it is not energetically favorable to bind both CO and O₂ to Au₂^q; this anti-cooperativity may be important in the catalytic cycle.

The computational work is an effort to support matrix-isolation experiments, probed with infrared spectroscopy (FT-IR). Matrix-isolation experiments have been utilized to test interactions of copper anions with O₃ (and CO) in an overall neutralized Ar matrix (with Ar⁺). Results have shown very small peaks related to CuO₃ and copper carbonyls, Cu(CO)⁻ and Cu(CO)₃⁻ and peaks associated with O₃⁻ (ozonide) and ionic O₄ complexes (O₄⁻ and O₄⁺) are also observed; however, the very low intensity of the copper complex peaks and the (much) higher intensities of the “parent” peaks (O₃ and/or CO) lead to questions about what is happening to the Cu ions. The observation of O₄ ionic

complexes indicates that ozone is decomposing. For O₃ only (and O₃:CO) experiments, it is probable that O₃ is oxidizing Cu⁺ to form copper oxides, which are not observable with our current IR set-up. The formation of copper oxides would also explain the observation of very small (to no) copper carbonyl peaks in the IR spectra with O₃:CO mixes.

Chapter 1. Catalysis of CO Oxidation with Gold (Au) Nanoparticles

1.1 Motivation and Introduction

One application of CO-oxidation catalyzed by Au is hydrogen fuel cell technology. The utilization of hydrogen fuel cells is an option to lower dependence on fossil fuels for means of transportation and electricity generation. Development and integration of polymer electrolyte membrane fuel cells (PEM) into these systems are important pieces of the puzzle; however, the platinum catalyst in these cells can become poisoned, or passivated, by carbon monoxide (CO) over time.¹ Since hydrogen is prepared often from sources like gasoline and ethanol, the production process can lead to CO contamination in the hydrogen gas. When the H₂ gas enters the PEM fuel cell, CO, even very low concentrations, can adsorb onto the Pt catalyst. One way to overcome this passivation is to oxidize CO to carbon dioxide (CO₂) using gold (Au) nanoparticles (NPs) as the catalyst.

Metal oxide supported gold (Au) nanoparticles (NPs)

Metal oxide supported Au NPs (or clusters), such as Au/TiO₂, have been investigated and found to have high activity for CO oxidation. Unsupported Au NPs have also been examined for CO oxidation and were found to possess measurable activity for the oxidative process. In supported Au NP systems, particles with a diameter of approximately 5 nm have high activity for CO oxidation.¹ Through studies on metal oxide supported Au NPs, Haruta determined that these systems had high activity for several oxidation reactions, including CO oxidation.¹ Further studies of CO oxidation found that the activity of the supported Au NPs depends on the type of support, nanoparticle size, and shape of the nanoparticles on the support surface.¹ Many groups have studied CO oxidation over supported Au NPs, both experimentally and

theoretically, and have discussed probable locations for the active site on the Au cluster. Bond and Thompson suggested a probable active site at an edge or perimeter for Au clusters supported on MgO. The mechanism suggests that a vacancy in the support facilitates the reaction by adsorbing an oxygen molecule, which can interact with adsorbed CO.²

Similarly, Haruta also postulated a set of reaction pathways to occur on hemispherical Au NPs supported on TiO₂ with dependence on the temperature regime (< 200K, 200 to 300K, and > 300K).¹ Below 200K, the TiO₂ surface and the perimeter interfaces of Au and TiO₂ are covered with carbonate species, which are formed by reactions of CO with the surface. In all temperature regimes, the CO oxidation reaction only occurs on the Au surface and not on the TiO₂ support.¹

Another crucial question regarding the mechanism is the role of the charge on the gold cluster. On one hand, studies of model catalysts supported on MgO suggest that the active sites may correspond to gold clusters interacting with electrons trapped in surface defects of the oxide.³⁻⁶ The extra electron density acquired by these clusters is then thought to specifically⁴ catalyze the breaking of the O-O bond during the reaction.⁷ On the other hand, it has also been proposed that for the strongly-wetted Au NPs on highly oxidized supports like TiO₂ and Fe₂O₃, the strong Au-O interactions at the particle/support interface lead to a partial positive charge developing on the gold cluster.⁸ Experimental studies have shown that cationic gold is essential for activity of Fe₂O₃-supported gold,⁹ while a theoretical study has predicted a full catalytic cycle for CO oxidation on TiO₂-supported Au₇ clusters with partial positive charges.⁸

Unsupported Au Nanoparticles

Much can be learned from studying unsupported Au NPs and be applied to questions about supported Au NPs. Haruta has discussed that strong interaction between the Au NPs and the metal oxide support is necessary for successful and high activity for CO oxidation through stabilization of the small Au NPs by having a wide contact area and providing a large perimeter area.¹⁰ The metal oxides acting as supports can withdraw, e.g., TiO₂, or donate electron density to the Au NPs and provide sites at the perimeter of the hemispherical Au NP where reactants can be activated and involved in the catalytic reaction. Studying charged (positively and negatively) and neutral unsupported Au NPs can offer insight into how the support perturbs the ideal structures and electron density of Au NPs. Unsupported Au NPs have also been investigated for their own catalytic activity for CO oxidation, and have been reported less active than supported Au NPs,¹ but are still active as a catalyst for CO oxidation. For example, unsupported Au powder with an average particle diameter of 17 nm exhibits measurable activity for CO oxidation around 200K;¹ however, unsupported Au NPs can be synthesized with smaller diameters.

Since NP size is known to have an effect on catalytic properties of supported Au NPs, research into size-selected, unsupported Au NPs has been completed and shown an odd-even relationship for the catalytic activity for CO oxidation.¹¹ Wallace and Whetten have studied O₂ and CO co-adsorption on unsupported, gas phase anionic Au clusters, Au_N⁻, where N=2-20.¹¹ They noted that CO had size-dependent reactivity with the anionic clusters sized N=4-19, but no reaction for the dimer or trimer Au anions.¹¹ Yet,

molecularly adsorbed O₂ showed odd-even reactivity, in which O₂ showed varying reactivity with even N clusters and no reactivity with odd N clusters.¹¹

Unsupported Au Cluster Mechanisms

Other mechanisms for CO oxidation over unsupported Au NPs also have been proposed for small-sized Au NPs, where the NP structure was designed from experimental results of metal-oxide supported Au NPs. One such mechanism has been proposed by Lopez and Norskov, in which they utilize an unsupported Au₁₀ cluster designed from an experimental Au₁₀/TiO₂ catalyst as the model.^{12, 13} Therefore, this cluster was not designed in the most stable conformation for an unsupported cluster, but with a hemispherical shape formed on the TiO₂ support.¹³ This mechanistic model showed two possible pathways for CO oxidation, in which one involves molecular O₂ adsorption and the other features O₂ dissociation. The model indicated that O₂ adsorbs first and the dissociation pathway occurs after the adsorption of CO. Following these steps, their pathway splits because O₂ remained molecularly adsorbed or dissociated; however, the energy barrier of oxygen dissociation was highly dependent on the geometry of the Au cluster.¹³ In the dissociated oxygen pathway, CO migrated to one of the oxygen atoms attached to an edge of the Au cluster and formed CO₂ in the final complex. In the molecular O₂ pathway, there was direct coupling between CO and O₂, forming the final complex of CO₂ and [Au-O].¹² While different numbers of steps define the molecularly adsorbed and dissociated O₂ reaction pathways, each began and ended with approximately equal energy.

Based on the aforementioned experimental results, Wallace and Whetten proposed a mechanism in the form of a catalytic cycle for gas phase CO oxidation over

an anionic hexamer cluster, Au_6^- , which was chosen due to its high CO reactivity that is on the order of the Au_{16}^- cluster. Utilizing the calculated equilibrium structure of Au_6^- , they proposed a catalytic cycle from experimental results detected with mass spectrometry. Molecular O_2 is adsorbed first onto the bare Au_6^- , similar to the Lopez and Norskov pathway model, and resides as a superoxide (O_2^-).¹¹ Subsequently, CO is adsorbed onto the cluster to form a complex with a mass related to $\text{Au}_6\text{COO}_2^-$ and through CO or O_2 migration, they form a CO_3^- intermediate structure.¹¹ The system releases a CO_2 molecule and a single anionic oxygen atom on the Au_6^- remains, corresponding to the mass of Au_6O^- of step. Next, a second CO molecule adsorbs, produces a complex of Au_6CO_2^- , upon which CO_2 can desorb, and return to bare Au_6^- .¹¹

Another mechanism was proposed by Bernhardt *et al.* for CO oxidation over anionic gold dimers, Au_2^- , from kinetic measurements and density functional theory (DFT) calculations. A single O_2 molecule is adsorbed onto the dimer with a partial electron transfer from Au into the antibonding π -orbital of O_2 to form $[\text{Au}_2\text{O}_2]^-$ with a superoxide O_2 species, which also was indicated to occur in the Wallace and Whetten catalytic cycle.¹⁴ CO can co-adsorb on $[\text{Au}_2\text{O}_2]^-$ and form a carbonate, $[\text{Au}_2\text{CO}_3]^-$, or peroxyformate complex, $[\text{AuCOO}_2]^-$.¹⁴ Another CO molecule can adsorb and react to release two CO_2 molecules and return to bare Au_2^- .¹⁴

Neutral, cationic and anionic Au atoms have been investigated for CO oxidation.¹⁵⁻²³ Neutral Au atoms with CO and O_2 have been studied with matrix isolation experiments and calculations. Matrix isolation spectroscopy, in which gases and neutral Au atoms are deposited into a rare-gas matrix to trap and isolate intermediate complexes, has been used to study the three-component system ($\text{CO} + \text{O}_2 + \text{Au}$). Ozin and co-

workers utilized a Knudsen cell, a deposition source that produces neutral atoms, and have identified an OCAuCOO_2 (carbonylperoxycarbonylaurate) intermediate, as well as the photoproduction of CO_2 upon UV-irradiation of the matrix.¹⁵ A more recent study by Xu and Jiang using laser-ablated gold atoms produced similar results and also reported observation of an O_2AuCO (monocarbonyldioxoaurate) complex; they used DFT calculations to support their structural assignments.²³ In a recent DFT computational study, Fang *et al.* utilized double-hybrid DFT methods to study the pathway of CO oxidation over neutral gold atoms; they observed a peroxycarbonyl (AuCOO_2) structure as an intermediate, which is similar to the structures suggested by Woste *et al.* for larger, anionic clusters, but did not calculate a “carbonate-like” structure, nor explore the separated structures like those identified by Xu and Jiang.¹⁸

Many of these unsupported Au NP mechanisms discussed above have been formulated from mass spectrometry and/or calculation results. The mechanisms developed by Wallace and Whetten and Bernhardt *et al.* employ gas-phase reactions of Au NPs with CO and O_2 , which are analyzed by mass spectrometry. Mass spectrometry can produce information about the observed complex masses, which can be correlated to molecular formulas; however, no information about how the CO and O_2 are bonded to Au NPs is recoverable. Comparatively, studies with matrix isolation commonly utilize infrared spectroscopy (FT-IR), which provides structural information about how CO and O_2 are bonded to the Au atom or clusters and to one another. Finally, although calculations can produce fairly accurate results, these mechanisms need verification with experimental studies, especially spectroscopic studies for true understanding of the systems.

CO Oxidation with Ozone

Ozone, a reactive allotrope of oxygen, has been often utilized with UV light to clean surfaces or oxidize surfaces, especially for oxidative catalysis. CO oxidation by ozone has investigated without catalysts, with homogeneous catalysts, like methane, and heterogeneous catalysts, such as single crystal metals, metal nanoparticles and metal oxide surfaces.^{19, 20, 24-35} The direct reaction of CO and O₃ has been described as immeasurably slow at room temperature,^{25, 26} but impurities, especially methane,^{24, 26} and temperature have been shown to significantly increase the reaction rate. The kinetics and mechanism of O₃ and CO reaction has been studied at elevated temperatures (75-160°C); results indicate that the reaction occurs in two major steps, as follows: decomposition of O₃ first (to O₂ and O) and oxidation of CO by an O atom.^{25, 26}

Ozone has been used in different applications of CO oxidation on Au catalysts. In many experiments, ozone has been utilized as a pretreatment to clean the surface or pre-adsorb oxygen species to the Au surface.³⁶ Oxidation of CO with O₂, catalyzed by (supported) Au nanoparticles, has been studied to understand the active site, mechanism and role of the support, based on the findings of Haruta *et al.*¹ Similarly, the decomposition of O₃ has been observed to occur on metals, such as Pt and Au, metal oxides, and metal-oxide supported Pt and Au nanoparticles.³⁰⁻³³

Some investigators, including Samano *et al.* and Kim *et al.*, have used ozone to form a monolayer of oxygen species on Au(211) surface to study adsorption sites of oxygen adatoms and CO oxidation kinetics.²⁹ Kim *et al.* utilized the Au(211) surface to investigate possible dissociative adsorption of O₂ and O₃ due to the high density of step sites on the Au(211) surface. They determined that Au(211) is active for dissociation of

O₃, but not O₂, and the chemistry for surface oxygen is similar to other bulk Au surfaces, such as Au(111); however, they did not study interactions of CO with the oxygen-covered Au surface.^{28, 37} In a later paper, they utilized O₃ to pre-adsorb oxygen adatoms on Au(211) and found that the rate of oxidation depended on the surface oxygen concentration and initial conditions of the system. They chose a Langmuir-Hinshelwood mechanism to describe their system; however, they also reported that CO oxidation over Au(211) was not significantly enhanced or different from that on Au(111) or Au(110).^{27,}
²⁹ Conversely, Hao *et al.* studied the applicability of Fe₂O₃-supported Au NPs as a catalyst for simultaneous ozone decomposition and CO oxidation under various conditions, such as excess CO, excess O₃ or stoichiometric amounts of each, which could cause different reactions to occur between CO and O₃ based on those aforementioned concentrations.³⁴ They discussed the existence of carbonate species on the surface and mention that the reaction mechanism involves active surface oxygen species, but did not investigate the intermediates or what mechanism may occur.³⁴

Similar to the use of unsupported Au NPs in the O₂ studies, unsupported Au nanoparticles, especially Au_n ions, can be utilized to understand how the metal oxide support affects the electron density of the Au nanoparticles and the role of Au in the catalytic process. Castleman and coworkers conducted room-temperature flow-reactor mass spectrometry experiments to understand the reactivity of oxygen species and Au ions with CO.^{19, 20, 22, 35, 38} For anionic Au atoms, they found that AuO⁻ and AuO₃⁻ species, produced in their laser ablation plasma were reactive for CO and AuO₂⁻ was not.¹⁹ Supporting DFT calculations predicted barriers lower than the energy of reactants for the AuO⁻ and AuO₃⁻ cases and the AuO₂⁻ species was spin-forbidden with a higher

barrier.¹⁹ In general, cationic gold clusters have been thought to be less active than anionic clusters for CO oxidation; however, the Castleman group detected gas phase intermediates with masses corresponding to Au_nO_m^+ ($n=1-2, m=2-3$) and subsequent introduction of CO to pre-oxidized cationic species led to the formation of $\text{Au}_n\text{O}_m(\text{CO})_x^+$ ($n=1-2, m=0-3, x=0-2$) complexes.²⁰ Based on these experiments and related DFT calculations, the stronger binding of CO to cationic gold may act in an autocatalytic fashion, with the large complexation energy of the COs serving to drive the system over low barriers in a Langmuir-Hinshelwood type mechanism.²² This scenario is in contrast to that for the anionic clusters, which are predicted to react in an Eley-Rideal type fashion.²²

1.2 Project Goals

The specific goals of my project are to use a dual-pronged approach of calculation and experiments to study metal clusters with CO and oxygen species, especially O_2 and ozone, in an effort to evaluate the hypothesis that pre-reactive complexes of unsupported Au NPs, CO and O_2 (or ozone), predicted by calculations, can be verified to exist, stabilized and characterized using Fourier Transform Infrared (FT-IR) spectroscopy. Along with understanding the mechanisms over specifically sized Au clusters, we are also studying differently charged and sized unsupported Au NPs to elucidate trends in the mechanism with computational and experimental studies. Although many O_2 , CO and Au_n clusters have been (computationally) calculated individually for a certain charge and/or size, there has not been a detailed investigation exploring all conformers for all charge states of single atoms and dimers. With this in mind, we utilized the same level of theory in our calculations across all charges (cationic +1, anionic -1, and neutral), sizes

(atoms and dimers), and metal species (Cu or Au) to allow for comparison of all results, to build on (and compare with) the previously calculated structures and pathways, and provide original research on CO oxidation with ozone and metal atoms (and dimers).

1.3 References

- (1) Haruta, M. *Cattech* **2002**, *6*, 102.
- (2) Bond, G. C.; Thompson, D. T. *Gold Bulletin* **2000**, *33*, 41.
- (3) Sanchez, A.; Abbet, S.; Heiz, U.; Schneider, W.; Hakkinen, H.; Barnett, R.; Landman, U. *J. Phys. Chem. A* **1999**, *103*, 9573-9578.
- (4) Yoon, B.; Hakkinen, H.; Landman, U.; Worz, A. S.; Antonietti, J. M.; Abbet, S.; Judai, K.; Heiz, U. *Science* **2005**, *307*, 403-407.
- (5) Sterrer, M.; Yulikov, M.; Fischbach, E.; Heyde, M.; Rust, H. P.; Pacchioni, G.; Risse, T.; Freund, H. J. *Angew. Chem., Int. Ed.* **2006**, *45*, 2630-2632.
- (6) Ricci, D.; Bongiorno, A.; Pacchioni, G.; Landman, U. *Phys. Rev. Lett.* **2006**, *97*.
- (7) Arenz, M.; Landman, U.; Heiz, U. *Chemphyschem* **2006**, *7*, 1871-1879.
- (8) Wang, J. G.; Hammer, B. *Phys. Rev. Lett.* **2006**, *97*, 4.
- (9) Hutchings, G. J.; Hall, M. S.; Carley, A. F.; Landon, P.; Solsona, B. E.; Kiely, C. J.; Herzing, A.; Makkee, M.; Moulijn, J. A.; Overweg, A., et al. *J. Catal.* **2006**, *242*, 71-81.
- (10) Haruta, M. *Catal. Surv. Japan* **1997**, *1*, 61-73.
- (11) Wallace, W. T.; Whetten, R. L. *J. Am. Chem. Soc.* **2002**, *124*, 7499-7505.
- (12) Remediakis, I. N.; Lopez, N.; Norskov, J. K. *Appl. Catal., A* **2005**, *291*, 13-20.
- (13) Lopez, N.; Norskov, J. K. *J. Am. Chem. Soc.* **2002**, *124*, 11262-11263.
- (14) Bernhardt, T.; Socaciu-Siebert, L.; Hagen, J.; Woste, L. *Appl. Catal., A* **2005**, *291*, 170-178.
- (15) Huber, H.; McIntosh, D.; Ozin, G. A. *Inorg. Chem.* **1977**, *16*, 975-979.
- (16) McIntosh, D.; Ozin, G. A. *Inorg. Chem.* **1977**, *16*, 51-59.
- (17) Jiang, L.; Xu, Q. *J. Phys. Chem. A* **2005**, *109*, 1026-1032.
- (18) Fang, H.; Li, Z. H.; Fan, K. *Phys. Chem. Chem. Phys.* **2011**, *13*, 13358-13369.
- (19) Kimble, M. L.; Castleman, A. W., Jr.; Mitric, R.; Burgel, C.; Bonacic-Koutecky, V. *J. Am. Chem. Soc.* **2004**, *126*, 2526-2535.
- (20) Kimble, M.; Castleman, A. *Int. J. Mass Spectrom.* **2004**, *233*, 99-101.
- (21) Liang, B.; Andrews, L. *J. Phys. Chem. A* **2000**, *104*, 9156-9164.
- (22) Burgel, C.; Reilly, N. M.; Johnson, G. E.; Mitric, R.; Kimble, M. L.; Castleman, A. W., Jr.; Bonacic-Koutecky, V. *J. Am. Chem. Soc.* **2008**, *130*, 1694-1698.
- (23) Xu, Q.; Jiang, L. *J. Phys. Chem. A* **2006**, *110*, 2655-2662.
- (24) Arin, L.; Warneck, P. *J. Phys. Chem.* **1972**, *76*, 1514-1516.
- (25) Toby, S.; Ullrich, E. *Int. J. Chem. Kinet.* **1980**, *12*, 535-546.
- (26) Toby, S.; Sheth, S.; Toby, F. *Int. J. Chem. Kinet.* **1984**, *16*, 149-157.
- (27) Parker, D. H.; Koel, B. E. *J. Vac. Sci. Technol., A* **1990**, *8*, 2585-2590.
- (28) Kim, J.; Samano, E.; Koel, B. E. *Surf. Sci.* **2006**, *600*, 4622-4632.
- (29) Samano, E.; Kim, J.; Koel, B. E. *Catal. Lett.* **2009**, *128*, 263-267.
- (30) Naydenov, A.; Mehanjiev, D.; Andreeva, D.; Tabakova, T. *Oxidation Commun.* **2003**, *26*, 492-495.

- (31) Naydenov, A.; Stoyanova, R.; Mehandjiev, D. *J. Mol. Catal. A: Chem.* **1995**, *98*, 9-14.
- (32) Naydenov, A.; Konova, P.; Nikolov, P.; Klingstedt, F.; Kumar, N.; Kovacheva, D.; Stefanov, P.; Stoyanova, R.; Mehandjiev, D. *Catal. Today* **2008**, *137*, 471-474.
- (33) Egorova, G.; Voblikova, V.; Tkachenko, S.; Burenkova, L.; Sabitova, L.; Makhov, E.; Sabitov, D.; Lunin, V. *Russ. J. Phys. Chem.* **2003**, *77*, 1768-1772.
- (34) Hao, Z.; Cheng, D.; Guo, Y.; Liang, Y. *Appl. Catal., B* **2001**, *33*, 217-222.
- (35) Kimble, M. L.; Castleman, A. W.; Burgel, C.; Bonacic-Koutecky, V. *Int. J. Mass Spectrom.* **2006**, *254*, 163-167.
- (36) Menard, L. D.; Xu, F.; Nuzzo, R. G.; Yang, J. C. *J. Catal.* **2006**, *243*, 64-73.
- (37) Kim, J.; Samano, E.; Koel, B. E. *J. Phys. Chem. B* **2006**, *110*, 17512-17517.
- (38) Kimble, M. L.; Moore, N. A.; Johnson, G. E.; Castleman, A. W., Jr.; Burgel, C.; Mitric, R.; Bonacic-Koutecky, V. *J. Chem. Phys.* **2006**, *125*, 204311-1-204311-14.

Chapter 2. Computational Background and Methods and Experimental Methods

2.1 Computational Methods

Computational chemistry uses methods of theoretical chemistry to calculate electronic structure and properties of molecules and solids. The Schrodinger equation, $\hat{H}\Psi(\mathbf{R},\mathbf{r})=E\Psi(\mathbf{R},\mathbf{r})$, needs to be solved to gain information about the system, but it is very complex with the combined nuclear and electronic contributions. The Born-Oppenheimer approximation is utilized to separate the nuclear and electronic motions of the system, by taking account of the difference in mass of nuclei and electrons.¹ When nuclei move, electrons, because they are less massive and move faster, can respond nearly instantaneously; therefore, the nuclei appear stationary compared to the electronic motion. This approximation can be expressed mathematically by separation of the nuclear and electronic portions of the Hamiltonian. The full Hamiltonian is shown for an electron and nucleus;² z is the location of the electron and Z is the location of the nucleus,

Equation 2.1
$$\hat{H} = -\frac{\hbar^2}{2m_e} \frac{\partial^2}{\partial z^2} - \frac{\hbar^2}{2m} \frac{\partial^2}{\partial Z^2} .$$

This expression can be simplified to $\hat{H} = \hat{T}_e + \hat{T}_N + \hat{V}$. The Schrödinger equation can then be written, simply as $\hat{H}\Psi(z, Z)=E\Psi(z, Z)$. However, the nuclear and electronic components are going to be separated, so the total wavefunction can be represented by a product of the electronic and nuclear wavefunctions as shown below,

Equation 2.2
$$\Psi(z, Z) = \psi(z; Z)\chi(Z) ,$$

where $\psi(z;Z)$ indicates that the electronic wavefunction depends on the electron location and parametrically on the nuclear coordinates. Applying equation 2.2 to equation 2.1, or the more simplified version in the text ($\hat{H} = \hat{T}_e + \hat{T}_N + \hat{V}$) will lead to the following equation,²

Equation 2.3
$$\psi \hat{T}_N \chi + (\hat{T}_e \psi + \hat{V} \psi) \chi = E \psi \chi ,$$

where the operators are applied only to the wavefunctions with the same variable (i.e., \hat{T}_e is applied only to ψ , as χ does not depend on z , the electron location). If the nuclear coordinates are frozen, the following (electronic) equation results,

Equation 2.4
$$\hat{T}_e \psi + \hat{V} \psi = E_e(Z) \psi ,$$

which is the Schrödinger equation for an electron in potential V , which depends on the fixed location of the nuclei. Equation 2.4 can be substituted into Equation 2.3 and cancelling out ψ will produce the nuclear Schrodinger equation, $\hat{T}_N \chi + E_e \chi = E \chi$.² This separation allows the consideration of only the kinetic energy of the electrons in a system, and the nuclear kinetic energy can be ignored. This approximation greatly simplifies the calculations to the following electronic equation,

Equation 2.5
$$\hat{H} = \hat{T}_e - \hat{V}_{ne} + \hat{V}_{ee} ,$$

where \hat{T}_e represents the electronic kinetic energy, \hat{V}_{ne} is the potential energy of the electrons with respect to the nuclei, and \hat{V}_{ee} represents the (non-local) electron-electron repulsion. The purely nuclear contributions are not shown because this contribution is equivalent to zero with the Born-Oppenheimer approximation. *Ab initio* methods, such as Hartree-Fock calculations, and density functional theory use electronic wavefunctions in the forms of single electron molecular orbitals to solve the electronic Schrödinger equation.² Hartree-Fock calculations assume that the wavefunction of an N-body system can be approximated by a single Slater determinant, where a Slater determinant is a way to represent the system's wavefunction more concisely and also account for the Pauli exclusion principle.³ The variational method, upon which Hartree-Fock calculations are

built, is used to calculate the set of equations for the N orbitals (inside the Slater determinant), which is, in turn, used to solve for the wavefunction (Slater determinant) and energy. The Hartree-Fock method is also called the “self-consistent field” method because the calculations continue until the final energy calculated is “self-consistent” (i.e., identical) to the previous energy.² However, the Hartree-Fock method fails to account for electron correlation and also treats the electron-electron repulsion as an average, which produces less accurate energies.

2.1.1 Moller-Plesset Perturbation Theory

The second-order Moller-Plesset perturbation theory (MP2) is different from Hartree-Fock because MP2, as evidenced by its name, utilizes perturbation theory and Hartree-Fock is related to the variation principle.⁴ The MP2 method is known as a post-Hartree-Fock (HF) method, as it was designed to improve upon the HF method by including electron correlation.³ The MP2 method is a special application of the “normal” perturbation theory, as the MP2 zero-th order wavefunction is an eigenfunction of the exact Fock operator, which is the unperturbed operator in Hartree-Fock. For MP2, the second-order energy correction involves only the double excitations of electrons that have non-zero $H^{(1)}$ matrix elements to better estimate the true energy.²

2.1.2 Density Functional Theory

In density functional theory (DFT), which is less computationally expensive than post-Hartree-Fock (post-HF) calculations, the electronic energy is computed in terms of electron (probability) density, $\rho(r)$. The energy is calculated as a functional because the energy is a function of electron density, which is a function of position. The electron density can be represented by a sum of one electron orbitals in the Kohn-Sham

formalism,⁵ as shown in equation 2.6, where ϕ are the molecular orbitals, which will be discussed in more detail in the basis-sets section.

Equation 2.6
$$\rho = \sum_i^N \phi_i(r)$$

As stated above, the DFT-calculated (electronic) energy is a function of the electron density and also contains an electron-correlation term. The energy is calculated with reference to the Schrödinger equation with the addition exchange-correlation parameter in a self-consistent field manner, similar to HF. The DFT energy, shown in a simplified form in equation 2.7, can be understood as the sum of the (electronic) kinetic energy (\hat{T}_{ni}), electron-nuclear interaction (\hat{V}_{ne}), and Coulomb (or electron-electron) repulsion (\hat{V}_{ee}), and the exchange-correlation energy (E_{xc}),⁵ where exchange and correlation contributions are separate, but commonly represented together as E_{xc} .

Equation 2.7
$$E[p(\vec{r})] = \hat{T}_{ni} + \hat{V}_{ne} + \hat{V}_{ee} + E_{xc}$$

The exchange-correlation energy is calculated approximately and several approximations have been developed to provide more accurate energies, such as the local density approximation (LDA), local spin density approximation (LSDA), and generalized gradient approximations (GGA). The local density approximation for the exchange-correlation energy is represented by equation 2.8, where $\epsilon_{xc}[\rho(r)]$ is the exchange-correlation energy per electron in a homogeneous electron gas of constant density.^{5,6}

Equation 2.8
$$E_{XC} = \int \rho(r) \epsilon[\rho(r)] dr$$

Although a homogeneous electron gas does not mimic molecular structure well, the results can be surprising accurate. However, better approximations can be made to model the structures of atoms and molecules more accurately. The local spin density approximation (LSDA) is an extension of LDA to open-shell systems, where the

exchange-correlation energy depends on the spin density (difference in spin up and spin down electron densities) and the total electron density. The generalized gradient approximation (GGA) is also an adaptation of the LDA that accounts for inhomogeneity of the electron density, in which the non-local correction of the gradient of the electron density (moving away from the coordinate) is added to the exchange-correlation energy. The GGA exchange-correlation energy is shown (generally) in equation 2.9, where f is the GGA exchange-correlation function, ρ_{\uparrow} and $\nabla_{\rho_{\uparrow}}$ represent the spin up electron density and the gradient of the (spin up) electron density, respectively, and ρ_{\downarrow} and $\nabla_{\rho_{\downarrow}}$ represent the spin down electron density and gradient of this density.^{3, 5, 6} Calculations with GGA functionals have been shown to provide accurate and efficient methods for d-metal complex calculations.²

Equation 2.9
$$E_{XC}^{GGA} = \int d\tau f(\rho_{\uparrow}, \rho_{\downarrow}, \nabla_{\rho_{\uparrow}}, \nabla_{\rho_{\downarrow}})$$

Many functionals exist for DFT calculations, but some of the better-performing functionals include the hybrid-DFT functionals. The functionals are defined as hybrid DFT functionals based on the combination of exchange (and correlation) functionals utilized in the calculations. The exchange functional in hybrid-DFT functionals is a linear combination of Hartree-Fock and GGA exchange terms, which can be combined with the GGA correlation functional. A commonly used hybrid DFT functional, B3LYP, combines the Becke exchange functional, a generalized-gradient exchange functional with a fraction of exact Hartree-Fock exchange and the Lee, Yang, Parr correlation functional, which is a generalized-gradient correlation functional.⁴

2.1.3 Mixed Double Hybrid DFT

The mixed double-hybrid DFT functionals can be generally thought of as a combination of the variational method (DFT and Hartree-Fock portion) and perturbation theory (MP2). Specifically, these functionals add HF exchange and PT2 (second-order perturbation theory) correlation, and the perturbation correlation can correct for some of the HF exchange deficiencies and lower the self-interaction error.⁷ Two of the popular methods, which can be implemented in Gaussian 09 are B2PLYP and mPW2PLYP. The first double-hybrid functional, B2PLYP, is similar to the B3LYP hybrid-DFT functional, except B2PLYP adds in MP2 contributions and has less HF exchange. The second double hybrid functional, mPW2PLYP, utilizes the modified Perdew-Wang exchange functional, a fraction of HF exchange, and MP2 contributions to calculate a system's properties.⁸⁻¹⁰

2.1.4 Using Computational Methods to Investigate Minima on a Potential Energy Surface

Electronic structure calculations provide information about molecules and/or complexes, such as structural properties; furthermore, these methods can also be used to identify minima (and/or maxima) on potential energy surfaces of interest, such as $[\text{O}_2+\text{Au}+\text{CO}]^-$. For O_2AuCO^- , one of the first considerations is the ground electronic state of this system. Thinking about the components, CO and Au^- have singlet ground states (all electrons are paired) and O_2 has a triplet ground state (2 unpaired electrons), so it is probable that ground state of the complex is in a singlet or triplet spin state. As these spin states have different numbers of unpaired electrons (singlet vs. triplet), two separate Slater determinants will be formulated. For the singlet spin state, a representative, but greatly

simplified, Slater determinant (has two electrons of different spin in the same spatial orbital as follows,

$$\text{Equation 2.10} \quad \psi(r_1\alpha, r_1\beta) = \frac{1}{\sqrt{2}} \begin{vmatrix} \varphi_1(1)\alpha(1) & \varphi_1(2)\alpha(2) \\ \varphi_1(1)\beta(1) & \varphi_1(2)\beta(2) \end{vmatrix},$$

where φ_1 represents the first spatial orbital, α represents “spin up” or $m_s = +1/2$, and β represents “spin down” or $m_s = -1/2$. The triplet Slater determinant has two electrons of the same spin in different spatial orbitals and is represented,

$$\text{Equation 2.11} \quad \psi(r_1\alpha, r_1\alpha) = \frac{1}{\sqrt{2}} \begin{vmatrix} \varphi_1(1)\alpha(1) & \varphi_1(2)\alpha(2) \\ \varphi_2(1)\alpha(1) & \varphi_2(2)\alpha(2) \end{vmatrix},$$

where φ_1 represents the first spatial orbital, φ_2 is the second spatial orbital and α and β are the same as in Equation 2.10. To determine which spin state is lower in energy, electronic structure methods can be used to optimize the O_2AuCO^- (singlet and triplet) guesses into energetic minima and/or calculate the energy. When optimizing a structure in two different spin states, the resulting structures, energies, and vibrational frequencies will be different, and are used to determine the ground electronic state.

A search for structural isomers usually involves systematic changes in the attachment of O_2 to Au or CO, etc. from the initial hypothesized structures and calculations. With this survey of isomers (and spin states), the energies, structures, vibrational frequencies, electrostatic potentials and many other properties can be compared to gain understanding of the minima of the potential energy surface (PES) and determine the global ground state; trends can be observed as a function of charge, spin, or stoichiometry. For example, the structural data (bond lengths and angles), vibrational frequencies and electrostatic potentials of O_2AuCO^- can be compared with respect to the same charge, and trends may emerge relating the number of unpaired electrons and these

parameters. The molecular orbitals can also be examined for differences as a function of spin state.

2.1.5 Gaussian Program

The Gaussian 09 suite of computational methods was used to study the structures at critical points along the reactions pathways of Au atoms (ions and clusters) with CO, O₂ and/or O₃ with density functional theory (DFT).¹¹ Hybrid-DFT method/functionals were used in our calculations for d-metal complexes, specifically B3LYP, mPW1PW91, and B3PW91, of which the latter two are often used for testing anomalies in structures. Structural verification was also completed with other methods, including MP2, mixed double-hybrid methods (B2PLYP), and some coupled-cluster calculations (CCSD or CCSD(T)), where CCSD calculations were used in the difficult binary gold complexes, AuCO⁻ and AuO₂, which are discussed in Chapter 3 and Appendix A3. Utilizing one of the above computational methods, several calculations can be completed, to focus specifically on stability, minimum or transition state geometry, frequency, energy, intrinsic reaction coordinate, and molecular dynamics simulations.

2.1.6 Basis Sets

Basis sets are the mathematical functions from which a wavefunction, or electron densities in the Kohn-Sham formalism of DFT, can be constructed.^{3, 12} When studying molecules, basis functions are representative of the atomic orbitals (χ_i), where the linear combination of the atomic orbitals form the molecular orbitals (φ_i) (or basis sets) and is represented by Equation 2.12.

Equation 2.12

$$\varphi_i(r) = \sum_{\mu}^n c_{\mu i} \chi_{\mu}(r)$$

It is important to note that these single-electron atomic orbitals are also commonly described by a linear combination of basis sets to better approximate the electron density, as shown in Equation 2.13 for contracted Gaussian-type orbitals (c-GTO), where N is the normalization factor, c is a constant, x, y, and z are Cartesian coordinates of the electron (orbital), a, b, and c represent the angular momentum, and ζ is the diffusivity of the function.^{3, 12}

Equation 2.13
$$\chi_{abc}^{CGTO}(r) = N \sum_{i=1}^n c_i x^a y^b z^c e^{-\zeta_i r^2}$$

In the DFT calculations, a Pople basis set of 6-311+G(3df), generally described as a polarized, diffuse, triple-zeta, split-valence basis set, was utilized to describe carbon and oxygen atoms.^{13, 14} The first section of the Pople basis set, 6-311, splits the core and valence electrons functions and assigns the number of primitive functions, denoted as G, to the “core” electrons (6 functions) and the number of c-GTOs for the valence electrons (311). In this case, primitive functions are the Gaussian functions inside of the c-GTO (Equation 2.13). The splitting of the core and valence electrons/functions is known as a split valence basis set, as core electrons are not involved in bond breaking and formation. The “311” section is known as a triple-zeta basis set, in which three basis functions are used for each (valence) orbital-type; the numbers indicate the number of primitive functions per c-GTO, so that c-GTO has three primitive functions, and the second and third c-GTOs each have one primitive function. Polarization functions, denoted as 3df in the Pople basis set above, contribute higher orbitals (or functions of higher angular momentum) than those occupied in the atoms, which allows the orbitals to distort from their original atomic symmetry to better adapt to the molecular environment. Finally, diffuse functions, denoted by +, contribute additional, large versions of s and p-type

functions to assist in modeling orbitals (electrons) far from the nucleus. The application of diffuse functions is especially important for molecules with lone pairs, anions, and excited states, which is applicable to the study of molecular ions, such as O_2^- and CO_2^+ .

While the Pople basis sets can describe the lower-mass elements well, these basis sets are less accurate for higher mass, relativistic elements, such as transition metals. Since transition metals, such as Au, have relativistic effects at the core due to the faster moving electrons, more sophisticated basis sets are necessary. Effective core potential basis sets (ECP) with relativistic corrections better approximate transition metals. These basis sets replace the core electron functions with analytical functions (potential) that represent a combined nuclear-electronic core to the valence electrons.³ These relativistic corrections are incorporated by fitting the potentials to atomic calculations that explicitly incorporate these effects. Two common and reliable ECPs are LANL2DZ and SDD, which utilize the Stuttgart-Dresden relativistically-corrected effective core potential basis for transition metals.^{15, 16}

2.1.7 Types of Calculations and Their Applications:

Stability

Stability calculations are utilized to evaluate the stability of a single-determinant-DFT wavefunction by relaxing various constraints, such as reducing the symmetry of orbitals and the system.¹² The wavefunction is computed in this type of calculation and then is evaluated to determine if it is a local minimum with the specified degrees of freedom. If the wavefunction is unstable, it will be re-calculated by relaxing the constraints, until a stable wavefunction is determined. The stable function can then be utilized in geometry-optimization calculations.

Exploring the Potential Energy Surface with Geometry Optimizations and Calculating Vibrational Frequencies

Geometry optimizations are computed to find critical points along a PES, in which the energy is minimized for local or global minima or maximized to find transition states.¹⁷ Energy is calculated iteratively until there is no decrease in energy or the decrease is smaller than the set threshold value. The energy of the system is calculated; then the gradient of the energy is calculated to determine the next step, or if another step is necessary. This process continues iteratively until the slope is zero or increases in all directions, which characterizes a stationary, or critical, point; however, zero gradient does not differentiate between minima, maxima, or saddlepoints. Therefore, the 2nd derivative of energy with respect to nuclear coordinates is calculated to determine the slope around the stationary point and whether it is a minimum, maximum, or saddlepoint.

After optimizations, (harmonic) vibrational frequencies are calculated from the force constants, which are the 2nd derivatives of energy with respect to nuclear coordinates. The number of negative frequencies, known as imaginary frequencies and calculated from the negative, if any, force constants, indicates whether a structure is a minimum (no imaginary frequencies), transition state (one imaginary frequency), or n-th order saddlepoint (n imaginary frequencies).¹⁷ A negative (or imaginary) frequency indicates that the structure is at a potential energy maximum, a transition state, and the vibration should correspond to the motion across the saddle point. The zero-point energy correction is also determined in the frequency calculation, and the optimization energy is the equilibrium energy at the bottom of the well, that is an over-estimation of the depth of the well. Application of the zero-point correction gives the energy of the ground state

and more accurate energies and reaction barriers, if minima and transition states are being investigated.

For geometry optimizations, certain program commands, also called keywords, are included in a Gaussian 09 input file for better performance of the DFT calculations; one such command is “tight.” Tight convergence criteria define values for maximum force, displacement, root mean squared (RMS) force and RMS displacement, which indicate the thresholds for the convergence to a critical point. Optimization is complete when the values of the four criteria fall below the thresholds for “tight” convergence. The tight criteria take longer to compute, but give better results. Efficiency of convergence depends on the quality of the initial guess for the calculation. By explicitly calculating the second derivatives of energy of the starting structure on the PES once at the beginning of the calculation (calcfc), initial guesses of force constants are generated and can be used in the optimization steps, as the constants do not change by much, unless there are significant geometric changes. The number of optimization cycles is another parameter (maxcyc) that can be altered because the default parameter does not always guarantee sufficient number of optimization cycles to reach convergence.

Calculation of transition states are also completed with geometry optimizations as discussed above; however, transition states require one imaginary frequency, which occurs when there is a negative force constant. In Gaussian 09, the synchronous transit-guided quasi-Newton method (STQN), developed by H.B. Schlegel and co-workers, is a method used to find transition states or maxima.¹⁸ Three main transition-state optimizations exist in the STQN method, the TS optimization, QST2 and QST3. The TS keyword requests optimization to a transition state, rather than a minimum, and starts

from an initial guess for the transition state. The QST2 keyword, quadratic synchronous transit 2, requires input of the reactant and product structures and the program will generate a transition state guess from these two molecular specifications. The QST3 keyword, also quadratic synchronous transit, requires input of the reactant and product structures and an initial guess at the transition state structure. It has been observed, in the following calculations and chapters, that calculations with QST3 input are most likely to converge, as more information is provided to the program. The aforementioned optimization keywords are also input for transition state calculations. Additional keywords, found in Appendix A2, may also be utilized in the transition-state calculations that are related to the self-consistent field convergence, commonly used to provide additional flexibility and time for the transition state to converge.

Single Point Energy (Counterpoise Correction)

The single-point energy calculations are the simplest and evaluate the energy of the input structures (molecule) at one particular set of nuclear coordinates. Energy calculations can be coupled with counterpoise corrections, which correct for basis-set superposition error, and population analyses on structures produced by geometry optimizations. Counterpoise corrections using the method of Boys and Bernardi,¹⁹ give the basis-set superposition error that results from the interactions of two molecules or atoms and molecules. If a system contains an Au atom and carbon monoxide (CO) molecule, each of these have their own (“monomer”) basis sets. As these two species interact, the electrons of one monomer borrow basis sets from the other, which forms an artificial polarization of electron density between the two species and increases the interaction. This borrowing of basis sets causes a superposition error, which can be

calculated and removed with counterpoise calculations. The counterpoise correction is shown in Equation 2.14 for two interaction monomers,

$$\text{(Equation 2.14)} \quad \Delta E_{corr}^{CP} = (E_A - E_A^{CP}) + (E_B - E_B^{CP}) ,$$

where E_A is the energy of monomer A in its own basis set and E_A^{CP} is the energy of monomer A in the “dimer” basis set (counterpoise corrected), and the same idea applies to monomer B energies. If the counterpoise-corrected energy matches the “monomer” energy, then the counterpoise correction is zero. Typically, there is some discrepancy, with counterpoise correction of 1 kcal/mol or less. Counterpoise correction is calculated in terms of fragments in the complex. For example, AuCO has two fragments, Au and CO, and counterpoise=2 would be used. The charge and spin of the states must also be assigned to the fragments and identified in the molecular specification section of the input file; an example is found in Appendix A2.

Population Analysis

Population analyses are commonly used in an energy calculation after geometry optimizations to investigate electrostatic potential surfaces and charge distributions. Several population-analysis packages can be used in Gaussian, which include natural bond order analysis (NBO), Hirshfeld charges, and ChelpG (CHarges from ELeCtrostatic Potentials using a Grid-based method).¹¹ The NBO method calculates electron density as a function of the “natural bonding orbitals” in the atoms and bonds between atoms.²⁰⁻²⁵ Hirshfeld charges (Hirshfeld stockholder method) are calculated as a function of the deformation energy, which is the difference between the molecular and un-relaxed atomic charge densities, whereby the charge density is shared at each point between atoms, relative to their free-atom densities at the corresponding distances from the nuclei.²⁶⁻²⁸

ChelpG charges are calculated by atomic charges fit to reproduce the molecular electrostatic potential at a number of points around the molecular surface.²⁹ Energy calculations with population analysis need a previously converged optimization file to produce the charges of the structures accurately; therefore, the wavefunction guess must be read from the (previously generated) checkpoint file. Also, no SCF cycles should be run to change the structure, as it has already been optimized. Specific population analyses are run in Gaussian 09 by using certain keywords, which are outlined in Appendix A2.

Intrinsic Reaction Coordinate

After computing the minima and transition states of a potential energy surface, it is necessary to confirm that the transition states are connected with the reactant and product, which can be achieved with intrinsic reaction coordinates (IRC). Intrinsic reaction coordinate calculations are used to follow the path of steepest descent downhill to the reactant and product and can also show if there are intermediates.¹⁷ As implemented in Gaussian 09, IRC calculations use a predictor-corrector method, which uses the force constants to guess, evaluate and correct each step along the IRC in an effort to connect the transition state to its related minima.³⁰⁻³² The predictor integrator moves from the current point (x_i) to the next guess of the point (x_{i+1}), while the corrector integrator takes the information of the guess point and re-integrates over the same interval to refine x_{i+1} . This method continues iteratively until a minimum, or near-minimum, is reached, or the maximum number of steps has been exceeded. Several keywords are utilized to assist the IRC calculation in reaching completion, which are highlighted in the appendix (A2). Commonly after IRC calculations have finished, a

geometry optimization is completed to verify the reactant (or product) or identify a new intermediate.

***Ab initio* Molecular Dynamics**

To further understand the potential energy surface, *ab initio* molecular dynamics (AIMD) have been calculated within Gaussian 09. These AIMD calculations are completed by computing the forces acting on the nuclei from the electronic structure calculations as the molecular dynamics trajectory is calculated.³³⁻³⁵ Atom-centered density matrix propagation (ADMP) is implemented in Gaussian 09, in which ADMP uses atom-centered Gaussian basis functions and propagates the electronic structure (in the electronic density matrix) at each nuclear trajectory step, rather than calculating the SCF (the entire system) at each point.³³⁻³⁵ This approach allows the calculation to run faster than Born-Oppenheimer dynamics, which involves convergence of the SCF at each nuclear trajectory step. Another benefit to ADMP is that hybrid-DFT functionals can be used routinely with this method, and the overall dynamics pathway can be compared to the individually calculated points along the potential energy surface. Like other calculations in Gaussian 09, the ADMP calculation can be modified with various keywords, depending on the needs of the calculation. When starting from a minimum, it is advantageous to input a nuclear kinetic energy (NKE) slightly higher than the barrier to provide enough energy to pass over the barrier; however, the default NKE can be used with starting from a transition state, or a higher NKE, depending on the needs of the user. The step size is a commonly altered parameter; the default is 0.1 femtoseconds, and ADMP calculations herein utilize a smaller stepsize of 0.05 fs. The number of points

along the trajectory can also be altered; the default is 50, and calculations typically had maximum number of points of 5000 to provide a longer trajectory to form products.

2.2 Experimental Methods

This project, as outlined in the goals and motivation of Chapter 1, involves a two-prong investigation of CO oxidation with Au with computational methods, described above, and experiments. Although computational results provide insight regarding the CO oxidation pathway, experiments can be used to verify these stable minima complexes. One major goal of the project was to experimentally interrogate the interactions of ozone, carbon monoxide, and metal atoms (specifically Cu) as a proof of concept. In this section, the copper atom (ions) source and ion deposition system, ozone generation and storage system, and ozone deposition are described.

2.2.1 Gas-aggregation Nanoclusters Source System

Under high vacuum conditions (10^{-5} to 10^{-7} torr), unsupported Au NPs are generated in a magnetron-gas-aggregation nanocluster source (modified Oxford Applied Research source). The gas-aggregation source produces a plasma of Ar^+ ions, which impact the metal (Cu) target and eject or “sputter” metal atoms from the surface, where only approximately one in 1,000 of the metal atoms are ionized.³⁶ The sputtered metal atoms are decelerated through collisions with argon sputtering gas and carried by the viscous gas flow into the aggregation region (set to 17 cm long), where these atoms can aggregate into clusters. The size of metal clusters depends on the length of aggregation region; for example, clusters moving through a long aggregation region typically will grow large because there is more time for cluster aggregation.³⁶ Much of the metal clusters possess positive or negative character due to charged species and electronically

excited species present from the sputter discharge.³⁶ The schematic design of the cluster beam system is shown in Figure 2.1. After the clusters have passed through the aggregation region, the cluster beam continues through a (22-mm) quadrupole, which acts as an ion guide and collisional dampener to average the cluster energy, and proceeds into a resolving quadrupole mass filter to size-select the cluster beam for the desired size. The ionic cluster beam is then redirected with a quadrupole bender to ensure the beam is only ionic clusters of desired charge. The beam can be bent left towards an electron-multiplier detector to determine the ion signal strength or to the right and through an octopole ion guide towards the IR window. If the ion beam is bent to the right, the ionic clusters can be deposited with a matrix gas onto an IR window (KBr, Koch Crystal Finishing), which is cooled by a cryostat (Advanced Research Systems model CS204SF-X20B) to 10-20K. Or, if the window is raised out of the beam path with the Z translator coupled with a differentially pumped rotary platform (McAllister Technical Services), the ion current can be detected on a flag to determine the amount of deposited Cu ions and also to balance the charge, when a counter-ion is introduced. Since the matrix may be positively or negatively charged, counter-ions are introduced into the system through the ionizer on the bender. For example, a matrix containing anionic Cu clusters can be neutralized through introduction of Ar^+ (Kr^+ or SF_5^+) as a counter-ion.

Our existing matrix isolation system is designed for infrared spectroscopy studies to characterize matrix-stabilized pre-reactive complexes of small molecules with metal clusters. Differentially pumped windows (DPWs) are on the sides of the chamber 180° from one another to transmit the IR beam from the infrared spectrometer (Thermo-Nicolet 6700) through the sample window and deposited matrix to the MCTA detector.

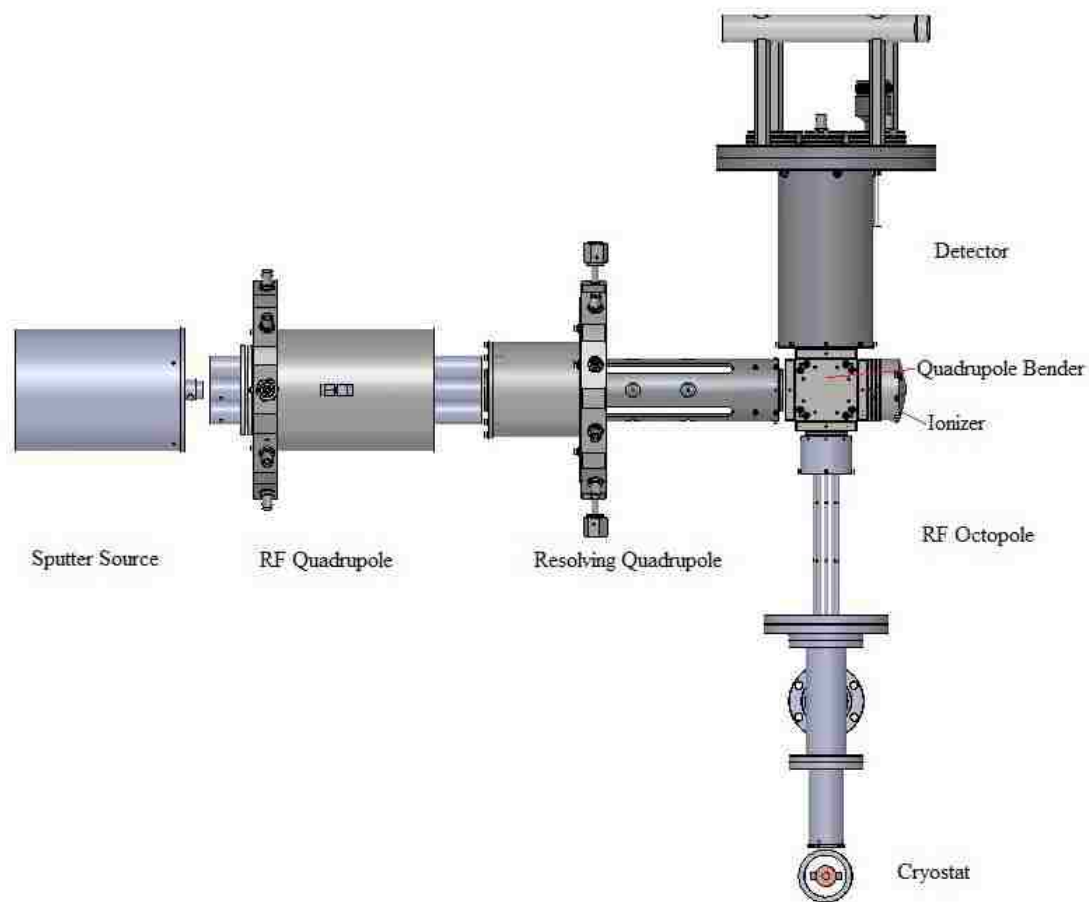


Figure 2.1. Solidworks rendering of internal components for nanocluster experimental system (courtesy of Alex Hunter).

Infrared spectra are observed after a Fourier transform is performed on the interferograms (OMNIC software). For gas depositions, the host matrix gas is also doped with desired reactant(s), which are co-deposited with the metal clusters on the IR window, which is on a rotary platform and Z translator (McAllister Technical Systems). Prior to deposition, the ion beam is turned into the electron multiplier to prevent copper plating the window when starting deposition. The gas mixture is typically deposited for approximately 5 minutes to provide a “cushion” of a matrix before turning the ion beam to the right for deposition. For optimum IR signal, the window and deposited matrix can be rotated to 45° on the rotary platform, which is 90° to the IR beam and spectra after deposition are all taken at this rotation. Spectra can also be taken during deposition to monitor the formation of complexes, but are not compared to the “post-deposition” spectra, since the pathlengths through the sample are different. Following deposition and rotation to 45°, the sample is cooled to 10K to take a “post-deposition” spectrum and is then annealed to 15-30K to allow diffusion of reactants through the matrix to the metal clusters, at which point pre-reactive or intermediate complexes can form.³⁷ The sample may also be exposed to light to photolyze the complexes in the matrix. The matrix is exposed to 590 nm and 470 nm LED lights (Thor Labs), separately, at medium and high intensity for different amounts of time, depending on how the spectra change as a function of the wavelength, intensity, and exposure time. The samples are also exposed to UV light through a fiber optic cable for 30 minutes, where the window is rotated to 0° and raised to approximately 3.10 inches for better exposure of the sample to the (less intense) UV light. Prior to and after annealing and photolysis, the sample is analyzed

with FT-IR for pre-reactive and intermediate complexes, which can be used to elucidate the mechanism of CO oxidation.

As briefly stated above, reactant gases are mixed with the matrix gas, argon, to deposit simultaneously with the metal clusters. For the experiments discussed in later chapters, ozone and carbon monoxide (CO) were the typical dopant gases. Argon (Praxair, >99.998% purity) and carbon monoxide (Praxair, 10% CO in He) were sourced from compressed gas cylinders. Since ozone is a reactive gas and decomposes in approximately 24 hours, it was generated in the lab with an ozone generation system that was constructed in the laboratory.

2.2.2 Gas Rack and Ozone-Generation System

A simple schematic diagram of the gas rack, mixing bottle system, ozone generation and storage systems and deposition lines to both chambers is shown in Figure 2.2. The ozone generation occurred in a ½-inch-diameter heat-resistant borosilicate (12 inch) glass tube (McMaster Carr) that was blown closed at one end, courtesy of Ryan Ludwig. The glass tube was connected to the gas rack with a Swagelok ½-to-¼ inch reducing union with a Teflon ferrule on the glass tube and hand-tightened. Wrenches were not utilized to prevent cracking the glass and hand-tightening produced no observable leaks when tested with Snoop and with helium. The glass tube is wrapped with copper wire (covering approximately 1 inch of the middle of the tube), which was then connected to the tip of the Tesla coil (ElectroTechnic Products, BD-10A). The copper wire was covered with electrically insulating tape (McMaster Carr). The Tesla coil and glass tube set-up was surrounded by a Faraday cage, which was grounded, to prevent electric interference of the Tesla coil with the nearby computers and instruments; there was a hole in the

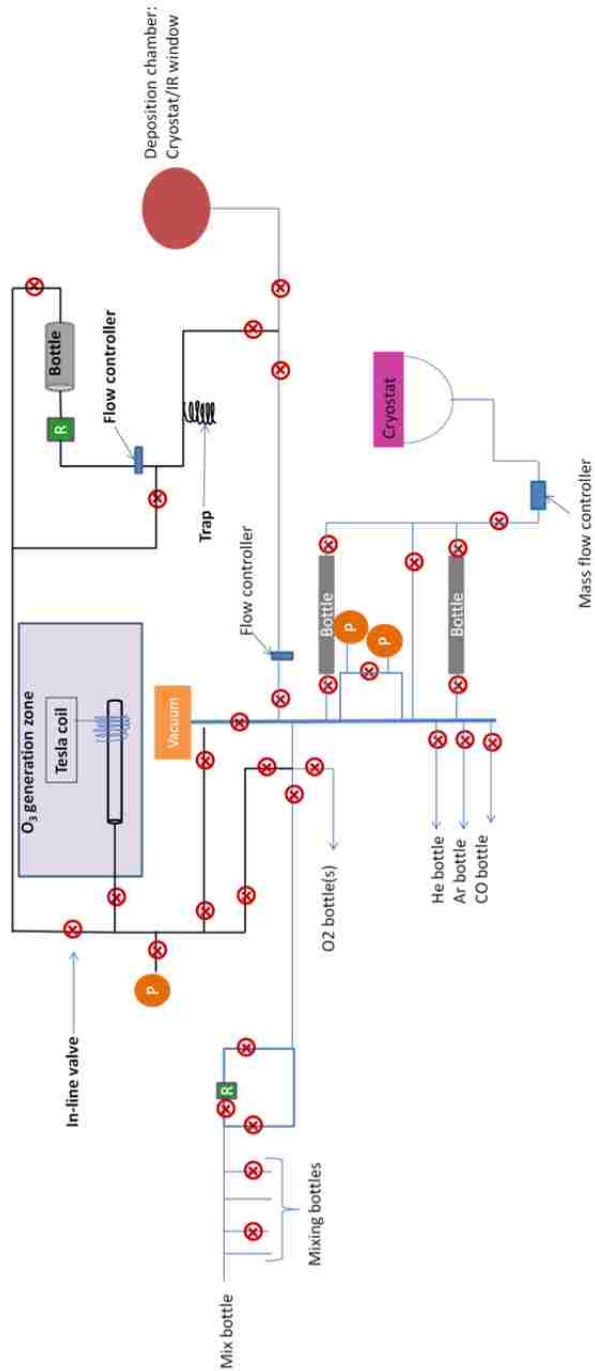


Figure 2.2. Simple schematic, not to scale, of the gas rack, mixing rack and deposition lines (shown with blue lines) and the ozone generation, storage and deposition systems (shown with black lines). The ozone generation system is shown in the purple box with the glass tube and copper wire wrap attached to a Tesla coil. Red circle Xs represent valves, green R rectangles are regulators, orange P circles are pressure gauges, blue bars are flow controllers, the orange rectangle is the vacuum pump, and the ozone bottle is the gray cylinder.

cage where the stainless steel tubing comes out of the top of the Faraday cage to connect the glass tube with the rest of gas rack, which was well-covered with copper mesh to prevent current leakage. Pressure in the ozone systems was monitored with a Pirani gauge (MKS Instruments HPS 945 Pirani Vacuum Sensor System; 1×10^{-4} to 100 torr) and pressure in the gas rack, and generally all systems and deposition lines, was monitored with a Bourdon gauge (for pressures greater than 1000 torr), piezo gauge (MKS 902 series Piezo transducer; 1 to 1000 torr), and thermocouple (KJL-6000 thermocouple and KJLC 610TC controller; 1-1000 millitorr).

2.2.3 Ozone Generation for Use in Reactant and Matrix Gas Mix

The ozone-generation system, including the storage bottle, deposition line tubing and fittings were constructed of stainless steel because it has a good to excellent tolerance of ozone.³⁸ The system was fitted with a Pirani pressure gauge and connected on a gas rack as shown in Figure 2.2. To prepare the system for ozone generation, the in-line valve was closed to prevent sending oxygen to the bottle or deposition lines and the system was purged three times with ~ 1 atm of oxygen. Then, 60-100 torr of oxygen was introduced into the glass tube, below 150 torr at which oxygen liquefies at liquid-nitrogen temperature. After adding oxygen, the glass tube was immersed in liquid nitrogen within an inch or two of the copper coil, the Faraday cage closed, and the Tesla coil turned on for 15 minutes. A deep purple line, consistent with the color of liquid ozone, formed near the top of the liquid nitrogen within \sim three minutes and more purple appeared to condense down the sides of the tube as the time continued. After 15 minutes, the Tesla coil was turned off and more liquid nitrogen was added to the dewar to trap as much ozone as possible. After ~ 5 minutes, the oxygen in the tube above the liquid nitrogen

level was removed, so that only, or mostly, ozone was retained. The liquid nitrogen bath was replaced with an isopentane-liquid nitrogen bath (110K) in an effort to trap carbon dioxide, but not ozone. The valve above the glass tube was opened, the gas above the isopentane-liquid-nitrogen bath was allowed to fill the volume of the stainless steel lines up to the in-line valve and the bottle was closed to trap the ozone. With both the glass tube and bottle valves closed, the lines were evacuated and purged with argon to remove possible contamination, especially by carbon dioxide. The desired percentage of ozone in argon (or ozone and carbon monoxide in argon) was calculated from the amount of ozone (in torr) that was trapped in bottle and, the required amount of the other reactant gas(es) and argon were added to the bottle that contained the ozone. Argon was added to the ozone-containing bottle at pressures of ~ 700 torr and at room temperature, in which the argon pressure was, at least, four times greater than the pressure of ozone in the bottle and was high enough to prevent back-flow of ozone into the lines. The bottle was closed and the mix was allowed to interact for approximately 1-2 hours. Ozone was verified by observation of a deep purple liquid in the glass tube (prior to delivery to storage bottle) and a (doublet) peak at $\sim 1040 \text{ cm}^{-1}$ in the IR spectrum, after deposition of a gas mixture.

2.2.4 Ozone Mix Deposition

The day prior to an experiment, ozone was generated and dosed into all of the ozone lines (and bottle) three separate times to clean the system. On the day of an experiment, the valve adjacent to the deposition chamber was opened prior to cooling the cryostat to prevent a burst of water and other contaminating gases from collecting on the IR window, while the final valve on the ozone deposition line was closed. Prior to deposition and after the mix was made, the deposition line was evacuated and purged with argon three

times. Approximately 10-15 minutes before deposition, an isopentane-liquid nitrogen bath (110K) was added onto the deposition line trap, indicated in Figure 2.2. When the cryostat reached the desired deposition temperature, the ions and gas mix could be deposited. The regulator was opened to pressurize the line up to the flow controller (MKS 1179A Series flow controller, N₂, 100scm). When ready to deposit, the MKS flow controller was set to the desired flow rate, 10 sccm, and the last ozone valve is opened. The gas was allowed to flow for ~5 minutes before dropping the IR window in line with the ion beam and gas deposition lines. The gas was deposited on the IR window for another 5 minutes without ions to provide a “cushion” for the ions and prevent metal plating of the window; then the ion beam was turned towards the deposition chamber. During the gas-only deposition, the residual gas analyzer (Extrel) was on to observe the gases in the chamber and ion gauges were on to watch the pressures. It was observed by another graduate student (Ryan Ludwig) that anionic metal carbonyls can neutralize when the laboratory lights were on; therefore, depositions were completed with the laboratory lights off, the purge boxes around the MCTA detector and differentially pumped windows covered, and the ion gauges and RGA turned off.

2.3 References

- (1) Jensen, F., Ed.; In *Introduction to Computational Chemistry*; Wiley: Hoboken, NJ, 2007; .
- (2) Atkins, P.; Friedman, R., Eds.; In *Molecular Quantum Mechanics*; Oxford University Press: New York, NY, 2005.
- (3) Cramer, C., Ed.; In *Essentials of Computational Chemistry: Theories and Models*; Wiley: Hoboken, NJ, 2004.
- (4) Becke, A. D. *J. Chem. Phys.* **1993**, *98*, 5648-5652.
- (5) Fiolhas, C.; Noguera, F.; Marques, M., Eds.; In *A Primer in Density Functional Theory*; Springer: New York, 2010.
- (6) Koch, W.; Holthausen, M., Eds.; In *A Chemist's Guide to Density Functional Theory*; Wiley: Hoboken, NJ, 2001.
- (7) Zhao, Y.; Lynch, B. J.; Truhlar, D. G. *J. Phys. Chem. A* **2004**, *108*, 4786-4791.

- (8) Schwabe, T.; Grimme, S. *Phys. Chem. Chem. Phys.* **2006**, *8*, 4398-4401.
- (9) Schwabe, T.; Grimme, S. *Phys. Chem. Chem. Phys.* **2007**, *9*, 3397-3406.
- (10) Grimme, S. *J. Chem. Phys.* **2006**, *124*, 034108.
- (11) ; Frisch, M. J.; Trucks, G. W.; Schlegel, H. B.; Scuseria, G. E.; Robb, M. A.; Cheeseman, J. R.; Scalmani, G.; Barone, V.; Mennucci, B.; Petersson, G. A., et al. Gaussian 09, Revision A.02, Gaussian, Inc., Wallingford, CT **2009**.
- (12) Foresman, J.; Frisch, E., Eds.; In *Exploring Chemistry with Electronic Structure Methods*; Gaussian, Inc.: Pittsburgh, PA, 1996.
- (13) Krishnan, R.; Binkley, J. S.; Seeger, R.; Pople, J. A. *J. Chem. Phys.* **1980**, *72*, 650-654.
- (14) Frisch, M. J.; Pople, J. A.; Binkley, J. S. *J. Chem. Phys.* **1984**, *80*, 3265-3269.
- (15) Schwerdtfeger, P.; Dolg, M.; Schwarz, W. H. E.; Bowmaker, G. A.; Boyd, P. D. W. *J. Chem. Phys.* **1989**, *91*, 1762-1774.
- (16) Andrae, D.; Haussermann, U.; Dolg, M.; Stoll, H.; Preuss, H. *Theor. Chim. Acta* **1990**, *77*, 123-141.
- (17) Hratchian, H. P.; Schlegel, H. B. In *Finding minima, transition states and following reaction pathways on ab initio potential energy surfaces*; Dykstra, C. E., Frenking, G., Kim, K. S. and Scuseria, G. E., Eds.; *Theory and Applications of Computational Chemistry: The First 40 Years*; Elsevier: Amsterdam, 2005.
- (18) PENG, C.; SCHLEGEL, H. *Isr. J. Chem.* **1993**, *33*, 449-454.
- (19) Boys, S. F.; Bernadi, F. *Mol. Phys.* **1970**, *19*, 553-566.
- (20) Foster, J. P.; Weinhold, F. *J. Am. Chem. Soc.* **1980**, *102*, 7211-7218.
- (21) Reed, A. E.; Weinhold, F. *J. Chem. Phys.* **1983**, *78*, 4066-4073.
- (22) Reed, A. E.; Weinstock, R. B.; Weinhold, F. *J. Chem. Phys.* **1985**, *83*, 735-746.
- (23) Reed, A. E.; Weinhold, F. *J. Chem. Phys.* **1985**, *83*, 1736-1740.
- (24) Reed, A. E.; Curtiss, L. A.; Weinhold, F. *Chem. Rev.* **1988**, *88*, 899-926.
- (25) Carpenter, J. E.; Weinhold, F. *J. Mol. Struct. -Theochem* **1988**, *46*, 41-62.
- (26) Hirshfeld, F. L. *Theor. Chim. Acta* **1977**, *44*, 129-138.
- (27) Ritchie, J. P. *J. Am. Chem. Soc.* **1985**, *107*, 1829-1837.
- (28) Ritchie, J. P.; Bachrach, S. M. *J. Comput. Chem.* **1987**, *8*, 499-509.
- (29) Breneman, C. M.; Wiberg, K. B. *J. Comput. Chem.* **1990**, *11*, 361-373.
- (30) Hratchian, H.; Schlegel, H. *J. Chem. Theory Comput.* **2005**, *1*, 61-69.
- (31) Hratchian, H.; Schlegel, H. *J. Chem. Phys.* **2004**, *120*, 9918-9924.
- (32) Peng, C.; Ayala, P.; Schlegel, H.; Frisch, M. *J. Comput. Chem.* **1996**, *17*, 49-56.
- (33) Schlegel, H.; Millam, J.; Iyengar, S.; Voth, G.; Daniels, A.; Scuseria, G.; Frisch, M. *J. Chem. Phys.* **2001**, *114*, 9758-9763.
- (34) Iyengar, S.; Schlegel, H.; Millam, J.; Voth, G.; Scuseria, G.; Frisch, M. *J. Chem. Phys.* **2001**, *115*, 10291-10302.
- (35) Schlegel, H.; Iyengar, S.; Li, X.; Millam, J.; Voth, G.; Scuseria, G.; Frisch, M. *J. Chem. Phys.* **2002**, *117*, 8694-8704.
- (36) Haberland, H.; Karrais, M.; Mall, M.; Thurner, Y. *J. Vac. Sci. Technol. A* **1992**, *10*, 3266-3271.
- (37) Willson, S.; Andrews, L. In *Matrix Isolation Infrared Spectroscopy*; 2002; Vol. 1, pp 1342-1351.
- (38) Horváth, M.; Bilitzky, L.; Hüttner, J. In *Ozone*; Elsevier: New York, 1985.

Chapter 3. Charge-dependent Trends in Structures and Vibrational Frequencies of [CO-Au-O₂]^q (q=-1,0,+1) Complexes: Evidence for Cooperative Interactions

This chapter includes material that has been reproduced in part with permission from: Smith, Angela N.; Moore, David T. *J. Phys. Chem. A*, **2012**, *116* (37), 9370–9381.

3.1 Abstract

Charge-dependent trends in the structures, vibrational frequencies and binding energies of binary [AuCO]^q and [AuO₂]^q and ternary [O₂AuCO]^q complexes (q=-1,0,+1), have been investigated using density functional theory calculations. Three different geometrical motifs, given descriptive names of “separated”, “pre-reactive” and “long-range”, are identified for the ternary complexes. For the binary systems, the general trend is that the complexes become more diffuse as the charge becomes more negative, having longer intermolecular bond distances and weaker binding energies. The trends shown by the ternary complexes are more complicated, and are different for the various geometrical motifs. However, a general trend is that there is a cooperative interaction involving both the CO and O₂ with the Au center, which becomes more pronounced as the negative charge on the complexes increases from cationic to neutral to anionic. This cooperative interaction leads to increased electron density on the O₂ moiety, as is reflected in the bond-lengths and vibrational frequencies. Furthermore, it is found that for the pre-reactive complexes, the role of the Au center is to stabilize the formation of a conjugated π -system between the CO and O₂ molecules.

3.2 Introduction

The low-temperature catalysis of CO oxidation by supported gold nanoparticles has been known and studied for almost 3 decades,¹ but there is still ambiguity about the

mechanism and active site.² One of the key factors that is still not completely understood is the precise role of the gold in the catalytic process. One approach to addressing this question is through model studies that exclude the support material and focus on the interactions of unsupported gold atoms and small clusters with the reactant molecules, consequently there have been many experimental³⁻²² and theoretical^{6-8, 10, 12-14, 17-20, 23-30} studies in this vein. A crucial question regarding the mechanism is the role of the charge on the gold cluster. On one hand, studies of model catalysts supported on MgO suggest that the active sites may correspond to gold clusters interacting with electrons trapped in surface defects of the oxide.³¹⁻³⁴ The extra electron density acquired by these clusters is then thought to specifically³² catalyze the breaking of the O-O bond during the reaction.³⁵ On the other hand, it has also been proposed that for the strongly-wetted Au NP's on highly oxidized supports like TiO₂ and Fe₂O₃, the strong Au-O interactions at the particle/support interface lead to a partial positive charge developing on the gold cluster.³⁶ Experimental studies have shown that cationic gold is essential for activity of Fe₂O₃-supported gold,³⁷ while a theoretical study has predicted a full catalytic cycle for CO oxidation on TiO₂-supported Au₇ clusters with partial positive charges.³⁶

Wallace and Whetten conducted room temperature flow reactor studies of the binding of CO and O₂ and to gold cluster anions (Au_N, N=2-20) which showed an odd-even oscillation based on cluster size, with even clusters adsorbing one O₂ molecule, and odd clusters failing to adsorb any.³⁸ They also observed strong evidence of a cooperative binding effect, where the affinity of either reactant (CO or O₂) for the cluster was enhanced by pre-adsorbing the other reactant.³⁸ Subsequent cooled ion trap studies by the Woste group on the Au₂⁻ cluster were able to determine a complete catalytic cycle for

CO₂ formation, with accompanying DFT computational study that proposed two possible mechanisms involving CO₃ “carbonate” and OCOO “peroxyformate” intermediates with low (<7-13 kcal/mol) activation barriers.¹⁰ The Castleman group performed similar studies on the reactivity of atomic gold anions with O₂ and CO, and they found that AuO⁻ and AuO₃⁻ species produced in their laser ablation plasma were reactive for CO, while AuO₂⁻ was not.¹³ Supporting DFT calculations predicted barriers smaller than the energy of reactants, also called the reactant asymptote, for the AuO⁻ and AuO₃⁻ cases, while the AuO₂⁻ species was spin-forbidden with a higher barrier.¹³ In general, cationic gold clusters have been thought to be less active than anionic clusters for CO oxidation; however, a more recent study from the Castleman group suggests that this may not be the case. Rather, the stronger binding of CO to cationic gold may act in an autocatalytic fashion, with the large complexation energy of the CO’s serving to drive the system over low barriers in a Langmuir-Hinshelwood type mechanism.¹⁹ This is in contrast to the anionic clusters, which are predicted to react in an Eley-Rideal type fashion.¹⁹

Matrix isolation spectroscopy has also been used to characterize the binary AuO₂³,^{7, 23} and AuCO^{4, 6} complexes. The original studies were completed by the Ozin group, who reported FTIR spectra for AuO₂³ and AuCO⁴ complexes in rare gas matrices, using a thermal gold atom source.^{3-5, 39} Similar studies were done more recently by the Andrews group using Au atoms and ions produced by laser ablation.^{6, 7} The Ozin group also reported matrix isolation studies of the three-component system (CO + O₂ + Au), identifying several possible pre-reactive complexes, as well as the photoproduction of CO₂ upon UV-irradiation of the matrix.⁵ A more recent study using laser-ablated gold atoms produced similar results and also reported observation of several new species.¹⁷

The more recent studies have used DFT calculations to support their structural assignments.¹⁷ In general, the agreement of the calculations with experiment is good; however, one significant discrepancy lies with the structure of the Au-O₂ binary complex. Experimental studies are consistent with a side-on η^2 binding motif for the O₂ based on isotopic substitution studies;^{3,7} however, the computational studies predict a bent Au-O₂ geometry.⁷ Additionally, the experimental vibrational frequency for the Au-O₂ complex in argon was drastically red-shifted with respect to both the analogous species in neon, as well as the computational prediction.⁷ Andrews *et al.* attributed this to the argon complex being a different chemical species with greater ionic character (i.e. not the Au-O₂ ground state) that was stabilized by the polarizable argon matrix; however, no suitable candidates for such a species were identified computationally.⁷

One important aspect of these studies is understanding how the structures and vibrational frequencies of the complexes respond to different charges on the Au-center. The standard model for interpreting the vibrational shift of the C-O stretching mode in metal carbonyls is the Blyholder model.⁴⁰ The Blyholder model states that the two different bonding modes of CO to metals, σ -donation and π -back bonding, lead respectively to blue- and red-shifting of the CO stretch, due to their differing effects on the nominal CO bond-order.⁴⁰ Thus, for a cationic binary metal carbonyl, the CO stretching mode starts out blue shifted from the free molecule, since the positive charge on the metal center enhances donation from the CO, and suppresses the back-bonding interaction. As charge is added to the metal center, going from neutral to anionic, these trends are reversed with the extra electron density leading to enhanced π -back donation, and a concomitant red-shifting of the vibrational mode.⁴⁰ Recent studies have indicated

that in some cases, the blue shifting of the CO band for metal cations can be better explained in terms of the electrostatic interaction with the charged metal center, which in turn leads to a tightening of the C-O bond.⁴¹ This is particularly relevant to late transition metals like gold, where the filled or nearly-filled d-shell tends to inhibit σ -donation from the CO. Using IRMPD spectroscopy of gas-phase clusters, Fielicke *et al.* have shown that this electrostatic based model is quite effective at modeling size and charge-dependent vibrational shifts of CO probe-molecules binding to metal clusters.⁴²

In the current study, we report a comprehensive DFT study of the charge-dependent trends in the structures and vibrational frequencies of the binary and ternary complexes of CO and O₂ with monatomic gold cations, neutrals and anions. While many of the species investigated here have been previously studied computationally,^{6, 7, 13, 14, 17, 24, 27, 43, 44} there have not been any studies using a single DFT functional and basis set to allow side-by-side comparison of all of the various complexes. There have been concerns reported about the appropriateness of using DFT methods to predict the structures complexes involving gold and O₂, which have been shown to be susceptible to severe spin-contamination issues.^{24, 27} Fang *et al.* reported a comprehensive comparison for the performance of 42 DFT functionals in the prediction of structures and energetics of stationary points on the potential energy surface for catalysis of CO oxidation by neutral gold atoms.⁴⁴ The top performers were found to be the double-hybrid DFT methods, B2PLYP and mPW2PLYP; however, B3LYP showed, by far, the best performance of all of the commonly used DFT functionals,⁴⁴ and thus its choice for the current work is appropriate.

3.3 Computational Methods

Density functional theory (DFT) geometry optimizations and frequency calculations were carried out using the GAUSSIAN 09 suite of computational chemistry programs.⁴⁵ Except where otherwise noted, all reported data reflect results obtained using the B3LYP hybrid functional,⁴⁶ with a mixed basis set employing the Stuttgart-Dresden relativistically-corrected effective core potential basis (SDD) for Au atoms,^{47, 48} and the Pople 6-311+G(3df) basis for C and O atoms.^{49, 50} All geometry optimizations were performed using the tight convergence criteria and the ultrafine integration grid (Gaussian keywords: “opt=tight” and “integral=ultrafine”); this was required to achieve convergence for weakly-bonded systems, and was maintained for all calculations to ensure comparability of the results. All reported geometries reflect stable minima on their respective potential energy surfaces with no imaginary frequencies. The stabilities of the SCF wavefunctions for each reported wavefunction were verified using the method of Davidson.⁵¹ Counterpoise corrections, using the method of Boys and Bernardi,⁵² were carried out to correct for the effects of basis-set superposition error (BSSE) on the binding energies of the complexes. All reported binding energies have been corrected for both BSSE and the vibrational zero-point energy (ZPE). Atomic charges were calculated using the Hirshfeld stockholder method⁵³⁻⁵⁵, CHELPG molecular electrostatic potential method,⁵⁶ and the natural bond orbital (NBO) method,⁵⁷⁻⁶² as implemented within GAUSSIAN 09.

3.4 Results and Discussion

3.4.1 Structures, Relative Energies and Vibrational Frequencies

Figure 3.1 displays illustrations of the stable minima for binary complexes formed from either CO or O₂ binding to a gold atom or ion, along with their respective structural

data. Figure 3.3 shows illustrations of the stable minima for ternary complexes formed from both CO and O₂ binding to a gold atom or ion, along with their respective structural data. Calculated vibrational frequencies (unscaled) are collected in Table 3.1. The binding energies, corrected for ZPE and BSSE effects, of the various isomers of the binary and ternary complexes are collected in Table 3.2 (raw B3LYP energies, BSSE and ZPE corrections are collected in Table A3.6 of Appendix A3). Except where otherwise noted, all binding energies are relative to the ground states of the component O₂, CO and Au^q species, where the “q” superscript indicates that any charge is carried by the Au center in the reference system.

As mentioned above, the B3LYP DFT functional was chosen for this study, both to ensure comparability with previous work, and also due to its superior performance in the recent study by Fan *et al.*⁴⁴ However, in order to try to ensure that our results were not influenced by known issues associated with B3LYP and other DFT methods,⁶³ the minimum geometries were checked using other hybrid DFT functionals (mPW1PW91 and B3PW91), as well as the double-hybrid B2PLYP functional, which includes non-local MP2 as part of the correlation functional.⁶⁴ Basis set effects were also examined by re-optimizing the structures reported here using the larger aug-cc-pVQZ correlation-consistent basis set⁶⁵⁻⁶⁹ for the C and O atoms. With the exception of the anionic Au-CO binary complex (discussed in more detail below), no qualitative differences from the B3LYP/mixed:(SDD/6-311+G3df) results reported here were found, and all of the reported trends were preserved.

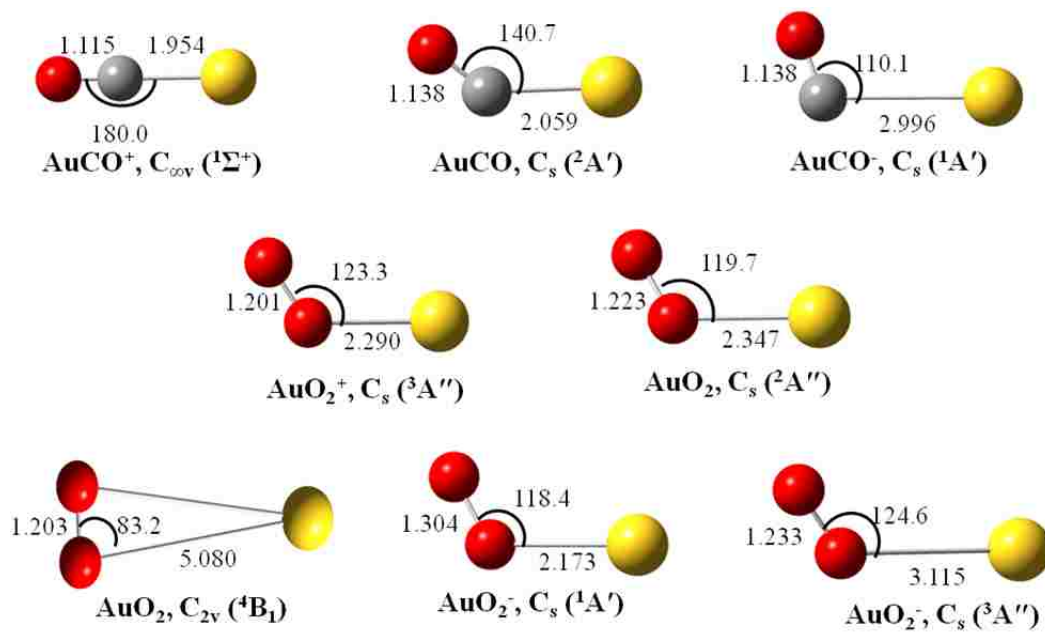


Figure 3.1. Geometry and structural characteristics of cationic, neutral and anionic binary complexes, $[\text{AuCO}]^q$ and $[\text{AuO}_2]^q$ calculated with B3LYP/SDD/6-311+G(3df).

Table 3.1. Calculated stretching vibrational frequencies in cm^{-1} and intensities (in parentheses) of optimized binary and ternary complexes^{a,b} for B3LYP-SDD/6-311+G(3df).

Species	Electronic state	Stretching frequency – cm^{-1} (Intensity)			
		Au-C	C-O	Au-O	O-O
[AuCO] ⁺	¹ A ₁ (¹ Σ ⁺)	377 (12.8)	2308 (194.7)		
AuCO	² A'	349 (6.51)	2077 (819.5)		
[AuCO] ⁻	¹ A'	42 (3.27)	2075 (647.2)		
[AuO ₂] ⁺	³ A''			264 (0.762)	1579 (36.1)
AuO₂	² A''			74 (9.36)	1444 (63.8)
AuO₂	⁴ B ₁			12 (0.0)	1645 (0.015)
[AuO ₂] ⁻	¹ A'' ^c			173 (0.114)	1144 (718.4)
[AuO ₂] ⁻	³ A''			35 (0.22)	1387 (1969.3)
[O ₂ AuCO] ⁺ A	³ A''	404 (19.8)	2305 (299.5)	299 (2.00)	1592 (6.64)
O₂AuCO B	² A''	438 (3.62)	2215 (549.1)	539 (9.47)	1158 (9.52)
Au(CO)O₂ E	² A''	806 (139.4)	1910 (414.7)		1189 (99.5)
			453 (27.8)		
[O ₂ AuCO] ⁻ C	¹ A ₂	542 (24.6)	2005 (1250.1)	456 (52.8)	839 (181.8)
[Au(CO)O ₂] ⁻ F	¹ A'	626 (37.4)	1719 (624.6)		883 (183.6)
			1127 (282.4)		
[O ₂ AuCO] ⁻ D	³ A''	465 (11.0)	1824 (718.2)	369 (4.71)	1169 (48.9)
Reference frequencies^d	CO – 2217 CO+ – 2300 CO- – 1665	O ₂ – 1645	O ₂ - – 1181	O ₂ ²⁻ – 703	

^a Labels A-F correspond to the structures shown in Figure 3.3.

^b Lowest energy state for species of the same charge and molecular components are in **bold**.

^c [AuO₂]⁻ singlet was calculated as restricted (closed shell) due to high spin contamination in the unrestricted singlet calculation.

^d Calculated at same level of theory: B3LYP/6-311+G(3df) and O₂ reference bond length is from the triplet ground state species.

Au-CO

The cationic Au-CO binary complex shows a linear geometry, consistent with the expected σ -donor, π -acceptor model for the interaction of the CO with a transition metal atom. The CO vibrational frequency is blue shifted by $+91\text{ cm}^{-1}$ and the C-O bond is $\sim 0.009\text{ \AA}$ shorter, relative to the free CO, as expected for CO interacting with a cationic center.⁴¹ Both the neutral and anionic complexes have bent structures, with the Au-C and C-O bond lengths increasing with increasing electronic density on the Au center. For the neutral complex, the Au-C bond lengthens by 0.105 \AA , while the CO bond increases by 0.023 \AA relative to the cationic complex. The CO stretching frequency is red shifted by -140 cm^{-1} with respect to free CO, consistent with the longer CO-bond length.

The anionic complex has an anomalously long Au-C distance, and thus the 142 cm^{-1} red shift of the CO-frequency is significantly underestimated. This analysis was confirmed by calculations using the same basis set with both the mPW1PW91 functional and B2PLYP double-hybrid functional, which yielded Au-C bond lengths of 2.414 and 2.371 \AA , with corresponding red shifts of 235 and 273 cm^{-1} , respectively. Additionally, at the B3LYP level, a significant contraction of the Au-C distance to 2.589 \AA was obtained using the larger aug-cc-pVQZ basis set. This anomalous behavior of B3LYP for the Au-CO anion has been observed previously; Tielens *et al.* reported a B3LYP bond distance of 2.971 \AA , compared with a MP2 distance of 2.062 \AA using the same 6-311+G(3df) basis set for C and O.²⁷ Interestingly, the strong basis-set dependence of the Au-C distance is still present in the MP2 results: using the larger aug-cc-pVQZ basis set shortens it to 1.874 \AA . An even larger discrepancy is observed for calculations using the CCSD method. Here, the aug-cc-pVQZ basis yields an Au-C distance of 1.952 \AA , while

the smaller 6-311+G(3df) set predicts a much larger separation of 3.567 Å. These results suggest that this system may be computationally “pathological” with regard to its sensitivity to details of method and basis set, requiring more careful study with higher-end computational techniques. Still, the B3LYP-derived qualitative effects of longer Au-C and C-O bonds, and the red-shifted CO stretching band are in the expected direction for having additional electron density in the complex.

Overall, the trends in the structures and vibrational frequencies are consistent with the expected change in character of the OC-Au interaction as electrons are added to the 6s orbital. In the cationic complex, the CO bond is strongly polarized by the positive charge, leading to an increase in the CO stretching force constant.⁴¹ In addition, the empty 6s orbital allows the complex to assume a linear geometry that should maximize orbital overlap for π -back-bonding, leading to a large stabilization energy of -45 kcal/mol (c.f., Table 3.2) for the complex. Adding a single electron to the 6s orbital in the neutral complex forces a bent geometry, weakening the intermolecular bond to -7.5 kcal/mol, and filling the 6s orbital in the anionic complex leads to an even weaker bond, although the -1.4 kcal/mol stabilization energy is likely underestimated, based on the anomalous B3LYP geometry mentioned above.

Au-O₂

The ground state of the cationic Au-O₂ binary complex is ³A'' with a bent geometry. The O-O stretching frequency shows a small red-shift of 66 cm⁻¹, and the O-O bond distance is essentially unchanged from the free monomer at the same level of theory (c.f., Tables 3.2, 3.3, and 3.4), indicating that there is only weak electrostatic interaction between the Au⁺ and the O₂, as might be expected since both tend to be electron acceptors. The

Table 3.2. ZPE and BSSE corrected binding energies^a for cationic, neutral and anionic binary and ternary complexes^{b,c} calculated with the B3LYP-SDD/6-311+G(3df) in kcal/mol and cooperative binding evaluated as a function of like charges.

		AuCO	AuO ₂	O ₂ AuCO or Au(CO)O ₂ ^d	Cooperative Binding ^{d,e}
Separated					
Cationic^f		-44.97	-10.95	-61.51 A	-5.59
Neutral	Doublet	-7.49	-0.12	-30.07 B	-22.45
	Quartet		0.45		
Anionic	Singlet	-1.35	13.84 (-24.64) ^g	-11.25 (-49.72) C	-6.68 (-23.73)
	Triplet		-3.22	-11.05 D	-6.48
Pre-reactive					
Neutral doublet				-8.12 E	-0.51
Anionic singlet				-16.95 (-55.42) F	-12.37 (-29.43)

^a Computed relative to optimized values of the *ground state* fragments, with charge (if any) localized on gold center.

^b Labels A-F correspond to the structures shown in Figure 3.3.

^c Lowest energy state per species with the same charge and molecular components are in **bold**.

^d Parenthetical values computed relative to the energy of O₂ singlet, as shown here: [E_{AuOO-} - (E_{Au-} + E_{OOsinglet})] or [E_{OOAuCO-} - (E_{Au} + E_{CO} + E_{OOsinglet})].

^e Cooperative binding is calculated as the difference between total binding energy of ternary complex and summed binary complexes as shown here: E_{OOAuCO} - E_{AuOO} - E_{AuCO}. The AuO₂ energy used in cooperative binding is the ground state triplet. Parenthetical cooperative binding values are calculated in the same fashion, but utilize the parenthetical values of the binary and ternary singlet complexes, where applicable.

^f [AuCO]⁺ has a singlet ground state and other cationic complexes have triplet ground states.

^g [AuO₂]⁻ singlet was calculated as restricted (closed shell) due to high spin contamination in the unrestricted singlet calculation.

Table 3.3. Calculated bond lengths (in Å) for binary and ternary complexes ^{a,b} with B3LYP-SDD/6-311+G(3df).

		AuCO		O₂AuCO or Au(CO)O₂				AuO₂	
		Au-C bond	C-O bond	Au-C bond	C-O bond	Au-O bond	O-O bond	Au-O bond	O-O bond
Separated									
Cationic ^c		1.954	1.115	1.943	1.116	2.190	1.206 A	2.290	1.201
Neutral	Doublet	2.059	1.138	1.912	1.127	2.028	1.323 B	2.347	1.223
	Quartet							5.080	1.203
Anionic	Singlet	2.996	1.138	1.841	1.162	1.947 ^d	1.495 C	2.173	1.304 ^e
	Triplet			2.025	1.182	2.161	1.321 D	3.115	1.233
Pre-reactive									
Neutral (doublet)				2.017	1.170		1.299 E		
					1.494				
Anionic (singlet)				2.075	1.205		1.447 F		
					1.300				
Reference lengths^f		C-O	1.124						
		C-O ⁺	1.108	O-O (O ₂)	1.203	O-O (O ₂) ⁻	1.341	O-O (O ₂) ²⁻	1.559
		C-O ⁻	1.183						

^aLabels A-F correspond to the structures shown in Figure 3.3.

^bLowest energy state for species of the same charge and molecular components are in bold.

^c[AuCO]⁺ has a singlet ground state and other cationic complexes have triplet ground states.

^dPerpendicular distance to O-O bond center in C_{2v} complex

^e[AuO₂]⁻ singlet is restricted (closed shell) due to high spin contamination in the unrestricted singlet calculation.

^fcalculated at same level of theory: B3LYP/6-311+G(3df) and O₂ reference bond length is from the triplet ground state species.

Table 3.4. Calculated shifts in vibrational frequencies (in cm^{-1}) of optimized binary and ternary complexes ^{a,b} in B3LYP-SDD/6-311+G(3df).

		AuCO	O₂AuCO or Au(CO)O₂		AuO₂	
		CO frequency (in cm^{-1})	CO frequency (in cm^{-1})	O ₂ frequency (in cm^{-1})	O ₂ frequency (in cm^{-1})	
separated						
Cationic^c		91.16	87.83	-53.06 A	-66.14	
Neutral	Doublet	-139.77	-2.33	-486.63 B	-200.80	
	Quartet				-0.15	
Anionic	Singlet	-141.65	-212.31	-806.03 C	-500.50 ^d	
	Triplet		-393.35	-475.51 D	-257.45	
pre-reactive						
Neutral	Doublet		-306.75	-455.39 E		
Anionic	Singlet		-498.12	-761.59 F		
Reference frequencies^e	CO	2217	O ₂	1645	O ₂ ⁻	1181
	CO+	2300			O ₂ ²⁻	703
	CO-	1665				

^aLabels A-F correspond to the structures shown in Figure 3.3.

^bLowest energy state for species of the same charge and molecular components are in bold.

^c[AuCO]⁺ has a singlet ground state and other cationic complexes have triplet ground states.

^d[AuO₂]⁻ singlet is restricted (closed shell) due to high spin contamination in the unrestricted singlet calculation.

^ecalculated at same level of theory: B3LYP/6-311+G(3df) and O₂ reference frequency is the triplet ground state.

neutral Au-O₂ complex has a ²A'' ground state, again with a bent geometry, although the structure is a bit expanded with respect to the cation, with the Au-O and O-O distances increasing by 0.057 and 0.022 Å, respectively. The O-O stretching frequency is red-shifted from free O₂ by 201 cm⁻¹, significantly more than in the cation, suggesting a stronger intermolecular interaction in the neutral species. However, this stronger interaction does not result in more stabilization of the complex; the BSSE and ZPE corrected binding energy of the complex is only a fraction of a kcal/mol (Table 3.2). There is also a quartet state with a C_{2v} geometry (⁴B₁) lying only ~0.6 kcal/mol higher in energy. However, the Au-O distance in this complex is >5 Å, suggesting that the interaction is pure van der Waals, which is not well-predicted by the B3LYP functional. The small energy separation between these states leads to a large spin-contamination of the doublet wavefunction ($\langle S^2 \rangle = 1.374$), as has been reported previously,^{24, 27, 44} making the computational results (particularly the small binding energy) somewhat suspect. However, we note that the geometry and binding energy obtained here are at least consistent with those predicted in the comprehensive study of 42 DFT functionals by Fang et al.⁴⁴ Those authors further found that the spin contamination was persistent in all single-reference methods up to CCSD(T), and furthermore that even multi-reference MRCI calculations predicted a qualitatively similar structure (although with a larger Au-O distance of 3.58 Å), with <1 kcal/mol binding energy.⁴⁴ Tielens *et al.* used a restricted open-shell calculation for the doublet state, and obtained a qualitatively different result that was unstable with respect to dissociation and had a much shorter Au-O distance.²⁷

The electronic ground state of the anionic Au-O₂ complex was predicted as ³A", although there is also predicted to be a ¹A" state within ~17 kcal/mol. Both complexes have a bent shape, although the structures are qualitatively different. The triplet geometry is consistent with a weakly interacting complex, with Au-O and O-O bond lengths that are expanded with respect to the neutral by 0.768 and 0.010 Å, respectively. Even with the very large Au-O distance of 3.115 Å, the O-O stretching frequency for this complex is red-shifted by 258 cm⁻¹ from free O₂, suggesting there is still considerable long-range delocalization of the negative charge from the Au center onto the O₂, lowering the bond order. The triplet complex is predicted to have a small stabilization energy of -3.2 kcal/mol. The geometry of the singlet anion complex is much more compact by comparison, with the Au-O bond contracted by 0.174 Å with respect to the neutral complex, and the O-O bond expanded by 0.081 Å to 1.304 Å, which is approaching that of the superoxide ion (O₂⁻) calculated at the same level of theory (1.341 Å). This leads to a drastic red shift in the O-O stretching frequency of 501 cm⁻¹ with respect to the free O₂ molecule, which is 37 cm⁻¹ lower than the corresponding superoxide ion. These trends suggest a significant amount of charge transfer to the O₂ in the singlet complex. It should be noted that the singlet complex is unstable by 13.8 kcal/mol with respect to dissociation into ground state triplet O₂ and Au⁻, although it does lie 24.6 kcal/mol lower in energy than the dissociation asymptote yielding Au⁻ + ¹O₂.

Linear O-Au-O isomers

For completeness, we also considered linear O-Au-O geometries that are shown in Figure 3.2, where the Au atom or ion has inserted into the center of the O-O bond; vibrational frequencies and structural data (Table A3.3), energies (Table A3.4) and

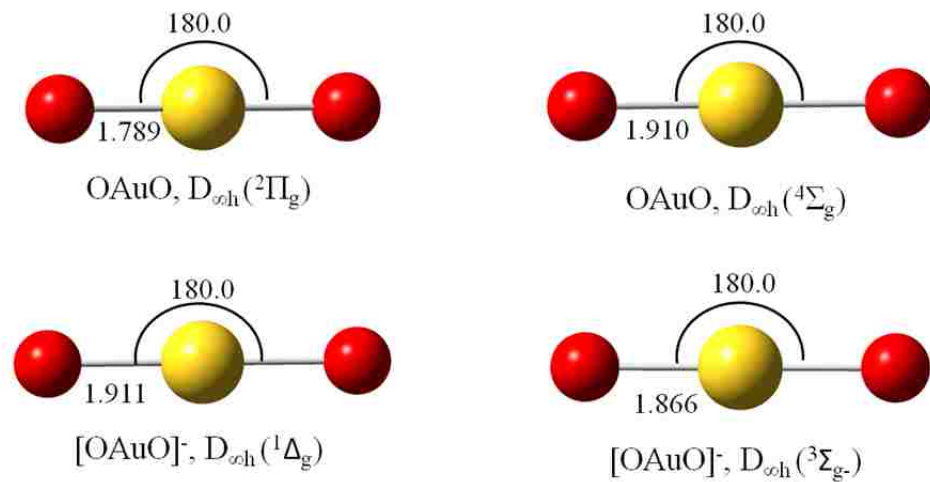


Figure 3.2. Structural details of the OAuO^q species shown as cartoons ($q=0,-1$).

Hirshfeld charges (Table A3.5) for the neutral and anionic complexes are provided in Appendix A3. For the neutral case, neither the $^2\Pi_g$ or $^4\Sigma_g$ states is predicted to be stable with respect to dissociation, lying higher in energy by 34.2 and 22.1 kcal/mol, respectively, than their same-spin counterparts described above. However, these species could possibly be formed and stabilized at low temperatures in rare-gas matrices, since there should be a significant barrier to dissociation.¹² On the other hand, for the anionic system, the $^1\Delta_g$ and $^3\Sigma_g^-$ O-Au-O molecules are the ground states in their respective spin manifolds, lying lower in energy by 5.8 and 10.7 kcal/mol, respectively, than the similarly-charged structures in Figure 3.2. The anion has been detected experimentally in previous matrix isolation studies, where vibrational bands near 850 cm^{-1} were assigned to the $^3\Sigma_g^-$ species.⁷ This was likely formed from energetic species produced in the laser ablation process, since previous DFT calculations have predicted a large barrier separating the Au-(η^1)O₂ geometry from the linear insertion molecule.⁷⁰

O₂-Au-CO

Three qualitatively different general types of structure were found for the various possible charge and spin multiplicity combinations for the ternary clusters. The different types were assigned descriptive names of “separated” for structures with CO and O₂ on opposite sides of the Au center (Figure 3.3 A-D), “pre-reactive” for structures with a covalent interaction between the CO and O₂ sub-units (Figure 3.3 E, F). In addition to the structures in Figure 3.3, several more weakly-bound energy minima were also located and are collected in Figure 3.4. These “long-range” complexes have intermolecular distances in the range where van der Waals forces start to become important, and thus are likely subject to the same sorts of DFT-specific issues as for the anionic Au-CO complex

discussed above. Of the various ternary species depicted in Figure 3.3, B and E (along with Figure 3.4 A) are similar to structures reported previously in the literature;^{17, 44} however, the rest of the species reported represent new results to the best of our knowledge. A straightforward way to assess cooperative effects associated with having both CO and O₂ present in the ternary complexes is to define a cooperativity of binding, ΔE_{coop} , as the difference between the total binding energy of the ternary complex, and the summed binding energies of the component binary complexes. For example, the calculation for this cationic ternary complex is: $\Delta E_{\text{coop}} = E_{\text{bind}}[\text{O}_2\text{AuCO}^+] - E_{\text{bind}}[\text{AuO}_2^+] - E_{\text{bind}}[\text{AuCO}^+]$. It should be emphasized that this is not the only way to categorize cooperative effects, as will be explained in more detail below.

Only one stable species was found for the cationic ternary complex (Figure 3.3 A), a separated-type structure that is basically an amalgam of the structures of the two cationic binary complexes, with a linear Au-CO arrangement and a bent η^1 -O₂ geometry. The Au-C and C-O bond distances are similar to those in the binary Au-CO complex, however the Au-O distance is contracted by 0.100 Å with respect to the binary [Au-(η^1)O₂]⁺ complex. The vibrational frequencies are basically unchanged from the binary complex, although both the CO and O₂ modes show slight shifts of -3 and +13 cm⁻¹, respectively. Overall, this suggests that there is only slight cooperativity, if any, in the cationic complex. This is borne out by the binding energy data (Table 3.2), which indicates that although the overall stabilization of the ternary complex is relatively large (-61.5 kcal/mol), the cooperativity of binding is only -5.6 kcal/mol.

For the neutral ternary complex, the lowest energy isomer is found to be the separated structure (Figure 3.3 B), but pre-reactive (Figure 3.3 E) and long-range (Figure

3.4 A) structures were also obtained. These structures are in good agreement with previous studies, and have several interesting ramifications within the context of the current study. The first point is that the lowest lying separated structural isomer has the same general shape as the cationic complex; of particular note is the linear Au-CO geometry, reminiscent of the cationic $[\text{Au-CO}]^+$ complex, rather than the bent neutral Au-CO complex. The intermolecular Au-C and Au-O distances are also drastically contracted with respect to the corresponding neutral binary complexes by 0.147 Å and 0.319 Å, respectively, while the O-O bond is lengthened by 0.100 Å to within 0.020 Å of the distance in the free superoxide ion calculated at the same level of theory (1.343 Å). The predicted O-O stretching frequency is 1152 cm^{-1} , slightly to the red of the free superoxide ion at 1176 cm^{-1} , and representing a large red-shift of $\sim 300\text{ cm}^{-1}$ from the neutral Au-(η^1)-O₂ complex. At the same time, the CO bond length is contracted by 0.011 Å compared to the neutral binary complex, with a corresponding blue shift of the CO stretching frequency back up to 2207 cm^{-1} , within 1 cm^{-1} of the free CO stretch. Taken together, these trends suggest a cooperative interaction resulting in a significant amount of charge transfer to the O₂, such that the Au-CO interaction is akin to that in the binary $[\text{Au-CO}]^+$ complex. This conclusion is also supported by the large binding energy (-30.1 kcal/mol), as well as the large cooperativity of binding (-22 kcal/mol) in this structure.

The pre-reactive isomer (Figure 3.3 E) has a geometry that suggests an incipient reaction of O₂ with a neutral Au-CO complex. The Au-C bond is slightly shorter (0.042 Å) than in the binary complex, while the CO bond is significantly longer (0.055 Å). The O₂ bond is also significantly lengthened (0.094 Å) compared to the free monomer. The

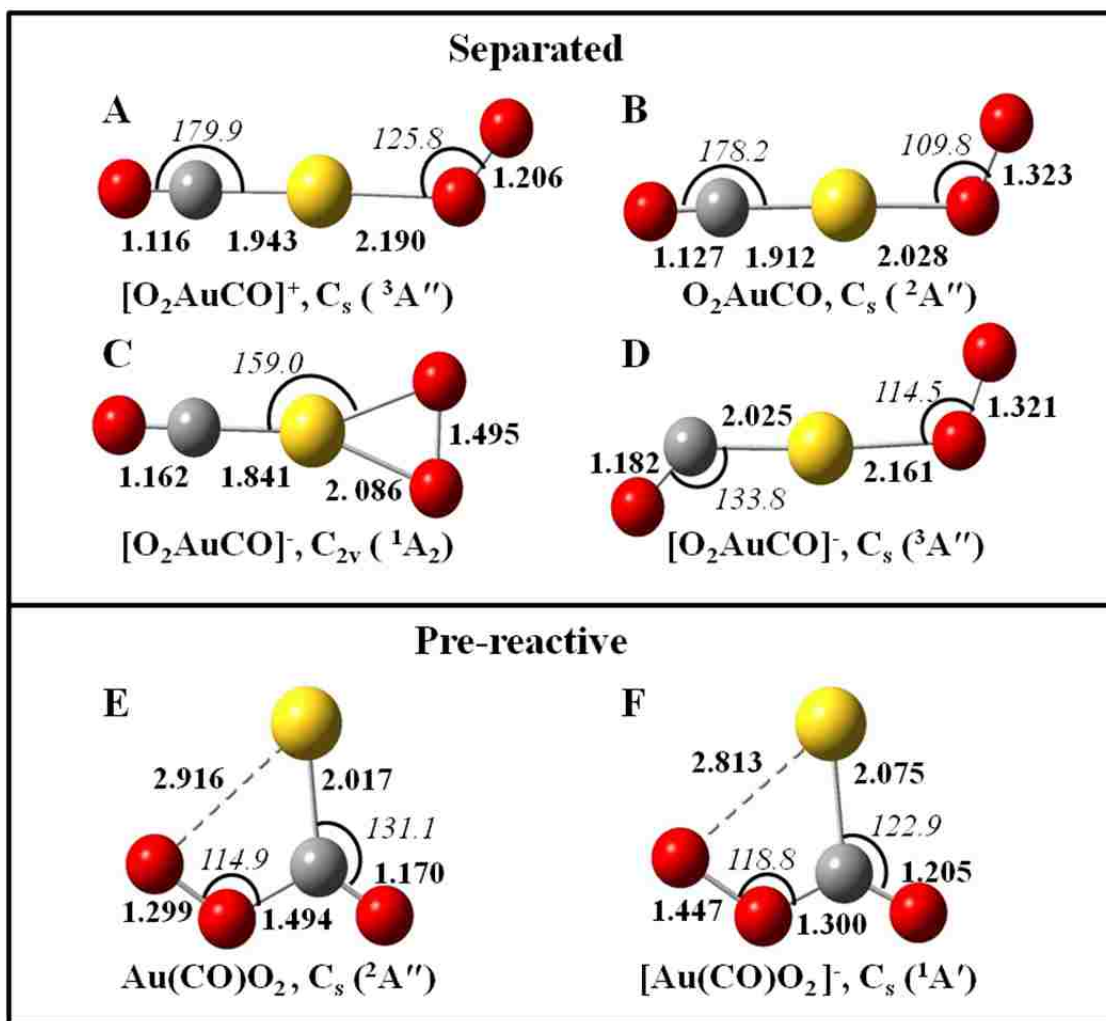


Figure 3.3. Geometry and structural characteristics of cationic, neutral and anionic ternary complexes, $[\text{O}_2\text{AuCO}]^q$ and $[\text{Au}(\text{CO})\text{O}_2]^q$, which can be described as separated (A-D), pre-reactive (E & F). *Italicized* numbers correspond to angles (in degrees) and **bold** numbers correspond to bond lengths (in angstroms).

vibrational frequencies of the associated bands show large red shifts of ~ 300 and ~ 450 cm^{-1} for the C-O and O-O modes, respectively, which is consistent with the bond length trends. The intermolecular O-C bond is still quite long (1.494 Å), and the associated stretching frequency is quite low (~ 430 cm^{-1}), indicating that the “intermolecular” C-O bond is rather weak. The binding energy for the complex is only -8.1 kcal/mol, significantly smaller than for the separated isomer discussed above, and there is no cooperative binding effect. A recent B3LYP study using a different basis set found an analogous pre-reactive structure to that reported here, although the reported binding energy was -15.1 kcal/mol.⁴⁴ That study did not correct for BSSE or ZPE,⁴⁴ however, these discrepancies are too large to be accounted for by those effects, which typically total only 1-2 kcal/mol for the complexes. For our calculations, even the re-optimized structure using the larger aug-cc-pVQZ basis set for C and O yielded a -9.85 kcal/mol binding energy (-12.79 uncorrected for ZPE and BSSE), in good agreement with the smaller basis set result above.

For the anionic ternary complexes, several different isomers were found, corresponding to different structural types and spin states. Separated geometries were located for two distinctly different structures correlating with the triplet and singlet electronic states. The $^3A''$ structure (Figure 3.3 D) exhibits bent η^1 geometry at both the CO and O₂ moieties. As with the neutral species, the intermolecular distances are rather drastically contracted with respect to the binary complexes, with the Au-O bond shortening by 0.9 Å. Strictly speaking, the Au-C bond also contracts by 0.9 Å; however, this is somewhat misleading, since the Au-C bond in the anionic Au-CO complex is anomalously long, as explained above. Based on results from other functionals

(presented above), a more reasonable value for the Au-C contraction is $\sim 0.4 \text{ \AA}$. As with the separated neutral ternary complex, the O-O bond length (1.321 \AA) and vibrational frequency (1169 cm^{-1}) are reminiscent of the values for the free superoxide species, suggesting significant charge transfer to the O_2 subunit. The C-O bond is also significantly expanded to be comparable to the distance predicted for the CO anion. Consistent with this, the CO stretching frequency for this complex also shows an extreme red shift to 1824 cm^{-1} , suggesting that there is significantly more electron density on the Au-center, with concomitant back-donation into the CO π^* -orbitals. Note that due to the bent Au-CO orientation, this back-donation likely occurs from overlap with the Au 6s orbital. These effects combine to produce a lower stabilization energy (-11.1 kcal/mol), and cooperativity of binding (-6.5 kcal/mol), than for the separated neutral species.

The separated structure for the singlet state of the anionic ternary complex is qualitatively different from the triplet state, having a T-shaped C_{2v} structure, with a linear Au-CO geometry and the O_2 binding in an η^2 orientation (Figure 3.3 C). The geometry is the most compact of all the separated structures, having the shortest Au-C (1.841 \AA), and Au-O (1.947 \AA perpendicular distance to center of O_2 bond; both Au-O bonds are 2.086 \AA) intermolecular distances. Additionally, the structures of the CO and O_2 subunits are strongly perturbed. The O-O distance of 1.495 \AA falls between the bond lengths of the free superoxide (1.341 \AA) and peroxide (1.559 \AA) ions, and at 839 cm^{-1} , the O-O stretching frequency is red-shifted by more than 800 cm^{-1} to a value close to that of the peroxide di-anion (703 cm^{-1}). The C-O frequency is also strongly red-shifted by 212 cm^{-1} , although this is perhaps less than might be expected based on the C-O bond length, which is expanded by 0.058 \AA relative to free CO. Strictly speaking, the CO red-shift is

larger for this structure than for the binary Au-CO anion, but recall that the latter complex is anomalous at the B3LYP level. Calculations with other functionals suggest that the red-shift of the CO frequency for $[\text{Au-CO}]^-$ should be $\sim 120 \text{ cm}^{-1}$ larger, and thus the CO frequency of the singlet separated ternary complex actually represents a *blue*-shift of $\sim 50 \text{ cm}^{-1}$ with respect to that value. In any case, the trends observed in this complex are strongly suggestive of significant cooperative charge transfer to the O_2 , which then makes the Au center more positive, strengthening the interaction with CO. It is thus perhaps surprising that the stabilization energy (-11.3 kcal/mol) and cooperative binding (-6.7 kcal/mol) for this complex are only slightly larger than for the triplet separated structure discussed above. One reason for this is that the use of ground state reference species to define the binding energy means that we are computing relative to the $^3\Sigma_g^- \text{O}_2$ ground state, and dissociation into (or indeed formation from) that state would require a spin-forbidden curve crossing. If we instead consider the binding relative to the dissociation asymptote on the singlet surface ($^1\Delta_g$ state of O_2 calculated at B3LYP level, c.f. Table A3.1 in Appendix A3), the binding energy and cooperative binding are much larger, -49.7 and -23.7 kcal/mol , respectively. Questions concerning the likelihood of such curve crossings, although interesting, are beyond the scope of the current work. However it is perhaps noteworthy that no experimental observations of anionic ternary complexes were reported from any of the previous matrix isolation studies.

The lowest-lying electronic state of the anion ternary complex was found to be a singlet state with a pre-reactive geometry (Figure 3.3 F), $\sim 6 \text{ kcal/mol}$ more stable than the separated structures discussed above. The C_s structure is qualitatively similar to the neutral pre-reactive complex, but is closer to the product state geometry. The

intermolecular C-O bond is contracted to 1.300 Å, and is much closer to the other CO bond, which has expanded to 1.205 Å. These changes are reflected in the inter- and intramolecular CO stretching frequencies, which have shifted to 1127 and 1719 cm⁻¹, respectively. At the same time, the O-O distance has expanded by 0.148 Å to 1.447 Å, with a concomitant red-shift of the stretching frequency from 1189 cm⁻¹ to 883 cm⁻¹, when compared to the neutral pre-reactive complex. Thus, this structure seems reflective of an incipient reaction to form a [CO₂-AuO]⁻ complex. The stabilization energy is -17.0 kcal/mol, relative to the triplet dissociation asymptote, with cooperativity of binding of -12.4 kcal/mol; both values are notably larger than the neutral pre-reactive complexes, suggesting that the negative charge lends additional stabilization to the complex. It should be noted that no structures corresponding to a pre-reactive geometry could be identified on the triplet surface.

It is interesting to note that for both the neutral and anionic pre-reactive structures, a secondary set of minima were found corresponding to rotation of the Au-C-O-O dihedral angle from 0° to 180° (c.f., Figure 3.4 E and F, and Tables A3.7 – A3.11 of Appendix A3). The structural and vibrational frequency trends of these 180° rotamers are quite similar to those of the pre-reactive complexes already discussed above. One point of interest is that while the neutral 180° rotamer is higher in energy by ~2.0 kcal/mol than the 0° rotamer, for the anionic species the two rotamer are essentially equi-energetic, with the 180° rotamer actually lying slightly lower in energy (~0.1 kcal/mol). This suggests that the interaction of the outer O-atom of the O₂ subunit with the Au atom affords some extra stabilization in the neutral complex, but not in the anionic complex. Future studies will extend these structural characterizations to include the transition state and product

complexes, using higher-level double-hybrid DFT methods and larger basis sets, to help predict weakly-bound “long-range” species with more confidence, thereby providing a more complete map of the singlet and triplet potential energy surfaces. It is also worth noting that the singlet surface could in principle be directly probed experimentally in matrix isolation studies, using photochemistry to access the singlet O₂ in the matrix.

Long-range ternary complexes and pre-reactive rotamers

In the course of the structure searches on the various spin- and charge-specific potential energy surfaces for the ternary complexes, we located several stable minima which had intermolecular separations that were quite long, with weak binding energies. For completeness, the vibrational shifts, structural comparisons, binding energies and fragment charges for these “long-range” geometries are collected in Tables A3.7-A3.11 in Appendix A3. True geometries for these long-range structures are probably quite sensitive to van der Waals interactions, and thus there are natural questions to raise concerning the validity of these results from a DFT functional that is known to give a poor representation of van der Waals forces.⁶³ This is particularly true for the anionic complexes with a large Au-CO intermolecular distance, given the difficulties detailed above with the binary anionic Au-CO complex.

The long-range isomer (Figure 3.4 A) of the separated neutral ternary complex is, as the name suggests, essentially an amalgam of the neutral Au-CO and free O₂ structures, with an intermolecular O-C bond length of 2.964 Å, and with the other structural parameters and vibrational frequencies effectively unperturbed relative to these reference systems. The binding energy for the long-range complex is -7.2 kcal/mol, which is essentially the same as the pre-reactive complex. We also located several long-

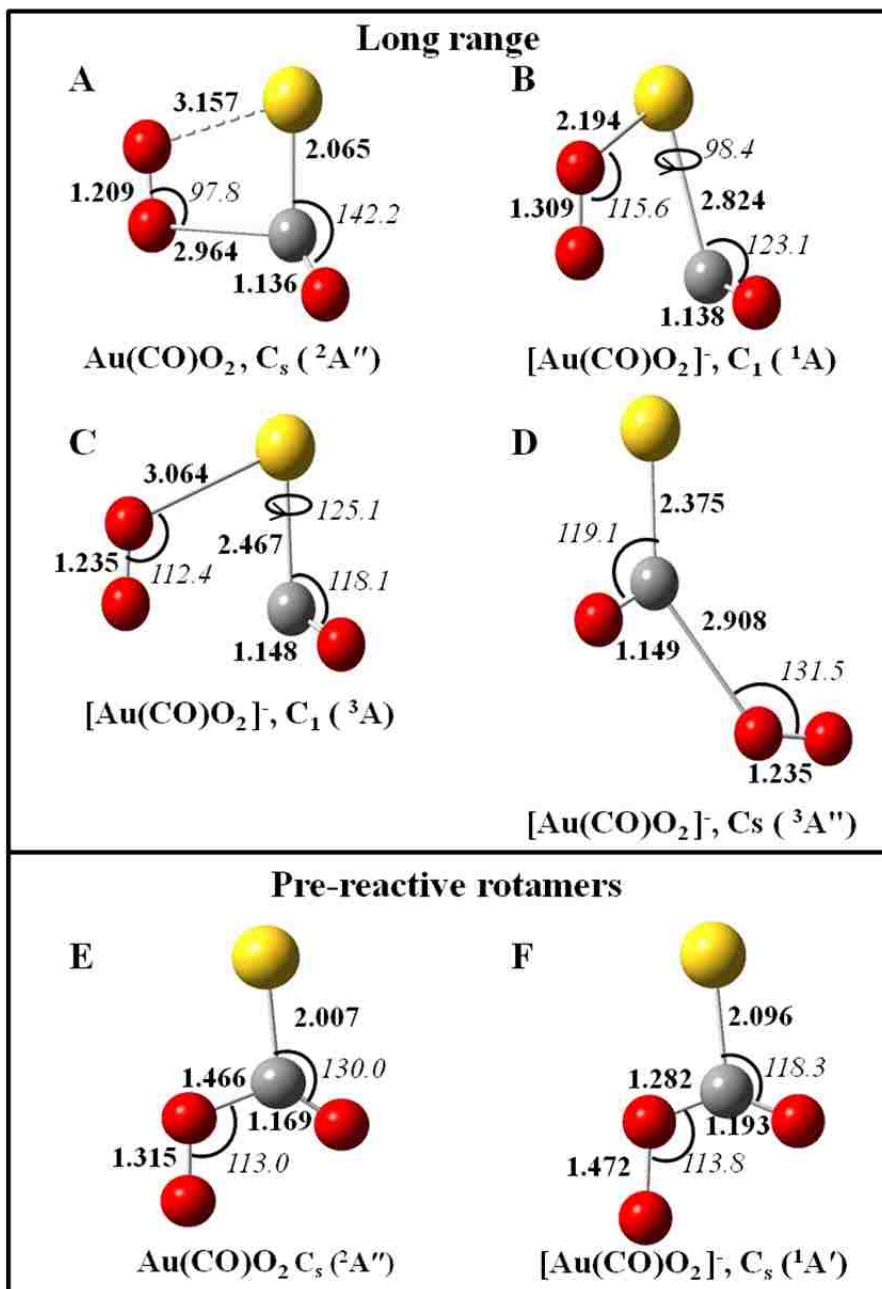


Figure 3.4. Geometry and structural characteristics of the neutral and anionic long range ternary complexes, labeled A-D, and pre-reactive rotamers, labeled E & F. Numbers in bold correspond to bond lengths in angstroms and numbers in italics are bond angles in degrees.

range ternary complexes in the triplet anion manifold, the lowest of which are shown in Figure 3.4 (C & D). Both structures can be characterized as $[\text{Au-CO}]^-$ moieties with weakly associated O_2 molecules $\sim 3 \text{ \AA}$ away. Although the O_2 molecules are far away, they still reflect intermolecular interactions comparable to those in the triplet $[\text{Au-O}_2]^-$ binary complex, with O-O bond distances stretched 0.032 \AA and O-O stretching frequencies red-shifted by $\sim 250 \text{ cm}^{-1}$, relative to the free monomer. The interaction also shortens the Au-C bonds to $\sim 2.35\text{-}2.45 \text{ \AA}$, with corresponding red-shifts of the CO frequency of $\sim 220\text{-}230 \text{ cm}^{-1}$. These values are similar to those predicted by mPW1PW91 and B2PLYP for the unperturbed $[\text{Au-CO}]^-$ binary complex, which suggests that the long-range interaction with the O_2 molecule may alleviate the anomalous effects observed for the B3LYP $[\text{Au-CO}]^-$ complex.

There is also a long-range structure for the singlet ternary anion (Figure 3.4 B), which is distinct from the triplet long-range structures (Figure 3.4 C and D), in that it resembles the singlet $[\text{Au-O}_2]^-$ moiety, with a weakly associated CO molecule, and the structural parameters and vibrational frequencies reflect this, in that the O_2 is more strongly perturbed from the free molecule parameters, relative to the CO. However, this structure is unstable by $\sim 12 \text{ kcal/mol}$ with dissociation into the triplet reference state (it is, of course, still stable by $\sim 26 \text{ kcal/mol}$ with respect to dissociation into the singlet reference state). In fact, no long-range complexes could be located on the singlet surface that were stable with respect to dissociation into the ground state, thus it is hard to identify a long-range “entrance-channel” complex akin to structure in Figure 3.4 A in the neutral doublet manifold. The triplet long-range complexes have the expected structural motifs, but would need to undergo a curve crossing onto the singlet surface in order to

form the pre-reactive geometry of Figure 3.3 F, since there are no pre-reactive triplet complexes. Likewise, the singlet long-range structure, 3.4 B, could only be formed (from ground state reactants) by curve crossing from the triplet surface.

3.4.2 Charge Dependent Trends

A major goal of this work was to examine the charge-dependent trends in the structures and vibrational frequencies of the complexes, in order to better understand the corresponding changes in the chemical bonding and activation of the complexes. Tables 3.3 and 3.4 organize the charge-dependent trends in the structural parameters and vibrational frequencies of the complexes, respectively. One striking point about the structural data in Table 3.3 is that the binary and ternary complexes show opposing trends in terms of how the intermolecular distances change with increasing negative charge. The binary complexes tend to show longer intermolecular distances going from cation to neutral to anionic species. On the other hand, the separated ternary complexes (Figure 3.3 A-D) show a clear contraction in the Au-C and Au-O distances with increasing charge. The triplet anion separated complex (Figure 3.3 D) doesn't quite follow this trend; however, it still has intermolecular Au-C and Au-O distances that are significantly contracted relative to the analogous binary complexes. Furthermore, the O-O bond distance increases quite drastically as a function of increasing negative charge, starting at a value close to the free molecule in the cationic complex, increasing to a value comparable to superoxide ion (O_2^-) in the neutral and triplet anionic complexes, and approaching the value for peroxide ion (O_2^{2-}) in the singlet anion complex (c.f. the reference lengths included in Table 3.3). As already noted, the charge-dependent trend in the pre-reactive complexes (Figure 3.3 E and F), is that the anionic complex seems to

reflect a structure that is “closer to product”, in that the CO bond lengths are more similar than in the neutral, while the O-O bond distance is longer. Thus for both the separated and pre-reactive geometries, the changes in the O-O bond length suggest significant charge transfer onto the O₂ moiety with increasing negative charge.

The charge-dependent vibrational frequency trends reflected in Table 3.4 are also revealing. The trends in the O-O stretching frequency parallel the structural changes noted above; as the negative charge increases, the O-O frequency is shifted drastically to the red, such that it is close to the value for the superoxide ion in the neutral and triplet anion complexes, and approaches the peroxide ion stretching frequency for the singlet anion complexes. This further supports the idea of charge transfer onto the O₂ subunit as the electron density in the complexes increases.

The trends in the CO stretching mode also support the notion of charge transfer. In the cationic ternary complex, the CO frequency is essentially the same as in the cationic binary complex. However, in the neutral separated ternary complex (Figure 3.3 B), the CO frequency is blue shifted by $\sim 135\text{ cm}^{-1}$ relative to the binary complex. Recall also that the local OC-Au geometry in structure B has a linear arrangement reflective of the [Au-CO]⁺ complex. These factors support the conclusion that the Au atom in structure B is more positive than in the neutral binary Au-CO complex. Although the vibrational shift data is a bit ambiguous for the separated singlet anion (due to the anomalous B3LYP [Au-CO]⁻ result), the fact that the local OC-Au geometry remains linear again supports the notion that the Au atom has a more positive charge than in the binary complex. The trends in the CO frequencies for the pre-reactive complexes are a bit different. In this case, the CO modes are strongly red-shifted, which is consistent with

the fact that the CO and O₂ are proximate in these complexes, and thus share the effects of the charge transfer into the collective O₂-CO moiety.

The B3LYP charge distributions are visualized in Figures 3.5 and 3.6 by mapping the electrostatic potential (ESP) onto isodensity surfaces for the binary and ternary complexes, respectively. Comparing binary and ternary systems with equivalent charges provides additional qualitative support for the cooperativity themes expressed so far. Specifically, for the cationic case, the surface for ternary complex looks like it was composed from the two binary complexes, with the highest positive charge remaining on the Au-center, and the most negative charge at the O₂ and CO ends. On the other hand, for the neutral case, the surfaces for the binary complexes show very little charge differentiation, while the separated ternary complex surface reflects a migration of electron density through the complex from the CO end to the more electron withdrawing O₂ end. A similar comparison can be drawn between the binary anionic complexes and the separated singlet anion complex; on the other hand, the separated triplet anion complex shows comparatively little charge separation. All of this is consistent with the trends noted above for the structural parameters and vibrational frequencies.

For the pre-reactive geometries, the surfaces in Figure 3.6 show an interesting shift going from the neutral to the anionic complex. In the neutral complex, which has a longer intermolecular distance between the CO and O₂, both the CO and O₂ acquire roughly equivalent amounts of negative charge on their “outer” O-atoms. On the other hand, in the anionic complex with a shorter O₂-CO distance, the electron density has shifted more completely from the CO onto the outer O-atom of the O₂, which is consistent with tighter intermolecular binding, leading to increased cooperativity, as

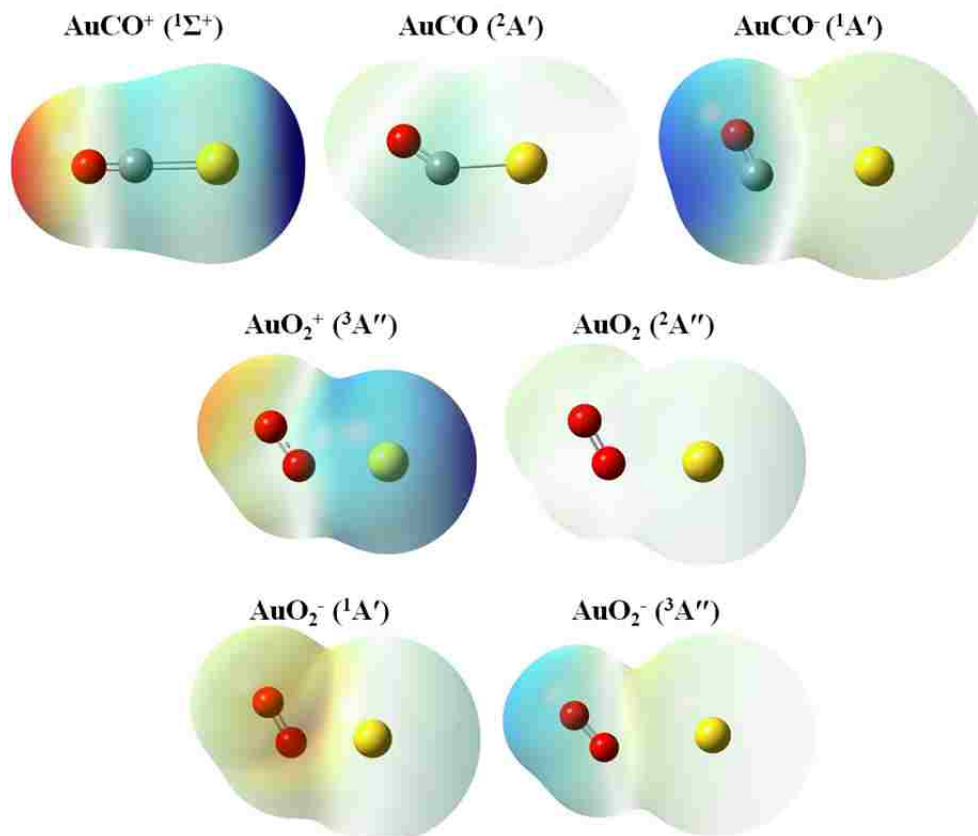


Figure 3.5. Electrostatic potential mapped on the total electron density isosurfaces (density =0.0004) for binary complexes calculated at B3LYP-SDD/6-311+G(3df). The color map spans a range of 0.1 in each case, with red (blue) as most negative (positive). The charges for anions are mapped over -0.21 to -0.11; neutrals, -0.05 to +0.05, and cationic, +0.13 to +0.23. Note that the color intensities are also mapped to the values, such that colors near the ends of the range appear brightest, while those in the center appear transparent.

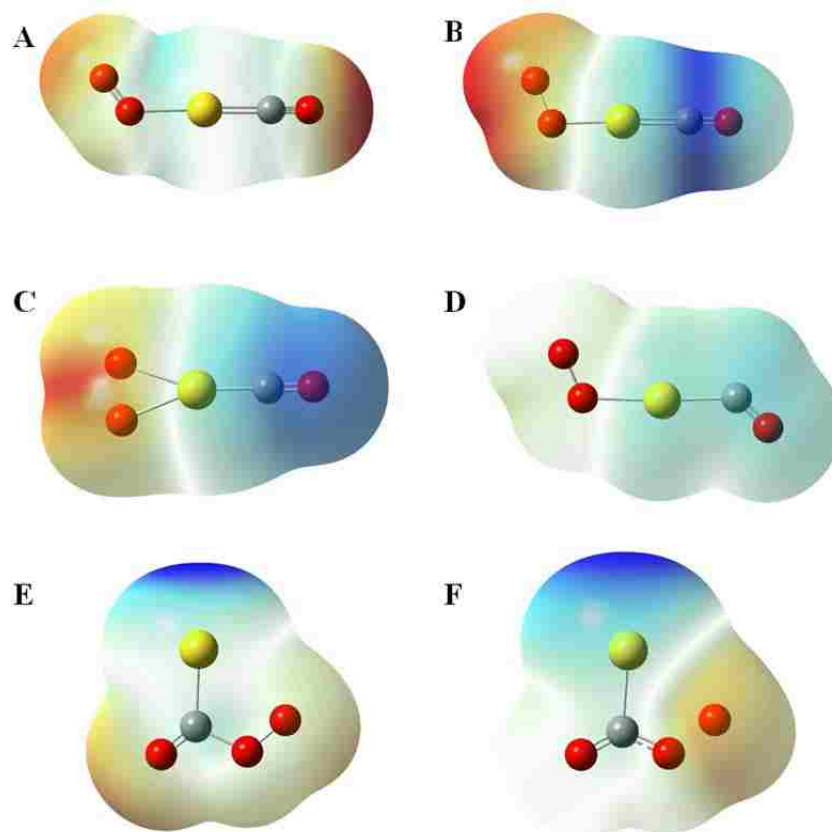


Figure 3.6. Electrostatic potential mapped on the total electron density isosurfaces (density =0.0004) for ternary complexes calculated at B3LYP-SDD/6-311+G(3df). The color map spans a range of 0.1 in each case, with red (blue) as most negative (positive). The charges for anions are mapped over -0.21 to -0.11; neutrals, -0.05 to +0.05, and cationic, +0.13 to +0.23. Note that the color intensities are also mapped to the values, such that colors near the ends of the range appear brightest, while those in the center appear transparent.

Table 3.5. Hirshfeld charges per fragment^a calculated from the Hirshfeld population analysis for cationic, neutral and anionic binary and ternary complexes^{b,c} calculated with B3LYP-SDD/6-311+G(3df).

		AuCO		O₂AuCO or Au(CO)O₂			AuO₂	
		q _{Au}	q _{CO}	q _{Au}	q _{CO}	q _{O₂}	q _{Au}	q _{O₂}
Separated								
Cationic ^d		+0.633	+0.367 (+0.315)	+0.381	+0.338 (+0.298)	+0.281 A (+0.178)	+0.724	0.277 (+0.110)
Neutral	Doublet	-0.054	0.055 (+0.152)	+0.153	+0.162 (+0.214)	-0.314 B (-0.133)	0.000	0.000 (+0.029)
	Quartet						0.000	0.000 (0.000)
Anionic	Singlet	-1.133	+0.149 (+1.641)	-0.071	-0.191 (0.029)	-0.736 C (-0.368)	-0.340	-0.654 ^e (-0.146)
	Triplet			-0.193	-0.316 (-0.058)	-0.489 D (-0.303)	-0.157	-0.834 (-0.064)
Pre-reactive								
Neutral (doublet)				+0.083	-0.007 (+0.175)	-0.075 E		
Anionic (singlet)				-0.266	-0.172 (+0.142)	-0.560 F		

^a The charge value in parentheses denotes the charge on the atom involved in an intermolecular bond with Au.

^b Labels A-F correspond to the structures shown in Figure 3.3.

^c Lowest energy state for species of the same charge and molecular components are in bold.

^d [AuCO]⁺ has a singlet ground state and other cationic complexes have triplet ground states.

^e [AuO₂]⁻ singlet was calculated as restricted (closed shell) due to high spin contamination in the unrestricted singlet calculation.

observed above. One point that should be noted about the ESP map for the separated ternary singlet anion complex is that the negative charge appears to be greatest in the region between the two O-atoms. This could be an indication that this structure is subject to an unphysical DFT electron delocalization error,^{63, 71} particularly given the very long O-O separation (1.495 Å).⁷² In order to check this, we re-optimized the structure at the MP2 level with the same basis set, and found a local minimum corresponding to a similar C_{2v} structure, where the O-O distance actually increased slightly to 1.519 Å. This small change suggests that while there may be some degree of additional stabilization in DFT calculations due to electron delocalization error, it is not the principal determining factor.

In order to quantitatively assess the extent of charge transfer in the complexes, atomic partial charges were computed based on the Hirshfeld “Stockholder model,”⁵³ and are collected in Table 3.5. Note that the fragment-based charges for CO and O₂ reflect the summed charges on their component atoms. In general, the calculated Hirshfeld charges for these complexes are consistent with the conclusions drawn on the basis of the structural and vibrational trends. In particular, the structures with elongated O-O bonds and strongly red-shifted O-O stretching modes have the largest negative partial charges on O₂, and the gold atom in the neutral and anionic ternary complexes is more positively charged than in corresponding binary complexes.

Furthermore, for a given value of the overall charge of the complex, the C-O bond lengths and stretching frequencies tend to be shorter and less red-shifted for complexes that have larger partial positive charges on the Au center, as is consistent with the electrostatic model for explaining the CO shifts.⁴¹ It is interesting that the largest partial negative charge on O₂ occurs for the triplet [Au-O₂]⁻ binary complex, yet that structure

does NOT show the longest O-O bond or the most strongly red-shifted O-O stretching frequency. This tends to further support of the importance of cooperative effects requiring both the CO and O₂ molecules interacting with the gold center in these complexes.

While Hirshfeld charges have been shown to be more accurate than other partitioning models such as Mulliken and AIM (Atoms in Molecules) schemes,^{73, 74} they have also been shown to be somewhat dependent on the (arbitrary) choice of neutral atoms for the promolecule reference.⁷⁵⁻⁷⁷ In addition, their suitability for calculation of atomic charges in non-neutral molecules has been questioned.⁷⁵ Therefore, partial charge analyses were also performed using the NBO and CHELPG schemes; these results are collected in Tables A3.12 and A3.13 of Appendix A3. Although the magnitudes of the NBO and CHELPG partial charges are generally somewhat larger than the Hirshfeld charges, all of the trends emphasized above as supporting the cooperative charge transfer are preserved. In particular, the more positive nature of the Au center in the ternary relative to the binary complexes is even more pronounced, as is the charge transfer to the O₂ moiety in the separated ternary species. It should be noted here that the three methods of calculating partial atomic charges are quite different; while Hirshfeld charges are a density-weighted atoms in molecules (AIM) scheme,⁵³ natural bond orbitals derive a set of orthogonalized natural orbitals consistent with chemical bonding concepts,⁵⁷ and CHELPG charges are based on the molecular electrostatic potential (i.e. the same quantity visualized in Figures 3.5 and 3.6).⁵⁶ The fact that these three different approaches all support the cooperative charge transfer trends identified here gives confidence that they may indeed have some physical validity.

3.4.3 Molecular Orbitals

A deeper understanding of the specific interactions responsible for the various trends identified above can be gained by examining the high-lying molecular orbitals. Figure 3.7 shows the orbitals most relevant to understanding the bonding trends in the binary and separated ternary complexes. In particular, the preference for bent structures in the neutral and anionic Au-CO binary complexes can be clearly understood as arising from the fact that the Au atom has population in the 6s orbital, which can only have a bonding interaction with one lobe of the CO π^* -orbital. In contrast, the cationic Au-CO complex does not have population in the Au 6s orbital, and thus can undergo a full Dewar-Chatt type interaction, with σ -donation to the Au from the CO σ -orbital (HOMO), and π -backbonding interaction between the Au d-orbitals and the CO π^* -orbital (HOMO-3). This same bonding motif can also be observed between the Au and CO in the ternary complexes having a linear Au-CO arrangement (Figure 3.3 A-C). The singlet anion complex in particular seems to have an extremely strong π -backbonding interaction that extends onto the π^* -orbitals of the O₂ subunit. On the other hand, the triplet anion separated structure with a bent Au-CO arrangement (Figure 3.3 D), has orbitals that are more reminiscent of the Au-CO interaction in the neutral binary complex,

Figure 3.8 shows the frontier orbitals for the ternary complexes with pre-reactive geometries (Figure 3.3 E and F). These orbitals show remarkable similarity between the neutral and anionic species, and clearly show the formation of a conjugated π -system between the CO and O₂ subunits (neutral HOMO-2 and anionic HOMO). Images of the high-lying molecular orbitals for the pre-reactive rotamer structures are presented in Figure A3.1 of Appendix A3 and can be discussed in a similar manner. Note that since

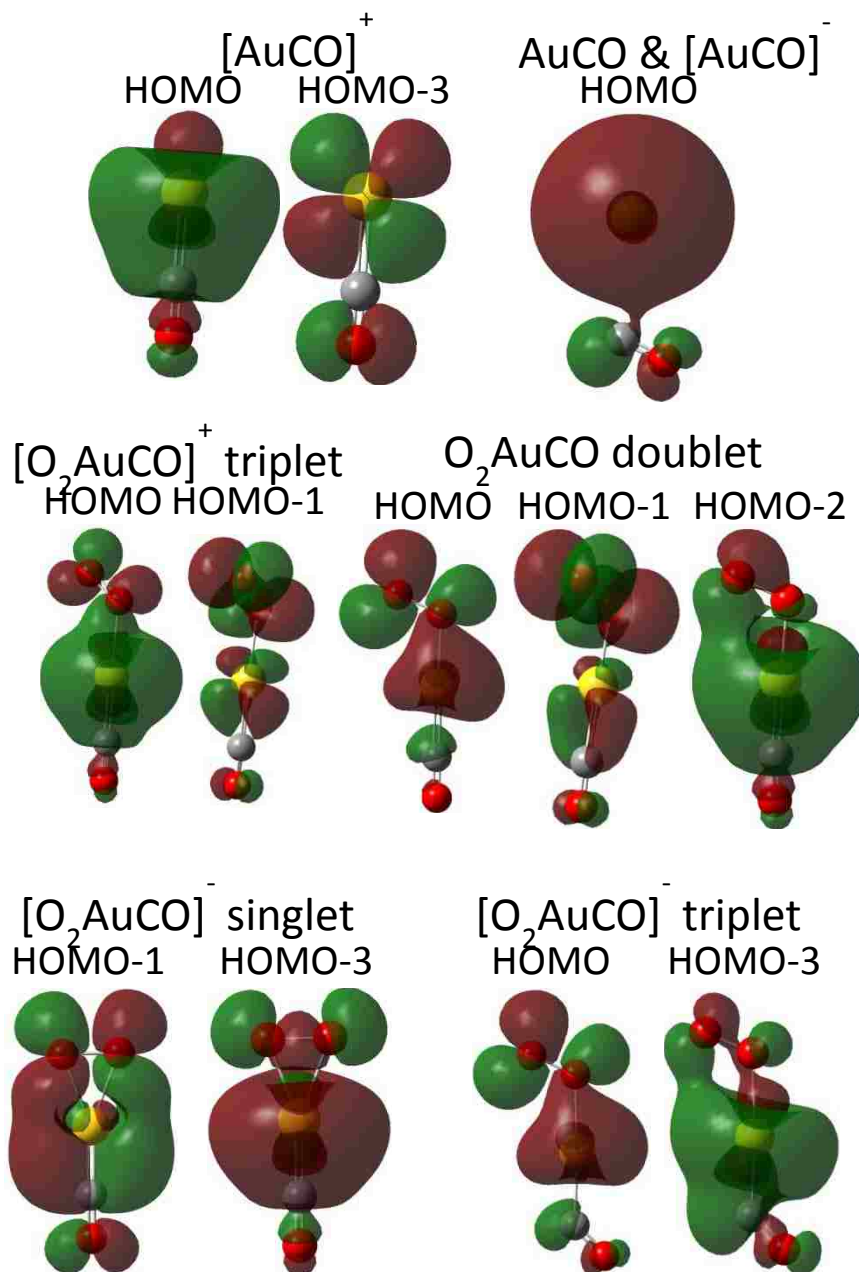


Figure 3.7. Selected molecular orbitals showing Au-CO σ -donation and π -backbonding character for binary $[\text{AuCO}]^q$ and ternary $[\text{O}_2\text{AuCO}]^q$ complexes, $q=+1,0,-1$.

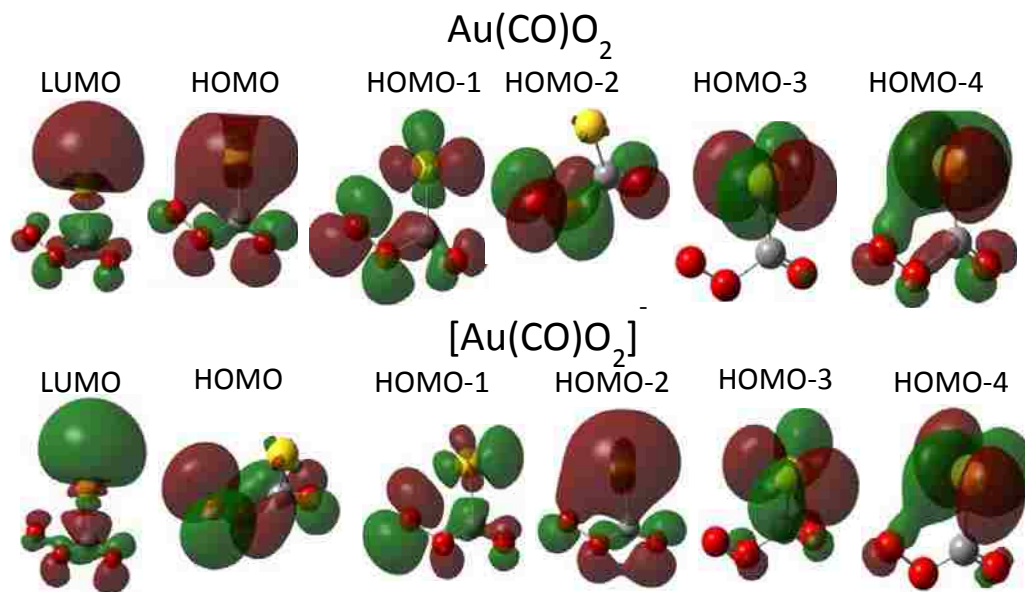


Figure 3.8. Five highest occupied molecular orbitals and LUMO of “pre-reactive complexes,” $\text{Au}(\text{CO})\text{O}_2$ (Fig. 3.3 C) and $[\text{Au}(\text{CO})\text{O}_2]^-$ singlet (Fig. 3.3 F). $\text{Au}(\text{CO})\text{O}_2$ β -spinorbitals are not shown, but are similar to the (shown) α -spinorbitals, except that the LUMO- β is the same structure as HOMO-2 α (shown in figure). Note that for both series, all orbitals feature a node in the “breaking” bond (O-O), and a bonding interaction in the “forming” bond (2nd C-O bond).

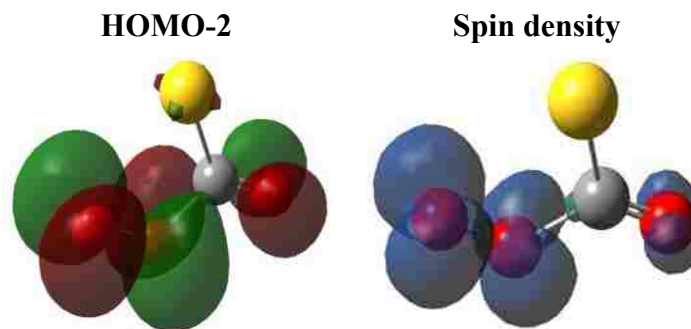


Figure 3.9. Comparison of the orbital HOMO-2(α) and spin density for the $\text{Au}(\text{CO})\text{O}_2$ doublet ternary species (Figure 3.3 E) calculated with B3LYP-SDD/6-311+G(3df).

there is very little spin-contamination in neutral complex, only the α -spinorbitals are shown; the β -spinorbitals are essentially identical, except that the HOMO-2 orbital is unoccupied in the β -manifold. Indeed the spin-density for the neutral pre-reactive complex is essentially identical to the HOMO-2 orbital (c.f., Figure 3.9). This seems quite significant, since it means that the anionic singlet pre-reactive complex is basically just the neutral complex with an extra electron added to the conjugated π -system formed between the CO and O₂ molecules. Even more strikingly, all of the 3 highest-lying orbitals for both species clearly have an anti-bonding interaction between the O-atoms in the O₂ subunit, but bonding interactions between the C and O atoms in the CO subunit, as well as in the intermolecular C-O interaction. These trends are quite consistent with the previously identified trends in the structures and frequencies, which indicate that the anion complex has a structure that more closely reflects the expected CO₂ product molecule. Thus our conclusions are that the role of the gold atoms in these pre-reactive complexes is to stabilize the formation of this conjugated π -system between the O₂ and CO, which will eventually result in formation of CO₂ in the exit channel of the reaction.

3.5 Conclusions

The comprehensive set of calculations presented here for the cationic, neutral and anionic binary and ternary complexes of CO and O₂ with Au^q (q= -1, 0, +1) have provided a fairly clear picture of how the charge of the complexes affects their structures, vibrational frequencies and binding energies. For the binary complexes, as the charge becomes more negative, the complexes become more diffuse, with longer intermolecular distances and smaller binding energies. Distinctly different trends are seen for the ternary complexes, where increasing negative charge leads to contraction of the intermolecular

distances for the complexes with separated geometries, and increased stabilization of the complexes with pre-reactive geometries. Furthermore, the trends in vibrational frequencies and bond distances for both the separated and pre-reactive ternary complexes indicate the presence of cooperative interactions that tend to localize the electron density on the O₂ moiety; a conclusion that is supported by calculated Hirshfeld charges (Table 3.5). Further support comes from the calculated cooperative binding values (Table 3.2), which for most cases show an increase as additional negative charge is added to a series of similar complexes, with the exceptions being the triplet and singlet anion complexes with separated geometries. In these cases, the complexes are stabilizing quite large distortions in the geometries of the CO and O₂ molecules (c.f., Table 3.3), which reduces the value of the cooperative binding (as calculated here). However the existence of the cooperative effects in these complexes can quite clearly be seen from their molecular orbitals, (Figure 3.7) which clearly show delocalization of electron density over the entire complex.

Finally, the charge-dependent trends for the pre-reactive complexes clearly show that there is additional stabilization of the anion complex relative to the neutral, and that the anion complex is “closer to product”, in terms of the structure being more reflective of the breaking of the O-O bond, and the formation of the second C-O bond to form the eventual CO₂ product. The high-lying molecular orbitals for these complexes further reveal that the role of the gold center is to stabilize the formation of a conjugated π -system between the CO and O₂ molecules. The singly-occupied orbital of the doublet-neutral complex is a conjugated π -orbital, with a node in the O-O bond, and a bonding interaction in the intermolecular C-O bond (i.e. the one that is forming). This orbital is

then populated with a second electron to form the anion, with almost no qualitative differences in the remaining high-lying molecular orbitals.

3.6 References

- (1) Haruta, M. *Cattech* **2002**, *6*, 102-115.
- (2) Hashmi, A. S. K.; Hutchings, G. J. *Angew. Chem. -Int. Edit.* **2006**, *45*, 7896-7936.
- (3) McIntosh, D.; Ozin, G. A. *Inorg. Chem.* **1976**, *15*, 2869-2871.
- (4) McIntosh, D.; Ozin, G. A. *Inorg. Chem.* **1977**, *16*, 51-59.
- (5) Huber, H.; McIntosh, D.; Ozin, G. A. *Inorg. Chem.* **1977**, *16*, 975-979.
- (6) Liang, B.; Andrews, L. *J. Phys. Chem. A* **2000**, *104*, 9156-9164.
- (7) Wang, X.; Andrews, L. *J. Phys. Chem. A* **2001**, *105*, 5812-5822.
- (8) Hakkinen, H.; Landman, U. *J. Am. Chem. Soc.* **2001**, *123*, 9704-9705.
- (9) Hagen, J.; Socaciu, L. D.; Eljazyfer, M.; Heiz, U.; Bernhardt, T. M.; Woste, L. *Phys. Chem. Chem. Phys.* **2002**, *4*, 1707-1709.
- (10) Socaciu, L. D.; Hagen, J.; Bernhardt, T. M.; Woste, L.; Heiz, U.; Hakkinen, H.; Landman, U. *J. Am. Chem. Soc.* **2003**, *125*, 10437-10445.
- (11) Bernhardt, T.; Socaciu-Siebert, L.; Hagen, J.; Woste, L. *Appl. Catal. A-Gen.* **2005**, *291*, 170-178.
- (12) Yoon, B.; Hakkinen, H.; Landman, U. *J. Phys. Chem. A* **2003**, *107*, 4066-4071.
- (13) Kimble, M. L.; Castleman, A. W., Jr.; Mitric, R.; Burgel, C.; Bonacic-Koutecky, V. *J. Am. Chem. Soc.* **2004**, *126*, 2526-2535.
- (14) Jiang, L.; Xu, Q. *J. Phys. Chem. A* **2005**, *109*, 1026-1032.
- (15) Fielicke, A.; von Helden, G.; Meijer, G.; Simard, B.; Rayner, D. *J. Phys. Chem. B* **2005**, *109*, 23935-23940.
- (16) Fielicke, A.; von Helden, G.; Meijer, G.; Pedersen, D.; Simard, B.; Rayner, D. *J. Am. Chem. Soc.* **2005**, *127*, 8416-8423.
- (17) Xu, Q.; Jiang, L. *J. Phys. Chem. A* **2006**, *110*, 2655-2662.
- (18) Kimble, M. L.; Moore, N. A.; Johnson, G. E.; Castleman, A. W., Jr.; Burgel, C.; Mitric, R.; Bonacic-Koutecky, V. *J. Chem. Phys.* **2006**, *125*.
- (19) Burgel, C.; Reilly, N. M.; Johnson, G. E.; Mitric, R.; Kimble, M. L.; Castleman, A. W., Jr.; Bonacic-Koutecky, V. *J. Am. Chem. Soc.* **2008**, *130*, 1694-1698.
- (20) Wang, Y.; Zhai, H.; Xu, L.; Wang, L. *J. Phys. Chem. A* **2010**, *114*, 1247-1254.
- (21) Hagen, J.; Socaciu, L. D.; Heiz, U.; Bernhardt, T. M.; Woste, L. *Eur. Phys. J. D* **2003**, *24*, 327-330.
- (22) Wallace, W. T.; Wyrwas, R. B.; Leavitt, A. J.; Whetten, R. L. *Phys. Chem. Chem. Phys.* **2005**, *7*, 930-937.
- (23) Citra, A.; Andrews, L. *J. Mol. Struct. -Theochem* **1999**, *489*, 95-108.
- (24) Varganov, S.; Olson, R.; Gordon, M.; Metiu, H. *J. Chem. Phys.* **2003**, *119*, 2531-2537.
- (25) Yuan, D.; Zeng, Z. *J. Chem. Phys.* **2004**, *120*, 6574-6584.
- (26) Molina, L. M.; Hammer, B. *J. Chem. Phys.* **2005**, *123*, 161104.
- (27) Tielens, F.; Gracia, L.; Polo, V.; Andres, J. *J. Phys. Chem. A* **2007**, *111*, 13255-13263.
- (28) Prestianni, A.; Martorana, A. *J. Phys. Chem. C* **2008**, *112*, 18061-18066.

- (29) Schwerdtfeger, P.; Lein, M.; Krawczyk, R. P.; Jacob, C. R. *J. Chem. Phys.* **2008**, *128*, 124302-124302.
- (30) Lin, L.; Nguyen, M. *Chem. Phys. Lett.* **2010**, *498*, 120-124.
- (31) Sanchez, A.; Abbet, S.; Heiz, U.; Schneider, W.; Hakkinen, H.; Barnett, R.; Landman, U. *J. Phys. Chem. A* **1999**, *103*, 9573-9578.
- (32) Yoon, B.; Hakkinen, H.; Landman, U.; Worz, A. S.; Antonietti, J. M.; Abbet, S.; Judai, K.; Heiz, U. *Science* **2005**, *307*, 403-407.
- (33) Sterrer, M.; Yulikov, M.; Fischbach, E.; Heyde, M.; Rust, H. P.; Pacchioni, G.; Risse, T.; Freund, H. J. *Angewandte Chemie-International Edition* **2006**, *45*, 2630-2632.
- (34) Ricci, D.; Bongiorno, A.; Pacchioni, G.; Landman, U. *Phys. Rev. Lett.* **2006**, *97*, 036106.
- (35) Arenz, M.; Landman, U.; Heiz, U. *Chemphyschem* **2006**, *7*, 1871-1879.
- (36) Wang, J. G.; Hammer, B. *Phys. Rev. Lett.* **2006**, *97*, 136107.
- (37) Hutchings, G. J.; Hall, M. S.; Carley, A. F.; Landon, P.; Solsona, B. E.; Kiely, C. J.; Herzing, A.; Makkee, M.; Moulijn, J. A.; Overweg, A., et al. *J. Catal.* **2006**, *242*, 71-81.
- (38) Wallace, W. T.; Whetten, R. L. *J. Am. Chem. Soc.* **2002**, *124*, 7499-7505.
- (39) McIntosh, D.; Ozin, G. A. *Inorg. Chem.* **1977**, *16*, 59-63.
- (40) Blyholder, G. J. *J. Phys. Chem.* **1964**, *68*, 2772-2777.
- (41) Goldman, A.; Krogh-Jespersen, K. *J. Am. Chem. Soc.* **1996**, *118*, 12159-12166.
- (42) Fiellicke, A.; von Helden, G.; Meijer, G.; Pedersen, D.; Simard, B.; Rayner, D. J. *J. Chem. Phys.* **2006**, *124*, 194305.
- (43) Wu, X.; Senapati, L.; Nayak, S.; Selloni, A.; Hajaligol, M. *J. Chem. Phys.* **2002**, *117*, 4010-4015.
- (44) Fang, H.; Li, Z. H.; Fan, K. *Phys. Chem. Chem. Phys.* **2011**, *13*, 13358-13369.
- (45) Frisch, M. J.; Trucks, G. W.; Schlegel, H. B.; Scuseria, G. E.; Robb, M. A.; Cheeseman, J. R.; Scalmani, G.; Barone, V.; Mennucci, B.; Petersson, G. A., et al. Gaussian 09, Revision A.02, Gaussian, Inc., Wallingford, CT **2009**.
- (46) Becke, A. D. *J. Chem. Phys.* **1993**, *98*, 5648-5652.
- (47) Schwerdtfeger, P.; Dolg, M.; Schwarz, W. H. E.; Bowmaker, G. A.; Boyd, P. D. W. *J. Chem. Phys.* **1989**, *91*, 1762-1774.
- (48) Andrae, D.; Haussermann, U.; Dolg, M.; Stoll, H.; Preuss, H. *Theor. Chim. Acta* **1990**, *77*, 123-141.
- (49) Krishnan, R.; Binkley, J. S.; Seeger, R.; Pople, J. A. *J. Chem. Phys.* **1980**, *72*, 650-654.
- (50) Frisch, M. J.; Pople, J. A.; Binkley, J. S. *J. Chem. Phys.* **1984**, *80*, 3265-3269.
- (51) Langhoff, S. R.; Davidson, E. R. *Int. J. Quant. Chem.* **1974**, *8*, 61-72.
- (52) Boys, S. F.; Bernardi, F. *Mol. Phys.* **1970**, *19*, 553-566.
- (53) Hirshfeld, F. L. *Theor. Chim. Acta* **1977**, *44*, 129-138.
- (54) Ritchie, J. P. *J. Am. Chem. Soc.* **1985**, *107*, 1829-1837.
- (55) Ritchie, J. P.; Bachrach, S. M. *J. Comput. Chem.* **1987**, *8*, 499-509.
- (56) Breneman, C. M.; Wiberg, K. B. *J. Comput. Chem.* **1990**, *11*, 361-373.
- (57) Foster, J. P.; Weinhold, F. *J. Am. Chem. Soc.* **1980**, *102*, 7211-7218.
- (58) Reed, A. E.; Weinhold, F. *J. Chem. Phys.* **1983**, *78*, 4066-4073.
- (59) Reed, A. E.; Weinstock, R. B.; Weinhold, F. *J. Chem. Phys.* **1985**, *83*, 735-746.
- (60) Reed, A. E.; Weinhold, F. *J. Chem. Phys.* **1985**, *83*, 1736-1740.

- (61) Reed, A. E.; Curtiss, L. A.; Weinhold, F. *Chem. Rev.* **1988**, *88*, 899-926.
- (62) Carpenter, J. E.; Weinhold, F. *J. Mol. Struct. -Theochem* **1988**, *46*, 41-62.
- (63) Cohen, A. J.; Mori-Sanchez, P.; Yang, W. *Chem. Rev.* **2012**, *112*, 289-320.
- (64) Grimme, S. *J. Chem. Phys.* **2006**, *124*, 034108.
- (65) Dunning, T. H. *J. Chem. Phys.* **1989**, *90*, 1007-1023.
- (66) Kendall, R. A.; Dunning, T. H.; Harrison, R. J. *J. Chem. Phys.* **1992**, *96*, 6796-6806.
- (67) Peterson, K. A.; Woon, D. E.; Dunning, T. H. *J. Chem. Phys.* **1994**, *100*, 7410-7415.
- (68) Wilson, A.; vanMourik, T.; Dunning, T. *J. Mol. Struct. -Theochem* **1996**, *388*, 339-349.
- (69) Davidson, E. R. *Chem. Phys. Lett.* **1996**, *260*, 514-518.
- (70) Sun, Q.; Jena, P.; Kim, Y.; Fischer, M.; Gantefor, G. *J. Chem. Phys.* **2004**, *120*, 6510-6515.
- (71) Cohen, A. J.; Mori-Sanchez, P.; Yang, W. *Science* **2008**, *321*, 792-794.
- (72) Johnson, E. R.; Mori-Sanchez, P.; Cohen, A. J.; Yang, W. *J. Chem. Phys.* **2008**, *129*, 204112.
- (73) Ayers, P. *J. Chem. Phys.* **2000**, *113*, 10886-10898.
- (74) Saha, S.; Roy, R. K.; Ayers, P. W. *Int. J. Quantum Chem.* **2009**, *109*, 1790-1806.
- (75) Davidson, E. R.; Chakravorty, S. *Theor. Chim. Acta* **1992**, *83*, 319-330.
- (76) Van Damme, S.; Bultinck, P.; Fias, S. *J. Chem. Theory Comput.* **2009**, *5*, 334-340.
- (77) Bultinck, P.; Van Alsenoy, C.; Ayers, P. W.; Carbo-Dorca, R. *J. Chem. Phys.* **2007**, *126*, 144111.

Chapter 4. DFT-calculated CO Oxidation Pathways for Au Atoms and Anions with O₂: Observation of Possibly De-activating Carbonate Species

4.1 Abstract

Density functional theory calculations (DFT) have been utilized to understand the CO oxidation pathway of anionically charged (-1) and neutral Au atoms, with separated O₂AuCO^q and “pre-reactive” AuCOO₂^q reactant-side minima (q=0, -1). Regardless of charge, the neutral and anionic singlet systems have similar reaction pathways with two “major” transition states from each of the “pre-reactive” complexes; the In-TS transition state is formed from the “pre-reactive” in complex, while the Out-TS transition state is formed from the “pre-reactive” out complex. The “In” pathway and desired OAuCO₂ product are energetically preferred for the neutral state, while the “Out” pathway and carbonate-like product are more favorable for the anionic singlet state. An AuCO₃^q carbonate-like product is observed and accessible from either “In” or “Out” pathways; the carbonate-like structure is the energetically favorable product in the anionic (singlet) state, while the OAuCO₂ product is favorable in the neutral system. However, the product is accessible from the carbonate-like minimum over a ~20 kcal/mol barrier. *Ab initio* molecular dynamics (AIMD) show agreement with the potential energy surfaces, where the formation of the carbonate-like structure is dependent on the AuCOO dihedral of the “pre-reactive” complex, and show formation of the desired, OAuCO₂^q, product.

4.2 Introduction

The observation of carbonate-like intermediates in theoretical and experimental studies of unsupported Au nanoparticles can be related to the deactivation of metal oxide-supported Au nanoparticles, which is thought to occur due to build up of carbonate or carboxylate species. Carbonate formation and subsequent catalyst deactivation were

discussed by Haruta to occur by formation of carbonates on the Au nanoparticles and migration of the carbonates onto the support and blocking oxygen vacancy sites.¹ The existence of carbonates on nanoscale Au supported on ZrO₂ after exposure to CO and O₂ has been observed with FT-IR, where bands between 1200-1700 cm⁻¹ were observed and indicated a surface layer of carbonates.² Diffuse-reflectance-infrared fourier-transform spectroscopy (DRIFTS) and FT-IR studies also showed carbonate and carboxylate species on various metal oxide-supported Au nanoparticle samples, such as Au/ α -Fe₂O₃, Au/TiO₂, and Au/Ni₂O₃, exposed to CO and O₂, which led to lower activity of the catalysts.³ In these cases, exposure of the supported Au nanoparticles to nitrogen gas reversed the deactivation. Another investigation that focused on carbonates was a theoretical study into carbonate adducts for small Au cluster anions, Au_{2n}⁻ (n=1-4). These carbonate adducts were found to play a certain role in CO oxidation, as the Au_{2n}CO₃⁻ isomers are thermodynamically more stable than the complex(es) with O₂ and CO separately adsorbed, i.e. O₂Au_{2n}CO⁻.⁴

Our previous research into binary and ternary minima led to observation of separated and pre-reactive structures similar to those of Xu and Jiang, and Fang *et al.*, respectively. Similar to the Wallace and Whetten work, the charged (+1, -1) and neutral Au atoms shows cooperative binding of O₂ and CO when one is “pre-adsorbed.”⁵ Unique to the neutral and anionic singlet charge states, the peroxyformate structures were also observed, which were found in the neutral atomic studies by Fang *et al.* and larger cluster studies by Woste and others. For the separated species, it was found that the O₂ sub-unit is electron-withdrawing enough to induce a positive charge on the CO moiety through the Au atom, whether no charge or an anionic charge was localized initially on the Au atom.⁵

In the pre-reactive “in” complexes (Pre_1), it was observed that the systems form an OCOO π -conjugated system and a node was found consistently between the two oxygen atoms in the molecular orbitals, indicating a probable cleavage point.⁵ Based on these results, $[\text{O}_2+\text{Au}+\text{CO}]$ pathways for neutral and anionic singlet charge states are described herein.

4.3 Results

Previous calculations indicated stable separated and pre-reactive complexes for neutral and anionic singlet states; as a result, the reaction pathways of these two charge states were further investigated and are shown in Figures 4.1 and 4.2. The separated, called Sep in this chapter, and pre-reactive “in” species (Pre_1) have been previously discussed in Chapter 3, where the structures are shown in Figure 3.3 B and E for the neutral separated and pre-reactive “in” complexes, respectively, and Figure 3.3 C and F for the anionic (singlet) separated and pre-reactive “in” complexes, respectively. These letters, B, E, C and F, are also referenced in Tables 3.1-3.4 for the vibrational frequencies, binding energies, bond lengths and shifts in vibrational frequencies, respectively, of each of these ternary complexes. The pre-reactive “out” complexes, Pre_2 in this chapter, were also discussed in Chapter 3, where the structures are shown in Figure 3.4 E and F for the neutral and anionic singlet complexes, respectively. Tables A3.7-A3.10 of the Chapter 3 appendix (A3) tabulate the vibrational frequencies, binding energies, bond lengths, and shifts in vibrational frequencies, respectively, for the pre-reactive “out” complexes. The bond lengths and vibrational frequencies are tabulated for each stable point along the reaction pathways and are divided into tables of reactant-side transition states (Tables 4.1 and 4.2), the In and Out “major” transition states (Tables 4.3 and 4.4), product-side

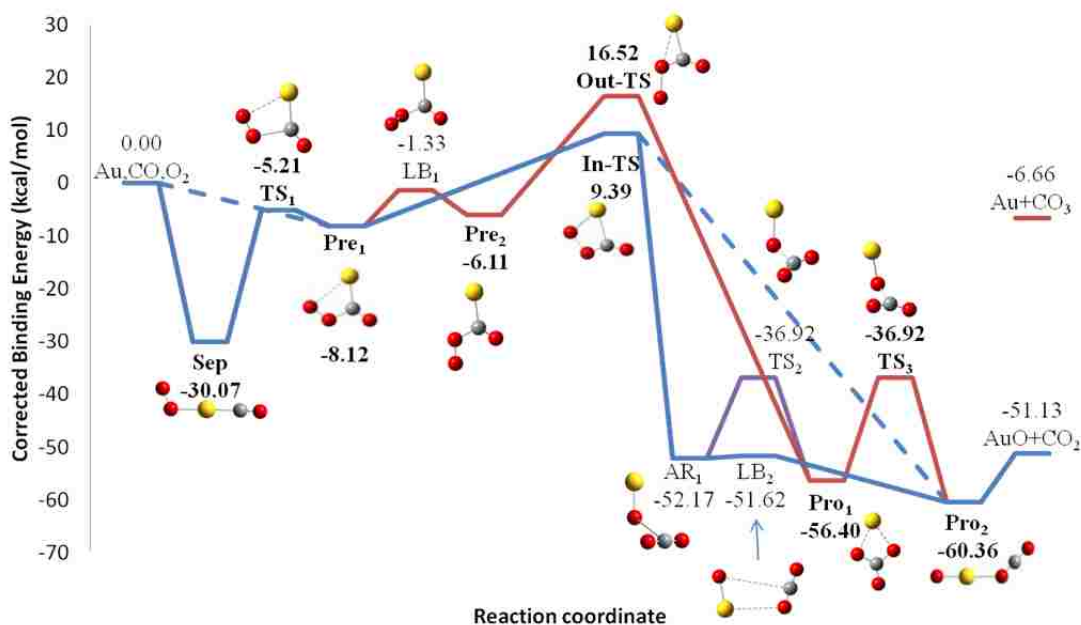


Figure 4.1. Reaction pathways of $[\text{O}_2+\text{Au}+\text{CO}]^0$ (doublet) towards CO oxidation with the relative energies (in kcal/mol) of the stable points. The In-TS pathway is represented by the blue and purple solid lines; the Out-TS pathway is represented with the solid red line. The main minima and transition states, described in the text, are bold. The blue dotted line indicates the minima and transition states that can be “skipped”, where the barriers are lower than the reactant energies.

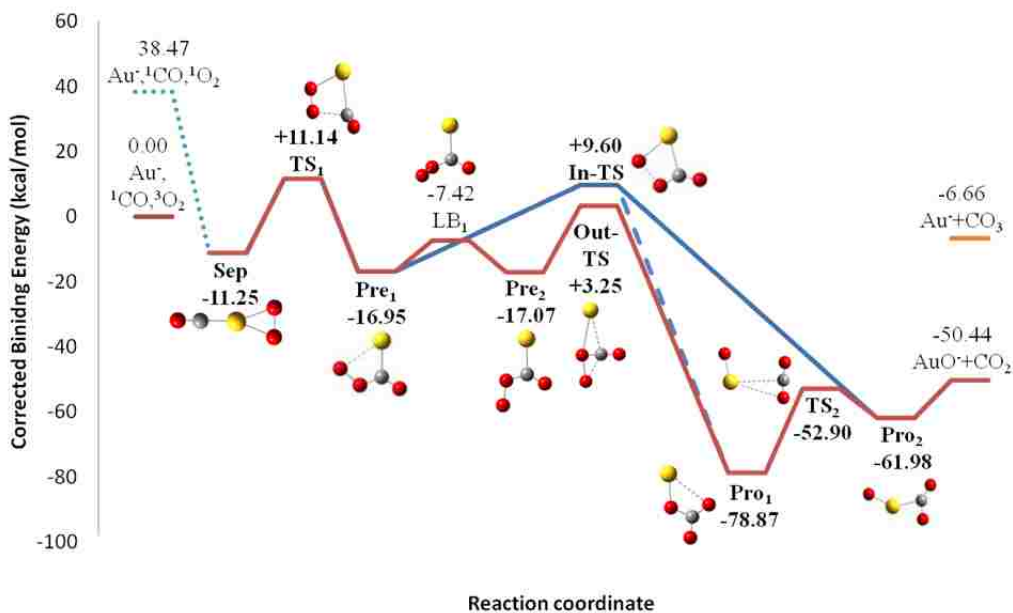


Figure 4.2. Reaction pathways of $[\text{O}_2+\text{Au}+\text{CO}]$ (singlet) towards CO oxidation with the relative energies (in kcal/mol) of the stable points. The In-TS pathway is represented by the blue solid (and blue dotted) lines; the Out-TS pathway is represented with the solid red line. The main minima and transition states that are described in text are in bold.

transition states (Tables 4.5 and 4.6), and product minima (Tables 4.7 and 4.8).

As mentioned above, the neutral and anionic singlet charge states both have reaction pathways that are based on the similar pre-reactive isomers and this likeness continues through the reaction pathways, which can be discussed in a general overview. The separated minimum (Sep) can be formed from the separated reactants of $O_2 + Au^q + CO$ with strong charge transfer into the O_2 moiety and induced positive character on CO. The pathway continues to the pre-reactive isomers with a large alteration of structure and electrostatic potential surface, where an OCOO π -conjugated system is formed with a large change in the charge transfer of the complex with positive character on Au and negative character spread across the conjugated system. The pre-reactive isomers, in and out, lead to two different “major” transition states, where the pre-reactive “in” minimum continues along the “In” pathway (to In-TS) and “out” minimum continues along the “Out” pathway (Out-TS). The two “major” transition states do retain similar structures to the pre-reactive isomers, and both pathways involve elongation of the OO bond, but this elongation leads to different outcomes. Elongation of the OO bond in the In-TS transition state can easily be observed as splitting open the complex to form $OAuCO_2^q$; however, elongation of the OO bond in the Out-TS transition state shows inclination to form a carbonate-like product. The formation and trapping of $AuCO_3^q$ is not desired, as experiments have shown carbonates to deactivate Au catalysts. However, the Out pathway does not end at the carbonate-like minimum; this complex is more likely to re-arrange to $OAuCO_2^q$ than CO_3 to “desorb” from Au, as $OAuCO_2^q$ is lower in energy than the separated Au, CO_3^q products. For the cases in which the Out pathway is followed, especially in the anionic singlet as the Out pathway is the lower energy

pathway, addition of heat after formation of AuCO_3^q will surmount the barrier to form the OAuCO_2 product. Details related to the changes in structures, vibrational frequencies and electrostatic potential surfaces will be discussed in the neutral and anionic singlet pathway descriptions (sections 4.3.1 and 4.3.2).

4.3.1 Neutral Pathway Description: In the neutral (doublet) charge state, the pathway starts with the formation of the separated minima (Sep, $[\text{O}_2\text{AuCO}]^q$), which is the reactant side global minimum at -30.07 kcal/mol. A transition state (TS_1) between the separated and pre-reactive “in” minima has been calculated at 24.86 kcal/mol above Sep, where O_2 rotates around Au to form a long intermolecular O-C bond of 2.111 Å. With respect to Sep, there are large increases in the Au-O and Au-C bonds, slight increases in CO and O-O bonds (Table 4.1) with an accompanying red shift for the CO frequency and blue shift for the OO frequency (Table 4.2), and decrease in the AuCO angle from 180° to 145° . The electrostatic potential (ESP) is mapped onto the isodensity surfaces to visualize charge distribution throughout the complex; the ESP surfaces are shown in context of the reaction pathways for both charge states and are shown in Figures 4.3 (neutral) and 4.4 (anionic singlet). Compared to Sep, the ESP surface of TS_1 , shown in Figure 4.3, looks less polarized with slight positive character on AuCO and slight negative charge on O_2 . This transition state has been previously identified by Fan *et al.* and their reported data are in agreement with these calculations.⁶

From TS_1 , the pre-reactive “in” minimum, Pre_1 , is formed, which has been previously described in greater detail in a previous publication (and Chapter 3).⁵ From Pre_1 , there are two possible pathways to traverse: the “In” pathway that continues to the In-TS transition state, or the “Out” pathway, which continues over a small rotational

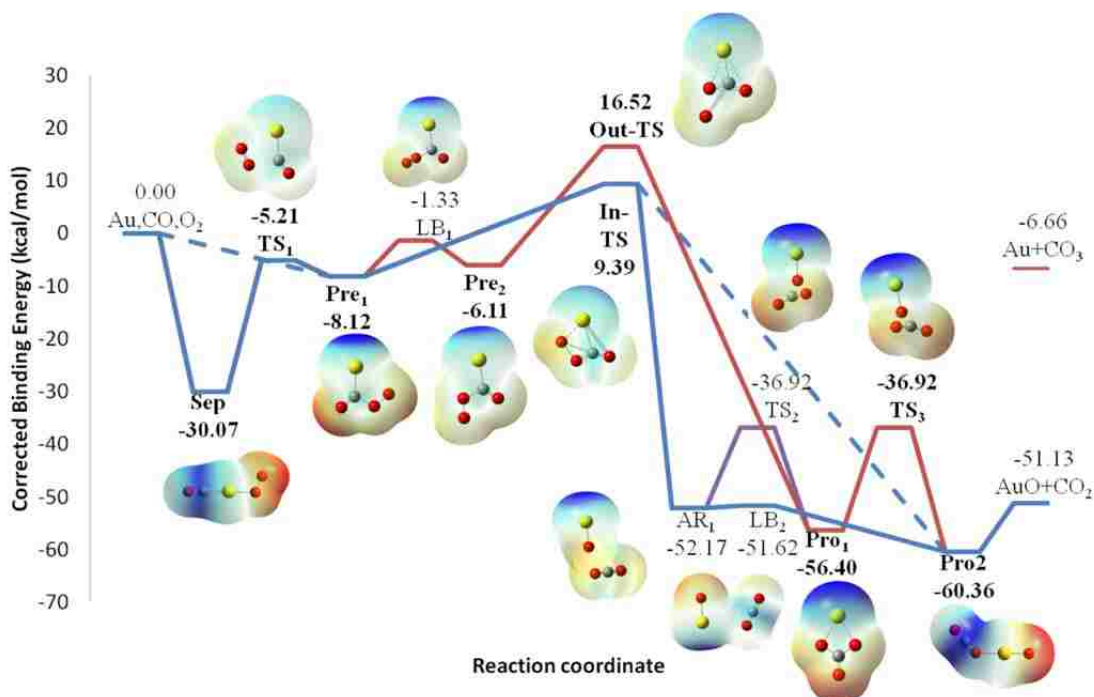


Figure 4.3. The reaction pathway(s) for the neutral doublet state is shown for $[\text{O}_2+\text{Au}+\text{CO}]^0$, where each position is now represented by the respective electrostatic potential (ESP) mapped on total electron density isosurface (density = 0.0004). The color map spans a range of 0.1 with red (blue) as most negative (positive) from -0.05 to +0.05.

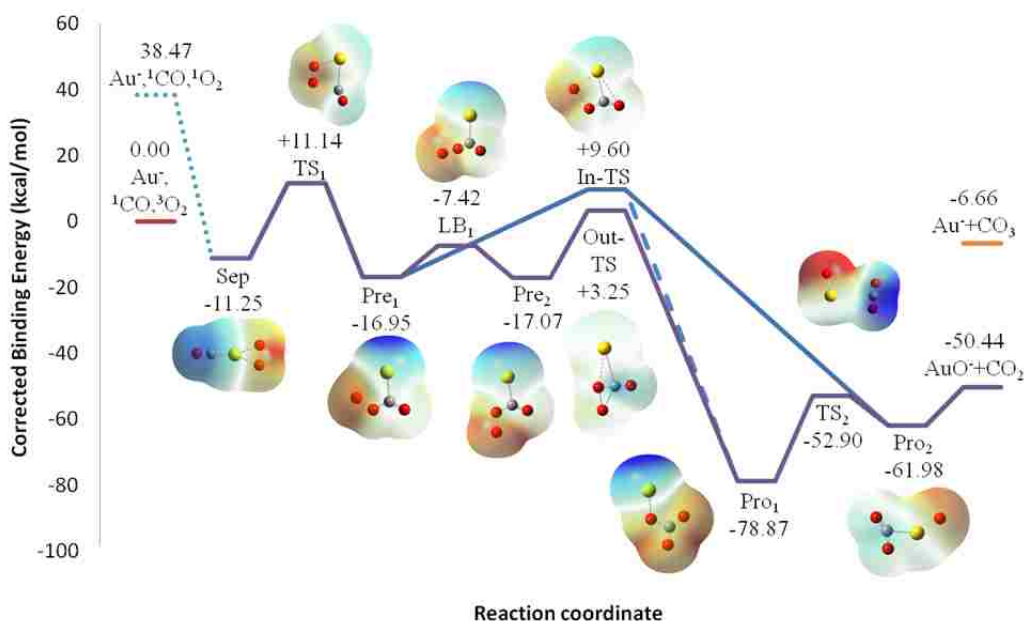


Figure 4.4. The reaction pathway(s) for the anionic singlet state is shown for $[\text{O}_2+\text{Au}+\text{CO}]^-$, where each position is represented by the respective electrostatic potential (ESP) mapped on to the total electron density isosurface (density = 0.0004). The color map spans a range of 0.1 with red (blue) as most negative (positive) from -0.2 to -0.1.

Table 4.1. Calculated bond lengths (in Å) for reactant-side transition state complexes^a with B3LYP-SDD/6-311+G(3df).

Species	Name	Au-C bond	C-O bond	Au-O bond	O-O bond
Transitions between sep and pre minima					
AuCOO ₂	TS ₁	2.057	1.138 2.111	2.830	1.236
AuCOO ₂ ⁻ singlet	TS ₁	2.484	1.146 2.252	2.281	1.312
Low barrier transition between pre-reactive minima					
AuCOO ₂	LB ₁	2.002	1.168 1.495		1.311
AuCOO ₂ ⁻	LB ₁	2.095	1.191 1.299		1.502

^aLabels correspond to Figures 4.1 and 4.2.

Table 4.2. Calculated stretching vibrational frequencies (in cm⁻¹) of the reactant-side transition states^a for B3LYP-SDD/6-311+G(3df).

Species	Name ^a	Stretching frequency –cm ⁻¹			
		Au-C	CO	Au-O	O-O
Transitions between sep and pre minima					
{AuCOO ₂ }	TS ₁	504	2089	86	1377
{AuCOO ₂ } ⁻	TS ₁	424	2014	163	1114
Low barrier transition between pre-reactive minima					
AuCOO ₂	LB ₁	739	1907 484		1158
AuCOO ₂ ⁻	LB ₁	647	1801		758

^aLabels correspond to Figures 4.1 and 4.2.

Table 4.3. Calculated bond lengths (in Å) for “major” transition state complexes^a with B3LYP-SDD/6-311+G(3df).

Species	Name ^a	Au-C bond	C-O bond	Au-O bond	O-O bond
AuCO ₂ O in	In-TS	2.353	1.176 1.239	2.108	1.667
AuCO ₂ O out	Out-TS	2.136	1.175 1.262	2.570	1.781
AuCO ₂ O ⁻ in	In-TS	2.370	1.202 1.222	2.248	1.864
AuCO ₂ O ⁻ out	Out-TS	2.892	1.154 1.204 1.985	2.912	1.701

^a Labels correspond to Figures 4.1 and 4.2.

Table 4.4. Calculated stretching vibrational frequencies (in cm⁻¹) of the “major” transition states^a for B3LYP-SDD/6-311+G(3df).

Species	Name ^a	Stretching frequency –cm ⁻¹					
		Au-C	CO	O-C-O anti-sym	OCO sym	Au-O	O-O
{AuCO ₂ O} in	In-TS	656	1950 1131			481	
{AuCO ₂ O} out	Out-TS	231	1940 1088				
{Au(CO ₂)O} ⁻ in	In-TS	113	1841 1160			356	
{Au(CO ₂)O} ⁻ out	Out-TS	90	317	2266	1243		374

^a Labels correspond to Figures 4.1 and 4.2.

barrier to the pre-reactive “out” complex, Pre₂. The In-TS transition state is formed by elongation of the O-O bond to 1.667 Å, and shortening of the Au-O and intermolecular O-C bonds with 17.51 kcal/mol of energy (from Pre₁). The In-TS transition state (and In pathway) is the energetically favorable pathway of the neutral system. The Au-C and CO bonds decrease slightly with a similar blue shift in the related frequency, while the intermolecular CO frequency blue shifts greatly to 1131 cm⁻¹ (Tables 4.3 and 4.4). The Au atom carries less positive character than the ESP surface of Pre₁ and retains negative character on the separating O atom. This transition state was previously described on the Fan *et al.* pathway with a relative energy of 19.7 kcal/mol between minimum and this transition state.⁶

From Pre₁ and over a small rotational barrier (LB₁) with rotation of the AuCOO dihedral, the pre-reactive “out” (Pre₂) rotamer is formed with an AuCOO dihedral of 180° (shown in Figure 3.4). The bonds of Pre₂ are similar to those of Pre₁ with differences of less than 0.015 Å (Table A3.9 for Pre₂ in Appendix A3 and Table 3.3 for Pre₁), except there is no AuO bond. The CO frequencies are similar to those in Pre₁, while the OO frequency is red shifted compared to Pre₁ (Table A3.7 for Pre₂ and Table 3.1 for Pre₁). The ESP surface, in Figure 4.3, shows positive character residing on the Au atom and slight negative character on the OCOO moiety.

The “Out” pathway continues from Pre₂ up to the Out-TS transition state at 22.63 kcal/mol above Pre₂. Similar to the existence of “in” and “out” pre-reactive complexes, there is an “out” transition state (Out-TS in Fig. 4.1), which is, in simple terms, an elongated version of the Pre₂ minimum. Compared to Pre₂, the Au-C and OO bonds increase significantly to 1.781 Å (for OO) , and a long (2.570 Å) Au-O bond is formed;

the CO bond increases slightly with a similar blue shift in frequency, while the intermolecular OC bond decreases with a red shift in its frequency (Tables 4.3 and 4.4). The ESP surface (Figure 4.3) shows positive character on the Au-C bond and slight negative character on the OCOO moiety, similar to Pre₂.

A product minimum with a carbonate-like structure of AuCO₃, Pro₁, can be formed from the “Out” and “In” pathways. Formation of Pro₁ from Out-TS occurs via translation of the dangling O atom to form the third C-O bond, along with breaking the Au-C bond and formation of two symmetric Au-O bonds. From In-TS, the neutral system reaches Pro₁ via a post-reactive minimum (AR₁) and transition state (TS₂). The neutral Pro₁ complex has C_{2v} symmetry, where the Au-O and related (“top”) CO bonds are symmetric, respectively, and the CO bonds are similar to CO₃⁻ with accompanying frequencies (Tables 4.7 and 4.8). The third “dangling” CO bond is shorter at 1.226 Å with a frequency similar to CO₂⁻. The ESP surface shows negative character on the CO₃ moiety with the strongest character on “dangling” CO bond and positive character residing on the Au atom.

There is a transition state, TS₃, between the “product” minima at 19.48 kcal/mol above Pro₁, in which CO₂ is formed and separating from AuO with an elongated O-C bond in the non-planar structure. The AuO and separated CO₂ bonds have shortened significantly with symmetric and anti-symmetric frequencies similar to free CO₂, while the third CO bond is elongated greatly to 1.694 Å (Tables 4.5 and 4.6). The ESP surface (Fig. 4.3) shows positive character on the Au atom and negative character on all three O atoms, which is similar to the Pro₁ ESP surface.

Table 4.5. Calculated bond lengths (in Å) for ternary low barrier and post-reactive transition state complexes^a with B3LYP-SDD/6-311+G(3df).

Species	Name ^a	Au-C bond	C-O bond	Au-O bond
OAuCO ₂	LB ₂		1.157	1.928
			1.161	3.521
			4.278	
AuO-CO ₂	TS ₂ , TS ₃		1.178	1.980
			1.207	
			1.694	
OAuCO ₂ ⁻	TS ₂	3.519	1.158	1.900
			1.162	3.667

^a Labels correspond to Figures 4.1 and 4.2.

Table 4.6. Calculated stretching vibrational frequencies (in cm⁻¹) of ternary low barrier and post-reactive transition state complexes^a for B3LYP-SDD/6-311+G(3df).

Species	Name ^a	Stretching frequency –cm ⁻¹			
		Au-C	O-C-O anti	OCO sym	Au-O
OAuCO ₂	LB ₂		2413	1374	541
					47
AuO-CO ₂	TS ₂ , TS ₃		2030	1262	621
OAuCO ₂ ⁻	TS ₂	44	2399	1367	607

^a Labels correspond to Figures 4.1 and 4.2.

Table 4.7. Calculated bond lengths (in Å) for post-reactive and product complexes^a with B3LYP-SDD/6-311+G(3df).

Post-reactive and product complexes				
Species	Name^a	Au-C bond	C-O bond	Au-O bond
Au(O)CO ₂	AR ₁		1.159 1.159 2.926	1.928
AuCO ₃	Pro ₁		1.301 1.301 1.226	2.216 2.216
AuCO ₃ ⁻	Pro ₁		1.233 1.397 1.250	2.020 3.037
OAuCO ₂	Pro ₂		1.149 1.169	1.917 2.247
OAuCO ₂ ⁻	Pro ₂	2.090	1.194 1.237	1.860
Reference lengths^b	C-O	1.124	CO ₂	1.159
	C-O ⁺	1.108	CO ₂ ⁺	1.170
	C-O ⁻	1.183	CO ₂ ⁻	1.227

^a Labels correspond to Figures 4.1 and 4.2.

^b calculated at same level of theory: B3LYP/6-311+G(3df) and O₂ reference bond length is from the triplet ground state species.

Table 4.8. Calculated stretching vibrational frequencies (in cm⁻¹) of ternary post-reactive and product complexes^a for B3LYP-SDD/6-311+G(3df).

Species	Name	Stretching frequency –cm⁻¹				
		Au-C	CO	OCO anti	OCO sym	Au-O
Post-reactive						
AuOCO ₂	AR ₁		76	2406	1373	542
Products						
AuCO ₃	Pro ₁		1436	1292	1010	238
AuCO ₃ ⁻	Pro ₁		835	1684	1264	319
OAuCO ₂	Pro ₂			2425	1375	588
						213
OAuCO ₂ ⁻	Pro ₂	271		1934	1207	714

^a Labels correspond to Figures 4.1 and 4.2.

The desired product, $\text{O}(\text{AuCO}_2)$, (Pro_2 in Figure 4.1) is the global minimum of the neutral pathway and can be formed from In-TS or Out-TS pathways, similar to Pro_1 . On the In-TS pathway, Pro can be formed directly from In-TS, or over a small barrier of ~ 0.5 kcal/mol from a post-reactive, Lewis acid-base stabilized complex (AR_1). From Pro_1 over a barrier of 19.48 kcal/mol, the product can be formed by breaking one O-C bond and rotation of AuO away from CO_2 . The Pro_2 structure is constructed of an AuO and linear CO_2 moieties, where CO_2 is attached to Au through an O atom. The AuO and CO_2 bonds are shortened from those in In-TS and Pro_1 (AuCO_3) with CO_2 frequencies similar to those of free CO_2 , while the AuO bond of CO_2 is longer at 2.247 Å (Tables 4.7 and 4.8). The ESP surface (Figure 4.3) shows negative character on the AuO moiety with positive character on CO_2 , where most of that positive character is on carbon. This minimum was also observed by Fan *et al.*, in which their calculated energy relative to In-TS was 74.4 kcal/mol and is within ~ 5 kcal/mol of the Pro_2 energy relative to In-TS (69.75 kcal/mol) in these calculations.⁶

As mentioned in the product results, there is a post-reactive minimum and transition states that lead to the formation of either product from this Lewis acid-base stabilized AuO- CO_2 complex (AR_1). The transition state, TS_2 , which leads to Pro_1 , is a rotamer of TS_3 with the same energy and structural and vibrational frequency data. The other transition state, LB_2 , is ~ 0.5 kcal/mol above AR_1 and leads to the formation of Pro_2 . More details about these post-reactive complexes can be found in the appendix (A3), along with a detailed description of each complex along the pathway and the structural and vibrational frequency changes.

4.3.2 Anionic Singlet Pathways Description: The anionic singlet pathways (Figure 4.2) have many similarities with the neutral pathways in the structures; however, there are also differences between the two, which will be highlighted. The anionic singlet separated (Sep) minimum has a C_{2v} symmetric structure with O_2 side-on (η^2) bonded to Au, which has been discussed in detail previously, but this complex is not the global minimum of the reactant side minima for the anionic singlet charge state. Like the neutral pathway, TS_1 is formed via rotation of O_2 around Au with 22.39 kcal/mol above Sep; however, this transition state is higher than the energy of reactants, or reactant asymptote. There are increases in the AuC and AuO bonds and a decrease in the AuCO bond from 180° . The CO bond contracts slightly with a small blue shift in its frequency and OO bond decreases significantly with a strong blue shift in its frequency (Tables 4.1 and 4.2). In the ESP surface (Figure 4.4), negative character remains on the O_2 moiety and positive character remains on the AuCO moiety, but is less strongly polarized than the separated complex, which is similar to the neutral TS_1 .

From TS_1 , the anionic singlet pre-reactive “in” minimum, Pre_1 , is formed and is lower in energy than the separated minimum. Like the neutral case, there are two possible pathways to traverse: the “In” pathway that continues to the In-TS transition state, or the “Out” pathway, which continues over a small rotational barrier to the pre-reactive “out” complex, Pre_2 . The In-TS anionic singlet pathway (Figure 4.2) can continue over a barrier of 26.5 kcal/mol above Pre_1 , where the In-TS structure is visually similar to the neutral structure. The AuC and OO bonds have large increases to 1.864 Å for OO, which is longer than the O_2^{2-} bond length (Tables 4.3 and 4.4). The two CO bonds decrease slightly to lengths similar to CO_2^- with accompanying blue shifts in the

frequencies. The ESP surface (Fig. 4.4) is similar to rotational barrier between the pre-reactive structures (LB_1), where the negative character remains on the O_2 moiety with a majority of the negative character on the separating O atom and a slight positive charge on Au.

From Pre_1 and over a small rotational barrier (LB_1) with rotation of the AuCOO dihedral, the pre-reactive “out” (Pre_2) rotamer is formed with an AuCOO dihedral of 180° . Pre_2 is 0.12 kcal/mol lower than Pre_1 and the global minimum of the anionic singlet reactant-side complexes. Compared to the “in” minimum, the AuC and OO bonds increase slightly, with accompanying red shift of the OO frequency (Tables A3.7 and A3.9 for Pre_2 in Appendix A3 and Tables 3.1 and 3.3 for Pre_1). The CO bonds decrease with accompanying blue shifts in the frequencies. The ESP surface shows positive character on Au and strong negative character on the O_2 moiety, similar to Pre_1 .

Similar to the neutral system, the Out-TS is on the “Out” pathway at 20.32 kcal/mol above Pre_2 and mainly characterized by large elongation of the AuC and OO bonds with a large red shift of 372 cm^{-1} for the OO frequency. The CO bonds decrease slightly and have formed symmetric and anti-symmetric CO_2 frequencies. A long CO bond of 1.985 \AA is also formed with a corresponding low frequency of 317 cm^{-1} (Tables 4.3 and 4.4). The ESP surface (Figure 4.4) shows a very diffuse charge across the entire complex, which is different from the other anionic singlet and all neutral ESP surfaces.

Unlike the neutral $AuCO_3$ structure, Pro_1 ($AuCO_3^-$ singlet) is the product global minimum and has C_s symmetry, where Au is connected to CO_3 via one O atom with a second “long range” AuO bond of 3.037 \AA . Like the neutral, the carbonate-like product can be formed from either In-TS or Out-TS pathways; however, the anionic singlet

pathway has no additional post-reactive minima or transition states. The Au-C bond is broken and the Au-O bond shortens significantly by 0.9 Å. The two “top” CO bonds increase, where the CO bond closer to Au (interior OC) increases by twice that of the “exterior” CO; the “interior” CO frequency has an accompanying low frequency. The third CO bond decreases significantly by 0.74 Å, which is now similar to the “exterior” CO and these two bonds form symmetric and anti-symmetric CO₂ frequencies (Tables 4.7 and 4.8). The longer OC bond, which is connected to Au, has a very low frequency of 835 cm⁻¹, which is in agreement with the elongated CO bond. The ESP surface shows a strong positive character on Au with negative character on the CO₃ moiety, similar to the neutral surface.

While Pro₁ is the most stable product, the desired OAuCO₂⁻ (singlet) product can be formed over a barrier of ~26 kcal/mol (Fig. 4.2 TS₂), where the CO₃ moiety is broken and the structure is OAu—CO₂ for TS₂. CO₂ becomes nearly linear (175.1°) and rotates around Au away from AuO with long AuC and AuO bonds tethering it to Au. Both CO₂ and the AuO bonds decrease from Pro₁ with accompanying blue shifts in the CO₂ frequencies (Tables 4.5 and 4.6). The ESP surface shows strong negative character on O atom and less on CO₂.

The desired product, OAuCO₂⁻ (singlet) can be formed directly from In-TS or from Pro₁ via TS₂ and is ~17 kcal/mol above Pro₁. The product is an AuO moiety with a bent CO₂ bonded to Au via the carbon atom. From In-TS and TS₂, the AuC and AuO bonds decrease, while the CO bonds increase from TS₂, which are most similar to CO₂⁻ with accompanying frequencies (Tables 4.7 and 4.8). The ESP surface shows negative character on the AuO moiety and relatively neutral character on the CO₂ moiety.

4.3.3 *Ab initio* Molecular Dynamics (AIMD/ADMP)

Ab initio molecular dynamics (AIMD) of both charge states were conducted, where the starting species were pre-reactive (Pre₁ and Pre₂) minima to follow the reaction pathways. All MD simulations start with 30-50 kcal/mol to provide sufficient energy to cross the ~25 kcal/mol barriers. Starting from the neutral Pre₁ structure (shown in Figure 4.5), the simulation snapshots show O-O bond elongation and a structure that looks similar to the In-TS within 50 fs and the OO bond cleaves between 50 and 100 fs, where the AuO moiety rotates away from CO₂. At 100 fs, CO₂ is linear with an overall OAuOCO structure, reminiscent of Pro₂. At 250 fs, AuO has rotated for the O atom to face CO₂, with a distance between AuO and CO₂ of greater than 4 Å, which looks like an elongated version of LB₂. For the anionic singlet, the MD snapshots in Figure 4.6 starts from them Pre₁ structure and the In-TS-like structure is also observed; upon OO cleavage, AuO rotates away from CO₂. At 200 fs, the CO₂ moiety is linear, which is more similar to the neutral Pro₂ and suggests that AuO carries the anionic charge. Simulations were also conducted from the neutral Pre₂ (“out”) complex with snapshots in Figure 4.7; the OO bond is greatly elongated, similar to the Out-TS structure and the CO₂ moiety forms within 50 fs. The distance between the separating O atom, CO₂, and Au atom continues to increase, which appears rather unphysical in a gas phase reaction, but could be stabilized in matrix isolation experiments. From the anionic singlet Pre₂ complex in Figure 4.8, a non-planar carbonate-like structure is formed within 100 fs, which is generally similar to Pro₁. Within 150 fs, an Au-O bond has formed and the related O-C bond has elongated, where this snapshot looks like the neutral TS₃ structure. At the end of the simulation (500 fs), an OAuCO₂-like structure is formed like the ending

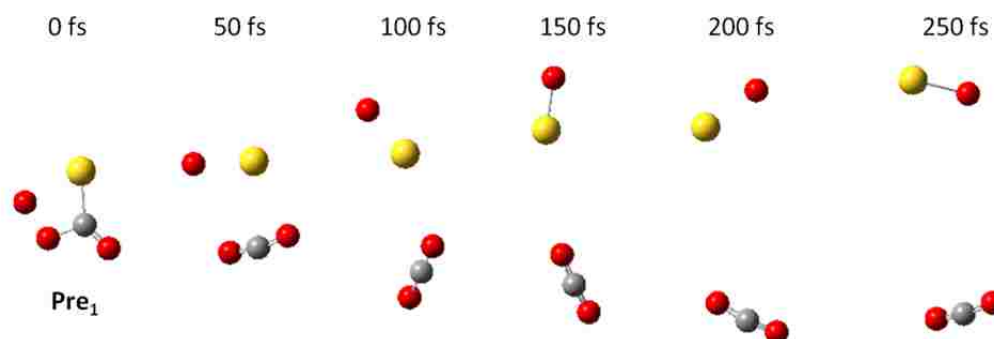


Figure 4.5. Snapshots of MD simulations starting from the neutral (doublet) pre-reactive (in, Pre_1) structure with a fictitious electron mass of 0.1 amu, time step of 0.05 fs, and nuclear kinetic energy of 30 kcal/mol.

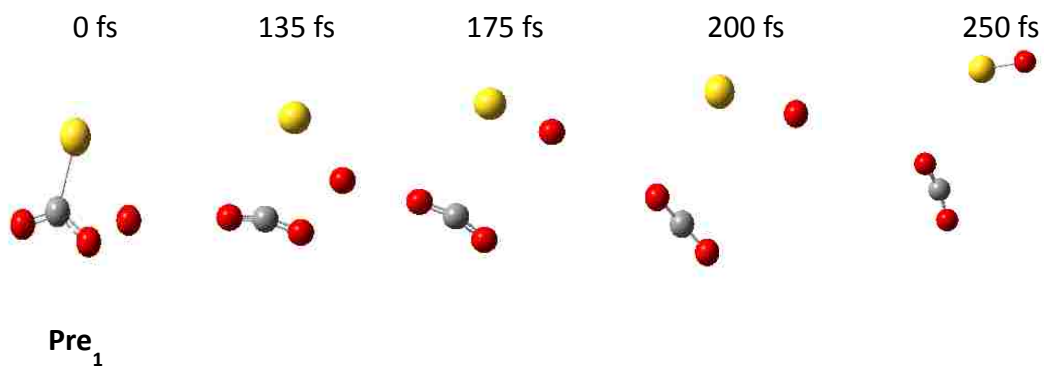


Figure 4.6. Snapshots of MD simulations starting from the anionic singlet pre-reactive (in, Pre_1) structure with a fictitious electron mass of 0.1 amu, time step of 0.05 fs, and nuclear kinetic energy of 30 kcal/mol.

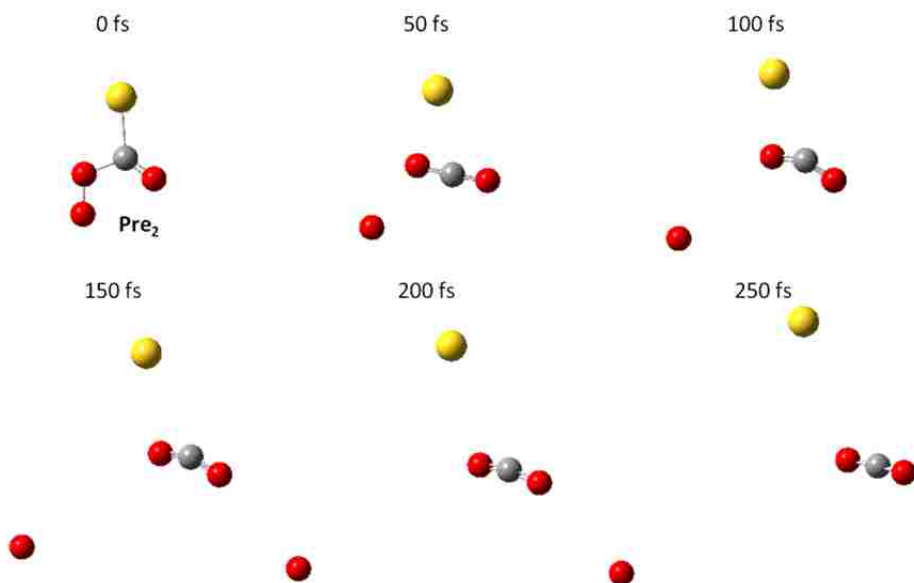


Figure 4.7. Snapshots of MD simulations starting from the neutral (doublet) pre-reactive (out, Pre_2) structure with a fictitious electron mass of 0.1 amu, time step of 0.05 fs, and nuclear kinetic energy of 50 kcal/mol.

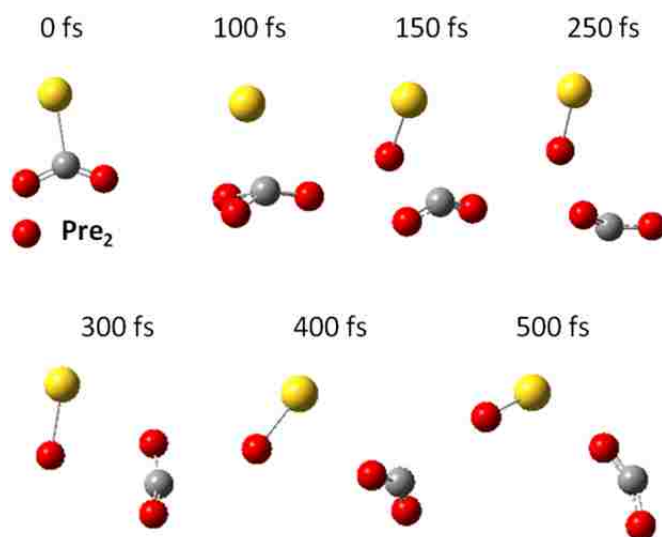


Figure 4.8. Snapshots of MD simulations starting from the anionic singlet pre-reactive (out, Pre_2) structure with a fictitious electron mass of 0.1 amu, time step of 0.05 fs, and nuclear kinetic energy of 50 kcal/mol.

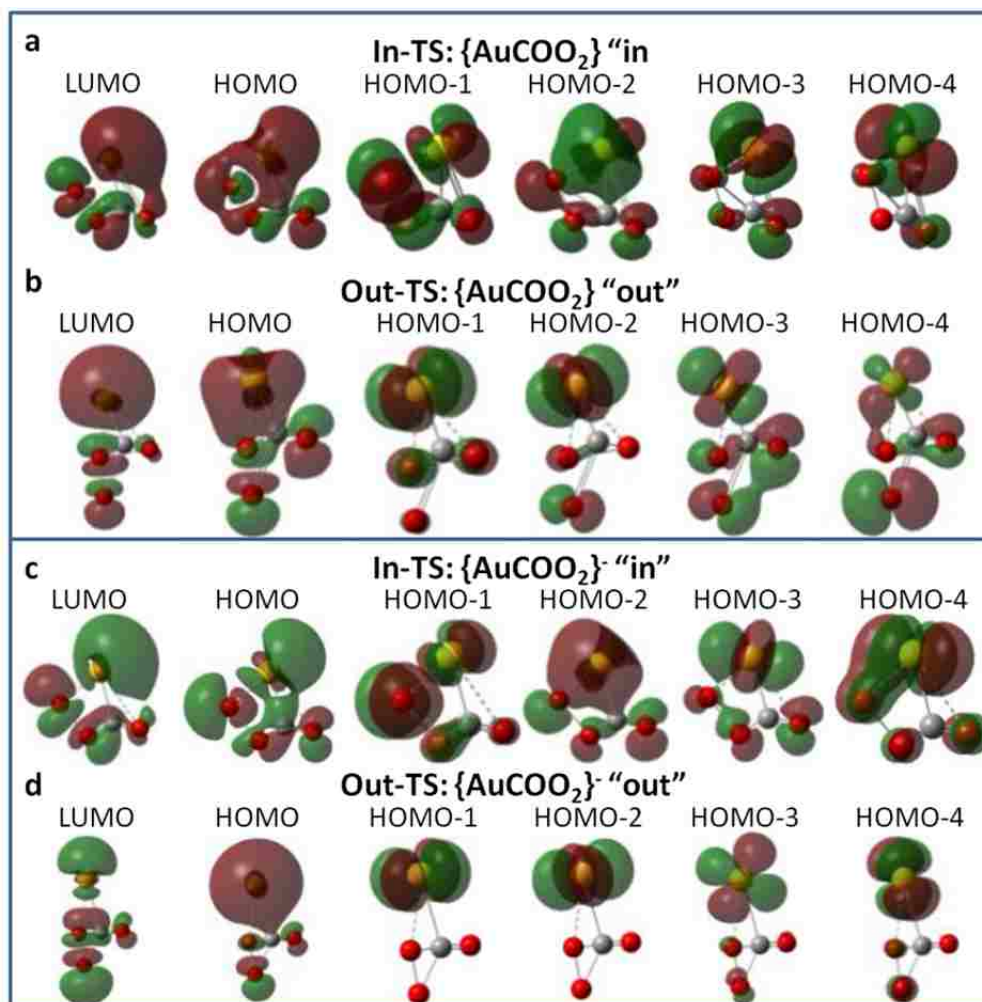


Figure 4.9 Five highest occupied molecular orbitals and LUMO of the "In" and "Out" transition states of the neutral and anionic (singlet) charge states, where a and b are neutral In-TS and Out-TS and c and d are anionic singlet In-TS and Out-TS, respectively.

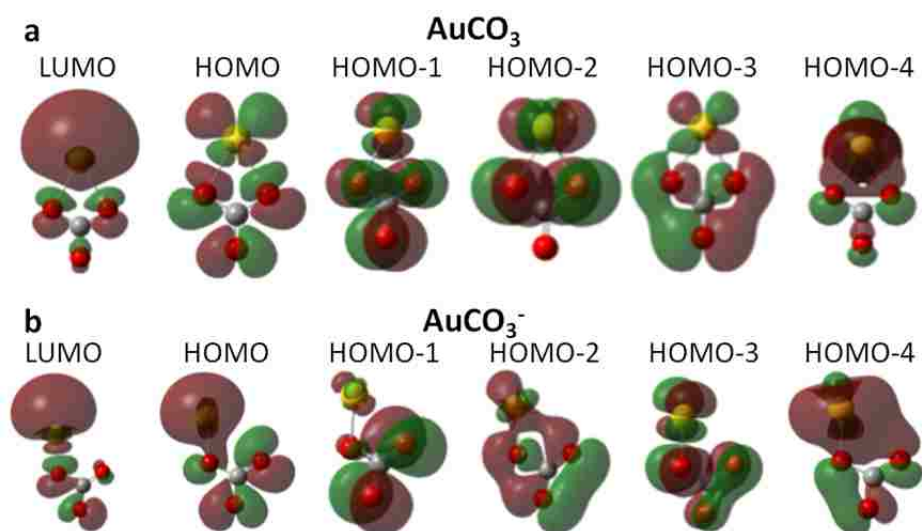


Figure 4.10 Five highest occupied molecular orbitals and LUMO of the carbonate-like product, Pro_1 (AuCO_3), of the neutral and anionic (singlet) charge states, where a and b are neutral and anionic charge states, respectively.

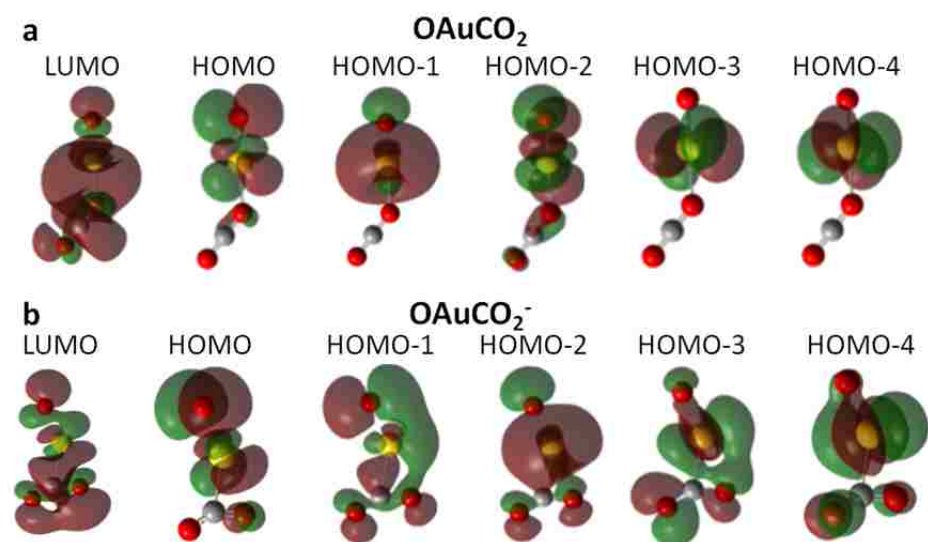


Figure 4.11 Five highest occupied molecular orbitals and LUMO of the carbon dioxide product, Pro_2 (OAuCO_2), of the neutral and anionic (singlet) charge states, where a and b are neutral and anionic charge states, respectively.

of the anionic singlet MD simulation, where the structure is visually more similar to the neutral product. The neutral In pathway and both anionic singlet pathways match with the MD simulations; the neutral Out pathway suggests formation of AuCO₃ and OAuCO₂, but this result is not reflected in the MD simulation, where the O atom separated from CO₂ and Au.

4.4 Discussion

4.4.1 Neutral Pathways

The ESP surfaces (Figures 4.3 and 4.4) can be used to track the electrostatic character of the complexes along the reaction pathways to understand how the ESP character evolves with structural changes, the energetically favorable pathways and AIMD results. The molecular orbitals (Figures 4.9-4.11) can also be used to look at whether, and how long, the OOCO π -conjugated system is retained after the pre-reactive complexes.

In the neutral system, there is positive character residing on CO in the separated structure (Sep), which moves onto the Au atom in TS₁ and most of the positive character remains on Au up to Pro₂ (OAuCO₂), where the majority moves to CO₂. In Pre₁, the negative charge is spread across the OOCO moiety and retains the negative charge close to the positive Au atom. The negative charge then re-localizes onto the O₂ moiety of Pre₂ with less on CO, where the negative charge is further from the positive Au atom; there is greater charge separation, but both pre-reactive complexes retain the π -conjugated OOCO moiety in the molecular orbitals (Chapter 3). In the In-TS ESP surface (Figure 4.3), the negative charge is localized on O₂ with slight positive on C (and strong positive on Au). The molecular orbitals are shown in Figure 4.9a, where In-TS HOMO-1 orbital is most

similar to HOMO-2 of Pre₁ and the In-TS orbitals are similar in appearance to those of Pre₁; this also suggests that the conjugated system is still intact. When looking at the OAuCO₂ ESP surfaces and orbitals (Figure 4.3 and 4.11), the In-TS structure is most similar to Pro₂, as one could imagine cracking open the OO bond and opening to the OAuCO₂ structure and the overall charge profile is preserved (positive on AuC and negative on the O atom).

In the Out-TS complex, elongation of the OO bond in O-TS transition state greatly alters the molecular orbitals, where it is hard to tell if π -conjugation is retained (possibly in HOMO-3 or HOMO-4). The strain and charge separation in Out-TS may be why the O atom separates from Au and CO₂ in MD simulations, where it may be easier to slough off the negatively charged O atom, rather than re-arrange to form the C_{2v} symmetric AuCO₃. Additionally, the negative character on the “dangling” O atom in AuCO₃ is even greater than Out-TS and requires switching the charge of the CO moiety from positive in Out-TS to negative. The In-TS pathway may be energetically preferred due to the AuO stabilization, conjugated π -system, and ESP distribution similar to Pro₂, while Out-TS involves lengthening of the OO bond, greater charge separation between the positive Au atom and negative OO moiety and switching the charge of CO to form AuCO₃, which may further strain the complex.

4.4.2 Anionic Singlet Pathways

Like the neutral system, most of the negative character resides on O₂ from Sep to the pre-reactive complexes, where the negative character is heavily localized in O₂ of the Pre₂ (out) complex and makes CO is positive. For the In-TS ESP surface (Figure 4.4), the negative character on O₂ is more than that on AuCO; this ESP surface looks like a

less polarized version of Pre_1 and the molecular orbitals look generally similar between In-TS and Pre_1 . Like the neutral case, the molecular orbital most similar to the Pre_1 HOMO-2 π -conjugated orbital is HOMO-1, which suggests π -conjugation may still exist in the system. Comparison of ESP surfaces for In-TS and Pro_2 leads to a similar observation as in the neutral system; the product looks like the opened version of In-TS, where the O atom retains negative character and the AuCO_2 moiety has a well-distributed charge. When looking at the Out pathway, the Out-TS ESP surface shows negative character spread across Au and the “dangling” O atom, while CO_2 is positive, which is very different from the other ESP surfaces. The Out-TS molecular orbitals (Figure 4.9d) show population on the Au atom and do not suggest retention of the π -conjugated system. The Out-TS HOMO and LUMO (Figure 4.9d) show similarities to the Pro_1 (AuCO_3^-) HOMO and LUMO (Figure 4.10), which suggests that formation of AuCO_3^- is facile. Also with the positively charged CO_2 and negative O and Au atom, the charges may be attracted and catalyze the formation of AuCO_3^- . MD simulations from Pre_2 show formation of the AuCO_3^- , but the simulation continues to the separated OAuCO_2^- product. The AuCO_3^- ESP shows strong polarization of the negative charge onto CO_3 and less on Au; again, charge attraction along the long AuO bond may facilitate the separation of CO_2 from AuO.

4.5 Computational Methods

Density functional theory (DFT) geometry optimizations and frequency and intrinsic reaction coordinate (IRC) calculations were carried out using the GAUSSIAN 09 suite of computational chemistry programs.⁷ Except where otherwise noted, all reported data reflect results obtained using the B3LYP hybrid functional,⁸ with a mixed

basis set employing the Stuttgart-Dresden relativistically-corrected effective core potential basis for Au atoms,^{9, 10} and Pople 6-311+G(3df) basis for C and O atoms.^{11, 12} All geometry optimizations were performed using the tight convergence criteria and the ultrafine integration grid (Gaussian keywords: “opt=tight” and “integral=ultrafine”); this was required to achieve convergence for weakly-bonded systems, and was maintained for all calculations to ensure comparability of the results. Transition states were calculated with the quadratic synchronous transition approach (qst3 keyword) with three molecule specifications for the “reactant,” “product,” and transition-state guess.^{13, 14} All reported geometries reflect stable minima (maxima for transition states) on their respective potential energy surfaces without (with) imaginary frequencies. The stabilities of the SCF wavefunctions for each reported wavefunction were verified using the method of Davidson.¹⁵ Counterpoise corrections, using the method of Boys and Bernardi,¹⁶ were carried out to correct for the effects of basis-set superposition error (BSSE) on the binding energies of the complexes. All reported binding energies have been corrected for both BSSE and the vibrational zero-point energy (ZPE). IRC calculations were applied to understand the connections between calculated transition states and minima.¹⁷⁻²⁰ Atomic charges were calculated using the Hirshfeld stockholder method²¹⁻²³, CHELPG molecular electrostatic potential method,²⁴ and natural bond orbital (NBO) method,²⁵⁻³⁰ as implemented within GAUSSIAN 09. To understand the progression of the system with a set amount of energy and test what products are formed, *ab initio* molecular dynamics (MD) were completed with Atom-Centered Density Matrix Propagation (ADMP) calculations at B3LYP-SDD/6-31+G(d).^{31, 32} The stationary points on the potential energy surfaces (PESs) from quantum-mechanical calculations were used as starting

points for the MD simulations. A fictitious electron mass of 0.1 amu was utilized and time step of 0.05 fs was chosen. The nuclear kinetic energy was set to a sufficient value to cross the barriers of transition states, when starting from the minima.

4.6 References

- (1) Haruta, M. *Cattech* **2002**, *6*, 102-115.
- (2) Konova, P.; Naydenov, A.; Tabakova, T.; Mehandjiev, D. *Catalysis Communications* **2004**, *5*, 537-542.
- (3) Schubert, M. M.; Plzak, V.; Garche, J.; Behm, R. J. *Catal. Lett.* **2001**, *76*, 143-150.
- (4) Lin, L.; Nguyen, M. *Chem. Phys. Lett.* **2010**, *498*, 120-124.
- (5) Smith, A. N.; Moore, D. T. *J. Phys. Chem. A* **2012**, *116*, 9370-9381.
- (6) Fang, H.; Li, Z. H.; Fan, K. *Phys. Chem. Chem. Phys.* **2011**, *13*, 13358-13369.
- (7) ; Frisch, M. J.; Trucks, G. W.; Schlegel, H. B.; Scuseria, G. E.; Robb, M. A.; Cheeseman, J. R.; Scalmani, G.; Barone, V.; Mennucci, B.; Petersson, G. A., et al. *Gaussian 09*, Revision A.02, Gaussian, Inc., Wallingford, CT **2009**.
- (8) Becke, A. D. *J. Chem. Phys.* **1993**, *98*, 5648-5652.
- (9) Schwerdtfeger, P.; Dolg, M.; Schwarz, W. H. E.; Bowmaker, G. A.; Boyd, P. D. W. *J. Chem. Phys.* **1989**, *91*, 1762-1774.
- (10) Andrae, D.; Haussermann, U.; Dolg, M.; Stoll, H.; Preuss, H. *Theor. Chim. Acta* **1990**, *77*, 123-141.
- (11) Krishnan, R.; Binkley, J. S.; Seeger, R.; Pople, J. A. *J. Chem. Phys.* **1980**, *72*, 650-654.
- (12) Frisch, M. J.; Pople, J. A.; Binkley, J. S. *J. Chem. Phys.* **1984**, *80*, 3265-3269.
- (13) PENG, C.; SCHLEGEL, H. *Isr. J. Chem.* **1993**, *33*, 449-454.
- (14) Peng, C.; Ayala, P.; Schlegel, H.; Frisch, M. J. *Comput. Chem.* **1996**, *17*, 49-56.
- (15) Langhoff, S. R.; Davidson, E. R. *Int. J. Quant. Chem.* **1974**, *8*, 61-72.
- (16) Boys, S. F.; Bernadi, F. *Mol. Phys.* **1970**, *19*, 553-&.
- (17) FUKUI, K. *Acc. Chem. Res.* **1981**, *14*, 363-368.
- (18) Hratchian, H.; Schlegel, H. J. *J. Chem. Phys.* **2004**, *120*, 9918-9924.
- (19) Hratchian, H.; Schlegel, H. J. *J. Chem. Theory Comput.* **2005**, *1*, 61-69.
- (20) Hratchian, H. P.; Schlegel, H. B. In *Finding minima, transition states and following reaction pathways on ab initio potential energy surfaces*; Dykstra, C. E., Frenking, G., Kim, K. S. and Scuseria, G. E., Eds.; *Theory and Applications of Computational Chemistry: The First 40 Years*; Elsevier: Amsterdam, 2005; .
- (21) Hirshfeld, F. L. *Theor. Chim. Acta* **1977**, *44*, 129-138.
- (22) Ritchie, J. P. *J. Am. Chem. Soc.* **1985**, *107*, 1829-1837.
- (23) Ritchie, J. P.; Bachrach, S. M. *J. Comput. Chem.* **1987**, *8*, 499-509.
- (24) Breneman, C. M.; Wiberg, K. B. *J. Comput. Chem.* **1990**, *11*, 361-373.
- (25) Foster, J. P.; Weinhold, F. *J. Am. Chem. Soc.* **1980**, *102*, 7211-7218.
- (26) Reed, A. E.; Weinhold, F. *J. Chem. Phys.* **1983**, *78*, 4066-4073.
- (27) Reed, A. E.; Weinstock, R. B.; Weinhold, F. *J. Chem. Phys.* **1985**, *83*, 735-746.
- (28) Reed, A. E.; Weinhold, F. *J. Chem. Phys.* **1985**, *83*, 1736-1740.

- (29) Reed, A. E.; Curtiss, L. A.; Weinhold, F. *Chem. Rev.* **1988**, *88*, 899-926.
- (30) Carpenter, J. E.; Weinhold, F. *J. Mol. Struct. -Theochem* **1988**, *46*, 41-62.
- (31) Schlegel, H.; Millam, J.; Iyengar, S.; Voth, G.; Daniels, A.; Scuseria, G.; Frisch, M. *J. Chem. Phys.* **2001**, *114*, 9758-9763.
- (32) Schlegel, H.; Iyengar, S.; Li, X.; Millam, J.; Voth, G.; Scuseria, G.; Frisch, M. *J. Chem. Phys.* **2002**, *117*, 8694-8704.

Chapter 5. Calculations of Two CO Oxidative Pathways with Au^q (q=+1, 0, -1) and Ozone: Direct O₃ Oxidation of CO Catalyzed by Au^q Atoms or “Secondary” Oxidation of CO by (O₂)AuO^q.

5.1 Abstract

Ozone (O₃) interactions with carbon monoxide (CO) and Au^q atoms (q=+1,0,-1) and probable pathways for CO oxidation have been investigated using density functional theory (DFT) calculations. The probable pathways can be grouped, regardless of charge or spin state, into two distinct pathways for CO oxidation catalyzed by Au^q atoms (q=+1,0,-1) with molecular ozone, in which the Au species are chemically distinct. The first pathway involves direct oxidation of CO by ozone (catalyzed by Au^q) and the second is characterized by Au^q oxidation by ozone to AuO (or ozone decomposition on Au) and subsequent oxidation of CO by [AuO]^q with a spectator O₂ remaining on Au. Energetically favorable pathways per charge (and spin) state are dependent on the spin state, where triplet states show the Au oxidation pathway to be energetically favorable, while the singlet (and doublet) states are opposite with O₃ oxidation as more favorable. The preference may be explained by spin state curve crossing from ground state reactants (Au^q, CO, O₃) to ground state products (Au^q, CO₂, O₂).

5.2 Introduction

Metal-oxide supported Au nanoparticles (Au/Fe₂O₃) have been observed to simultaneously decompose ozone and oxidize CO at room temperature in a flow reactor at atmospheric pressure.¹ In the evaluation of these results with stoichiometric and excessive amounts of each gas, it was stated that the elimination of the reactants should occur in two reactions, ozone-oxidation of CO and ozone decomposition.¹ Another perspective on the heterogeneous catalysis of CO oxidation can be provided with unsupported nanoparticles. Some joint experimental and theoretical studies utilized pre-

oxidized Au species to understand the influence of dissociated oxygen on oxidation of CO. Comparatively, understanding the reaction of molecular O₃ and CO can provide useful insights into O₃ decomposition on Au and the oxygen species involved in CO oxidation.

Utilizing DFT calculations, we report pathways for CO oxidation with O₃ and catalyzed by Au^q atoms (q=+1, 0, -1). In all charge and spin states, there are two chemically distinct pathways, which are identified as the O₃ molecular oxidation pathway and the Au oxidation pathway. The O₃ molecular oxidation pathway (O₃ pathway) can be described as CO oxidation with molecular O₃, which is catalyzed by Au^q. The Au oxidation pathway (AuO pathway) is described by O₃ decomposition over Au^q and subsequent oxidation of CO by [O₂AuO]^q, where, for the anionic triplet system, this pathway also provides an entry onto pathways reported by Castleman *et al.*

5.3 Results

The bond lengths and frequencies are collected into tables for the “reactant side” [O₃AuCO]^q minima (Tables 5.1 and 5.2), O₃ oxidation pathway (Tables 5.3 and 5.4) and AuO oxidation pathway (Table 5.5 and 5.6) transition states, post-reactive minima (Tables 5.7 and 5.8), and product (Tables 5.9 and 5.10) complexes. The bond lengths and vibrational frequencies for the reactant-side and post-reactive low barrier transition states are found in the Chapter 5 appendix (A5), Tables A5.1-A5.4. The two types of “reactant side” (separated) minima, [O₃AuCO]^q, can be seen in Figure 5.1, where the main difference is the AuOOO dihedral angle of 0° for “O₃ in” and 180° dihedral for “O₃ out”. Oxygen atoms and their connectivity are discussed in the tables and text with respect to distance from Au, where O_α is attached to Au, O_β is next, and O_γ is the third O atom.

Two distinct pathways have been calculated for the $[\text{O}_3+\text{Au}+\text{CO}]^q$ ($q = -1, 0, +1$) systems, where all charge and spin states display generally similar structures and pathways. The pathways diverge after the “O₃ in, reactant-side” minimum (**BR₁**), continue over two structurally and chemically distinct transition states, and end at the same product, $[\text{O}_2\text{AuCO}_2]^q$. The first pathway involves rotation of O₃ around the Au atom to directly interact with CO and form an $\{\text{AuCOO}_3\}^q$ structure with retention of the Au-O bond and formation of an intermolecular O-C bond. This pathway is called the O₃ oxidation pathway, as Au catalyzes the direct oxidation of CO by ozone (denoted as O-TS in figures). The other pathway forms the “O₃ out” minimum and continues to a transition state, which involves decomposition of ozone and oxidation of Au. This forms AuO and O₂ with a structure of $\{\text{O}_2(\text{O})\text{AuCO}\}^q$ (denoted as G-TS); subsequently, CO is oxidized by AuO to form the product. This pathway is identified as the AuO oxidation pathway, as AuO oxidizes CO. While these pathways are different, both are below the energy of reactants (or reactant asymptote) in most of the charge and spin states; the cationic singlet AuO oxidation pathway is higher than the reactant asymptote. As all charge and spin states have the same general steps and structures along the calculated reaction pathways, the neutral (doublet) O₃ oxidation and AuO oxidation pathways will be discussed, where the “major” stationary points are in **bold** in Figure 5.2.

5.3.1 O₃ Oxidation Pathway

The reactant-side minima, O_3AuCO , are denoted as BR in the figures for “before reaction,” where the “O₃ in” complex (**BR₁** in Figure 5.2) is the global reactant-side minimum at -71.76 kcal/mol for the neutral system. The structure is reminiscent of the O_2AuCO separated minima, where both have a linear AuCO moiety and bent Au-oxygen

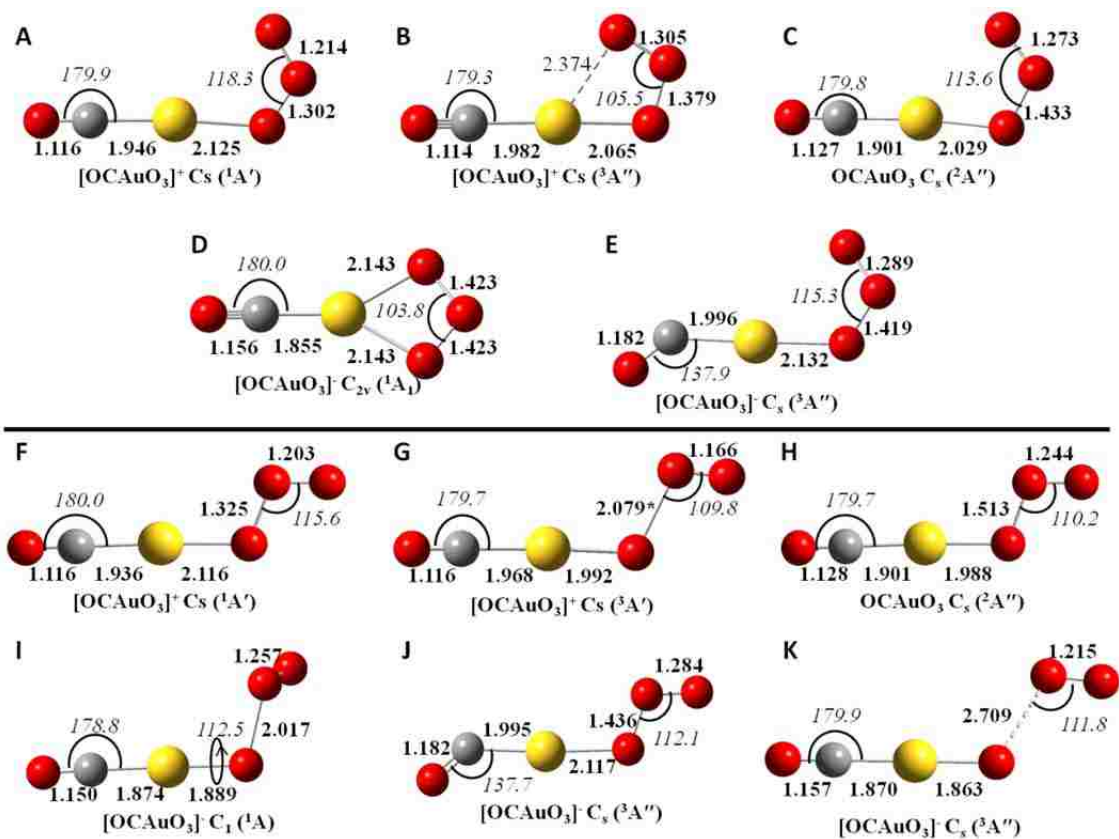


Figure 5.1 The reactant-side complexes (BR) for all charge and spin states (cationic, neutral (doublet) and anionic; singlet and triplet) with the bond lengths (in bold, Å) and angles (in italics, °) shown in the structures, calculated at B3LYP-SDD/6-311+G(3df).

Table 5.1. Bond lengths (in Å) for ternary, reactant-side $[\text{O}_3\text{AuCO}]^q$ complexes, $q=(+1,0,-1)$, calculated with B3LYP-SDD/6-311+G(3df).

O ₃ AuCO							
Charge	Spin	Name	Au-C bond	C-O bond	Au-O _α bond ^b	O _α -O _β bond	O _β -O _γ bond
Cationic	singlet	¹BR₁⁺	1.946	1.116	2.125	1.302	1.214^c
		¹ BR ₂ ⁺	1.936	1.116	2.116	1.325	1.203
	triplet	³ BR ₁ ⁺	1.982	1.114	2.065	1.379	1.305
		³ BR ₂ ⁺	1.968	1.116	1.992	2.079	1.166
Neutral	doublet	²BR₁⁰	1.901	1.127	2.029	1.433	1.273^c
		² BR ₂ ⁰	1.901	1.128	1.988	1.513	1.244
Anionic	singlet	¹ BR ₁ ⁻	1.855	1.156	2.143	1.423	1.423
		¹ BR ₂ ⁻	1.874	1.150	1.889	2.017	1.257
	triplet	³ BR ₁ ⁻	1.996	1.182	2.132	1.419	1.289
		³ BR ₂ ⁻	1.995	1.182	2.117	1.436	1.284
		³BR₃⁻	1.870	1.157	1.863	2.709	1.215^c
Reference lengths^{d,e}		C-O	1.124	O-O (O ₂)	1.203	O-O (O ₃)	1.251
		C-O ⁺	1.108	O-O (O ₂) ⁻	1.341	O-O (O ₃) ⁺	1.227
		C-O ⁻	1.183	O-O (O ₂) ²⁻	1.559	O-O (O ₃) ⁻	1.346

^a O₃ in structure is listed first and O₃ out structure is listed second per charge/spin state.

^b O_α, O_β, and O_γ refer to the order of oxygen atoms, where O_α is the closest to (or attached to) Au.

^c Lowest energy state of similarly charged complexes are in bold

^d Reference lengths are calculated at the same level of theory: B3LYP-SDD/6-311+G(3df).

^e Only one bond length is shown for reference O₂^q, O₃^q and CO₂, as these molecules are symmetric & both bonds are same length.

Table 5.2. Vibrational frequencies (in cm⁻¹) of ternary^a (reactant side) $[\text{O}_3\text{AuCO}]^q$ ($q=-1,0,+1$) complexes calculated with B3LYP-SDD/6-311+G(3df).

O ₃ AuCO									
Charge	Spin	Name	Au-C	C-O	Au-O	O _α -O _β ^b	O _β -O _γ	O ₃ sym	O ₃ anti
Cationic	Singlet	¹BR₁⁺	403	2301	330	1035	1371		
		¹ BR ₂ ⁺	414	2299	294	968	1423		
	Triplet	³ BR ₁ ⁺	376	2311	353	602	1137		
		³ BR ₂ ⁺	379	2298	484	348	1666		
Neutral	Doublet	²BR₁⁰	465	2214	433	729	1229		
		² BR ₂ ⁰	455	2209	749	594	1308		
Anionic	Singlet	¹ BR ₁ ⁻	512	2026	344			907	873
		¹ BR ₂ ⁻	487	2051	691	365	1321		
	Triplet	³ BR ₁ ⁻	459	1831	324	748	1176		
		³ BR ₂ ⁻	458	1833	279	764	1201		
		³BR₃⁻	494	2011	740	152	1516		
Reference frequencies^c									
		CO	2217	O-O (O ₂)	1645	O ₃ sym	1265	O ₃ anti	1214
		CO ⁺	2300	O-O (O ₂) ⁻	1181	O ₃ ⁺ sym	1325	O ₃ ⁺ anti	2400
		CO ⁻	1665	O-O (O ₂) ²⁻	703	O ₃ ⁻ sym	1068	O ₃ ⁻ anti	896

^aLowest energy state for species of the same charge and molecular components are in bold.

^b O_α, O_β, and O_γ refer to the order of oxygen atoms, where O_α is the closest to (or attached to) Au.

^c calculated at same level of theory: B3LYP/6-311+G(3df).

allotrope bonds.² The CO bond length is slightly longer than free CO with an accompanying red shift in the frequency. The two OO bonds are similar to the lengths of O_3^{2-} ($O_\alpha O_\beta$) and O_3 ($O_\beta O_\gamma$), with related OO frequencies (Tables 5.1 and 5.2).

Electrostatic potential surfaces (ESPs) help to visualize the charge distribution in each complex and can be used to interpret charge transfer throughout the complexes and how the charge distributions change along the reaction pathways. For the reactant-side complexes, the ESP surfaces are analyzed to understand how connectivity and orientation affect the charge distributions. The “ O_3 in” surface shows strong positive character on CO and negative character on the O_3 moiety, where O_α has slightly more negative character than O_γ (Figure 5.3).

From the BR_1 complex, the blue pathway of Figure 5.2a can continue with 47.85 kcal/mol of energy above BR_1 to the O_3 oxidation transition state, O-TS, with rotation of O_3 around Au to form an intermolecular bond between O_γ and carbon. This structure is reminiscent of the previously described “pre-reactive, in” structure of $AuCOO_2$,² but O-TS has an additional oxygen atom to form O_3 . The Au- O_α bond remains intact with a significant increase to 2.307 Å and the AuCO angle decreases from 180° to 159.2°. The AuC, CO, and $O_\beta O_\gamma$ bonds lengthen slightly with an accompanying red shift for CO, while the $O_\alpha O_\beta$ bond length decreases and the O_3 moiety reforms symmetric and anti-symmetric O_3 frequencies (Tables 5.3 and 5.4). The ESP surface shows retention of negative character on the O_3 moiety, which is distributed more evenly across O_α and O_γ than in BR_1 , while positive character has migrated onto the Au atom from CO.

From the O-TS transition state, a post-reactive minimum can be formed along the solid blue pathway in Figure 5.2a, or the product can be formed by following the dashed

blue line. For the post-reactive minimum (AR₁), the O_αO_β and AuC bonds are broken, the second CO bond shortens to form CO₂ and CO₂ moves away from AuO₂. This minimum (AR₁) appears to be a Lewis acid-base stabilized complex with the long bonds between Au, CO₂ and O₂ (Tables 5.7 and 5.8) and resides at -114.34 kcal/mol. The ESP surface shows neutral CO₂, Au and O₂ moieties (Figure 5.3). From AR₁, the pathway can continue over a very small barrier (0.01 kcal/mol) where the CO₂ moiety is moving away from O₂. Both Au-O bonds increase, while CO₂ and O₂ moieties remain similar to their respective “free” molecules in lengths and frequencies (Tables A5.4 and A5.5 in Appendix A5). The ESP surface is similar to AR₁ with neutral Au, O₂ and CO₂ moieties.

The product, O₂AuCO₂, can be directly formed from O-TS or from LB₂ with shortening of the “newly formed” O-C bond and breaking of the Au-C bond (in O-TS). The O₂ moiety is bonded to Au opposite from the linear OCO. The AuO_α and O_αO_β bonds decrease with an OO length and frequency similar to O₂⁻ and the CO₂ bonds and frequencies are similar to “free” CO₂ (Tables 5.9 and 5.10). The ESP surface shows negative character on O₂ with a strong positive character on CO₂, especially on carbon, which is reminiscent of the charge profile on the OAuCO₂ product of the O₂ system.

5.3.2 AuO Oxidation Pathway

From BR₁, the (O₃ “out”) BR₂ complex with an energy of -70.19 kcal/mol is formed over a small rotational barrier (LB₁), as seen in Figure 5.2b. The AuC and CO bond lengths (and frequencies) are similar for both BR complexes, while AuO and O_βO_γ shorten slightly with an accompanying blue shift in the OO frequency (Tables 5.1 and 5.2). The O_αO_β bond increases slightly to 1.513 Å with a red shifted OO frequency, where both are similar to O₂²⁻. The ESP surface of BR₂ is very similar to BR₁.

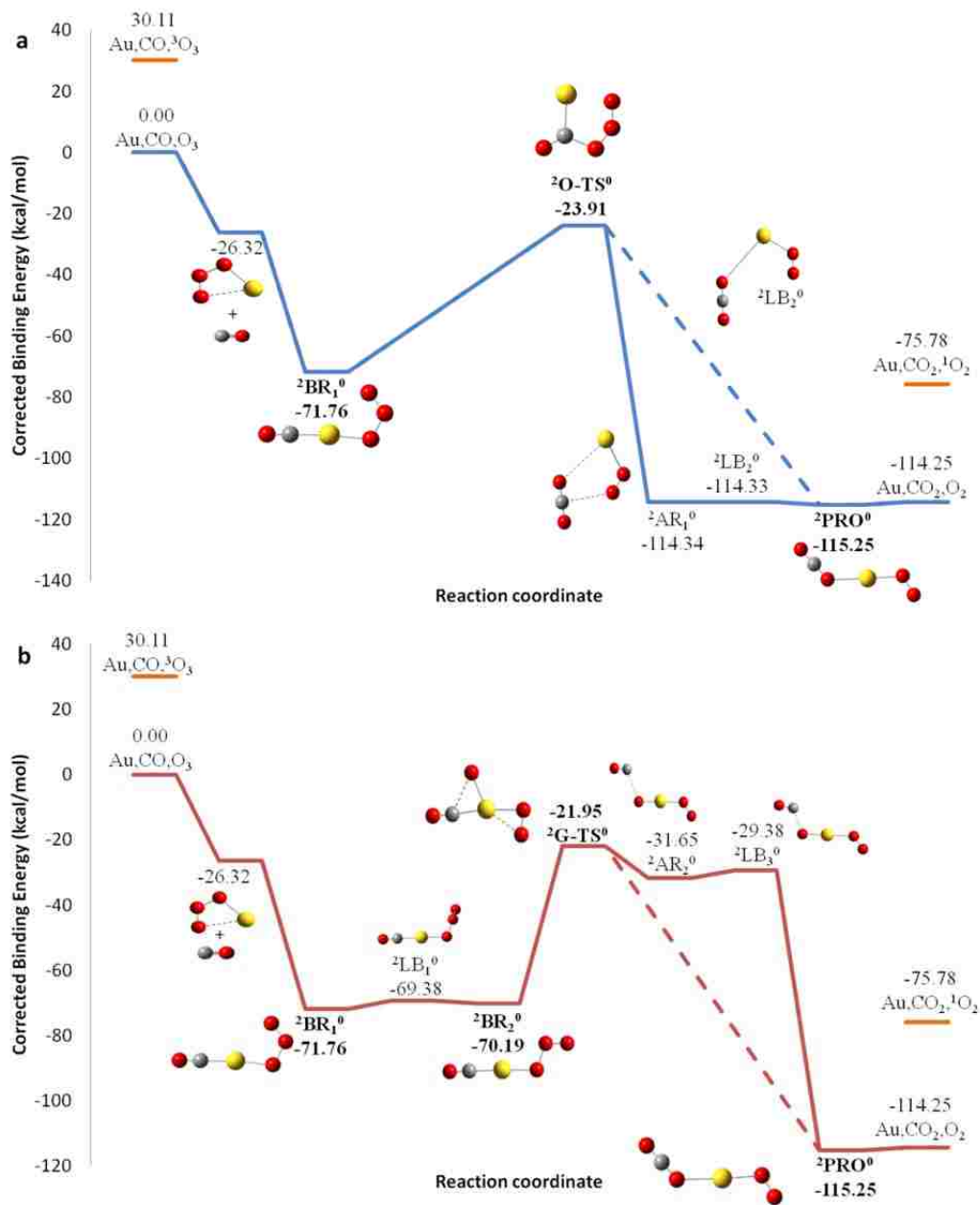


Figure 5.2. a) The neutral doublet reaction pathway(s) for $[\text{O}_3+\text{Au}+\text{CO}]$ along the “ O_3 oxidation” pathway is shown with relative energies for calculated stable points. The main minima and transition states, described in the text, are in bold. The solid blue line shows the O_3 oxidation process; the dashed blue line indicates the possible, shorter pathway from ${}^2\text{O-TS}^0$ to structure ${}^2\text{PRO}^0$. **b**) The neutral doublet reaction pathway(s) for $[\text{O}_3+\text{Au}+\text{CO}]$ along the “ AuO oxidation” pathway is shown with relative energies for calculated stable points. The dashed blue line shows the AuO oxidation process over one transition state (${}^2\text{G-TS}^0$); the dashed red line indicates the possible, shorter pathway from ${}^2\text{G-TS}^0$ to structure ${}^2\text{PRO}^0$.

From BR₂, the AuO oxidation transition state (G-TS) is reached with 48.24 kcal/mol of energy. The G-TS structure has linear AuCO with O₂ on the opposite side of Au and “migrating” oxygen atom on top of the Au atom; this is visually similar to the previously reported O₂AuCO structure with an additional O atom bonded to the Au atom. Compared to BR₂, the O_α-O_β bond has been broken and new Au-O_β and (long) O_α-C bonds are formed. The Au-C, AuO_α and O_βO_γ bonds increase with an accompanying red shift of the OO frequency, where O_βO_γ values are similar to O₂⁻. The CO bond decreases slightly as the related frequency blue shifts and remains similar to “free” CO (Tables 5.5 and 5.6). The ESP surface has positive character remaining on AuCO like the BR complexes, negative character on the O_α atom, and slight negative character on O₂.

From the G-TS transition state on the solid red pathway, a post-reactive minimum (AR₂) is found ~10 kcal/mol below G-TS, where the Au-C bond has been broken and the intermolecular OC bond increases, so that the complex is O₂AuO—CO. Both AuO bonds and the O₂ bond decrease with an accompanying blue shift in the OO frequency (Tables 5.7 and 5.8). The ESP surface has a well distributed charge with a negative charge on O_α and nearly equivalent positive charge on Au (with very slight positive character on CO and O₂).

From AR₂, the LB₃ transition state is reached with 2.27 kcal/mol, where the intermolecular OC bond decreases significantly by 0.648 Å. The O₂ bond decreases slightly and the related frequency blue shifts, while the AuO bonds and CO bond increase slightly with an accompanying red shift in the CO frequency (Tables A5.4 and 5.5). The ESP surface, similar to AR₂, has a well distributed charge with negative character on O_α and positive character on Au. Like the O₃ oxidation pathway, the product can be formed

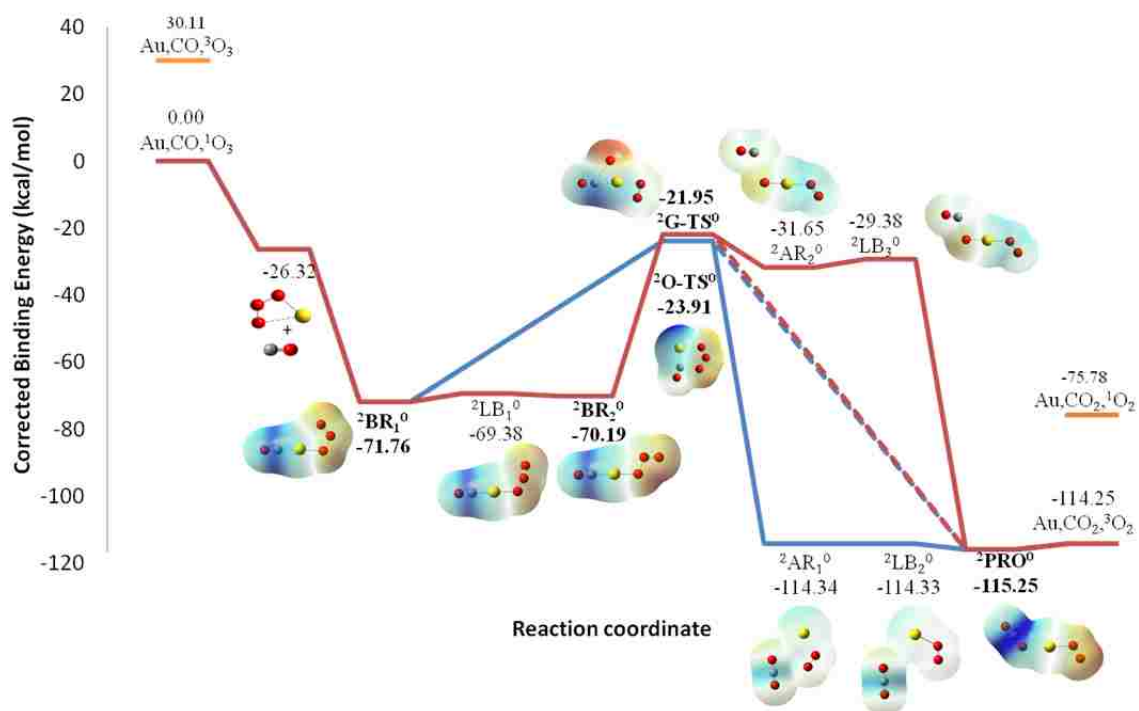


Figure 5.3. The reaction pathway(s) for the neutral doublet state is shown for Au atom, CO and O₃, where each position is now represented by the respective electrostatic potential (ESP) mapped on to the total electron density isosurface (density = 0.0004). The color map spans a range of 0.1 with red (blue) as most negative (positive) from -0.05 to +0.05.

Table 5.3. Bond lengths (in Å) for O₃ oxidation transition state (O-TS) complexes^a, {AuCOO₃}^q q=(+1,0,-1), calculated with B3LYP-SDD/6-311+G(3df).

{AuCOO₃} O-TS transition state							
Charge	Spin	Name	Au-C bond	C-O bond	Au-O _α ^b bond	O _α -O _β bond	O _β -O _γ bond
Cationic	Singlet	¹ O-TS ₁ ⁺	2.067	1.129 1.827	2.285	1.278	1.306
		¹ O-TS ₂ ⁺	2.005	1.151 1.579		1.189	1.440
	Triplet	³ O-TS ⁺	2.011	1.125 1.980	2.227	1.334	1.306
Neutral	Doublet	² O-TS ⁰	2.031	1.135 2.049	2.307	1.359	1.338
Anionic	Singlet	¹ O-TS ⁻	1.986	1.154 2.121	2.105	1.529	1.409
	Triplet	³ O-TS ⁻	2.100	1.143 2.496	2.641	1.352	1.340

^a O₃ in structure is listed first and O₃ out structure is listed second per charge/spin state.

^b O_α, O_β, and O_γ refer to the order of oxygen atoms, where O_α is the closest to (or attached to) Au.

Table 5.4. Vibrational frequencies (in cm⁻¹) for O₃ oxidation transition state (O-TS) complexes, {AuCOO₃}^q q=(+1,0,-1), calculated with B3LYP-SDD/6-311+G(3df).

{AuCOO₃} O-TS transition state									
Charge	Spin	Name	AuC	CO	AuO	O _a O _b ^a	O _b O _c	O ₃ sym	O ₃ anti
Cationic	Singlet	¹ O-TS ₁ ⁺	463	2167	316	993	1125		
		¹ O-TS ₂ ⁺	694	2005		863	1464		
	Triplet	³ O-TS ⁺	439	2202	308	792	1125		
Neutral	Doublet	² O-TS ⁰	337	2128	195			1048	821
Anionic	Singlet	¹ O-TS ⁻	417	1998	344	532	870		
	Triplet	³ O-TS ⁻	324	2036	165			1059	858

^a O_α, O_β, and O_γ refer to the order of oxygen atoms, where O_a is the closest to (or attached to) Au.

Table 5.5. Bond lengths (in Å) for AuO oxidation, $\{\text{O}_2(\text{O})\text{AuCO}\}^q$ transition state complexes, $q=(+1,0,-1)$, calculated with B3LYP-SDD/6-311+G(3df).

$\{\text{O}_2(\text{O})\text{AuCO}\}$ G-TS transition state							
Charge	Spin	Name	Au-C bond	C-O bond	Au-O_x^{a,b} bond	O_α-O_β bond	O_β-O_γ bond
Cationic	Singlet	¹ G-TS ⁺	1.985	1.113	1.930		1.199
	Triplet	³ G-TS ⁺	1.996	1.116	2.119		1.205
Neutral	Doublet	² G-TS ⁰	1.966	1.122	2.052		1.286
				2.422	2.121	2.384	
Anionic	Singlet	¹ G-TS ⁻	1.898	1.145	2.000		1.310
	Triplet	³ G-TS ⁻	2.136	1.144	1.927		1.300
					2.249		

^a O_α, O_β, and O_γ refer to the order of oxygen atoms, where O_α is the closest to (or attached to) Au.

^b AuO_α bond length is listed first and AuO_β bond length is second.

Table 5.6. Vibrational frequencies (in cm⁻¹) for AuO oxidation, $\{\text{O}_2\text{O}\text{AuCO}\}^q$ transition state complexes, $q=(+1,0,-1)$, calculated with B3LYP-SDD/6-311+G(3df).

$\{\text{O}_2(\text{O})\text{AuCO}\}$ G-TS transition state						
Charge	Spin	Name	Au-C	C-O	Au-O_α^a	O_b-O_c
Cationic	Singlet	¹ G-TS ⁺	385	2321	586	1524
	Triplet	³ G-TS ⁺	381	2283	238	1580
Neutral	Doublet	² G-TS ⁰	335	2241	409	1234
Anionic	Singlet	¹ G-TS ⁻	440	2063	547	1136
	Triplet	³ G-TS ⁻	144	2038	568	1164
					395 (AuO ^β)	

^a O_α, O_β, and O_γ refer to the order of oxygen atoms, where O_α is the closest to (or attached to) Au.

from either the G-TS or LB₃ (post-reactive) transition state, where the AuC bond is broken and new AuO bond is formed from the G-TS transition state. The “original” CO and AuO(CO) bonds increase, while the second CO bond decreases significantly to form symmetric and anti-symmetric CO₂ bonds and frequencies. The AuO(O) and OO bonds decrease with a small red shift in the OO frequency.

Other Charge States’ O₃ Oxidation Pathway: Like the neutral BR₁ complex, the cationic (singlet and triplet) and anionic singlet reactant-side complexes have linear AuCO angles, while anionic triplet BR₁ has a bent AuCO angle, which is similar to the O₂AuCO^q systems (Figure 5.1; Tables 5.1 and 5.2). Anionic singlet BR₁ has C_{2v} symmetry and is the reactant-side global minimum, which is reminiscent of the O₂AuCO⁻ (singlet) complex. The cationic singlet BR₁ complex is also the reactant-side global minimum. Similar to the neutral ESP surface, the anionic singlet ESP surface shows strong positive character on CO and negative character on the O₃ moieties (Figure A5.5 in Appendix A5). In contrast, the cationic singlet and triplet and anionic triplet ESP surfaces show well distributed charge across the entire complex.

The O-TS transition states are below the reactant asymptote for all of the charge (and spin) states, where only the cationic triplet structure is planar. Similar to the neutral O-TS, the anionic triplet O-TS also forms a symmetric O₃ moiety, while the other charge states have non-symmetric O₃ moieties. Unique to the cationic singlet is a second O-TS transition state with a COOO dihedral of 180° with no Au-O bond; this species is ~ 9 kcal/mol higher in energy than O-TS₁ (Figure 5.4). Like the neutral system, the cationic and anionic singlet O₃ oxidation pathways are the energetically favorable pathways.

The product of other charge states is formed directly from O-TS; only the neutral system has post-reactive states on the O₃ oxidation pathway. The products can be divided and discussed based on the connectivity of CO₂ to Au. The cationic products are similar to the neutral, where the linear OCO moiety is bonded to Au via an oxygen atom (Tables 5.9 and 5.10). The anionic complexes have bent CO₂ moieties, connected to Au with the carbon atom, and non-planar structures (anionic singlet: CAuOO dihedral of 85.7°; anionic triplet: CAuOO dihedral of 180°). The ESP surfaces show well-distributed charge for cationic and anionic charge states.

Other Charge States' AuO Oxidation Pathway: Like the BR₁ complex, most BR₂ (and anionic triplet BR₃) complexes have linear AuCO moieties, except the anionic triplet BR₂ complex. Different from the planar (neutral and cationic) BR₂ complexes, the anionic singlet BR₂ complex has a significantly elongated O_αO_β and 90° AuOOO dihedral, which makes the complex is non-planar (Figure 5.6). Like the anionic singlet BR₂ complex, the anionic triplet BR₃ complex has a significantly elongated O_αO_β bond of 2.709 Å. Also, the cationic triplet BR₂ displays a long O_αO_β and shorter O_βO_γ bonds; however, this elongation is an artifact of B3LYP, since the B2PLYP calculations show the O_αO_β bond to be 1.369 Å (O_βO_γ, 1.330 Å), which is in better agreement with the other charge states. The cationic triplet and anionic triplet “O₃ out” complexes are the reactant-side global minimum on the respective pathways. The ESP surfaces are similar to the BR₁ ESP surfaces for the respective charge (and spin) states. Similar to the neutral G-TS transition state, the cationic singlet and anionic triplet states also have planar structures, while the cationic triplet and anionic singlet states have non-planar structures. Unlike all

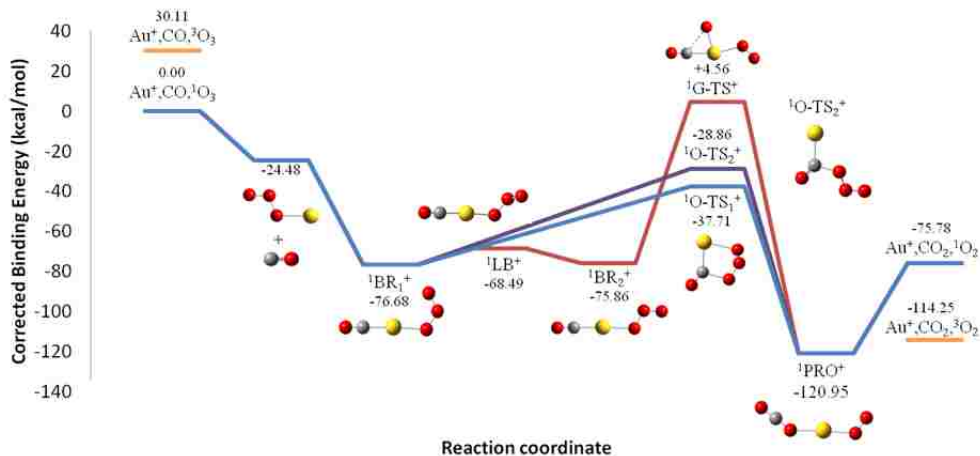


Figure 5.4. The reaction pathways for the cationic singlet state for Au^+ , CO and O_3 are shown, where the blue and purple lines represent the two O_3 oxidation pathways, ${}^1\text{O-TS}_1^+$ & ${}^1\text{O-TS}_2^+$ and red line represents the AuO oxidation pathway, ${}^1\text{G-TS}^+$.

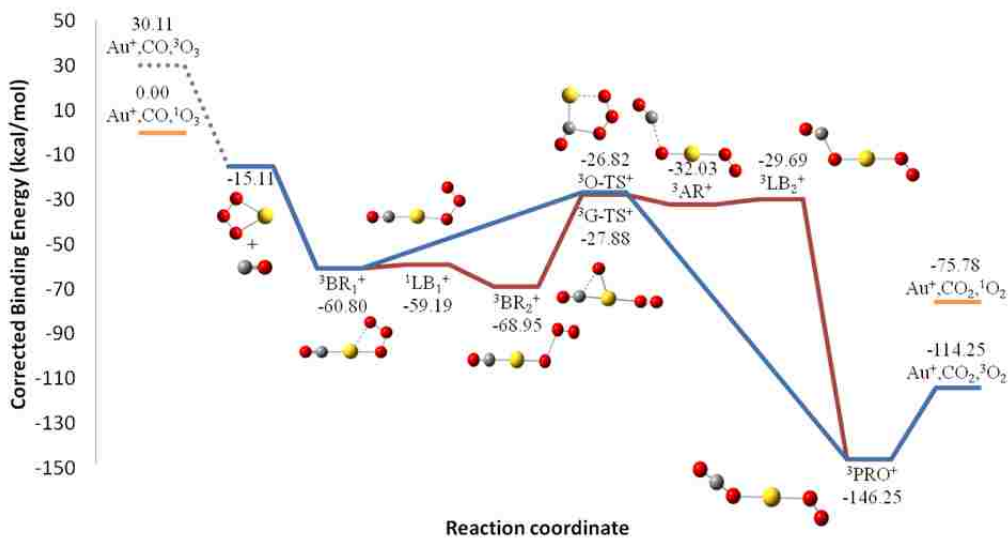


Figure 5.5. The reaction pathways for the cationic triplet states are shown, where ${}^3\text{G-TS}^+$ (red line) represents the AuO pathway and ${}^3\text{O-TS}^+$ (blue line) represents the O_3 pathway and both pathways start from the “ O_3 in” minimum (${}^3\text{BR}_1^+$). The dotted purple line shows the reactants with triplet ozone and indicates the instability of that ozone species.

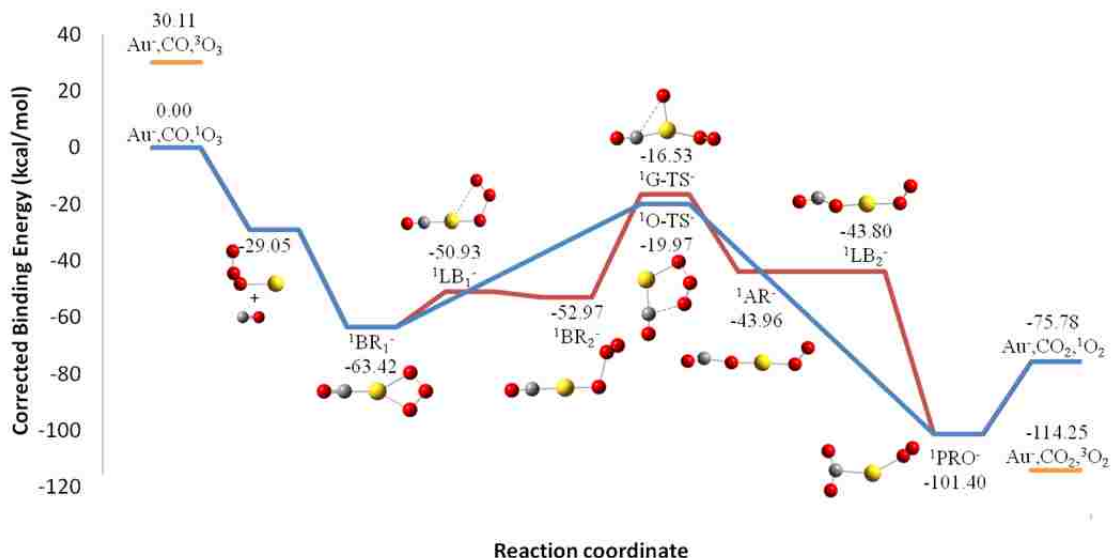


Figure 5.6. The reaction pathway(s) for the anionic singlet state is shown for Au atoms, CO and O₃, where both pathways originate with the C_{2v} “O₃ in” minimum (¹BR₁⁻). The blue line shows the O₃ oxidation pathway and the red line represents the AuO pathway.

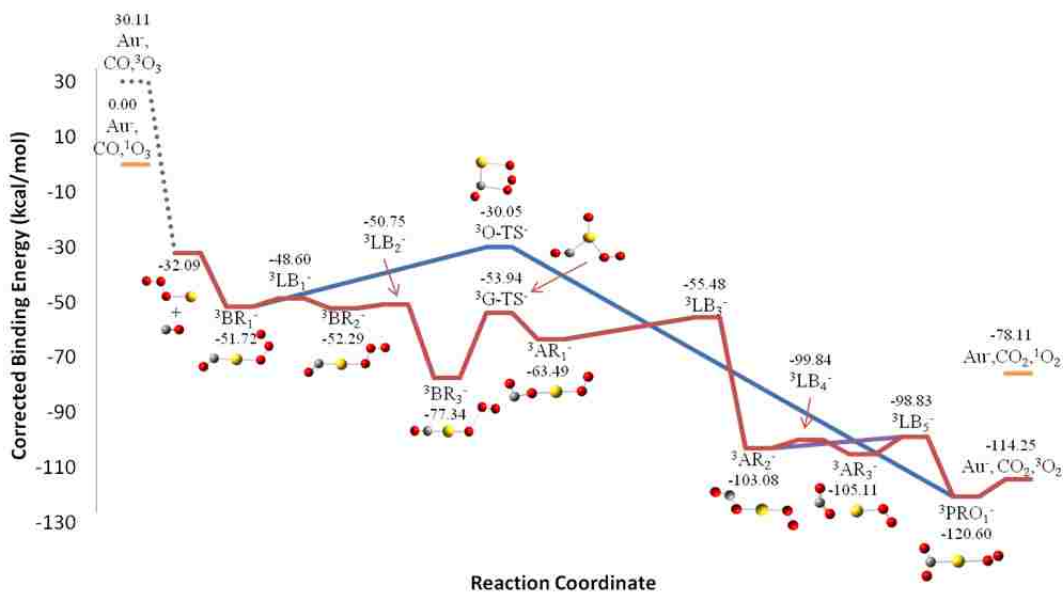


Figure 5.7. The reaction pathways for the anionic triplet system for Au⁻, CO and O₃ are displayed with the related structures and energies per minima and transition state. The dotted purple line shows the reactants with triplet ozone and indicates its instability. The blue line indicates the O₃ pathway; the solid red line indicates the AuO oxidation pathway and the purple pathway shows the alternate post-reactive pathway that can continue over ³LB₄⁻ to structure ³AR₃⁻ (red line).

Table 5.7. Bond lengths (in Å) for the post-reactive minima, [O₂AuOCO]^q or [AuO₂CO₂]^q, complexes, q=(+1,0,-1), calculated with B3LYP-SDD/6-311+G(3df).

Post-reactives						
Charge	Spin	Name	C-O bond	Au-O _x ^{a,b} bond	O _α -O _β bond	O _β -O _γ bond
Cationic	triplet	³ AR ⁺	1.117	1.932		1.205
			2.312	2.138		
Neutral	doublet	² AR ₁ ⁰	1.160	3.737	1.230	
			1.158	2.291		
Anionic	singlet	² AR ₂ ⁰	1.124	1.902		1.237
			2.795	2.041		
			¹ AR ⁻	1.134	1.866	
	triplet	³ AR ₁ ⁻	2.374	1.968		
			1.130	1.950		1.324
			2.686	2.064		
³ AR ₂ ⁻	1.206	2.076		1.317		
	1.277	2.042				
	³ AR ₃ ⁻	1.202	2.137		1.310	
			1.250	2.075		

a O_α, O_β, and O_γ refer to the order of oxygen atoms, where O_α is the closest to (or attached to) Au.

b AuO_α bond length is listed first and AuO_β bond length is second.

Table 5.8. Vibrational frequencies (in cm⁻¹) for post-reactive minima, [O₂AuOCO]^q or AuO₂CO₂, q=(+1,0,-1), calculated with B3LYP-SDD/6-311+G(3df).

Charge	Spin	Name	CO	AuO _x ^{a,b}	O _α -O _β	O _β -O _γ	CO ₂ sym	CO ₂ anti
Cationic	Triplet	³ AR ⁺	2270	512		1559		
			249	323				
Neutral	Doublet	² AR ₁ ⁰		18	1403		1374	2413
				105				
Anionic	Singlet	² AR ₂ ⁰	2216	599		1324		
			124	390				
	Triplet	¹ AR ⁻	2124	714		1180		
			240	543				
			³ AR ₁ ⁻	2158	546		1181	
			162	452				
³ AR ₂ ⁻	1738	328		1181				
	1253	507						
³ AR ₃ ⁻		326		1174	1198	1823		
			468					

a AuO_α vibrational frequency is listed first and AuO_β is second.

b O_α, O_β, and O_γ refer to the order of oxygen atoms, where O_α is the closest to (or attached to) Au.

Table 5.9. Bond lengths (in Å) for the product, $[\text{O}_2\text{AuCO}_2]^q$, complexes, $q=(+1,0,-1)$, calculated with B3LYP-SDD/6-311+G(3df).

Products							
Charge	Spin	Name	Au-C bond	C-O ^a bond	Au-O ^b bond	O-O bond	
Cationic	Singlet	¹ PRO ⁺		1.139 1.181	2.143 2.075	1.200	
	Triplet	³ PRO ⁺		1.139 1.180	2.161 2.152	1.208	
Neutral	Doublet	² PRO ⁰		1.151 1.168	2.369 2.069	1.273	
Anionic	Singlet	¹ PRO ⁻	2.222	1.199 1.214	2.117	1.300	
	Triplet	³ PRO ⁻	2.210	1.212 1.212	2.352	1.260	
Reference lengths ^{c,d}		C-O	1.124	CO ₂	1.159	O-O (O ₂)	1.203
		C-O ⁺	1.108	CO ₂ ⁺	1.170	O-O (O ₂) ⁻	1.341
		C-O ⁻	1.183	CO ₂ ⁻	1.227	O-O (O ₂) ²⁻	1.559

^a Exterior CO bond is listed first and interior (attached to Au) CO bond is second.

^b AuOCO bond length is listed first and AuO₂ bond length is second.

^c Reference lengths are calculated at the same level of theory: B3LYP-SDD/6-311+G(3df).

^d Only one bond length is shown for O₂^q, O₃^q and CO₂, as these molecules are symmetric and both bonds are same length.

Table 5.10. Vibrational frequencies (in cm⁻¹) of the products, $[\text{O}_2\text{AuCO}_2]^q$ ($q=+1,0,-1$), calculated with B3LYP-SDD/6-311+G(3df).

Charge	Spin	AuC	CO ₂ sym	CO ₂ anti	AuO ^a	OO	
Cationic	Singlet		1373	2438	290 436	1545	
	Triplet		1373	2438	247 332	1560	
Neutral	Doublet		1366	2409	141 491	1219	
Anionic	Singlet	150	1237	1944	407	1152	
	Triplet	191	1282	1897	81	976	
Reference frequencies ^b							
		CO ₂ sym	1374	CO ₂ anti	2414	O-O (O ₂)	1645
		CO ₂ ⁺ sym	1315	CO ₂ ⁺ anti	1483	O-O (O ₂) ⁻	1181
		CO ₂ ⁻ sym	1218	CO ₂ ⁻ anti	1770	O-O (O ₂) ²⁻	703

^a AuO(CO) vibrational frequency is listed first and AuO(O) is second.

^b Reference frequencies are calculated at the same level of theory: B3LYP-SDD/6-311+G(3df).

other transition states, the cationic singlet G-TS is 4.56 kcal/mol above the reactant asymptote. The cationic and anionic triplet states G-TS transition states, the AuO oxidation pathways, are the lower energy pathways.

In other charge states, post-reactive species are only observed on the G-TS pathway; therefore, these post-reactive complexes are identified as AR or AR₁ (for anionic triplet), except the cationic singlet has no post-reactive complexes (Tables 5.7 and 5.8). Like the neutral structure, the cationic triplet structure is planar, while the anionic (singlet and triplet) structures are non-planar. The anionic triplet state is the only charge state to have an “extended” post-reactive pathway with several post-reactive complexes and transition states, which has been previously identified by Castleman and colleagues as the reaction pathway for OAuO₂⁻ + CO. For AR₂ and AR₃ complexes of the anionic triplet pathway, a compact CO₂ moiety is formed with an overall O₂AuCO₂⁻ structure, where the complexes differ by AuOCO dihedral angles (Figure 5.7).

There are post-reactive, low-barrier transition states, denoted as LB_x (x=2-5), on the G-TS pathway. Similar to the neutral system, the very long OC bond is significantly shortened from the post-reactive minimum (AR/AR₁) for the cationic triplet and anionic singlet LB₂ and anionic triplet LB₃ transition states (Tables A5.4 and A5.5). As mentioned above, the anionic triplet state is the only charge state to have an “extended” post-reactive pathway, where the post-reactive transition states (LB₄ and LB₅) differ by the AuOCO dihedral angles. Review of the literature has shown similarities of these post-reactive species to the ³[O₂AuO]⁻ + CO pathway outline by Castleman and co-workers; therefore, the AuO oxidation pathway provides an entryway on this oxidized Au⁻ pathway.

5.4 Discussion

5.4.1 O₃ Oxidation Pathway

The linearity of AuCO in most reactant-side complexes, except the anionic triplet BR₁ and BR₂, is induced by charge transfer into the electron withdrawing effects of O₃ on AuCO, similar to the O₂AuCO^d work discussed in Chapter 3. For the states with BR₁ as the reactant-side global minimum, there may be additional stabilization from the Au-O_γ interaction, which allows a somewhat more evenly distribution of charge across O₃. The neutral ESP surface, Figure 5.3, agrees with the charge transfer idea, where the O₃ moiety has negative character and CO has positive character. With the formation of O-TS transition state, the O₃ moiety retains the electron density, but rotation of O₃ and formation of the intermolecular O-C bond disrupts the linear bonding of AuCO. With the loss of AuCO linearity and retention of negative character on O₃, positive character is induced on the Au atom, as observed in the ESP surface. The post-reactive minimum (AR₁) of a Lewis acid-base stability complex can be formed after O-TS, where the ESP surface shows that charge transfer is no longer occurring, as all moieties have neutral character. The low barrier transition state (LB₂) associated with this minimum also has a very neutral ESP surface. From the O-TS transition state, negative character remains on the O₂ moiety, while the positive character has migrated onto the CO₂ moiety, which indicates charge transfer into O₂ that induces positive character on CO₂.

5.4.2 AuO Oxidation Pathway

The ESP surface of BR₂ has negative character on O₃ and CO has positive character, similar to BR₁. In forming the G-TS transition state, AuCO remains linear and the ESP surface shows retention of positive character on CO, suggesting that the Dewar-Chatt-Duncanson-like bonding is retained. Au has catalyzed the decomposition of O₃ to

form AuO and a separate, possibly spectator O₂ moiety, where Au acts chemically distinct from Au in O-TS transition state. The ESP surface, as stated above, has positive character on CO and negative character on O_α, while O₂ is relatively neutral, which further suggests that O₂ is a spectator. The orbitals of the O₂ moiety are similar to “free” O₂ orbitals and show no interactions with the separated O_α atom, further suggesting that O₂ is a spectator.

As discussed in the Results section, a different post-reactive minimum (AR₂) is formed from G-TS transition state, where the ESP surface has very slight negative character on O_α, a neutral CO moiety and slightly positive AuO₂ moiety; this surface is more neutralized than G-TS and indicates less charge transfer. The post-reactive transition state ESP is similar to AR₂. In forming the product, the O₂ moiety gains negative character, which induces positive charge on the CO₂ moiety and switches the charge on the O_α atom. The product can also be directly accessed directly from G-TS, and based on the G-TS ESP surface, it appears that the migrating O atom of AuO is carrying the negative charge to “neutralize” the positive CO component and form CO₂. This neutralization should leave a complex with neutral moieties; however, the ESP surface of the product shows evidence for charge transfer into O₂, as discussed above.

5.4.3 Similarities of O-TS & G-TS

There are structural similarities between the O-TS and G-TS transition states, as both transition states retain the AuO_α bond, form long intermolecular O-C bonds and share similar Au-C and C-O bond lengths. The ESP surfaces also display similarities, where the negative character resides on the oxygen species of O-TS (O₃ moiety) and G-TS (O₂ and O atom sub-units). The clearest similarities between orbitals may be in the

HOMO-4 of G-TS and O-TS, as both have large $s-d_z^2$ mixed orbitals on Au, which bond with the CO orbitals and O_2 and O orbitals of G-TS (O_3 moiety of O-TS). Again, simple rotation of the O atom towards O_2 would then look similar to the O-TS orbitals. These molecular orbitals show that the G-TS structure appears to be the broken open version of O-TS.

Other Charge States O_3 Oxidation Pathway: The anionic singlet BR_1 complex has an ESP surface similar to the neutral, while the cationic (singlet and triplet) and anionic triplet have well-distributed charge, respectively (figures found in Appendix A5). The O-TS ESPs are generally similar to the neutral surface across all charge states with charge transfer that was not observed in the cationic (both spin states) and anionic (triplet) BR_1 complexes. Slightly different from the neutral surface is that both anionic states have positive charge spread across AuCO (in O-TS), rather than contained mostly on Au. Unlike the neutral product, all other charge (and spin) state products have well distributed charges in the ESP surfaces.

Other Charge States' AuO Oxidation Pathway: The cationic BR_2 ESP surfaces are similar to BR_1 and show well distributed charge across the complex, as does the anionic triplet. The anionic singlet BR_2 and triplet BR_3 structures carry most of the negative character on O_α with positive character on CO and a neutral O_2 . The cationic and anionic triplet “ O_3 out” structures are the reactant-side global minimum, which may be a result of these states preferring a triplet-like O_2 moiety over the O_3 singlet moiety, as the O_2 ground state triplet would best match the overall spin state. The G-TS ESP surfaces for the other charge states are again similar to the neutral surface with negative character on the migrating O_α atom and positive on CO; the positive charges are distributed slightly

differently in the cationic systems, which have positive on O_2AuCO and negative character in the anionic triplet is spread across $OAuO_2$. Like the BR_1 to O-TS transition, the cationic singlet and triplet states G-TS surfaces show that charge transfer occurs upon formation of G-TS, while the BR_2 surfaces had well-distributed charge. Similar to the reactant-side triplet “ O_3 out” energetics, the G-TS states are the lower energy pathways the cationic and anionic triplet states. With clear formation of an O_2 moiety, which prefers a triplet state, it is understandable that G-TS would be lower in energy, based on spin-state matching of O_2 and the overall complex. As stated above, non-neutral charge states have well-distributed charge in the product ESP surfaces. For these charge states when forming the product from G-TS, the negative character on the migrating O atom does appear to “neutralize” the positive character of CO to the appropriate overall charge of the product (+1 or -1).

5.4.4 Comparison of O_2 and O_3 Systems

There are several similarities between the O_2 and O_3 systems and the related pathways in structural data, ESP surfaces, and charge transfer. Most obvious is the similarity in the $[O_3AuCO]^q$ complexes to the $[O_2AuCO]^q$ structures, ESP surfaces and molecular orbitals, which show synergic back-bonding in the AuCO moieties of the orbitals. Like the O_2 system, the neutral and anionic singlet O_3AuCO ESP surfaces indicate charge transfer with the negative character on O_3 and positive in CO, while the cationic and anionic (triplet) surfaces have well-distributed charge. Similarities are also observed in the products of the two systems, $O_2AuCO_2^q$ and $OAuCO_2^q$. These structural, ESP surface, and molecular orbital similarities across the O_2 and O_3 systems indicate that

the different oxygen allotrope did not grossly change the “separated” and “product” complexes.

Structural and ESP surface similarities are also observed between AuCOO_3^q , the O-TS transition state, and the neutral and anionic singlet pre-reactive “in” AuCOO_2 minima; however, the type of stationary point is opposite with a maximum for O-TS and minimum for AuCOO_2 . In this case, the addition of the O atom promoted the complex into a transition state, as the OO bonds of the O-TS transition states are similar to free O_3 and O_3^- . Comparatively, the AuCOO_2 transition states (In-TS) had OO bonds elongated to values beyond the peroxide (O_2^{2-}) length. In the O_3 system, transition states on both pathways were observed for all charge states, while pre-reactive complexes and pathways were not observed with cationic and anionic triplet in the O_2 system. Furthermore, all of the transition states, except G-TS in cationic singlet, are below the energy of reactants (reactant asymptote), while the calculated barriers for In-TS and Out-TS pathways (Chapter 4) were greater than the reactant asymptote; the O_3 system reactions are “spontaneous” with respect to energy barriers residing below the reactant asymptote, but could be trapped in cryogenic matrices. The O_3 system also has the AuO oxidation pathway with post-reactive stationary points, which was not discussed in Chapter 4 for the O_2 system; however, some recent work on possible Au insertion into O_2 has shown O(O)AuCO^q transition states that are above reactant asymptote at ~ 30 kcal/mol or greater for cationic triplet, neutral and anionic singlet states. It is striking that so many similarities exist across O_2 and O_3 system, but on the other hand the similarities are understandable since the systems involve oxygen allotropes.

5.5 Conclusions

This work indicates that oxidation of CO can occur via two chemically distinct pathways, whereby CO is oxidized directly by ozone (catalyzed by Au) or by AuO after O₃ decomposition catalyzed by Au. Originally surprising, both pathways start from the same, stable O₃AuCO minima with an intact molecular O₃, indicating that pre-oxidation of Au is not required for CO oxidative catalysis. The calculation of these two distinct pathways suggests that Au can act as a stabilizing agent for molecular ozone or provide a location for O₃ decomposition to AuO. The appearance of these two pathways across the three charge states (and spin states) indicate that subtraction or addition of an electron beyond neutral Au does not grossly alter the catalytic reaction and may result from the ability of these complexes to balance charge.

The singlet and doublet states have O-TS pathway as the lower energy pathway, while G-TS pathway is lower for the triplet states, which may be related to a curve crossing barrier as the ground state reactants (O₃, Au⁰, CO) are all singlet states, while the products (O₂, Au⁰, CO₂) have the triplet O₂. G-TS involves the formation of [O₂AuO+CO]⁰, which is preferred by the triplet systems, since G-TS forms O₂, a triplet, sooner than the O-TS pathway. Comparatively, the O-TS pathway retains the molecular O₃ structure in the transition state, which is preferred for the singlet and doublet systems, as the ground state of O₃ is a singlet. Since the reactants are singlets and products involve triplet O₂, the pathways are spin-forbidden processes and reactions to form the products would depend on the spin-orbit coupling of the singlet and triplet electronic states along the reaction coordinate.

5.6 Computational Methods

Density functional theory (DFT) geometry optimizations and frequency calculations were carried out using the GAUSSIAN 09 suite of computational chemistry programs.³ Except where otherwise noted, all reported data reflect results obtained using the B3LYP hybrid functional,⁴ with a mixed basis set employing the Stuttgart-Dresden relativistically-corrected effective core potential basis for Au atoms,^{5,6} and the Pople 6-311+G(3df) basis for C and O atoms.^{7,8} All geometry optimizations were performed using the tight convergence criteria and the ultrafine integration grid (Gaussian keywords: “opt=tight” and “integral=ultrafine”); this was required to achieve convergence for weakly-bonded systems, and was maintained for all calculations to ensure comparability of the results. Transition states were calculated with the quadratic synchronous transition approach with three molecule specifications (qst3 keyword) for the “reactant,” “product,” and transition state guess.^{9,10} All reported geometries reflect stable minima (maxima for transition states) on their respective potential energy surfaces without (with) imaginary frequencies. The stabilities of the SCF wavefunctions for each reported wavefunction were verified using the method of Davidson.¹¹ Counterpoise corrections, using the method of Boys and Bernardi,¹² were carried out to correct for the effects of basis-set superposition error (BSSE) on the binding energies of the complexes. All reported binding energies have been corrected for both BSSE and the vibrational zero-point energy (ZPE). IRC calculations were then applied to understand the connections between calculated transition states and minima.¹³⁻¹⁶ Atomic charges were calculated using the Hirshfeld stockholder method¹⁷⁻¹⁹, CHELPG molecular electrostatic

potential method,²⁰ and the natural bond orbital (NBO) method,²¹⁻²⁶ as implemented within GAUSSIAN 09.

Computational Details for Electrostatic Potential Surfaces: Electrostatic potential (ESP) has been mapped onto the B3LYP total electron density isosurfaces (density=0.0004) for the structures along each pathway. The color map spans a range of 0.1 in each case, where red (blue) as most negative (positive). The charges for cationic species are mapped over +0.10 to +0.20; neutral, -0.05 to +0.05, and anionic, -0.20 to -0.10. Spin densities were calculated using Gaussian 09 (density = 0.004), where spin density is the β (spin) density subtracted from the α (spin) density.

5.7 References

- (1) Hao, Z.; Cheng, D.; Guo, Y.; Liang, Y. *Appl. Catal. B: Environ.* **2001**, *33*, 217-222.
- (2) Smith, A. N.; Moore, D. T. *Journal of Physical Chemistry a* **2012**, *116*, 9370-9381.
- (3) ; Frisch, M. J.; Trucks, G. W.; Schlegel, H. B.; Scuseria, G. E.; Robb, M. A.; Cheeseman, J. R.; Scalmani, G.; Barone, V.; Mennucci, B.; Petersson, G. A., et al. Gaussian 09, Revision A.02, Gaussian, Inc., Wallingford, CT **2009**.
- (4) Becke, A. D. *J. Chem. Phys.* **1993**, *98*, 5648-5652.
- (5) Schwerdtfeger, P.; Dolg, M.; Schwarz, W. H. E.; Bowmaker, G. A.; Boyd, P. D. W. *J. Chem. Phys.* **1989**, *91*, 1762-1774.
- (6) Andrae, D.; Haussermann, U.; Dolg, M.; Stoll, H.; Preuss, H. *Theor. Chim. Acta* **1990**, *77*, 123-141.
- (7) Krishnan, R.; Binkley, J. S.; Seeger, R.; Pople, J. A. *J. Chem. Phys.* **1980**, *72*, 650-654.
- (8) Frisch, M. J.; Pople, J. A.; Binkley, J. S. *J. Chem. Phys.* **1984**, *80*, 3265-3269.
- (9) Peng, C.; Schlegel, H. *Isr. J. Chem.* **1993**, *33*, 449-454.
- (10) Peng, C.; Ayala, P.; Schlegel, H.; Frisch, M. J. *Comput. Chem.* **1996**, *17*, 49-56.
- (11) Langhoff, S. R.; Davidson, E. R. *Int. J. Quant. Chem.* **1974**, *8*, 61-72.
- (12) Boys, S. F.; Bernadi, F. *Mol. Phys.* **1970**, *19*, 553-566.
- (13) Fukui, K. *Acc. Chem. Res.* **1981**, *14*, 363-368.
- (14) Hratchian, H.; Schlegel, H. *J. Chem. Phys.* **2004**, *120*, 9918-9924.
- (15) Hratchian, H.; Schlegel, H. *J. Chem. Theory Comput.* **2005**, *1*, 61-69.
- (16) Hratchian, H. P.; Schlegel, H. B. In *Finding minima, transition states and following reaction pathways on ab initio potential energy surfaces*; Dykstra, C. E., Frenking, G., Kim, K. S. and Scuseria, G. E., Eds.; *Theory and Applications of Computational Chemistry: The First 40 Years*; Elsevier: Amsterdam, 2005.
- (17) Hirshfeld, F. L. *Theor. Chim. Acta* **1977**, *44*, 129-138.
- (18) Ritchie, J. P. *J. Am. Chem. Soc.* **1985**, *107*, 1829-1837.

- (19) Ritchie, J. P.; Bachrach, S. M. *J. Comput. Chem.* **1987**, *8*, 499-509.
- (20) Breneman, C. M.; Wiberg, K. B. *J. Comput. Chem.* **1990**, *11*, 361-373.
- (21) Foster, J. P.; Weinhold, F. *J. Am. Chem. Soc.* **1980**, *102*, 7211-7218.
- (22) Reed, A. E.; Weinhold, F. *J. Chem. Phys.* **1983**, *78*, 4066-4073.
- (23) Reed, A. E.; Weinstock, R. B.; Weinhold, F. *J. Chem. Phys.* **1985**, *83*, 735-746.
- (24) Reed, A. E.; Weinhold, F. *J. Chem. Phys.* **1985**, *83*, 1736-1740.
- (25) Reed, A. E.; Curtiss, L. A.; Weinhold, F. *Chem. Rev.* **1988**, *88*, 899-926.
- (26) Carpenter, J. E.; Weinhold, F. *J. Mol. Struct. -Theochem* **1988**, *46*, 41-62.

Chapter 6. DFT Investigations of CO Oxidation Pathways with Two Oxygen Species (O₂ and O₃) and Cu^q Atoms (q= +1, 0, -1): Observation of CuO and O₃ Oxidation Pathways for Oxygen Allotropes

6.1 Abstract

Density functional theory calculations (DFT) have been utilized to understand the CO oxidation pathway of Cu^q atoms (q=+1, 0,-1) with O₂ and O₃ as oxygen (atom) sources. The probable pathways can be grouped, regardless of charge or spin state or oxygen species, into two distinct pathways, where the Cu species are chemically distinct. The first set of pathway(s) involves direct oxidation of CO by O₂ (O₃), catalyzed by Cu^q, and the second is characterized by Cu^q oxidation by the oxygen allotrope to [OCuO]^q ([OCuO₂]^q) and subsequent oxidation of CO by [OCuO]^q ([OCuO₂]^q). Unique to the O₂ systems, there are two types of reactant-side minima, separated [O₂CuCO]^q and “pre-reactive” [CuCOO₂]^q reactant-side minima (q=0, -1), which lead to the O₂ oxidation transition states, denoted as In-TS and Out-TS. Both of these transition states can lead to the formation of the [CuCO₃]^q (carbonate-like) product, which is the energetically favorable product in the neutral and anionic charge states. The O₃ systems have “separated” [O₃CuCO]^q (q=+1, 0,-1) reactant-side complexes and one product, [O₂CuCO₂]^q, which can be formed from either O₃ oxidation or CuO oxidation pathways. In both oxygen allotrope systems, the energetically favorable pathways are dependent on the spin states, which may be a result of curve crossing between singlet and triplet surfaces as O₃, O₂ and O atom ground states are different.

6.2 Introduction

The oxidation of carbon monoxide (CO) has been tested with various catalysts, such as supported gold (Au) or copper (Cu) nanoparticles; however, questions still

remain as the specific active site and mechanisms.¹⁻⁴ One approach to addressing these questions is through model studies that exclude the support material and focus on the interactions of unsupported Au or Cu atoms and small clusters with the reactant molecules, such as CO, O₂ and O₃. Binary complexes, CuCO, CuO₂, and CuO₃, have been investigated to understand the structures of the respective complexes and provide insight into the interactions of individual types of reactants with Cu centers. The copper (atom) carbonyl clusters ([Cu(CO)_n]^q, n=1-3 and q = +1, 0, -1) and the adsorption of CO onto larger Cu clusters has been well studied experimentally and theoretically, and these works have indicated that CuCO and CuCO⁻ have bent structures, while CuCO⁺ is linear.⁵⁻¹⁰ Matrix isolation experiments have identified CuO, (OCuO)^q, and (CuO₂)^q complexes (q=+1, 0, -1), where DFT calculations have indicated bent structures for all of the CuO₂ complexes, but the neutral CuO₂ complex has been calculated with two different structures, in which one has an end-on structure (C_s) and C_{2v} structure with side-on (η^2) bonding of O₂ to Cu.¹¹⁻¹⁴ CuO₃ complexes (copper ozone or OCuO₂ structures) have been identified experimentally, in which Tevault and co-workers identified CuO₃ with a vibrational frequency of 802 cm⁻¹ in an Ar matrix that is ~2 cm⁻¹ below O₃⁻ and CuO₃ was explained to exist as Cu⁺O₃⁻. Calculations have indicated [CuO₃]^q (q = +1, 0, -1) structures that are highly dependent on the charge state, where the lowest energy neutral CuO₃ complex has a C_{2v} structure; the [OCuO₂]^q complexes also have been calculated and found to be lower in energy than the “ozone conserved” complexes, which is similar to the CuO₂ and OCuO system.^{13, 15, 16} Larger anionic and neutral CuO_x (x=4-6) complexes have been identified by Zhou and co-workers in matrix isolation experiments with laser ablated copper co-deposited with O₂ (or O₃) in argon and density

functional theory (DFT) calculations were utilized to gain insight on probable structures related to the spectra.^{13, 17, 18} Oxidation of CO with Cu atoms has been investigated by co-depositing O₂, CO and Cu atoms in matrix isolation experiments by Xu and Jiang, in which they assigned new peaks to O₂CuCO and O₂Cu(CO)₂ and stated that the CO₂ peak increased upon UV irradiation, which indicated CO oxidation over Cu atoms.¹⁹ They also completed DFT calculations, which produced a C_{2v} O₂CuCO structure, where O₂ is side-on (η^2) bonded to Cu.

6.3 Results

The binary and ternary complexes of O₂, Cu^q, and CO (q= +1, 0, -1) are discussed first, followed by the reaction pathways calculated for all of the charge states. The [O₃+Cu+CO]^q complexes and pathways are discussed after the O₂ pathways section. Figure 6.1 displays cartoons of all of the stable minima for binary complexes formed from either CO or O₂ binding to a copper atom or ion, along with their respective structural data. Figure 6.2 shows illustrations of the stable minima for ternary complexes formed from CO and O₂ binding to a copper atom or ion, along with their respective structural data. Calculated vibrational frequencies (unscaled) are collected in Table 6.1 and bond lengths are found in Table 6.2. The binding energies, corrected for ZPE and BSSE effects, of the various isomers of the binary and ternary complexes are collected in Table 6.3. Except where otherwise noted, all binding energies are relative to the ground states of the component O₂, CO and Cu^q species, where the “q” superscript indicates that any charge is carried by the Cu center in the reference system.

6.3.1 O₂, Cu^q, CO Complexes and Pathways

The binary complexes of [CuCO]^q and [CuO₂]^q and ternary complexes, [O₂CuCO]^q have been calculated to compare to previous studies and identify similarities (and differences) between the Cu and Au systems. The ternary complexes were tracked along possible reaction pathways by calculating transition states and products, [CuCO₃]^q and [OCuCO₂]^q, to understand the barriers to CO oxidation with O₂ and Cu atoms and ions.

CuCO^q: The cationic copper carbonyl complex, CuCO⁺, has a linear structure with a CO bond length of 1.114 Å and frequency of 2317 cm⁻¹, which is slightly longer than and blue shifted from CO⁺. The neutral CuCO complex has a bent CuCO angle of 140.6° and CO bond length and frequency at 1.140 Å and 2050 cm⁻¹ are similar to “free” CO. The anionic complexes, CuCO⁻, also can be characterized by the bent angle of 118.7° and bond length and frequency of 1.160 Å and 1894 cm⁻¹, which is shorter than and blue shifted from CO⁻. A trend of increasing CuC and CO bond lengths as a function of a more negative charge and concomitant decreases in CuC and CO frequencies can be seen; a similar trend has been previously discussed with respect to the Au system in Chapter 3. The [CuCO]^q structures are generally in agreement with B3LYP calculations completed by Andrews *et al.*⁸

CuO₂^q: All of the CuO₂^q structures have bent CuOO angles of varying degrees and have been previously identified.¹¹⁻¹³ The CuO₂⁺ (triplet) structure, with an angle of 128.5°, has an O-O bond length of 1.207 Å and frequency of 1585 cm⁻¹, which are similar to “free” O₂ values. The bent, neutral (doublet) CuO₂ complex has an angle of 116.9°, an O-O bond length of 1.276 Å and the OO frequency of 1201 cm⁻¹ is slightly blue shifted from

Table 6.1 B3LYP predicted stretching vibrational frequencies (in cm^{-1}) of optimized binary, $[\text{CuCO}]^q$ and $[\text{CuO}_2]^q$ and ternary, $[\text{O}_2\text{CuCO}]^q$ and $[\text{CuCOO}_2]^q$ complexes ($q=$, +1, 0, -1).

Species	Electronic state	Stretching frequency $-\text{cm}^{-1}$ (Intensity)			
		Cu-C	C-O	Cu-O	O-O
$[\text{CuCO}]^+$	$^1\text{A}_1$ ($^1\Sigma^+$)	374	2317		
CuCO	$^2\text{A}'$	341	2050		
$[\text{CuCO}]^-$	$^1\text{A}'$	288	1894		
$[\text{CuO}_2]^+$	$^3\text{A}''$			297	1585
$[\text{CuO}_2]$	$^2\text{A}''$			436	1201
$[\text{CuO}_2]^-$	$^1\text{A}'$			469	1021
$[\text{CuO}_2]^{-\text{b}}$	$^3\text{A}''$			358	1151
$[\text{O}_2\text{CuCO}]^+$	^1A	387	2315	359	1564
$[\text{O}_2\text{CuCO}]^+$	$^3\text{A}''$	392	2312	294	1599
O_2CuCO	$^2\text{A}''$	543	2188	425	1153
$\text{CuCOO}_2^{\text{out}}$	^2A	830	1890		1123
			510		
$[\text{O}_2\text{CuCO}]^-$	$^1\text{A}_2$	588	2011	478	830
$\text{CuCOO}_2^{\text{in}}$	^1A	288	1698		880
			957		
$\text{CuCOO}_2^{\text{out}}$	^1A	287	1727		745
			1047		
$[\text{O}_2\text{CuCO}]^{-\text{b}}$	$^3\text{A}''$	381	1826	487	1164
$\text{CuCOO}_2^{\text{in}}$	^3A	217	1714	511	879
			1056		
		Reference frequencies^a			
		C-O	2217	O-O (O_2)	1645
		C-O^+	2300	$\text{O-O}(\text{O}_2)^-$	1181
		C-O^-	1665	$\text{O-O}(\text{O}_2)^{2-}$	703

^a Reference frequencies calculated at same level of theory: B3LYP/6-311+G(3df).

Table 6.2 B3LYP predicted bond lengths (in Å) of optimized binary, [CuCO]^q and [CuO₂]^q and ternary, [O₂CuCO]^q and [CuCOO₂]^q complexes (q=, +1, 0, -1).

	CuCO		O ₂ CuCO			CuO ₂		
	Cu-C bond	C-O bond	Cu-C bond	C-O bond	Cu-O bond	O-O bond	Cu-O bond	O-O bond
<i>Separated</i>								
Cationic (singlet)	1.873	1.114	1.881	1.114	1.944	1.206		
Cationic (triplet)			1.867	1.114	1.968	1.206	1.989	1.207
Neutral doublet	1.936	1.140	1.769	1.131	1.967	1.342 ^a	1.890	1.276
Anionic Singlet	2.210	1.160	1.736	1.159	1.872	1.309 ^a	1.848	1.348
Triplet			1.848	1.184	1.901	1.336	1.967	1.316
<i>Pre-reactive</i>								
Neutral Doublet (out)			1.889	1.172		1.309		
Anionic Singlet (in)			1.599	1.210	2.121	1.470		
Anionic Singlet (out)			1.937	1.203		1.465		
Anionic Triplet (in)			2.059	1.208	1.932	1.489		
Ref. lengths^b	C-O	1.128	O-O	1.206	O-O	1.346	O-O	1.566
	C-O ⁺	1.109	(O ₂)		(O ₂) ⁻		(O ₂) ²⁻	
	CO ⁻	1.186						

^aPerpendicular distance to O-O bond center in C_{2v} complex

^bcalculated at same level of theory: B3LYP/6-311+G(3df)

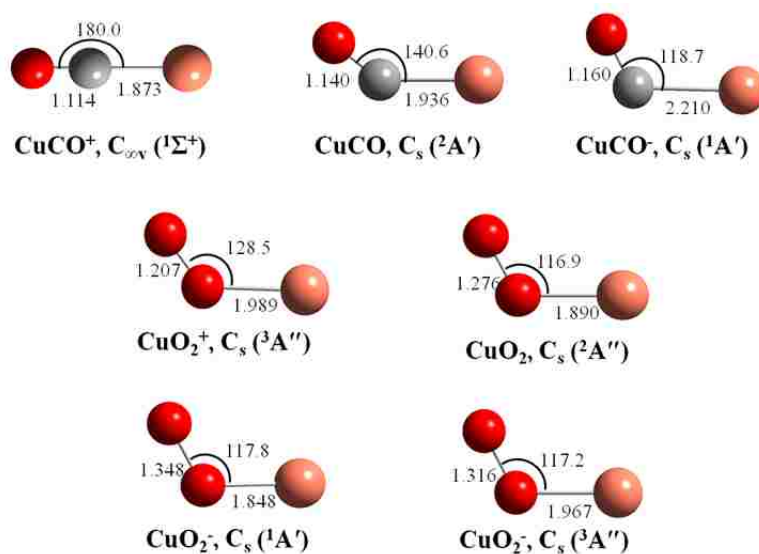


Figure 6.1 B3LYP predicted structures, bond lengths (Å), and angles (°) for [CuCO]^q and [CuO₂]^q (q=+1, 0, -1) binary complexes.

O_2^- . There are two CuO_2^- complexes, which differ with respect to spin multiplicity, a singlet and triplet; the triplet is lower in energy at -15.81 kcal/mol. The CuO_2^- triplet has an angle of 117.2° with a 1.316 Å OO bond, which is slightly shorter than O_2^- , and a red-shifted OO frequency at 1151 cm^{-1} . The CuO_2^- singlet complex, at -4.77 kcal/mol, has a bent angle of 117.8° , and OO bond of 1.348 Å with an OO frequency of 1021 cm^{-1} that is red shifted from the O_2^- frequency by 160 cm^{-1} . The CuO bond of 1.848 Å is shorter than the triplet CuO bond by 0.119 Å. A trend of decreasing CuO and increasing OO bond lengths as a function of more negative charge can be seen along with concomitant increase in CuO and decrease in OO frequencies; a similar trend previously has been discussed with respect to the O_2+Au^q+CO system in Chapter 3. For completeness, the insertion structures, $OCuO^q$, were calculated across all charge states, but only the anionic complexes (singlet and triplet spin states) were found to be stable with respect to the reactant asymptote of Cu^q and O_2 . In both spin states, the insertion complex is lower in energy than CuO_2^- complex, and the triplet $OCuO^-$ complex has the lowest overall energy of -49.23 kcal/mol.

Ternary Complexes, O_2+Cu^q+CO : When both CO and O_2 are bound to Cu^q , two types of structures can be identified: the separated complex of O_2CuCO^q with O_2 and CO bonded to opposite sides of Cu^q , and the “pre-reactive” complex of $[CuCOO_2]^q$, where CO and O_2 are covalently bound and suggests an incipient reaction between CO and O_2 . A straightforward way to assess cooperative effects associated with having both CO and O_2 present in the ternary complexes is to define a cooperativity of binding, ΔE_{coop} , as the difference between the total binding energy of the ternary complex, and the summed binding energies of the component binary complexes. For example, the calculation for

this cationic ternary complex is: $\Delta E_{\text{coop}} = E_{\text{bind}}[\text{O}_2\text{CuCO}^+] - E_{\text{bind}}[\text{CuO}_2^+] - E_{\text{bind}}[\text{CuCO}^+]$.

It should be emphasized that this is not the only way to categorize cooperative effects.

The cationic system has two separated structures, a singlet and triplet, with linear CuCO moieties, similar to the binary CuCO^+ structure, and bent CuOO angles; the triplet is the lower energy state at -53.39 kcal/mol. The triplet complex has a bent CuOO angle of 130.7° with an OO bond of 1.206 Å, which does not change from CuO_2 , while the CuO bond decreases. The CO bond also remains the same as CuCO^+ , while the CuC bond decreases slightly. The CO and CuO frequencies show very small red shifts from the binary values, while the OO and CuC frequencies have blue shifts in the respective frequencies from the binary complex values (Tables 6.1 and 6.2). For the singlet O_2CuCO^+ complex with an energy of -22.80 kcal/mol, the CuOO angle is 121.5° with no change in the O_2 length of 1.206 Å and shortened CuO bond of 0.045 Å to 1.944 Å (from CuO_2^+). The CO bond also remains the same length as in CuCO^+ , while the CuC bond increases slightly. Similar to the triplet state, the singlet has small red shifts in the CO and OO frequencies. The CuC and CuO frequencies blue shift from the binary values, which are in agreement with the bond length changes. The electrostatic potential (ESP) is mapped onto the isodensity surfaces to visualize charge distribution throughout the complexes and are compared across charge and spin states and along the pathways to observe the qualitative changes in charge distributions. The electrostatic potential (ESP) surfaces of both singlet and triplet separated structures show positive character on the Cu atom, which “bleeds” onto the CuC and CuO bonds.

The neutral (doublet) system forms a C_{2v} symmetric O_2CuCO complex at -44.32 kcal/mol, is the global minimum of the neutral “reactant-like” complexes, and has been

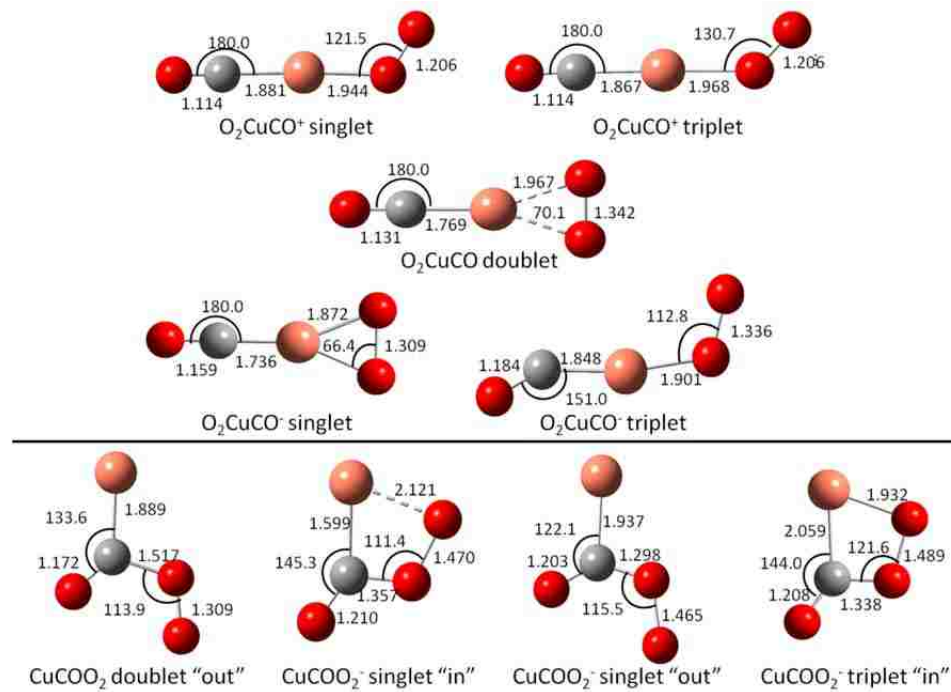


Figure 6.2 B3LYP predicted structures, bond lengths (Å), and angles (°) for $[\text{O}_2\text{CuCO}]^q$ and $[\text{Cu}(\text{CO})\text{O}_2]^q$ ($q=+1,0,-1$) ternary complexes, with designated structural types as “separated” or “pre-reactive” as described in the text.

Table 6.3 ZPE and BSSE corrected binding energies^a (kcal/mol) of [CuCO]^q and [CuO₂]^q and ternary, [O₂CuCO]^q and [CuCOO₂]^q complexes (q=, +1, 0, -1) and cooperative binding evaluated for similarly charged complex groups predicted with B3LYP.

		CuCO	CuO ₂	O ₂ CuCO ^b	Cooperative binding ^{b,c}
Cationic	Singlet	-37.79		-22.80 (-58.93)	+28.72 (-7.41)
	triplet		-13.73	-53.36	-1.84
Neutral	doublet	-7.05	-10.73	-44.32	-26.54
	(out)			-8.86	+8.93
Anionic	singlet	-0.88	-4.77 (-40.90) ^d	-45.31 (-81.45)	-28.61 (-39.66)
	(in)			-38.48 (-74.62)	-21.79 (-32.83)
	(out)			-28.31 (-64.44)	-11.61 (-22.66)
	triplet		-15.81	-35.21	-18.51
Anionic	(in)			-17.58	-0.88

^a Computed relative to optimized values of the *ground state* fragments, with charge (if any) localized on gold center.

^b Parenthetical values computed relative to the energy of O₂ singlet, as shown here: [E_{CuOO} - (E_{Cu} + E_{OOsinglet})] or [E_{OOCuCO} - (E_{Cu} + E_{CO} + E_{OOsinglet})].

^c Cooperative binding is calculated as the difference between total binding energy of ternary complex and summed binary complexes as shown here: E_{OOCuCO} - E_{CuOO} - E_{CuCO}. The CuO₂ energy used in cooperative binding is the ground state triplet. Parenthetical cooperative binding values are calculated in the same fashion, but utilize the parenthetical values of the binary and ternary singlet complexes, where applicable.

^d [CuO₂]⁻ singlet was calculated as restricted (closed shell) due to high spin contamination in the unrestricted singlet calculation.

previously identified.¹⁹ This symmetric structure also contains a linear CuCO moiety, which is reminiscent of the CuCO⁺ structure. The CO bond decreases slightly and remains similar to free CO, while the CuC bond decreases significantly. The OO bond increases to 1.342 Å, which is most similar to superoxide (O₂⁻) and the CuO bond also increases with a CuOO angle of 70.1°. The CuC and CO frequencies blue shift with respect to the CuCO complex by 202 cm⁻¹ and 138 cm⁻¹ (to 2188 cm⁻¹), respectively. Comparatively, the CuO and OO frequencies have small red shifts (Tables 6.1 and 6.2). The ESP surface has negative character on the O₂ moiety and positive character across the CuCO moiety (Figure A6.2 in Appendix A6).

The anionic system, like the cationic, has a separated [O₂CuCO]⁻ species in each spin state (singlet and triplet), where the anionic singlet has a lower energy of -45.31 kcal/mol. The anionic singlet complex has a linear CuCO moiety, reminiscent of CuCO⁺, and bent CuOO angle. Similar to the Au system and the neutral O₂CuCO structure, the anionic singlet structure has C_{2v} symmetry with a CuOO angle of 66.4°. The CO bond length remains the same as the binary complex, while the CuC bond decreases significantly. The OO bond decreases slightly from singlet binary complex and remains similar to superoxide, while the CuO bond increases (Tables 6.1 & 6.2). The CuC, CuO, and CO frequencies have blue shifts of varying degrees for their respective binary values, while the OO frequency red shifts significantly to 830 cm⁻¹, which is ~130 cm⁻¹ to the blue of O₂²⁻. The ESP surface, like the neutral, has negative character on the O₂ moiety, which is stronger in intensity of color and indicates that more charge is localized on the OO bond, and positive character on CO.

The anionic triplet complex resides at -35.21 kcal/mol with a CuOO angle of 112.8° and CuCO angle of 151.0°, similar to the O₂AuCO⁻ triplet structure (Chapter 3). The CuC bond decreases greatly by 0.362 Å from the binary complex; CuO also decreases to a smaller extent, while the CO and OO bonds increase slightly. The CuC, CuO, and OO frequencies blue shift from the respective binary complex values, while the CO frequency red shifts slightly (Tables 6.1 and 6.2). The anionic triplet ESP surface has a relatively well distributed negative charge, where there is slightly more negative character on O₂ than CuCO, but much less than the anionic singlet surface.

Across the charge states, trends can be identified in the bond lengths and frequencies of the separated complexes. With increasing negative charge, the CuC and CuO bond lengths decrease, except in the anionic triplet, and there are also concomitant increases in the CuC and CuO frequencies. The CO and OO bond lengths increase with increasing negative charge, except in the anionic triplet, and there are also concomitant decreases in the CO and OO stretching frequencies.

Pre-reactive complexes, which suggest an incipient reaction between CO and O₂, are observed in the neutral and anionic charge states and are described by the CuCOO dihedral angles (Figure 6.2). A dihedral angle of 0° for CuCOO is called the “pre-reactive in” complex and a dihedral of 180° is called “pre-reactive out.” The neutral system has one pre-reactive structure, which is the “out” structure and resides at -8.86 kcal/mol. Compared to the separated complex, the CuC and CO bonds increase; an intermolecular OC bond forms at 1.517 Å and the OO bond decreases slightly. The CuC frequency blue shifts by 287 cm⁻¹, while both CO and OO frequencies red shift from the separated complex values, which are in agreement with the bond lengths (Tables 6.1 and

6.2). The ESP surface has strong positive character on the Cu atom with negative character distributed across the OCOO moiety.

The anionic singlet state has both pre-reactive “in” and “out” complexes, which are at -38.48 and -28.31 kcal/mol, respectively, and higher in energy than the separated complex. When comparing the pre-reactive in structure to the separated species, the CuC bond decreases by 0.338 Å, and a new O-C bond forms at 1.357 Å, while the CO bond increases to 1.210 Å, which is ~0.02 Å longer than CO⁻. The CuO bond increases significantly and OO increases by 0.161 Å to 1.470 Å, which is most similar to peroxide length. The CuC frequency red shifts significantly by 300 cm⁻¹ and the CO frequency also red shifts to 1698 cm⁻¹, which is similar to CO⁻. The OO frequency blue shifts to 880 cm⁻¹ and remains similar to O₂²⁻. The ESP surface of the “in” complex has positive character on the Cu atom, negative character on the O₂ moiety, and slight negative character on CO (Figure 6.6). The pre-reactive “out” complex is a rotamer of the “in” structure and 10 kcal/mol higher in energy than the “in” structure, where the CuO bond is broken with the rotation of the CuCOO dihedral. The CuC bond increases significantly, while both CO bonds decrease slightly; the OO bond also decreases to 1.465 Å, which is between superoxide and peroxide lengths. The CuC frequency does not change, while the CO frequency blue shifts slightly to 1727 cm⁻¹, remaining similar to CO⁻, and the second CO frequency blue shifts slightly. The OO frequency red shifts to 745 cm⁻¹, which is similar to O₂²⁻. The “out” complex has very strong negative charge on the “dangling” O atom and strong positive character on the Cu atom.

The anionic triplet pre-reactive “in” complex is the only pre-reactive complex stable with respect to the reactants with an energy of -17.58 kcal/mol. Compared to the

separated structure, the CuC, CuO, OO, and CO bonds increase, as the intermolecular CO bond is formed, where the OO bond is most similar to peroxide. The CuC and CO frequencies red shift, while the CO frequency remains similar to CO^- . The CuO frequency blue shifts, while the OO frequency red shifts to 879 cm^{-1} , similar to O_2^{2-} . Similar to Sep, the ESP surface shows a well distributed charge across the “in” surface with slightly more negative character on O_2 (Figure A6.4 in Appendix A6).

6.3.2 O_2 Pathways: The aforementioned separated and pre-reactive complexes are the “reactant-side” complexes for building pathways from the O_2 , Cu^q , and CO reactants to the products of OCu^q and CO_2 (Figures 6.3-6.5 and Figure A6.1 in Appendix A6). As mentioned above, the neutral and anionic singlet and triplet charge states both have reaction pathways that are based on the similar pre-reactive isomers and the likeness continues through the reaction pathways, which can be discussed in a general overview. The separated minimum (Sep) can be formed from the separated reactants of $\text{O}_2 + \text{Cu}^q + \text{CO}$ with strong charge transfer into the O_2 moiety and induced positive character on CO. The pathway continues to the pre-reactive isomers with a large alteration of structure and ESP surface, where an OCOO π -conjugated system is formed with a large change in the charge transfer of the complex, in which positive character is found on Cu and negative character is spread across the conjugated system. The pre-reactive isomers, in and out, lead to two different “major” transition states along different pathways, where the pre-reactive “in” minimum continues along the “In” pathway (to In-TS) and “out” minimum continues along the “Out” pathway (Out-TS). The two “major” transition states do retain similar structures to the pre-reactive isomers and both pathways involve elongation of the OO bond, but this leads to different outcomes. Elongation of

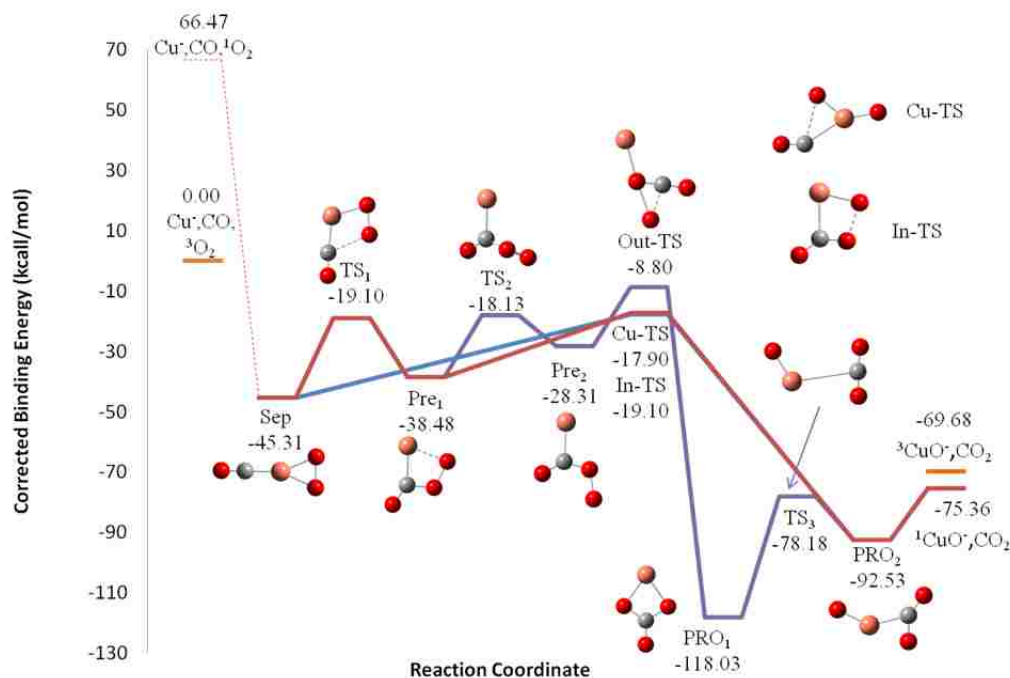


Figure 6.3 The reaction pathway(s) for the anionic singlet state is shown for Cu atoms, CO and O₂, where all pathways originate with the C_{2v} separated minimum (Sep). The red line shows the O₂ “in” oxidation pathway and the blue line represents the CuO pathway. The purple pathway represents the “Out” pathway.

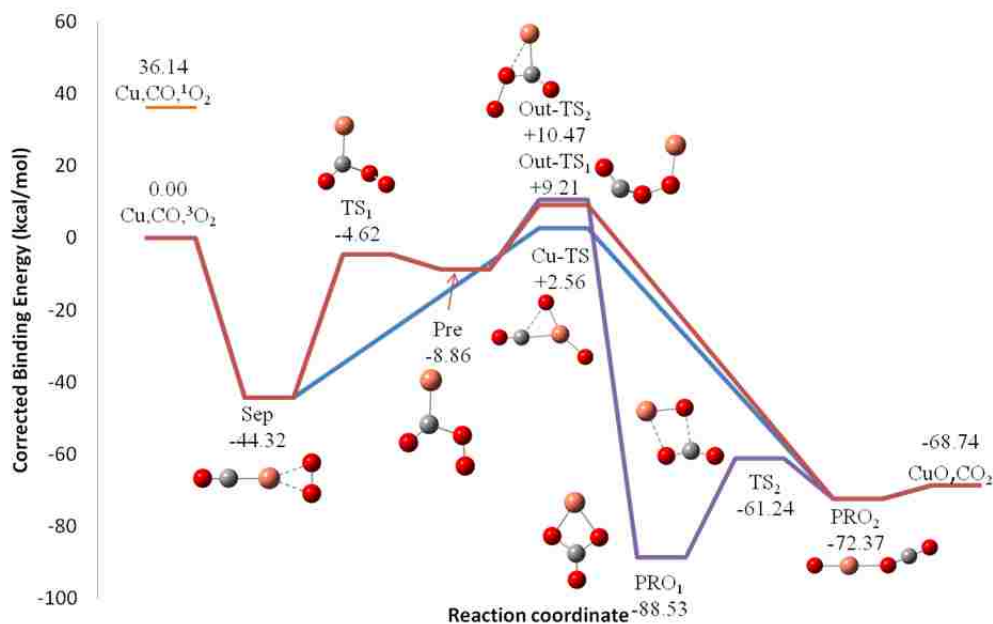


Figure 6.4 The reaction pathway(s) for the neutral doublet state is shown for Cu atoms, CO and O₂, where all pathways originate with the C_{2v} separated minimum (Sep). The red line shows the O₂ out oxidation pathway. The purple pathway shows the second “Out” pathway that leads to formation of CuCO₃. The blue line represents the CuO pathway.

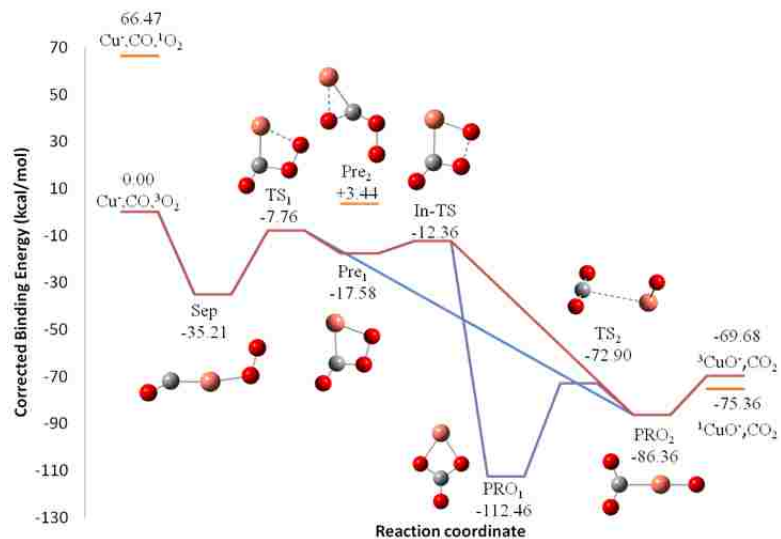


Figure 6.5 The reaction pathway(s) for the anionic triplet state is shown for Cu atoms, CO and O₂, where all pathways originate with the separated minimum (Sep). The red line shows the O₂ out oxidation pathway. The purple pathway moves from In-TS to form the lower energy product complex, PRO₁. The blue line shows the formation of PRO₂ from TS₁.

Table 6.4 Bond lengths (in Å) of reactant-side transition state complexes, q=(+1,0,-1), calculated with B3LYP-SDD/6-311+G(3df).

Separated-to-pre-reactive transition states						
Charge	Spin	Name	Cu-C bond	C-O bond	Cu-O bond	O-O bond
Neutral	Doublet	TS ₁	1.885	1.169 1.561		1.307
Anionic singlet	Singlet	TS ₁	1.833	1.146 2.277	1.878	1.480
Anionic	Triplet	TS ₁	2.034	1.192 1.509	2.202	1.367
Pre-reactive in-to-out transition state						
Anionic	Singlet	TS ₂	1.937	1.199 1.321		1.489

the OO bond in the In-TS transition state can easily be observed as splitting open the complex to form OCuCO_2^q ; however elongation of the OO bond in Out-TS transition state shows inclination to form a carbonate-like product, which occurs. However, the Out pathway does not end at the carbonate-like minimum; this complex is more likely to rearrange to OCuCO_2^q than CO_3 to “desorb” from Cu, as OCuCO_2^q is lower in energy than the separated Cu, CO_3^q products.

Another pathway can be found in all charge states, except the anionic triplet, in which the Cu^q atom inserts into the OO bond to form an O(O)CuCO^q transition state, which leads directly to the formation of the OCuCO_2^q product. Details related to the changes in structures (Tables 6.4, 6.6, 6.8, and 6.10), vibrational frequencies (Tables 6.5, 6.7, 6.9, and 6.11) and ESP surfaces (Figure 6.6) will be discussed for the anionic singlet pathway descriptions; the major differences between “other” charge states and the anionic singlet pathways will be described after the anionic singlet descriptions.

In O_2 Oxidation Pathway: The O_2 oxidation pathways start with the formation of the O_2CuCO^- separated complex. From Sep, the TS_1 transition state involves rotation of O_2 around Cu to form a long O-C bond with a barrier of 26.21 kcal/mol from the separated species. The CuC, CuO, and OO bonds increase with related red shifts in the frequencies, except CuO blue shifts very slightly (Table 6.4). The CO bond decreases slightly with an accompanying blue shift and the CuCO angle remains close to linear at 174.9° (Table 6.5). The ESP surface shows retention of strong negative character on the O_2 moiety and positive character on CuCO. The intermolecular OC bond shortens and forms the pre-reactive “in (Pre_1) complex, described above. From the Pre_1 minimum, the OO bond can further elongate with 19.38 kcal/mol, which corresponds to In-TS, the

energetically favorable pathway. In the formation of In-TS, the CuC and OO bonds elongate significantly where OO is longer than the peroxide length. The CO bond length increases slightly, while the second CO bond and CuO bond shorten more significantly with blue shifts in both CO frequencies. The ESP surface shows some positive character on Cu, negative character on O₂, and relatively no charge on CO (Figure A6.3 in Appendix A6). The desired OCuCO₂ product can be formed from the “in” O₂ oxidation transition state (In-TS), and resides at -92.53 kcal/mol. From In-TS, the CuC, CuO, and CO bond decrease with accompany blue shifts in the CuC and CuO frequencies, while the “newer” CO bond increases slightly and forms symmetric and anti-symmetric CO₂ frequencies. The structure involves a bent CO₂ moiety that is bonded to Cu through a CuC bond. The ESP surface has slight negative character on the O atom and the rest of the complex (CuCO₂) is relatively neutral.

Out O₂ Oxidation Pathway: By surmounting a rotational barrier of 20.35 kcal/mol from Pre₁, the pre-reactive “out” (Pre₂) complex is formed, where both pre-reactive complexes were described above. From Pre₂ and with 19.51 kcal/mol of energy, the OO bond elongates and a third CO bond forms, where this transition state is identified as Out-TS. A long CuO bond forms of 2.072 Å, as does a third CO bond of 1.757 Å. The CuC and OO bonds increase significantly with an accompany red shift in frequency. Both CO bonds decreases slightly and form symmetric and anti-symmetric CO₂ frequencies (Tables 6.6 and 6.7). The ESP surface has positive character on the Cu atom and negative character on the “dangling” O atom, while CO₂ is relatively neutral (Figure 6.6). PRO₁, the carbonate-like CuCO₃ complex, is formed from the “out” O₂ oxidation transition state and is the global minimum of the product complexes. From Out-TS, the

Cu-C bond is broken, the Cu-O bond decreases and a second, symmetric Cu-O bond forms at 1.979 Å with related O-Cu-O frequencies (Tables 6.10 and 6.11). Two C-O bonds increase significantly and retain the CO₂ symmetric and anti-symmetric frequencies, while the third C-O bond decreases significantly. The anionic singlet ESP surface has strong negative character on the CO₃ moiety and strong positive character on the Cu atom. Even though the PRO₁ minimum is the energetically favorable product, the desired product, OCuCO₂, can be formed over a barrier of 39.85 kcal/mol (TS₃), where Cu-O and C-O bonds are cleaved Cu-O rotates away from CO₂ (Tables 6.8 and 6.9). The Cu-C bond reforms; the remaining C-O and Cu-O bonds shorten with blue shifts in the CO₂ frequencies. The ESP surface shows a strong negative character on the O atom and positive character on CO₂.

CuO Oxidation Pathway: With 27.41 kcal/mol, Cu inserts into the O-O bond of the Sep complex to form the O(O)CuCO⁻ (Cu-TS) transition state, which is reminiscent of the AuO oxidation pathway in the O₃AuCO systems. The Cu-C and Cu-O bonds increase by varying amounts with formation of O-Cu-O symmetric and anti-symmetric frequencies, while the C-O bond decreases slightly with a related blue shift in the frequency, and a long C-O bond of 2.412 Å forms (Tables 6.6 and 6.7). The ESP surface has strong negative character on the O-Cu-O moiety and positive character on CO. From the Cu-TS transition state, the OCuCO₂ product is formed.

Other Charge States' In Pathway: The anionic triplet TS₁ transition state (27.45 kcal/mol above Sep) has a shorter intermolecular C-O bond than the anionic singlet (Figure 6.5; Table 6.4). In the anionic triplet system, it was also observed that this transition state (TS₁) can lead directly to the formation of product, since all other minima

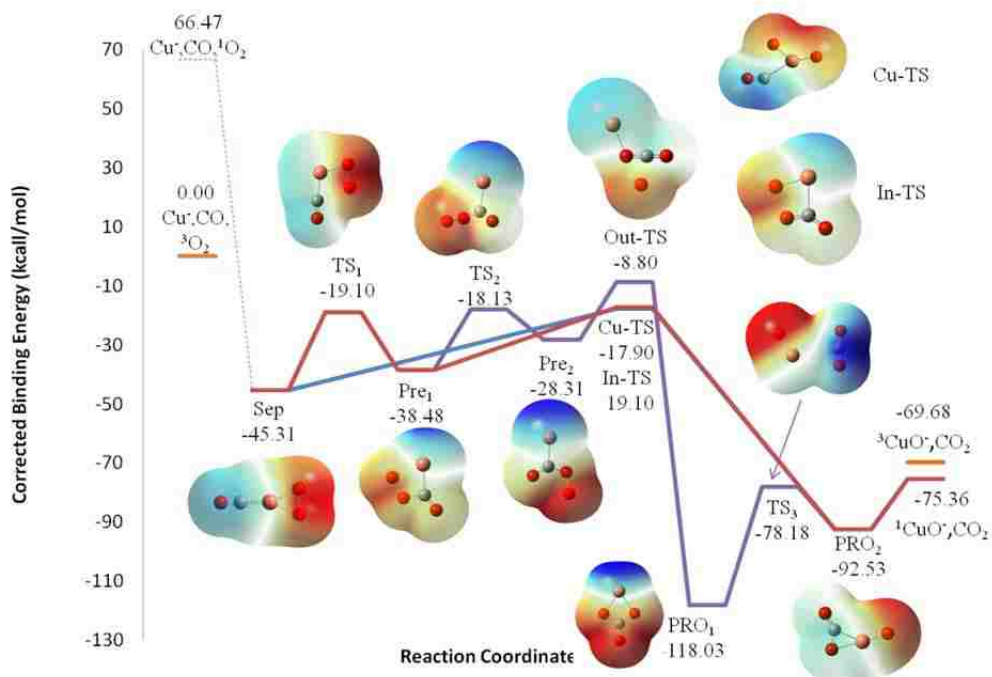


Figure 6.6. The reaction pathway(s) for the anionic singlet $[\text{O}_2+\text{Cu}+\text{CO}]^-$ is shown for, where each position is now represented by the respective electrostatic potential (ESP) mapped on to the total electron density isosurface (density = 0.0004). The color map spans a range of 0.1 with red (blue) as most negative (positive) from -0.05 to +0.05.

and barriers are lower in energy than TS₁. The ESP surface shows a well distributed charge with no “hot spots” of positive or negative character (Figure A6.3 in Appendix A6).

The anionic triplet system, which is the only other to have a pre-reactive “in” complex, has a similar In-TS transition state with elongation of the OO bond to 1.929 Å (Table 6.6). This transition state resides at 5.22 kcal/mol above Pre. The ESP surface has more charge localization than Sep, TS₁ and Pre, where there is slight positive character on Cu and more negative character on O₂. The neutral system has an In-TS-like transition state that is formed from the “out” minimum, which is Out-TS₁ and can be reached with 18.07 kcal/mol. The structure has a CuOOCO structure with connectivity through an “end” O atom, where the CuC bond is broken and a new CuO bond is formed. The OO and CO bonds increase, while the second CO bond decreases with red shifts in the OO and 2nd CO frequencies and blue shift in the “first” CO frequency (Tables 6.6 and 6.7). The ESP surface has strong positive character on the Cu atom and negative character is distributed across the OOCO moiety (Figure A6.2 in Appendix A6).

Like the anionic singlet, the anionic triplet OCuCO₂⁻ (Pro₂) complex has CO₂ bound to Cu through a CuC bond and a bent CO₂ moiety. The CO₂ bonds are symmetric at 1.225 Å and the ESP surface shows a well distributed charge with slightly more negative character on the O atom (Tables 6.10 and 6.11; Figure A6.3 in Appendix A6). In the neutral OCuCO₂ product, the CO₂ moiety is (nearly) linear at 178.8° and connected to Cu through a CuO bond with CO₂ bonds and frequencies similar to CO₂. The ESP surface shows strong positive character on CO₂ and negative character on the O atom.

Table 6.5 Vibrational frequencies (in cm^{-1}) of the reactant-side transition state of $[\text{O}_2+\text{Cu}+\text{CO}]q^a$ complexes, $q=(+1,0,-1)$, calculated with B3LYP-SDD/6-311+G(3df).

Charge	Spin	Name	Cu-C	C-O	Cu-O	O-O
Separated-to-pre-reactive transition states						
Neutral	Doublet	TS ₁	702	1902 386		1172
Anionic singlet	Singlet	TS ₁	399	2048	480	793
Anionic	Triplet	TS ₁	237	1788	145	991
Pre-reactive in-to-out transition state						
Anionic	Singlet	TS ₂	289	1737		762

Table 6.6 Bond lengths (in Å) for CuO oxidation and O₂ oxidation transition state complexes, $\{\text{CuCOO}_3\}^q$ $q=(+1,0,-1)$, calculated with B3LYP-SDD/6-311+G(3df).

{CuCOO ₂ } transition state							
Charge	Spin	Name	Cu-C bond	C-O bond	Cu-O bond	O-O bond	
Cationic	Singlet	Cu-TS		1.110	1.636		
				2.801	1.679		
Neutral	Triplet	Cu-TS		1.112	1.727		
				2.152	1.793		
	Doublet	Cu-TS		1.121	1.793		
				2.197	1.737		
	Out-TS ₁		1.177	1.828	1.463		
	Out-TS ₂	1.969	1.181	2.374	1.741		
Anionic	Singlet	Cu-TS		1.140	1.713		
				2.412	1.672		
			In-TS	2.152	1.219	1.920	1.884
	Triplet	Out-TS		2.787	1.180	2.072	1.929
					1.239		
					1.757		
	In-TS	2.054	1.211	1.843	1.713		
			1.321				

Table 6.7 Vibrational frequencies (in cm^{-1}) for CuO oxidation and O_2 oxidation transition state complexes (from pre-reactive complexes), $\{\text{CuCOO}_3\}^q$ $q=(+1,0,-1)$, calculated with B3LYP-SDD/6-311+G(3df).

Charge	Spin	Name	CuC	CO	CuO	OO	CO ₂ sym	CO ₂ anti	OCuO sym	OCuO anti
Cationic	Singlet	Cu-TS	294	2350	819					
					697					
	Triplet	Cu-TS	299	2319	466					
					656					
Neutral	Doublet	Cu-TS	256	2236					534	646
		Out-TS ₁	274	1845	524	820				
		Out-TS ₂	276	1893						
				1075						
Anionic	Singlet	Cu-TS		2075					684	799
		In-TS	159	1711	456					
				1085						
			Out-TS			206	457	1113	2048	
						573				
	Triplet	In-TS	217	1671	551					
				1063						

Table 6.8 Bond lengths (in Å) for post-reactive transition state, $\{\text{OCuO-CO}\}^q$, complexes, $q=(+1,0,-1)$, calculated with B3LYP-SDD/6-311+G(3df).

Charge	Spin	Name	Cu-C bond	C-O bond	Cu-O ^a bond	O-O bond
Neutral	Doublet	TS ₂		1.161	2.252	
					1.200	1.762
					2.001	
Anionic	Singlet	TS ₃	3.144	1.159	3.217	
					1.165	1.688
		Triplet	TS ₂	3.427	1.162	1.834
				1.162		

^a CuOCO bond length is listed first and CuO₂ bond length is second.

Table 6.9 Vibrational frequencies (in cm^{-1}) for post-reactive transition states, $\{\text{O}_2\text{OCuCO}\}^q$, $q=(+1,0,-1)$, calculated with B3LYP-SDD/6-311+G(3df).

Charge	Spin	Name	CuC	CO	CuO	CO ₂ sym	CO ₂ anti sym
Neutral	Doublet	TS ₂		111	581	1259	2212
Anionic	Singlet	TS ₃	43		711	1348	2375
	Triplet	TS ₂	44		522	1352	2382

Table 6.10 Bond lengths (in Å) for the product, $[\text{CuCO}_3]_q$ or $[\text{OCuCO}_2]_q$, complexes, $q=(+1,0,-1)$, calculated with B3LYP-SDD/6-311+G(3df).

Charge	Spin	Name	Cu-C bond	C-O ^a bond	Cu-O ^b bond
Cationic	Singlet	¹ PRO ⁺		1.135	1.899
				1.180	1.689
Neutral	Triplet	³ PRO ⁺		1.137	1.907
				1.178	1.731
	Doublet	² PRO ₁ ⁰		1.205	1.905
				1.329	1.905
Anionic	Singlet	² PRO ₂ ⁰		1.149	1.974
				1.165	1.739
		¹ PRO ₁ ⁻		1.236	1.979
				1.336	1.979
	Triplet	¹ PRO ₂ ⁻	1.919	1.194	1.672
				1.246	
		³ PRO ₁ ⁻		1.223	1.958
				1.324	1.958
	³ PRO ₂ ⁻	2.056	1.225	1.784	
			1.225		
Reference lengths ^{c,d}	C-O	1.124	CO ₂	1.159	
	C-O ⁺	1.108	CO ₂ ⁺	1.170	
	C-O ⁻	1.183	CO ₂ ⁻	1.227	

^a Exterior CO bond is listed first and interior (attached to Cu) CO bond is second.

^b CuOCO bond length is listed first and CuO₂ bond length is second.

^c Reference lengths are calculated at the same level of theory: B3LYP-SDD/6-311+G(3df).

^d Only one bond length is shown for O₂^q, O₃^q and CO₂, as these molecules are symmetric and both bonds are same length.

Table 6.11 Vibrational frequencies (in cm^{-1}) of the products, $[\text{O}_2\text{CuCO}_2]^q$ ($q=+1,0,-1$), calculated with B3LYP-SDD/6-311+G(3df).

Charge	Spin	Name	CuC	CO	CO ₂ sym	CO ₂ anti	CuO ^a	OCuO sym	OCuO anti
Cationic	Singlet	¹ PRO ⁺			1407	2471	296 729		
	Triplet	³ PRO ⁺			1409	2475	287 624		
Neutral	Doublet	² PRO ₁ ⁰		1636	964	1142		353	238
		² PRO ₂ ⁰			1390	2449	237 628		
Anionic	Singlet	¹ PRO ₁ ⁻		1614	978	1130		353	238
		¹ PRO ₂ ⁻	362		1188	1917	799		
	Triplet	³ PRO ₁ ⁻		1670	1002	1196		335	295
		³ PRO ₂ ⁻	219		1256	1760	534		
Reference frequencies			CO		CO ₂ sym	1374	CO ₂ anti	2414	
			CO+		CO ₂ ⁺ sym	1315	CO ₂ ⁺ anti	1483	
			CO-		CO ₂ ⁻ sym	1218	CO ₂ ⁻ anti	1770	

^a CuO(CO) vibrational frequency is listed first and CuO(O) is second.

^b Reference frequencies are calculated at the same level of theory: B3LYP-SDD/6-311+G(3df).

Other Charge States' Out Pathway: With 39.70 kcal/mol, the neutral TS₁ transition state can be reached from the separated species. The neutral TS₁ complex involves rotation of the OO molecule around Cu to interact with CO and breaks the Cu-O bond, as the CuCOO dihedral rotates to ~ 90° (Table 6.4). This transition state looks more like TS₂ of the anionic singlet pathway, as it bridges the gap between the separated and pre-reactive “out” minima. The neutral ESP surface has strong positive character on the Cu atom and negative character across the OCOO moiety (Figure A6.2 in Appendix A6). This transition state leads to the formation of the pre-reactive “out” complex (Pre). The neutral system forms an “out” O₂ oxidation transition state (Out-TS₂) from the pre-reactive “out” (Pre) complex with a barrier of 19.33 kcal/mol, where the structure is generally similar to the anionic singlet Out-TS (Tables 6.6 and 6.7). The ESP surface shows strong positive character on the Cu atom and negative character spread across the OCOO moiety, similar to Pre.

The CuCO₃⁻ minimum can be formed in the anionic triplet system from In-TS (“in” O₂ oxidation transition state), while the carbonate-like structure is formed from the Out-TS₂ transition state in the neutral system. PRO₁ looks similar in all three charge states, where C_{2v} symmetric structures are formed with two equidistant CuO and CO bonds, with one “dangling” CO bond (Tables 6.10 and 6.11). The neutral ESP surface is somewhat similar with strong positive character on Cu, but the negative character is more localized on the dangling O atom (Figure A6.2 in Appendix A6). The anionic triplet ESP surface is very different from the other two, where there is slight negative character on the CO₃ moiety and slight positive on Cu; in general, the anionic triplet ESP surfaces have (relatively) well distributed charges (Figure A6.3 in Appendix A6).

The neutral and anionic triplet systems also have similar transition states between Pro₁ and Pro₂, which are TS₂ in the neutral and anionic triplet systems. These structures are similar to the anionic singlet, but have variation in the angle of rotation of CuO away from CO₂ and the anionic triplet also has a non-planar structure (Tables 6.8 and 6.9). The neutral ESP surface shows (strong) positive character on Cu and negative character on the separating O atom and O atom of CO₂ further from Cu. The anionic triplet ESP surface has the most localized charges of the entire anionic triplet pathway, where there is clear positive character on CO₂ and negative character on CuO.

CuO Oxidation Pathway: The neutral state also has a CuO oxidation pathway (and transition state, Cu-TS) that has a similar transition state structure to the anionic singlet, but is higher than the reactant asymptote at 2.56 kcal/mol and 46.88 kcal/mol above the Sep complex (Figure 6.3). The Cu-TS transition state is the energetically favorable pathway for the neutral system. The ESP surface has positive character on the CuCO moiety and slight negative character on the two O atoms (Figure A6.2 in Appendix A6).

6.3.3 Ozone, Cu, and CO Interactions

The bond lengths and frequencies are collected into tables for the “reactant side” [O₃CuCO]^q minima (Tables 6.12 and 6.13), O₃ oxidation pathway (Tables 6.14 and 6.15) and CuO oxidation pathway (Table 6.16 and 6.17) transition state, post-reactive minima and transition states (Tables A6.3-A6.6 in Appendix A6), and product (Tables 6.18 and 6.19) complexes. The bond lengths and vibrational frequencies for the reactant-side and post-reactive low barrier transition states are found in the Chapt 6 appendix, Tables A6.1-A6.6. The two types of “reactant side” (separated) minima, [O₃CuCO]^q, can be seen in Figure 6.7, where the main difference is the CuOOO dihedral angle of 0° for “O₃ in” and

180° dihedral for “O₃ out”. Oxygen atoms and their connectivity are discussed in the tables and text with respect to distance from Cu, where O_α is attached to Cu, O_β is next, and O_γ is the third O atom.

Two distinct pathways have been calculated for the [O₃+Cu+CO]^q (q= -1,0,+1) systems, where all charge and spin states display (generally) similar structures and pathways. The pathways diverge after the “O₃ in, reactant-side” minimum (BR₁), continue over two structurally and chemically distinct transition states and end at the same product, [O₂CuCO₂]^q. The first pathway involves rotation of O₃ around the Cu atom to directly interact with CO and form a {CuCOO₃}^q structure with retention of the Cu-O bond and formation of an intermolecular O-C bond. This pathway is called the O₃ oxidation pathway, as Cu catalyzes the direct oxidation of CO by ozone (denoted as O-TS in figures). The other pathway forms the “O₃ out” minimum and then continues to a transition state, which involves decomposition of ozone and oxidation of Cu. This forms CuO and O₂ with a structure of {O₂(O)CuCO}^q (denoted as Cu-TS); subsequently, CO is oxidized by CuO to form the product. This pathway is identified as the CuO oxidation pathway, as CuO oxidizes CO. While these pathways are different, both are below the reactant asymptote (energy of reactants) in most of the charge and spin states; the cationic singlet CuO oxidation pathway is higher than the reactant asymptote. As all charge and spin states have the same general steps and structures along the calculated reaction pathways, the neutral (doublet) O₃ oxidation and CuO oxidation pathways will be discussed (Figure 6.8). The cationic singlet and triplet pathways are shown in the Appendix A6 in Figures A6.4 and 6.5; the anionic singlet pathways, Figure 6.9 of text; anionic triplet, Figure A6.6 in Appendix A6.

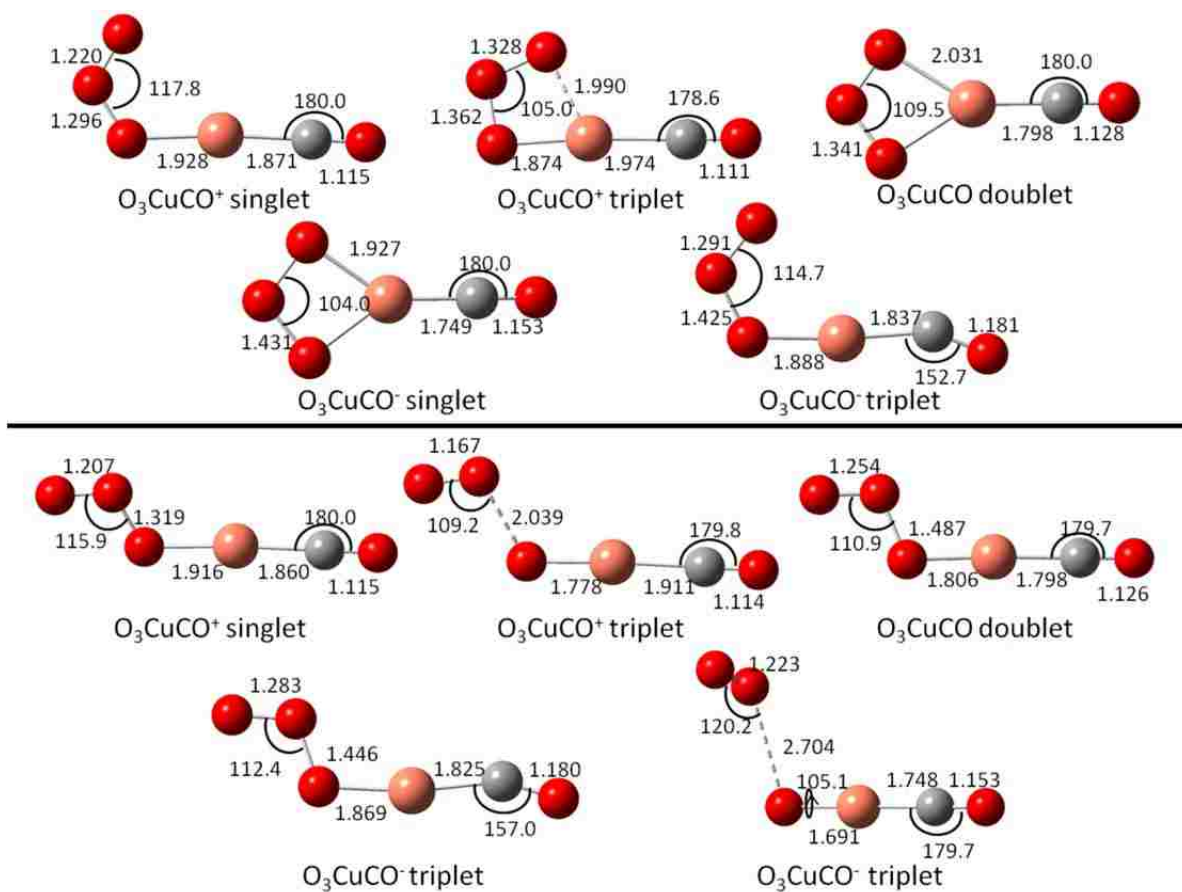


Figure 6.7 The reactant-side complexes (BR) for all charge and spin states (cationic, neutral (doublet) and anionic; singlet and triplet) with the bond lengths (Å) and angles (°) shown in the structures, calculated at B3LYP-SDD/6-311+G(3df).

Table 6.12. Bond lengths (in Å) for ternary, reactant-side $[\text{O}_3\text{CuCO}]^q$ ^a complexes, $q=(+1,0,-1)$, calculated with B3LYP-SDD/6-311+G(3df).

O₃CuCO bonds							
Charge	Spin	Name	Cu-C bond	C-O bond	Cu-O_α bond^b	O_α-O_β bond	O_β-O_γ bond
Cationic	Singlet	¹BR₁⁺	1.871	1.115	1.928	1.296	1.220
		¹ BR ₂ ⁺	1.860	1.115	1.916	1.319	1.207
	Triplet	³ BR ₁ ⁺	1.974	1.111	1.874	1.362	1.328
		³ BR ₂ ⁺	1.911	1.114	1.778	2.039	1.167
Neutral	Doublet	²BR₁⁰	1.798	1.128	2.031	1.341	1.341
		² BR ₂ ⁰	1.798	1.126	1.806	1.487	1.254
Anionic	Singlet	¹ BR ₁ ⁻	1.749	1.153	1.927	1.431	1.431
	Triplet	³ BR ₁ ⁻	1.837	1.181	1.888	1.425	1.291
		³ BR ₂ ⁻	1.825	1.180	1.869	1.446	1.283
		³BR₃⁻	1.748	1.153	1.691	2.704	1.223
Reference lengths^{d,e}		C-O	1.124	O-O (O ₂)	1.203	O-O (O ₃)	1.251
		C-O ⁺	1.108	O-O (O ₂) ⁻	1.341	O-O (O ₃) ⁺	1.227
		C-O ⁻	1.183	O-O (O ₂) ²⁻	1.559	O-O (O ₃) ⁻	1.346

^a O₃ in structure is listed first and O₃ out structure is listed second per charge/spin state.

^b O_α, O_β, and O_γ refer to the order of oxygen atoms, where O_α is the closest to (or attached to) Cu.

^c Lowest energy state of similarly charged complexes are in bold

^d Reference lengths are calculated at the same level of theory: B3LYP-SDD/6-311+G(3df).

^e Only one bond length is shown for reference O₂^q, O₃^q and CO₂, as these molecules are symmetric & both bonds are same length.

Table 6.13. Vibrational frequencies (in cm^{-1}) of ternary^a (reactant side) $[\text{O}_3\text{CuCO}]^q$ ($q=-1,0,+1$) complexes calculated with B3LYP-SDD/6-311+G(3df).

O₃CuCO									
Charge	Spin	Name	Cu-C	C-O	Cu-O	O_αO_β^b	O_βO_γ	O₃ sym	O₃ anti
Cationic	Singlet	¹BR₁⁺	399	2307	323	1064	1348		
		¹ BR ₂ ⁺	402	2305	291	985	1406		
	Triplet	³ BR ₁ ⁺	295	2340	419			1120	742
		³ BR ₂ ⁺	340	2313	545	358	1658		
Neutral	Doublet	²BR₁⁰	481	2205	308			1090	904
		² BR ₂ ⁰	466	2220	748	647	1277		
Anionic	Singlet	¹ BR ₁ ⁻	534	2036	397			894	849
	Triplet	³ BR ₁ ⁻	462	1835	345	738	1173		
		³ BR ₂ ⁻	443	1849	332	580	1198		
		³BR₃⁻	479	2026	783	783	1441		
Reference frequencies^c									
	CO	2217	O-O (O ₂)	1645	O ₃ sym	1265	O ₃ anti	1214	
	CO ⁺	2300	O-O (O ₂) ⁻	1181	O ₃ ⁺ sym	1325	O ₃ ⁺ anti	2400	
	CO ⁻	1665	O-O (O ₂) ²⁻	703	O ₃ ⁻ sym	1068	O ₃ ⁻ anti	896	

^aLowest energy state for species of the same charge and molecular components are in **bold**.

^b O_α, O_β, and O_γ refer to the order of oxygen atoms, where O_α is the closest to (or attached to) Cu.

^c calculated at same level of theory: B3LYP/6-311+G(3df).

O₃ Oxidation Pathway: The reactant-side minima, O₃CuCO, are denoted as BR in the figures for “before reaction, where the “O₃ in” complex (BR₁ in Figure 6.8) is the global reactant-side minimum at -87.92 kcal/mol for the neutral system. The structure is reminiscent of the O₂CuCO separated minima with the C_{2v} symmetric structure and linear CuCO moiety, such that it appears that an additional O atom was inserted into the OO bond of O₂CuCO. The CO bond length is slightly longer than free CO with an accompanying small red shift in the frequency. The symmetric OO bonds are similar to the lengths of O₃⁻, with related OO frequencies (Tables 6.12 and 6.13). For the reactant-side complexes, the ESP surfaces are analyzed to understand how connectivity and orientation affect the charge distributions. The “O₃ in” surface shows strong positive character on CO and negative character on the O₃ moiety, where O_α has slightly more negative character than O_γ (Figure 6.10).

From the BR₁ complex, the red pathway of the neutral O₃ system in Figure 6.8 can continue over a barrier of 37.75 kcal/mol, where the O-TS structure is formed by rotation of O₃ around Cu to form an intermolecular bond between O_γ and carbon. The formation of this transition state and structure is similar to the AuCOO₃ (O-TS) transition state, which was discussed in Chapter 5. From BR₁, the CuC bond increases significantly while the CO and OO bonds increase slightly with a related red shift in the CO frequency and the O₃ symmetry has been broken. The CuO bond remains intact and decreases slightly (Tables 6.14 and 6.15). The ESP surface has positive character on the Cu moiety and the negative charge appears to be well distributed across the OCO₃ moiety.

The product, O_2CuCO_2 , is directly formed the O-TS transition state by shortening of the “newly formed” O-C bond, cleavage of the $O_\beta O_\gamma$ and Cu-C bonds, and rotation of O_2 away from CO_2 (Tables 6.18 and 6.19). Like the O_2AuCO_2 product (Chapter 5), the CO_2 moiety is linear with connection to Cu via one oxygen atom. From O-TS, the CO, OO and CuO bonds shorten by varying amounts, where symmetric and anti-symmetric CO_2 are formed and the O_2 frequency blue shifts to 1157 cm^{-1} . The ESP surface of the neutral product displays positive character on the CO_2 moiety and negative character on the O_2 sub-unit (Figure 6.10).

CuO Oxidation Pathway: From the BR_1 complex, the (O_3 “out”) BR_2 complex with an energy of -81.03 kcal/mol is formed over a small rotational barrier (LB_1), as seen in Figure 6.8. The CuC and CO bond lengths (and frequencies) are similar for both BR complexes, while the CuO and $O_\beta O_\gamma$ shorten slightly with an accompanying blue shift in the OO frequency (Tables 6.12 and 6.13). The $O_\alpha O_\beta$ bond increases slightly to 1.487 \AA with a red shifted OO frequency, where both are similar to O_2^{2-} . The ESP surface of BR_2 is very similar to BR_1 with positive character on CO and negative on O_3 .

From BR_2 , the Cu-TS transition state is formed with 18.25 kcal/mol and is the energetically favored pathway for neutral system. The Cu-TS structure involves a geometry that that looks like the “separated” (planar) O_2CuCO complex with an “extra” oxygen atom bonded to one side of Cu. Similar to the O-TS, the Cu-TS formation and (general) structure are also similar to the Au system discussed in Chapter 5. The CuC and $O_\beta O_\gamma$ bonds increase, while CuO and CO bonds decrease with red shifts in all frequencies, except for a small blue shift in the CO frequency (Tables 6.16 and 6.17). The ESP surface shows positive character on CuCO, negative character on the migrating

O atom and less negative character on the O₂ moiety (Figure 6.10). The product can also be formed from the Cu-TS transition, where the CuC bond is broken. The OO and CuO(CO) bonds increase with a small red shift in the OO frequency, while both CO bonds decrease significantly to form symmetric CO₂ bonds and symmetric and anti-symmetric frequencies.

Other Charge States' O₃ Oxidation Pathway: Like the neutral BR₁ complex, the cationic (singlet and triplet) and anionic singlet reactant-side complexes have linear CuCO angles, while anionic triplet BR₁ has a bent CuCO angle, which is similar to the O₂CuCO^q systems (Figure 6.7; Tables 6.12 and 6.13). Anionic singlet BR₁ has C_{2v} symmetry and is the reactant-side global minimum, like the neutral BR₁ complex and the O₂CuCO⁻ (singlet) complex. The cationic singlet BR₁ complex is also the reactant-side global minimum. Similar to the neutral ESP surface, the anionic singlet ESP surface shows strong positive character on CO and negative character on the O₃ moieties (Figure 6.11). In contrast, the cationic singlet and triplet have positive charge localized on CuC, while anionic triplet ESP surface shows well distributed charge across the entire complex (figures found in the Appendix A6).

The O-TS transition states are below the reactant asymptote for all of the respective charge (and spin) states, where only the cationic triplet structure is planar. Different from the neutral O-TS, the cationic and anionic triplet O-TS transition states form symmetric O₃ moieties (Tables 6.14 and 6.15). Unique to the cationic singlet is a second O-TS transition state with a COOO dihedral of 180°, where there is no longer Cu-O interaction; this species is ~ 9 kcal/mol higher in energy than O-TS₁. The cationic and

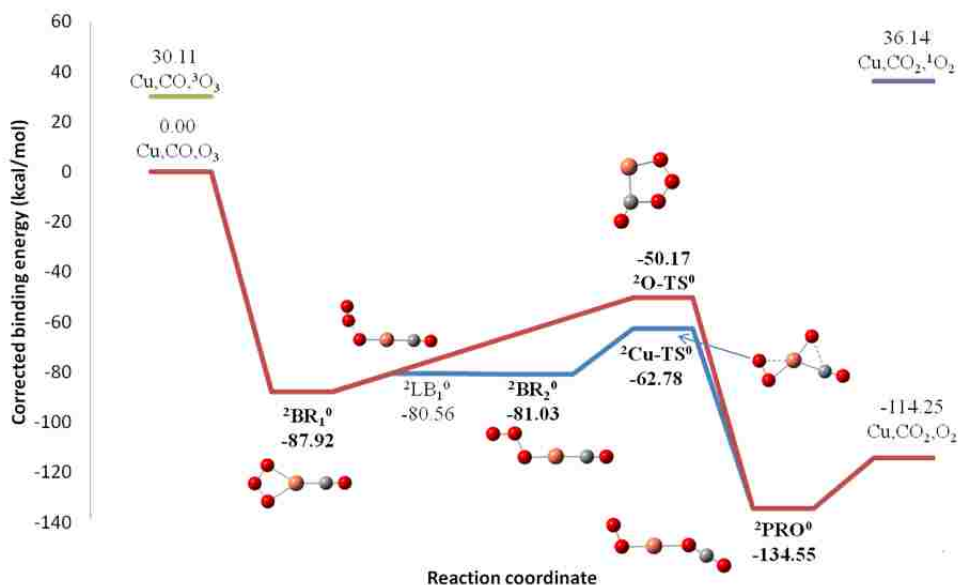


Figure 6.8 The reaction pathway(s) for the neutral doublet state is shown for Cu atom, CO and O₃; both O₃ and CuO oxidation pathways originate from the separated minimum (²BR₁⁰). The solid red line shows the O₃ oxidation process and the solid blue line represents the CuO pathway.

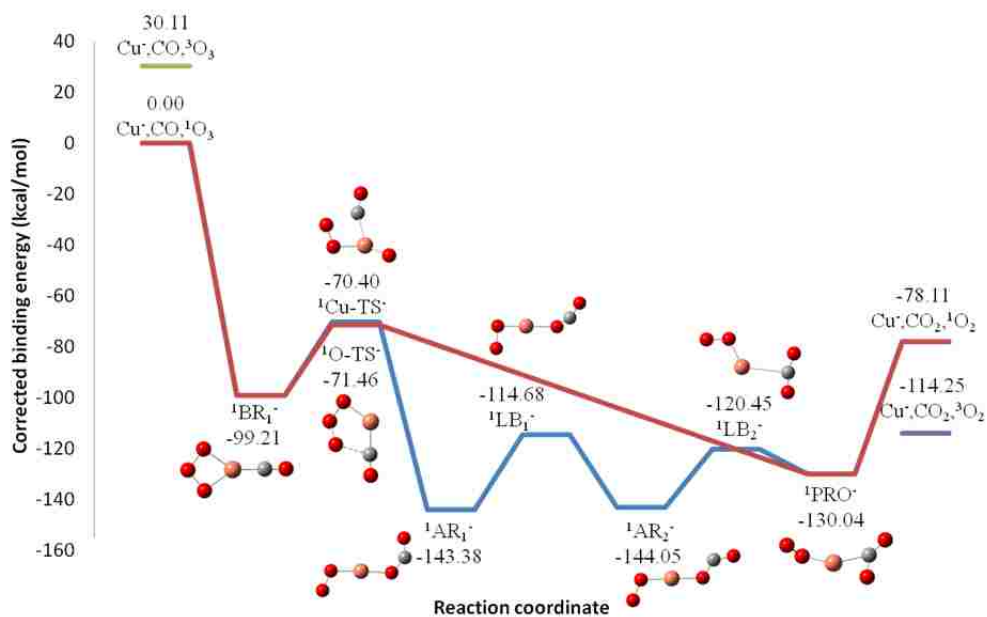


Figure 6.9 The reaction pathway(s) for the anionic singlet state is shown for Cu⁻, CO and O₃, where both pathways originate with the C_{2v} "O₃ in" minimum (¹BR₁⁻). The red line shows the O₃ oxidation pathway and the blue line represents the CuO pathway.

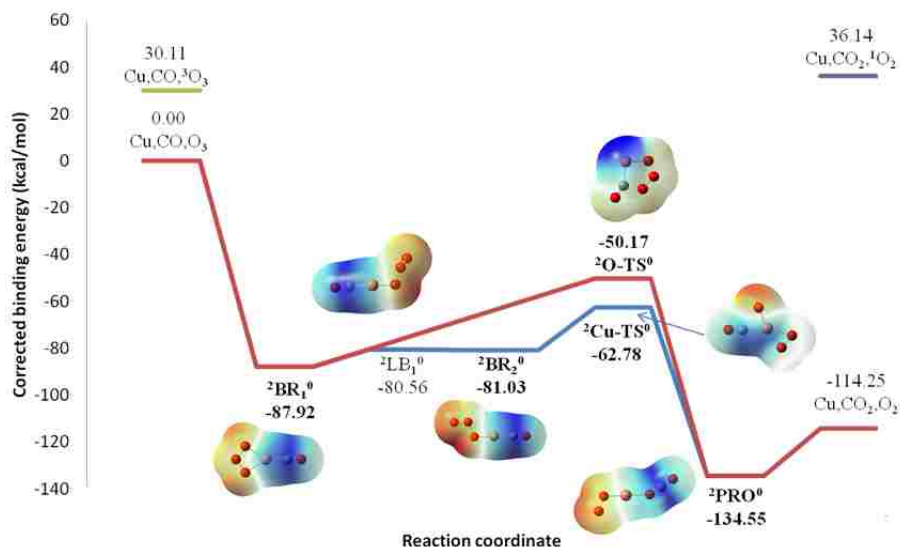


Figure 6.10. The reaction pathway(s) for the neutral doublet state is shown for Cu atom, CO and O₃, where each position is now represented by the respective electrostatic potential (ESP) mapped on to the total electron density isosurface (density = 0.0004). The color map spans a range of 0.1 with red (blue) as most negative (positive) from -0.05 to +0.05. The solid red line shows the O₃ oxidation process and the solid blue line represents the CuO pathway.

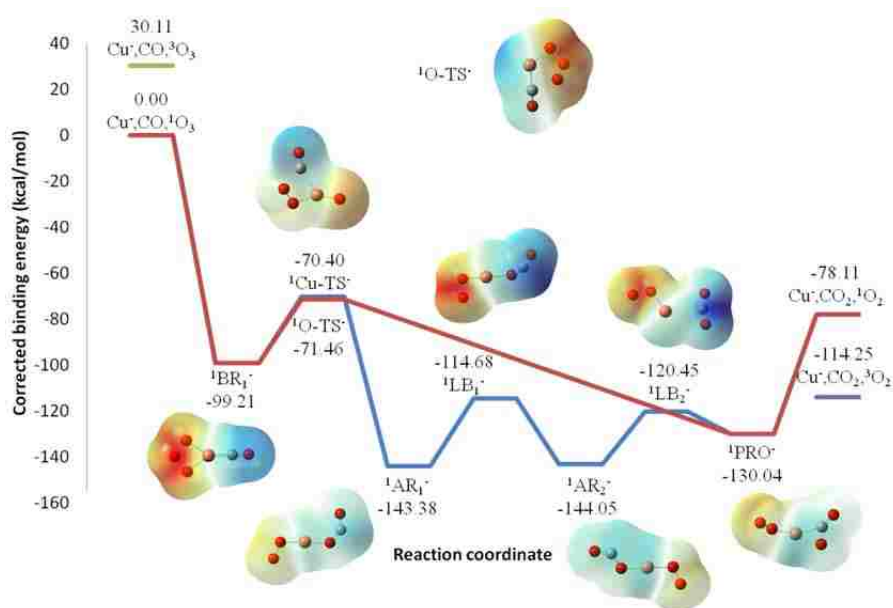


Figure 6.11. Anionic singlet reaction profiles are shown with electrostatic potentials mapped on B3LYP total electron density isosurfaces (density=0.0004) for each complex on the O₃ oxidation (red line) and CuO oxidation (blue line) pathways. The color map spans a range of 0.1 in each case with red (blue) as most negative (positive). The charges for anionic complexes are mapped over -0.20 to -0.10. Note that color intensities are also mapped to the values, such that colors near the ends of the range appear brightest, while those in the center appear transparent.

Table 6.14 Bond lengths (in Å) for O₃ oxidation transition state (O-TS) complexes^a, {CuCOO₃}^q q=(+1,0,-1), calculated with B3LYP-SDD/6-311+G(3df).

{CuCOO₃} O-TS transition state							
Charge	Spin	Name	Cu-C bond	C-O bond	Cu-O_α^b bond	O_α-O_β bond	O_β-O_γ bond
Cationic	Singlet	¹ O-TS ₁ ⁺	2.019	1.151 1.439	1.915	1.295	1.409
		¹ O-TS ₂ ⁺	1.980	1.127 1.439		1.713	1.168
	Triplet	³ O-TS ⁺	1.930	1.131 1.835	1.907	1.329	1.323
Neutral	Doublet	² O-TS ⁰	1.928	1.153 1.728	1.989	1.375	1.346
Anionic	Singlet	¹ O-TS ⁻	1.834	1.159 1.983	1.870	1.496	1.437
	Triplet	³ O-TS ⁻	2.026	1.157 1.867	2.034	1.363	1.372

^a O₃ in structure is listed first and O₃ out structure is listed second per charge/spin state.

^b O_α, O_β, and O_γ refer to the order of oxygen atoms, where O_α is the closest to (or attached to) Cu.

Table 6.15 Vibrational frequencies (in cm⁻¹) for O₃ oxidation transition state (O-TS) complexes, {CuCOO₃}^q q=(+1,0,-1), calculated with B3LYP-SDD/6-311+G(3df).

CuCOO₃									
Charge	Spin	Name	CuC	CO	CuO	O_aO_b^a	O_bO_c	O₃ sym	O₃ anti
Cationic	Singlet	¹ O-TS ₁ ⁺	250	1998	438	1085	820		
		¹ O-TS ₂ ⁺	398	2175		642	1640		
	Triplet	³ O-TS ⁺	467	2152	398			1030	849
Neutral	Doublet	² O-TS ⁰	507	2010	337	843	1009		
Anionic	Singlet	¹ O-TS ⁻	429	1978	485	675	861		
	Triplet	³ O-TS ⁻	471	1957	187			956	837

^a O_α, O_β, and O_γ refer to the order of oxygen atoms, where O_a is the closest to (or attached to) Cu.

^b Reference frequencies were calculated at same level of theory: B3LYP/6-311+G(3df).

Table 6.16 Bond lengths (in Å) for CuO (G-TS) oxidation, $\{O_2(O)CuCO\}^q$ transition state complexes, $q=(+1,0,-1)$, calculated with B3LYP-SDD/6-311+G(3df).

$O_2(O)CuCO$							
Charge	Spin	Name	Cu-C bond	C-O bond	Cu-O_x^{a,b} bond	O_α-O_β bond	O_β-O_γ bond
Cationic	Singlet	¹ Cu-TS ⁺	1.922	1.111	1.674 1.950		1.199
	Triplet	³ Cu-TS ⁺	2.013	1.112	1.768 1.934	2.611	1.210
Neutral	Doublet	² Cu-TS ⁰	1.986	1.220	1.800 1.922 2.074		1.288
Anionic	Singlet	¹ Cu-TS ⁻	2.275	1.159	1.700 1.835		1.330
	Triplet	³ Cu-TS ⁻	1.959	1.143	1.775 1.975		1.304

a O_α, O_β, and O_γ refer to the order of oxygen atoms, where O_α is the closest to (or attached to) Cu.
b CuO_α bond length is listed first and CuO_β bond length is second.

Table 6.17 Vibrational frequencies (in cm⁻¹) for CuO oxidation, $\{O_2OCuCO\}^q$ transition state complexes, $q=(+1,0,-1)$, calculated with B3LYP-SDD/6-311+G(3df).

$O_2(O)CuCO^q$						
Charge	Spin	Name	Cu-C	C-O	Cu-O^a	O-O
Cationic	Singlet	¹ Cu-TS ⁺	343	2334	740 379	1554
	Triplet	³ Cu-TS ⁺	291	2333	559	1463 180
Neutral	Doublet	² Cu-TS ⁰	269	2225	573 395	1243
Anionic	Singlet	¹ Cu-TS ⁻	115	2072	751 506	1079
	Triplet	³ Cu-TS ⁻	291	2047	562 343	1146

^a O_α, O_β, and O_γ refer to the order of oxygen atoms, where O_α is the closest to (or attached to) Cu.

Table 6.18 Bond lengths (in Å) for the product, $[\text{O}_2\text{CuCO}_2]^q$, complexes, $q=(+1,0,-1)$, calculated with B3LYP-SDD/6-311+G(3df).

Products						
Charge	Spin	Name	Cu-C bond	C-O ^a bond	Cu-O ^b bond	O-O bond
Cationic	Singlet	¹ PRO ⁺		1.139 1.175	1.915 1.884	1.210
	Triplet	³ PRO ⁺		1.140 1.175	1.921 1.920	1.210
Neutral	Doublet	² PRO ⁰		1.149 1.168	1.980 1.833	1.320
Anionic	Singlet	¹ PRO ⁻	1.955	1.201 1.261	1.774	1.350
	Triplet	³ PRO ⁻	2.009	1.225 1.225	1.908	1.324
Reference lengths ^{c,d}	C-O	1.124	CO ₂	1.159	O-O (O ₂)	1.203
	C-O ⁺	1.108	CO ₂ ⁺	1.170	O-O (O ₂) ⁻	1.341
	C-O ⁻	1.183	CO ₂ ⁻	1.227	O-O (O ₂) ²⁻	1.559

^a Exterior CO bond is listed first and interior (attached to Cu) CO bond is second.

^b CuOCO bond length is listed first and CuO₂ bond length is second.

^c Reference lengths are calculated at the same level of theory: B3LYP-SDD/6-311+G(3df).

^d Only one bond length is shown for O₂^q, O₃^q and CO₂, as these molecules are symmetric and both bonds are same length.

Table 6.19 Vibrational frequencies (in cm⁻¹) of the products, $[\text{O}_2\text{CuCO}_2]^q$ ($q=+1,0,-1$), calculated with B3LYP-SDD/6-311+G(3df).

Charge	Spin	CuC	CO ₂ sym	CO ₂ anti	CuO ^a	O-O
Cationic	Singlet		1408	2472	298 434	1529
	Triplet		1407	2471	254 370	1568
Neutral	Doublet		1381	2437	550 263	1157
Anionic	Singlet	332	1185	1834	593	1033
	Triplet	247	1249	1760	426	1149
Reference frequencies^b						
	CO ₂ sym	1374	CO ₂ anti	2414	O-O (O ₂)	1645
	CO ₂ ⁺ sym	1315	CO ₂ ⁺ anti	1483	O-O (O ₂) ⁻	1181
	CO ₂ ⁻ sym	1218	CO ₂ ⁻ anti	1770	O-O (O ₂) ²⁻	703

^a CuO(CO) vibrational frequency is listed first and CuO(O) is second.

^b Reference frequencies are calculated at the same level of theory: B3LYP-SDD/6-311+G(3df).

anionic singlet O₃ oxidation pathways are the energetically favorable pathways. The ESP surfaces are generally similar to the neutral, but the anionic singlet ESP surface shows positive character spread across the CuCO moiety and the anionic triplet ESP surface has a well distributed charge across the entire complex (Figures 6.11 for anionic singlet).

The product of other charge states is formed directly from O-TS, like the neutral pathway. The products can be divided and discussed based on connectivity of CO₂ to Cu. The cationic products are similar to the neutral, where the linear OCO moiety is bonding via an oxygen atom (Tables 6.18 and 6.19). The anionic complexes have bent CO₂ moieties, connected to Cu with the carbon atom, and non-planar structures (anionic singlet: CCuOO dihedral of 93.5°; anionic triplet: CCuOO dihedral of 180°). The ESP surfaces show well-distributed charge for cationic and anionic charge states, but anionic singlet has more negative character on O₂.

Other Charge States' CuO Oxidation Pathway: Like the BR₁ complex, most BR₂ (and anionic triplet BR₃) complexes have linear CuCO moieties, except the anionic triplet BR₂ complex. The cationic triplet BR₂ and anionic triplet BR₃ complexes have a significantly elongated O_αO_β bond of 2.039 Å and 2.704 Å (Table 6.12). The cationic triplet and anionic triplet "O₃ out" complexes are the reactant-side global minimum on the respective pathways. The ESP surfaces are similar to the BR₁ ESP surfaces for each respective charge (and spin) states. Similar to the neutral Cu-TS transition state, the cationic and anionic triplet states also have planar structures, while the cationic and anionic singlet states have non-planar structures. Unlike all other transition states, the cationic singlet Cu-TS transition state is 3.70 kcal/mol above the reactant asymptote. Like the neutral state, the cationic and anionic triplet states have Cu-TS transition states

as the lower energy pathways, while the cationic and anionic singlet(s) states have O-TS as the lower energy pathways.

Post-reactive Minima and Transition States: While the Au systems discussed in Chapter 5 had post-reactive complexes (and transition states) in all charge states, except the cationic singlet, the Cu system only has post-reactive pathways in the anionic states; the general structures and changes along the (post-reactive) reaction pathways are very similar between the anionic singlet and triplet states. From the anionic singlet Cu-TS transition state, a post-reactive minimum (AR₁) is formed by breaking the Cu-C bond and forming a CO₂ moiety that is connected to Cu through O_α, with a CuOCO dihedral of 0°. From Cu-TS, the CuO_α and CuO_β, CO and OO bonds increase for anionic singlet; the “newly formed” OC bond is 1.257 Å; however the anionic triplet AR₁ has a decrease in CuO_β and increases in CuO_α, CO and O₂, while the newly formed OC bond the same length as the anionic singlet bond (Tables A6.3 and A6.4 in Appendix A6). The ESP surfaces of both anionic spin states have well distributed charges with very slight negative character on O₂ and very slight positive character on CO₂.

The second post-reactive minimum (AR₂) is formed over a small rotational barrier, where the anionic singlet (LB₁) ESP surface has strong negative character on O₂ and positive character on CO₂ (Figure 6.11; Tables A6.5 and A6.6 for transition states in Appendix A6). The second post-reactive structure, AR₂, is formed by the continuation of the CuOCO dihedral rotation to 180°; both charge states also have small changes with respect to bond lengths and angles and frequencies (Tables A6.4 and A6.5 in Appendix A6). Both ESP surfaces have well distributed charge across the entire complex. From AR₂, another low barrier transition state (anionic singlet LB₂ and anionic triplet LB₄) can

be overcome with breaking the CuO(CO) bond (Tables A6.5 and A6.6 in Appendix A6), which ends at the product (in the respective spin state).

6.4 Discussion

6.4.1 O₂ Pathways

The ESP surfaces can be used to track the electrostatic character of the complexes along the reaction pathways to understand how the ESP character evolves with structural changes and the energetically favorable pathways. In the anionic singlet system, most of the negative character resides on O₂ from Sep to the pre-reactive complexes, where the negative character is heavily localized in O₂ of the Pre₂ (out) complex. For the In-TS ESP surface (Figure 6.6), the negative character on O₂ is more than that on CuCO; this ESP surface looks like a less polarized version of Pre₁. When comparing ESP surfaces for In-TS and Pro₂, the product looks like the opened version of In-TS, where the O atom retains (more) negative character and the CuCO₂ moiety has a well-distributed charge.

When looking at the Out pathway, the Out-TS ESP surface shows negative character spread across Cu and the “dangling” O atom, while CO₂ is positive, which is very different from the other ESP surfaces. Also with the positively charged CO₂ and negative O and Cu atom, the charges may be attracted and catalyze the formation of CuCO₃⁻. The CuCO₃⁻ ESP shows strong polarization of the negative charge onto CO₃ and less on Cu; again, charge attraction may facilitate the separation of CO₂ from CuO. For the CuO oxidation pathway, the positive character remains on CO (from Sep) in the ESP surface and the negative charge is spread across OCuO. In this case, it appears that the “migrating” O atom is carrying charge to neutralize the CO moiety, as the product has a “neutral” CO₂ moiety and negative character on the O atom.

The neutral ESP surfaces (Figure A6.2 in Appendix A6) are similar to the anionic singlet, where positive charge moves from CO moiety of Sep to the Cu atom in the Pre structure. The negative character is on O₂ of Sep and spreads across the OCOO moiety in Pre. Throughout the Out-TS pathways, the positive and negative charges stay in the same areas until the product, where the negative character re-localizes onto the O atom and induces positive character onto CO₂. The anionic triplet pathway can be described as having a “well distributed” anionic charge in most ESP surfaces (Figure A6.3 in Appendix A6); In-TS and Pro₁ show some localization of negative character on O₂ and CO₃, respectively, but the strongest charges are observed in TS₂, where there is negative character on CuO and strong positive character on CO₂.

6.4.2 Ozone Pathways

O₃ Oxidation Pathway: The linearity of CuCO in most reactant-side complexes, except the anionic triplet BR₁ and BR₂, is induced by charge transfer into the electron withdrawing effects of O₃ on CuCO, similar to the O₂AuCO^q work discussed in Chapter 3 and O₂CuCO^q discussed above. For the states with BR₁ as the reactant-side global minimum, there may be additional stabilization from the Cu-O_γ interaction, which allows a somewhat more evenly distribution of charge across O₃. The ESP surface of the neutral state, Figure 6.10, agrees with the charge transfer idea, where the O₃ moiety has negative character and CO has positive character. With the formation of O-TS transition state, the O₃ moiety retains the electron density, but the rotation of O₃ and formation of the intermolecular O-C bond disrupts the linear bonding of CuCO. With the loss of CuCO linearity but retention of the negative character on the O₃ moiety, positive character is induced on the Cu atom, as observed in the neutral ESP surface. From the O-TS

transition state, negative character remains on the (now) O₂ moiety of the product, while the positive character has migrated onto CO₂, which indicates charge transfer into O₂ that induces positive character on CO₂.

CuO oxidation pathway: The ESP surface of BR₂ has negative character on O₃ and CO has positive character, similar to BR₁. In forming the Cu-TS transition state, CuCO remains linear and the ESP surface shows retention of positive character on CO, suggesting that the synergic back-bonding is retained. Cu has catalyzed the decomposition of O₃ to form CuO and a separate, possibly spectator O₂ moiety, where Cu acts chemically distinct from Cu in the O-TS transition state. The ESP surface, as stated above, has positive character on CO and negative character on O_α, while O₂ is relatively neutral, which further suggests that O₂ is a spectator. In forming the product, it appears that the migrating O atom of CuO is carrying the negative charge to “neutralize” the positive CO component and form CO₂. This neutralization should leave a complex with neutral moieties; however, the neutral ESP surface of the product shows evidence for charge transfer into the O₂ moiety, as discussed above.

Similarities of O-TS & Cu-TS: There are structural similarities between O-TS and G-TS, as both transition states retain the CuO_α bond, form intermolecular O-C bonds and share similar Cu-C and C-O bond lengths. The ESP surfaces also display similarities, where the negative character resides on the oxygen species of O-TS (O₃ moiety) and Cu-TS (O₂ and O atom sub-units).

Other Charge States' O₃ Oxidation Pathway: The anionic singlet BR₁ complex has an ESP surface similar to the neutral, while the cationic ESP surfaces have positive charge mainly on CuC, and anionic triplet has a well-distributed charge. The O-TS ESPs are

generally similar to the neutral surface across most charge states with positive charge on the Cu atom, while the anionic triplet O-TS has well distributed charge in the ESP surface. Slightly different from the neutral surface is that the anionic singlet has positive charge spread across CuCO (in O-TS), rather than contained (mostly) on Cu. Also unlike the neutral product, all other charge- and spin-state products have relatively well distributed charges in the ESP surfaces, except the anionic singlet has slightly more negative character on O₂.

Other Charge States' CuO Oxidation Pathway: The cationic BR₂ ESP surfaces are similar to BR₁ with positive character on CuC, but the charge is less intense; the anionic triplet retains the well distributed charge. The anionic singlet BR₂ and triplet BR₃ ESP surfaces show charge transfer similar to the neutral BR₂, but carry most of the negative character on O_α with positive character on CO and a neutral O₂. The cationic and anionic triplet "O₃ out" structures are the reactant-side global minimum, which may be a result of these states preferring a triplet O₂ moiety over the O₃ singlet moiety, as the O₂ ground state triplet would best match the overall spin state.

The Cu-TS ESP surfaces for the other charge states are again similar to the neutral surface with negative character on the migrating O_α atom and positive on CO; the positive charges are distributed slightly differently in the cationic systems, which have positive on O₂CuCO, and the negative character in the anionic triplet is spread across OCuO₂. The Cu-TS states are the lower energy pathways the cationic, neutral and anionic triplet states. With the clear formation and of an O₂ moiety, which prefers a triplet state, it is understandable that Cu-TS would be lower in energy, based on spin state matching of O₂ and the overall complex. As stated above non-neutral charge states have well-

distributed charge in the product ESP surfaces. For these charge states when forming the product from Cu-TS, the negative character on the migrating O atom does appear to “neutralize” the positive character of CO to the appropriate overall charge of the product (+1 or -1).

The anionic singlet and triplet pathways also have additional post-reactive complexes with “tight” O_2CuCO_2 structures with differing CuOCO dihedral angles, where the minima in both charge states have generally well distributed charge across the complex; the anionic singlet shows slight negative character on the O_2 moiety, similar to its product. The anionic triplet post-reactive transition states also have well distributed charge, but the anionic singlet post-reactive transition states have strong negative character on O_2 and positive on CO_2 , indicating charge transfer into O_2 and induced positive charge on CO_2 .

6.4.3 Comparison of O_2 and O_3 Systems

There are several similarities between the O_2 and O_3 systems and pathways in structural data, ESP surfaces and charge transfer. Most obvious is the similarity in the $[O_3CuCO]^q$ complexes to the $[O_2CuCO]^q$ structures, ESP surfaces and molecular orbitals, which show synergic back-bonding in the CuCO moieties. Like the O_2 system, the neutral and anionic singlet O_3CuCO ESP surfaces indicate charge transfer with the negative character on O_3 and positive in CO. Similarities are also observed in the products of the two systems, $O_2CuCO_2^q$ and $OCuCO_2^q$. These structural and ESP similarities across the O_2 and O_3 systems indicate that the different oxygen allotrope did not grossly change the “separated” and “product” complexes.

Structural and ESP surface similarities are also observed between CuCOO_3^q , the O-TS transition state, and the anionic (singlet and triplet) pre-reactive “in” CuCOO_2 minima; however, the type of stationary point is opposite with a maximum for O-TS and minimum for CuCOO_2 . In this case, the addition of the O atom promoted the complex into a transition state, as the OO bonds of the O-TS transition states are similar to O_3 and O_3^- . Comparatively, the CuCOO_2 transition states (In-TS) had OO bonds elongated to values beyond the peroxide (O_2^{2-}) length. In the O_3 system, transition states on both pathways were observed for all charge states, while pre-reactive complexes and pathways were not observed with cationic states of the O_2 system. The $\text{O}_2(\text{O})\text{CuCO}^q$ transition states are very similar to the $\text{O}(\text{O})\text{CuCO}^q$ transition states in structure with an additional O atom, but the Cu-TS transition state was not observed for the anionic triplet (O_2) system. Furthermore, all of the transition states, except Cu-TS in cationic singlet, are below the reactant asymptote, while the calculated barriers for the $[\text{O}_2+\text{Cu}+\text{CO}]$ cationic and neutral pathways were greater than the reactant asymptote; the O_3 system and the anionic O_2 pathways are “spontaneous,” where the energy barriers exist below the reactant asymptote, but the minima could be trapped in cryogenic matrices. It is striking that so many similarities exist across O_2 and O_3 system, but on the other hand the similarities are understandable since the systems involve oxygen allotropes.

6.4.4 Comparisons to Au Systems

O_2 Structures: Similar to the Au system, the binary and ternary complexes show opposing trends in how the intermolecular distances change with increasing negative charge, which indicates a fundamental change in the interactions of CuCO , when O_2 is also interacting with Cu. Again like the Au system, the superoxo-like O_2 moieties of the

neutral and anionic singlet (C_{2v}) separated structures suggest charge transfer from the Cu atom (or anion) into the O_2 sub-unit, which induces the linear CuCO moiety. Similar to the Au system, there is synergic back-bonding in the $CuCO^+$ complex with σ -donation from CO into Cu^+ and π -backbonding from the d-orbitals (of Cu^+) into the π^* orbitals of CO, which is induced in the (neutral and anionic singlet) separated complexes by charge transfer into the O_2 sub-unit. Much of the discussion of Chapter 4 for the $[O_2+Au+CO]^q$ complexes is applicable to the copper system. While energies and some structures are different, similar phenomena occur in both systems, which suggests periodicity.

O_2 Pathways: Unlike the Au system, the separated complexes in all charge and spin states are the global minima for the reactant side complexes; also, the anionic singlet and triplet pathways are below the reactant asymptote, while the neutral pathways are higher than the reactant asymptote. It is possible that Cu ions provide a more activating surface for CO oxidation with O_2 , as the similar Au (anionic singlet) pathways have barriers greater than the reactant asymptote. In the anionic singlet Cu system, the pre-reactive “in” pathway is energetically favorable over the “out” pathway, while the Au anionic singlet pathways preferred the “out” pathway. For the Cu products, the carbonate-like structure is the global minimum across all charge states, while the $AuCO_3$ was the product minimum for only the anionic singlet Au system. Like the Au system, it is more likely for the carbonate-like product to re-arrange into the desired $OCuCO_2$ product than to separate into Cu and CO_3 (or CO_3^-), as the desired product is lower in energy than these ions.

We have also calculated CuO oxidation pathways for the cationic, neutral and anionic singlet system, where this pathway is the energetically favorable pathway for the

neutral system. The AuO oxidation pathways were not studied in the Au+CO+O₂ pathways (Chapter 4) from the separated complexes, as the pre-reactive complexes were the main focus. The CuO oxidation may be the favored pathway in the neutral system due to the lack of a pre-reactive “in” complex (and In-TS pathway); the neutral Out-TS₁ transition state with a CuOOCO is the closest transition state to the anionic singlet In-TS and the Au In-TS transition states.

O₃ Pathways: Similar to the Au systems, most charge and spin states have O₃ oxidation and CuO oxidation pathways that are below the respective reactant asymptotes, except the cationic singlet Cu-TS; this indicates the oxidation of CO by Cu⁰ and O₃ is also spontaneous. The reactant-side complexes (BR_x), O₃CuCO⁰, are generally similar to those observed in Au systems, except that the neutral “O₃ in” structure has C_{2v} symmetry and there is no “O₃ out” structure in the anionic singlet state. With the clear formation and separation of an O₂ moiety, which prefers a triplet state, it is understandable that Cu-TS would be lower in energy than O-TS for the triplet states, based on spin state matching of O₂ and the overall complex. The observation of Cu-TS (CuO oxidation pathways) as the lower energy pathway is somewhat surprising for the neutral doublet, as the neutral Au system has O-TS as the lower energy pathway; however, the formation of O₂CuCO₂ product from Cu-TS appears to require less bond breaking (Cu-C) and smaller angular changes or rotations (larger CuOO angle and forms linear OCO) than O-TS, which requires broken CuC and OO bonds, formation of a new CuO bond and a linear OCO moiety, and rotation of CuOO away from OCO). It is also interesting to note that there are no post-reactive complexes in the neutral or cationic Cu system. The anionic Cu systems have post-reactive complexes (O₂CuCO₂⁻), but they are similar to the “tight”

$\text{O}_2\text{AuCO}_2^-$ (triplet) structures in the anionic triplet “extended” pathway and not the long intermolecular OC bond complexes $\text{O}_2\text{AuO}^{\cdot\cdot}\text{CO}^{\cdot}$, which were observed in the cationic triplet, neutral and (both) anionic AuO oxidation pathways of Chapter 5. The contracted d-shell of Cu^{\cdot} , as Cu is in the “first d-row,” may be less conducive for “long-range” complexes than Au^{\cdot} .

6.5 Conclusions

This work indicates that oxidation of CO can occur via two chemically distinct pathways with two oxygen allotropes (O_2 and O_3), whereby CO is oxidized directly by an oxygen allotrope, catalyzed by Cu^{\cdot} , or by CuO, after Cu^{\cdot} insertion into O_2 or O_3 decomposition over Cu^{\cdot} , depending on the oxygen allotrope. Similar to the Au systems, both oxygen-allotrope sets of pathways start from “separated” minima with an intact molecular allotrope, indicating that pre-oxidation of Cu is not required for CO oxidative catalysis.

In the ozone systems and similar to calculations of $[\text{O}_3+\text{Au}^{\cdot}+\text{CO}]$, the observation of these two distinct pathways suggests that Cu can act as a stabilizing agent for molecular ozone or provide a location for O_3 decomposition to CuO. The appearance of these pathways across the three charge and related spin states indicate that subtraction or addition of an electron beyond neutral Cu does not grossly alter the catalytic reaction and may result from the ability of these complexes to balance charge. Since the reactants are singlets and products involve triplet O_2 , these pathways are spin-forbidden processes and reactions to form the products would depend on the spin-orbit coupling of the singlet and triplet electronic states along the reaction coordinate.

The general similarities in complexes along the O₂ and O₃ pathways, such as the separated minima, existence of O₂ (O₃) oxidation pathways and CuO oxidation pathways, and general structure of the related “main” transition states, suggests that the additional O atom does not greatly alter the main minima and transition states. Also, there is evidence of periodicity with all of the similarities between Cu and Au pathways for both oxygen allotropes, which can be expected as Cu and Au are in the same period on the periodic table and both have contracted d-shells.

6.6 Computational Methods

Density functional theory (DFT) geometry optimizations and frequency calculations were carried out using the GAUSSIAN 09 suite of computational chemistry programs.²⁰ Except where otherwise noted, all reported data reflect results obtained using the B3LYP hybrid functional,²¹ with a mixed basis set employing the Stuttgart-Dresden relativistically-corrected effective core potential basis for Cu atoms,^{22, 23} and the Pople 6-311+G(3df) basis for C and O atoms.^{24, 25} All geometry optimizations were performed using the tight convergence criteria and the ultrafine integration grid (Gaussian keywords: “opt=tight” and “integral=ultrafine”); this was required to achieve convergence for weakly-bonded systems, and was maintained for all calculations to ensure comparability of the results. Transition states were calculated with the quadratic synchronous transition approach with three molecule specifications (qst3 keyword) for the “reactant,” “product,” and transition state guess.^{26, 27} All reported geometries reflect stable minima (maxima for transition states) on their respective potential energy surfaces without (with) imaginary frequencies. The stabilities of the SCF wavefunctions for each reported wavefunction were verified using the method of Davidson.²⁸ Counterpoise

corrections, using the method of Boys and Bernardi,²⁹ were carried out to correct for the effects of basis-set superposition error (BSSE) on the binding energies of the complexes. All reported binding energies have been corrected for both BSSE and the vibrational zero-point energy (ZPE). IRC calculations were then applied to understand the connections between calculated transition states and minima.³⁰⁻³³ Atomic charges were calculated using the Hirshfeld stockholder method³⁴⁻³⁶, CHELPG molecular electrostatic potential method,³⁷ and the natural bond orbital (NBO) method,³⁸⁻⁴³ as implemented within GAUSSIAN 09.

Computational details for electrostatic potential surfaces: Electrostatic potential (ESP) has been mapped onto the B3LYP total electron density isosurfaces (density=0.0004) for the structures along each pathway. The color map spans a range of 0.1 in each case, where red (blue) as most negative (positive). The charges for cationic species are mapped over +0.10 to +0.20; neutral, -0.05 to +0.05, and anionic, -0.20 to -0.10. Spin densities were calculated using Gaussian 09 (density = 0.004), where spin density is the β (spin) density subtracted from α (spin) density.

6.7 References

- (1) Haruta, M. *Cattech* **2002**, *6*, 102-115.
- (2) Mozer, T. S.; Dziuba, D. A.; Vieira, C. T. P.; Passos, F. B. *J. Power Sources* **2009**, *187*, 209-215.
- (3) Chen, C. S.; You, J. H.; Lin, J. H.; Chen, Y. Y. *Catal. Comm.* **2008**, *9*, 2381-2385.
- (4) Boccuzzi, F.; Chiorino, A. *J. Phys. Chem.* **1996**, *100*, 3617-3624.
- (5) Ogden, J. *J. Chem. Soc. D-Chem. Comm.* **1971**, 978.
- (6) Huber, H.; Kundig, E. P.; Moskovits, M.; Ozin, G. A. *J. Am. Chem. Soc.* **1975**, *97*, 2097-2106.
- (7) Moskovits, M.; Hulse, J. *J. Phys. Chem.* **1977**, *81*, 2004-2009.
- (8) Zhou, M.; Andrews, L. *J. Chem. Phys.* **1999**, *111*, 4548-4557.
- (9) Zhou, M.; Andrews, L.; Bauschlicher, C. W. *Chem. Rev.* **2001**, *101*, 1931-1961.
- (10) Ludwig, R. M.; Moore, D. T. *J. Chem. Phys.* **2013**, *139*, 244202.
- (11) Chertihin, G.; Andrews, L.; Bauschlicher, C. *J. Phys. Chem. A* **1997**, *101*, 4026-4034.

- (12) Yuan, X.; Liu, L.; Wang, X.; Yang, M.; Jackson, K. A.; Jellinek, J. *J. Phys. Chem. A* **2011**, *115*, 8705-8712.
- (13) Baruah, T.; Zope, R. R.; Pederson, M. R. *Phys. Rev. A* **2004**, *69*, 023201.
- (14) Ozin, G. A.; Mitchell, S. A.; Garciaprieto, J. *J. Am. Chem. Soc.* **1983**, *105*, 6399-6405.
- (15) Uzunova, E. L. *J. Phys. Chem. A* **2011**, *115*, 1320-1330.
- (16) Deng, K.; Yang, J. L.; Zhu, Q. S. *J. Chem. Phys.* **2000**, *113*, 7867-7873.
- (17) Gong, Y.; Zhou, M. *Phys. Chem. Chem. Phys.* **2009**, *11*, 8714-8720.
- (18) Gong, Y.; Wang, G.; Zhou, M. *J. Phys. Chem. A* **2009**, *113*, 5355-5359.
- (19) Xu, Q.; Jiang, L. *J. Phys. Chem. A* **2006**, *110*, 2655-2662.
- (20) ; Frisch, M. J.; Trucks, G. W.; Schlegel, H. B.; Scuseria, G. E.; Robb, M. A.; Cheeseman, J. R.; Scalmani, G.; Barone, V.; Mennucci, B.; Petersson, G. A., et al. Gaussian 09, Revision A.02, Gaussian, Inc., Wallingford, CT **2009**.
- (21) Becke, A. D. *J. Chem. Phys.* **1993**, *98*, 5648-5652.
- (22) Schwerdtfeger, P.; Dolg, M.; Schwarz, W. H. E.; Bowmaker, G. A.; Boyd, P. D. W. *J. Chem. Phys.* **1989**, *91*, 1762-1774.
- (23) Andrae, D.; Haussermann, U.; Dolg, M.; Stoll, H.; Preuss, H. *Theor. Chim. Acta* **1990**, *77*, 123-141.
- (24) Krishnan, R.; Binkley, J. S.; Seeger, R.; Pople, J. A. *J. Chem. Phys.* **1980**, *72*, 650-654.
- (25) Frisch, M. J.; Pople, J. A.; Binkley, J. S. *J. Chem. Phys.* **1984**, *80*, 3265-3269.
- (26) Peng, C.; Schlegel, H. *Isr. J. Chem.* **1993**, *33*, 449-454.
- (27) Peng, C.; Ayala, P.; Schlegel, H.; Frisch, M. J. *Comput. Chem.* **1996**, *17*, 49-56.
- (28) Langhoff, S. R.; Davidson, E. R. *Int. J. Quant. Chem.* **1974**, *8*, 61-72.
- (29) Boys, S. F.; Bernadi, F. *Mol. Phys.* **1970**, *19*, 553-566.
- (30) Fukui, K. *Acc. Chem. Res.* **1981**, *14*, 363-368.
- (31) Hratchian, H.; Schlegel, H. *J. Chem. Phys.* **2004**, *120*, 9918-9924.
- (32) Hratchian, H.; Schlegel, H. *J. Chem. Theory Comput.* **2005**, *1*, 61-69.
- (33) Hratchian, H. P.; Schlegel, H. B. In *Finding minima, transition states and following reaction pathways on ab initio potential energy surfaces*; Dykstra, C. E., Frenking, G., Kim, K. S. and Scuseria, G. E., Eds.; *Theory and Applications of Computational Chemistry: The First 40 Years*; Elsevier: Amsterdam, 2005.
- (34) Hirshfeld, F. L. *Theor. Chim. Acta* **1977**, *44*, 129-138.
- (35) Ritchie, J. P. *J. Am. Chem. Soc.* **1985**, *107*, 1829-1837.
- (36) Ritchie, J. P.; Bachrach, S. M. *J. Comput. Chem.* **1987**, *8*, 499-509.
- (37) Breneman, C. M.; Wiberg, K. B. *J. Comput. Chem.* **1990**, *11*, 361-373.
- (38) Foster, J. P.; Weinhold, F. *J. Am. Chem. Soc.* **1980**, *102*, 7211-7218.
- (39) Reed, A. E.; Weinhold, F. *J. Chem. Phys.* **1983**, *78*, 4066-4073.
- (40) Reed, A. E.; Weinstock, R. B.; Weinhold, F. *J. Chem. Phys.* **1985**, *83*, 735-746.
- (41) Reed, A. E.; Weinhold, F. *J. Chem. Phys.* **1985**, *83*, 1736-1740.
- (42) Reed, A. E.; Curtiss, L. A.; Weinhold, F. *Chem. Rev.* **1988**, *88*, 899-926.
- (43) Carpenter, J. E.; Weinhold, F. *J. Mol. Struct. -Theochem* **1988**, *46*, 41-62.

Chapter 7. Matrix Isolation Experiments on the Interactions of Ozone (O₃), Carbon Monoxide (CO), Copper Ions (Cu⁻) and Counter-cations of Ar⁺

7.1 Abstract

In an effort to understand the catalysis of CO oxidation with ozone over copper ions, matrix-isolation studies of the interactions of copper ions (Cu⁻) and counter-ions (Ar⁺) and two types of gas mixtures were completed for different deposition temperatures, rates and counter-ion energies, as follows: ozone (O₃), and O₃ and carbon monoxide (CO). Peaks corresponding to CuO₃, O₃⁻, O₄⁻, trans-O₄⁺ and cyclic-O₄⁺ and copper carbonyls, Cu(CO)⁻ and Cu(CO)₃⁻, were observed in different experiments, but not consistently when changing deposition parameters. The O₄ ionic complexes appeared consistently with different Ar⁺ energies, when deposited at the same temperature and O₃ concentration (in argon gas mix); also, a thermal equilibrium was observed between the trans- and cyclic-O₄⁺ complexes, when annealing the matrix from 10K to 20K.

7.2 Introduction:

Much of the more recent matrix-isolated work has been completed with laser ablation sources, in which cationic, neutral and anionic copper clusters (or atoms) are produced, which makes a rather complex spectrum. Recent experiments and publication from our group have shown the ability to deposit Cu⁻ with counter-cations, like Ar⁺, with CO (in Ar), form anionic copper carbonyls and controllably neutralize them under photo-exposure or thermal annealing, depending on the deposition conditions.¹ In this chapter, the efforts to identify CuO₃^{0,-} and O₃Cu(CO)_n^{0,-} (n=1-3) are discussed.

7.3 Results:

Matrix-isolation experiments with Ar matrices have been completed at deposition temperatures of 10K, 20K, and 25K to test the interactions of the following: O₃ and CO

(no ions), Cu^- , Ar^+ and O_3 , and Cu^- , Ar^+ , O_3 and CO . Experimental details on the deposition rates and concentrations are found in the Experimental Methods section, 7.6, and the instrument has been described in Chapter 2. The results of matrix isolated experiments with and without ions are described within the Results section.

7.3.1 O_3 in Ar Experiments: Ozone in Ar mixes has been deposited at 10, 15, and 20K to obtain background spectra to compare with later studies with Cu^- and Ar^+ ions. Figure 7.1 shows an overview of the full FTIR spectrum ($650\text{-}4000\text{ cm}^{-1}$) taken for a 0.05% O_3 in Ar mixture after a 20K deposition for 2 hours at ~ 5 sccm. The largest peak is the anti-symmetric O_3 doublet peak at 1039.4 and 1041.1 cm^{-1} , which corresponds to the single and double substitutional sites, respectively, and are in agreement with the literature.² Even with pre-treatment of the deposition lines with ozone and isopentane baths to trap CO_2 , CO_2 is still observed during deposition. However, the anti-symmetric CO_2 peak (doublet of 2339.0 and 2345.1 cm^{-1}) is $\sim 40\%$ the height of O_3 , which was an improvement on previous experiments, in which the CO_2 peak(s) was larger than O_3 peak(s). Two combination bands of O_3 fundamental frequencies, 2108.5 and 2112.2 cm^{-1} , were commonly observed in experiments along with 1104.6 cm^{-1} (symmetric O_3 stretch) and 703.6 cm^{-1} (O_3 bending mode); other combination bands were observed with higher concentration mixes of $\sim 0.5\%$ O_3 in Ar; the O_3 -related peaks are collected in Table 7.1 and were in general agreement with literature values. CO_2 , water-related peaks and the broad hydrocarbon bump ($\sim 2800\text{-}3000\text{ cm}^{-1}$) are generally regarded as “background” peaks that are observed in all of the ozone spectra and other spectra taken on the same KBr window. When the matrix is thermally annealed (to 25 and 30K), no major changes are observed beyond transfer of intensity from the single to double

substitution sites for O₃ and CO₂. Exposure of the matrix to the flashlight (~5 minutes) and UV light also did not cause any visible changes in the spectra. Difference spectra were utilized to look for changes between the annealing (and photo-exposure) steps and showed the intensity transfer between substitutional sites (Appendix A7 Figure A7.2). When the region of the O₃ (or CO₂) peak, such as between 1030 and 1050 cm⁻¹, was integrated in the difference spectra, the area was very close to zero (~ -0.007 units), while the integrated peak area of O₃ in the post-deposition scan was ~0.122 units (exact values are found in Table A7.1 of Appendix A7).

7.3.2 O₃:CO Experiments: Gas mixtures of ozone and CO in Ar were deposited at 10K and 20K at 5 sccm to compare with spectra from experiments of O₃, CO and ions. A mixture of ~0.06% O₃ and ~0.14% CO in Ar was deposited at 20K for 2 hours at 5 sccm flow rate; the resulting spectra are shown in Figure 7.2. The full spectrum shows intense CO and CO₂ peaks and a much smaller O₃ peak (Fig. 7.2a). There are small peaks located to the blue of the O₃ (anti-symmetric stretch) peak at 1042.65 and 1043.37 cm⁻¹ and to the blue of the CO peak at 2140.10 and 2140.40 cm⁻¹, in which all of these peaks have been previously assigned to the weakly bound O₃:CO complexes.³ CO dimer also is observed and assigned to the side band of the CO peak at 2140.15 cm⁻¹. The two O₃:CO peaks are also side bands of the main CO 2138 cm⁻¹ peak and not fully resolved peaks, even though the resolution in Figure 7.2 b-d is 0.125 cm⁻¹. Weakly bound CO:CO₂ were also observed in the spectra near the CO peak at 2143.1 and 2143.4 cm⁻¹, and by the CO₂ doublet, where the CO:CO₂ peaks, 2346.02 and 2346.86 cm⁻¹, are larger than the CO₂ doublet, which have been previously observed.⁴ The matrix was annealed to 25K and 30K and exposed to light from a flashlight and a UV source, but no additional CO₂

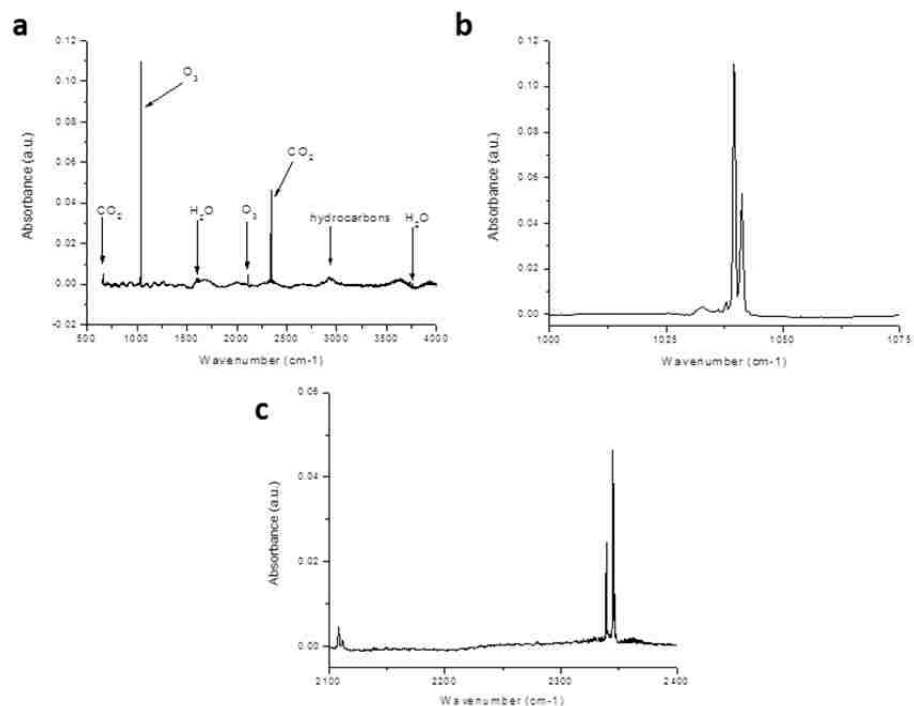


Figure 7.1 a) FTIR spectrum (650-4000 cm^{-1}) taken at 10K after deposition of a 0.05% O_3 in Ar mixture at 20K for 2 hours. b) Focus on the O_3 anti-symmetric peak (doublet) at 1039.4 and 1041.1 cm^{-1} . c) Focus on the 2100-2400 cm^{-1} region. Note that the spectrum in c) is on a different scale than those in a) and b).

Table 7.1. Peak assignments of main absorption frequencies (cm^{-1}) of ozone in argon for spectra taken at 10K. Resolution is 0.5 cm^{-1} for all peaks. Assignments were made based on previous assignments in the literature.²

O_3 peak assignments	Stretching frequencies (cm^{-1})
ν_2	703.4
ν_3	1039.4
ν_3	1041.1
ν_1	1104.6
$\nu_2+\nu_3$	1727.7
$\nu_2+\nu_3$	1728.6
$\nu_1+\nu_2$	1800.7
$2\nu_3$	2057.2
$\nu_1+\nu_3$	2108.3
$\nu_1+\nu_3$	2112.1
$\nu_1+\nu_2+\nu_3$	2786.9
$3\nu_3$	3041.4
$3\nu_3$	3046.7

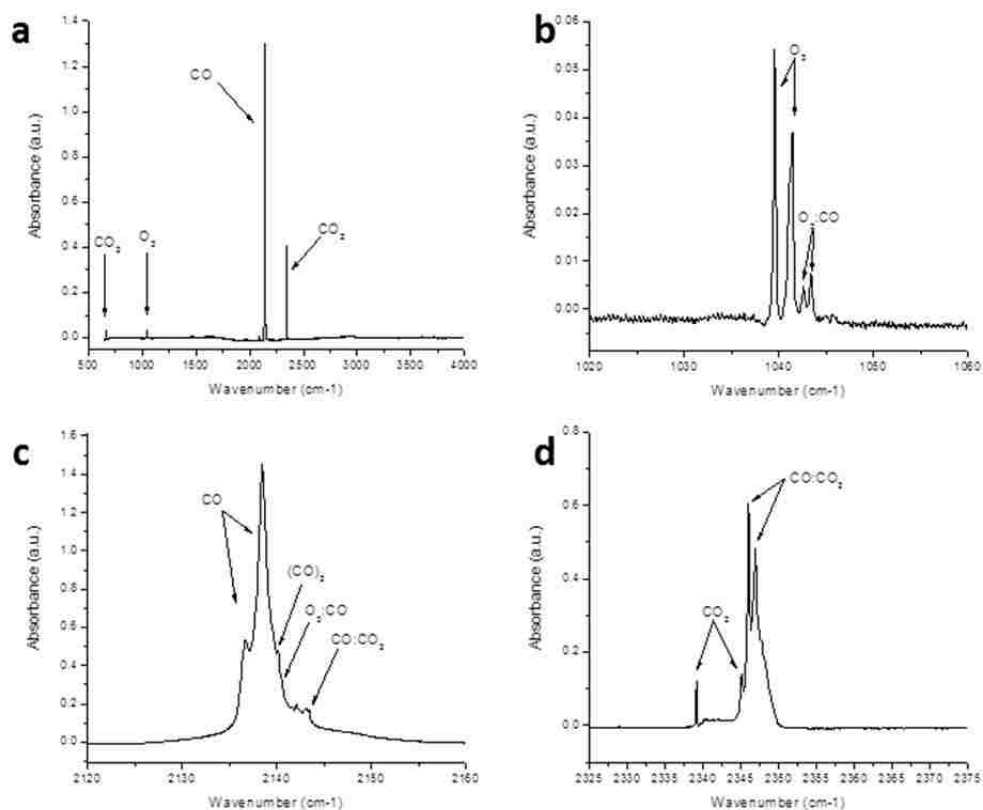


Figure 7.2 Note that all spectra (a-d) are on different wavenumber and absorbance scales. a) FTIR spectrum ($650\text{-}4000\text{ cm}^{-1}$) taken at 10K for deposition of a 0.06% O₃ and 0.14% CO in Ar mixture at 20K deposition for 2 hours at ~ 5 sccm (resolution of 0.5 cm^{-1}). b) Focus on O₃ region ($1020\text{-}1060\text{ cm}^{-1}$) of the high resolution (0.125 cm^{-1}) spectrum. c) Focus on the CO region around 2140 cm^{-1} . d) Focus on CO₂ anti-symmetric peak region ($2325\text{-}2375\text{ cm}^{-1}$).

intensity was observed in the spectra (Figure A7.3 in Appendix A7). Similar to the annealing of the O₃ in Ar, there was transfer in population between different substitutional sites, but the integrated area over the O₃, CO or CO₂ peak did not significantly change in the taken or difference spectra (Table A7.1 in Appendix A7).

7.3.3 Cu:O₃ Experiments: In the Cu⁻, Ar⁺ (30 eV), and (~0.5%) O₃ experiments at 10K, it was observed that deposition flow rate has significant impact on the observed complexes, since a slower deposition rate increases the amount of ions per gas molecules. Deposition at 2.5 sccm led to formation of a small peak at 802.96 cm⁻¹ (Figure 7.3), which was assigned to neutral CuO₃, as CuO₃ has been assigned to a peak at 802.3 cm⁻¹ by Tevault and co-workers and at 802.7 cm⁻¹ by Andrews and co-workers.^{5,6} Another peak is observed at 1118.5 cm⁻¹, where 1119 cm⁻¹ has been previously assigned to trans-O₄⁺ complex.^{7,8} When the matrix was annealed to 15K and 20K, the 1118.5 cm⁻¹ decreased, while a peak at 1548.08 cm⁻¹ increased, as observed in the stacked difference spectra in Figure 7.4b. The complex of H₂O:O₂ has been previously assigned to 1551 cm⁻¹;⁹ however, matrix-isolation experiments in our group with O₂, regardless of whether Cu⁻ is deposited, typically have shown a peak at 1548.08 cm⁻¹, which is attributed to H₂O:O₂. Further annealing of the matrix and exposure to the flashlight and UV sources did not show any other significant changes in the spectra; the CuO₃ peak was not affected by the annealing or photo-exposure steps, as can be observed in Figure 7.4a.

When the deposition rate was increased to 5 sccm and all other parameters were held constant (10K deposition for 2 hours of 0.5% O₃ in Ar with Cu⁻ and Ar⁺ (30eV)), the 802.96 and 1118.5 cm⁻¹ peaks are not observed; however, a broad feature is observed at 828 cm⁻¹, which is shown in Figure 7.5b. Andrews and co-workers have identified

complexes at 823 cm^{-1} as OCuO and 836.6 cm^{-1} as O_2CuO_2 , which are the closest peaks to 828 cm^{-1} .⁶ Difference spectra (Figure A7.4) of the $600\text{-}1000\text{ cm}^{-1}$ region do not show changes in the 828 cm^{-1} peak.

More recent Cu^- , Ar^+ (70eV and 30eV), 0.2% O_3 (in Ar) experiments were completed with a higher flow rate of 10 sccm and longer deposition time of 4 hours. Experiments deposited at 10K under these conditions have not shown formation of CuO_3 , but have shown formation of O_3^- and O_4^- ionic complexes (Figure A7.5 in Appendix A7). Based on other O_2 experiments in the group, slower annealing steps were taken and spectra was recorded at the annealing temperatures to observe changes in the O_4^+ peaks, which are shown in Figure 7.6. The O_4^- peak appears to blue shift by $\sim 1\text{ cm}^{-1}$ with increased temperature up to 20K and shifts back to 953 cm^{-1} , when the matrix is returned to 10K (shown in Figure A7.6 in Appendix A7). The trans- O_4^+ peak at 1118.5 cm^{-1} decreases with increasing temperature, while 1310 cm^{-1} and a doublet at 1329 and 1331 cm^{-1} grow in. The doublet at 1329 and 1331 cm^{-1} has been assigned to cyclic- O_4^+ and 1310 cm^{-1} has been observed, but not assigned to a complexes, based on the work by Andrews and co-workers. The 1310 cm^{-1} peak grows in up to 16K, while the 1329 and 1331 cm^{-1} doublet continues to grow up to 18K, at which point the doublet peak appears to move into a single peak 1330.8 cm^{-1} up to 20K. When the matrix is cooled to 10K, the 1118.5 cm^{-1} peak recovers most of the intensity, while 1310 cm^{-1} is lost and the 1329 and 1331 cm^{-1} doublet returns. When comparing the post- annealing 10K to the deposition 10K spectra, there is a small loss of 1118.5 cm^{-1} intensity and growth of the 1329 and 1331 cm^{-1} doublet. The sample was also exposed to the 470 nm and 590 nm LED lights and flashlight to observe how the complexes in the matrix responded, which is shown in

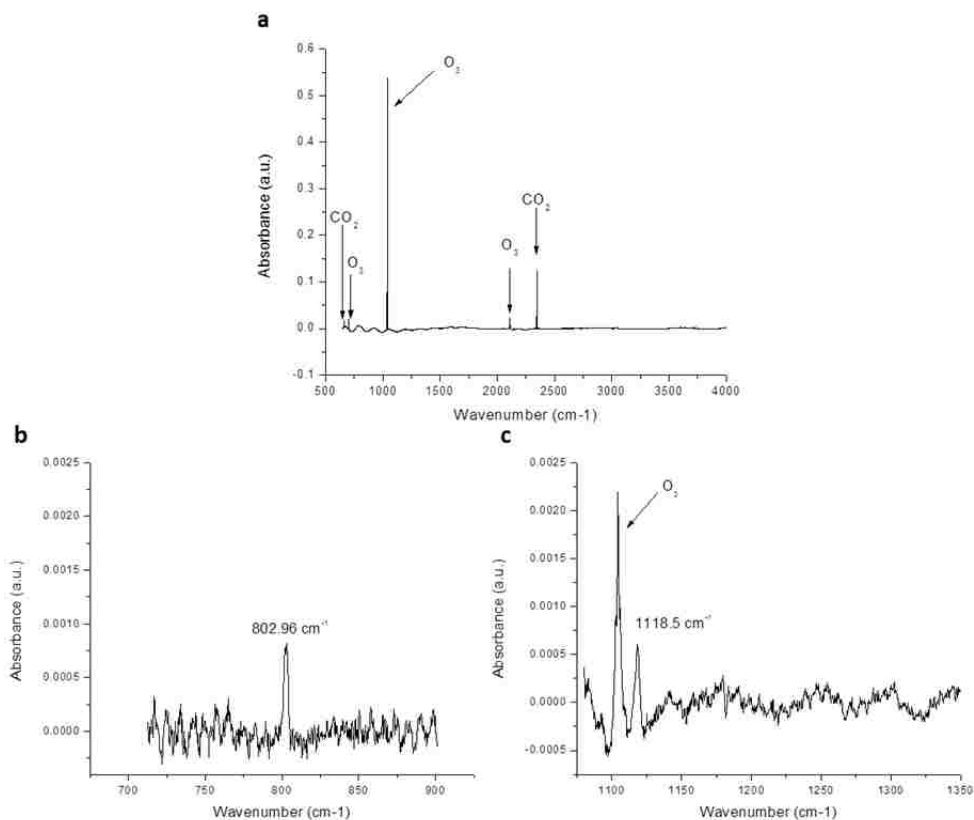


Figure 7.3 a) FTIR spectrum (650-4000 cm⁻¹) taken at 10K for co-deposition of Cu⁻ and Ar⁺ (30eV) with 0.5% O₃ in Ar mixture at 10K (and ~2.5 sccm) for 2 hours (resolution of 0.5 cm⁻¹). b) Focus on the 700-900 cm⁻¹ region. c) Focus on the 1100-1350 cm⁻¹ region. Note that all spectra are on different wavenumber and absorbance scales.

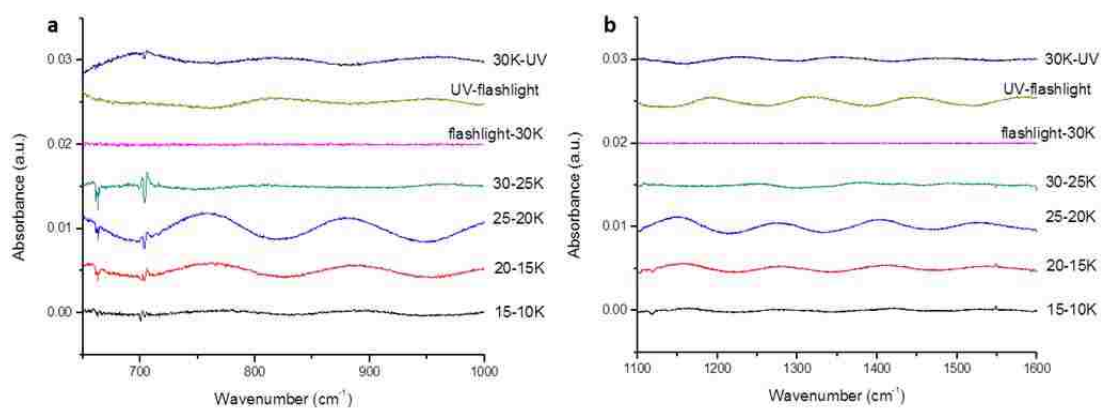


Figure 7.4 Difference spectra to identify changes during 5K annealing steps and photo-exposure steps for the data shown in Figure 7.3. a) Region between 650-1000 cm⁻¹ to look for changes in the CuO₃ peak. b) Region of 1100-1600 cm⁻¹ to look for changes in the trans-O₄⁺ complex.

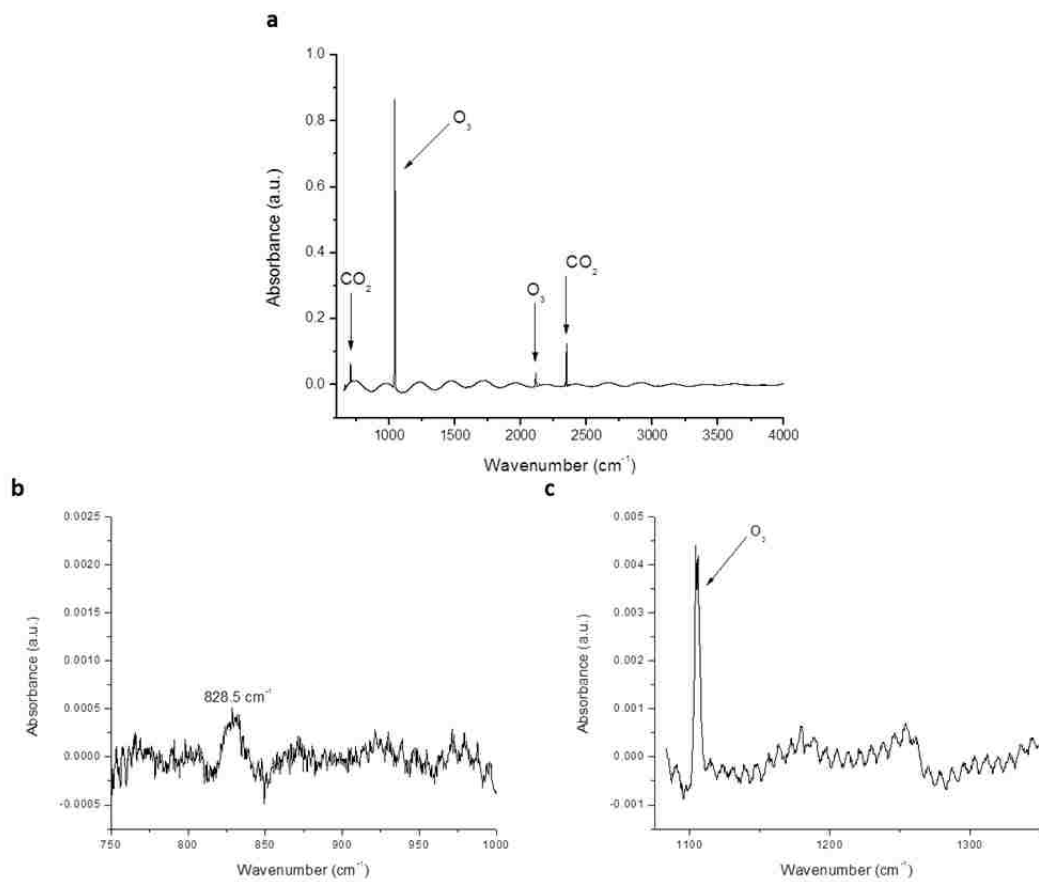


Figure 7.5 a) FTIR spectrum (650-4000 cm⁻¹) for Cu⁻ and Ar⁺ (30eV) co-deposition with 0.5% O₃ in Ar mixture at ~5 sccm at 10K for 2 hours (resolution of 0.5 cm⁻¹). b) Focus on the 700-1000 cm⁻¹ region. c) Focus on the 1100-1350 cm⁻¹; the high frequency, low amplitude sine wave is etaloning due to the matrix. Note that all spectra are on different wavenumber and absorbance scales.

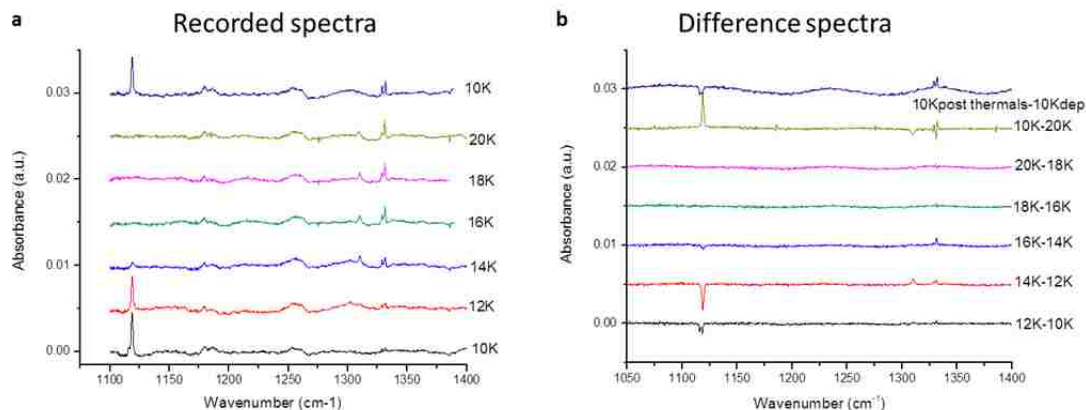


Figure 7.6 a) Recorded and b) difference spectra of the 2K annealing steps for Cu^- , Ar^+ (70eV), and 0.2% O_3 in Ar deposited at 10K and 10 sccm for 4 hours. The system is annealed from the 10K deposited spectrum up to 20K by 2K and then dropped back to 10K (post annealing). In b), the top (navy) line shows the differences observed between the deposited 10K and post-annealing 10K spectra.

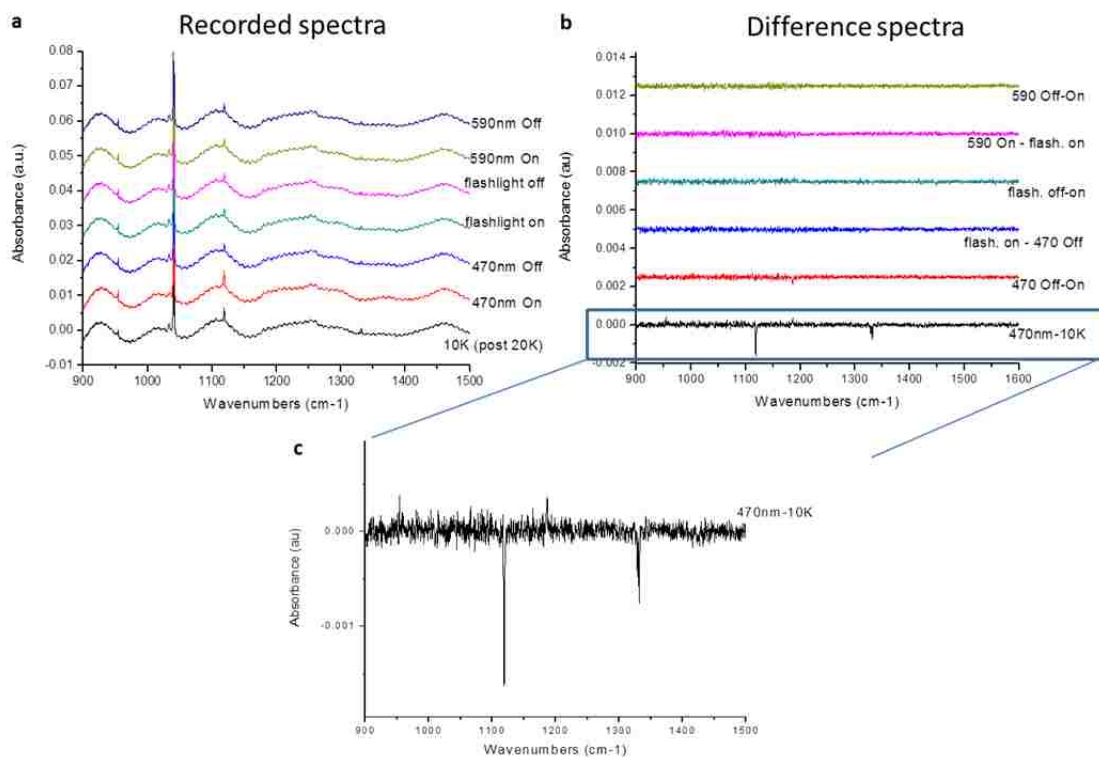


Figure 7.7 a) Recorded and b) difference spectra of the photo-exposure steps for Cu^- , Ar^+ (70eV), 0.2% O_3 in Ar deposited at 10K and 10 sccm for 4 hours. The sine wave in the baseline of a) is matrix etaloning. c) Zoom in on the 470nm-10K difference spectrum to better observe the changes in peaks as a function of light the sample with 470 nm. Note that the scales are different in a) and b).

Figure 7.7 a-c. Upon irradiation of the sample with 470 nm LED light, the trans-O₄⁺ (1118.5 cm⁻¹) and cyclic-O₄⁺ (1329 and 1331 cm⁻¹) peaks decrease, while 1186 cm⁻¹ grows in. In the closer view of the difference spectra (for 470nm On – 10K, Figure 7.7 c), there is also an increase in the O₄⁻ peak along with the 1186 cm⁻¹ increase. When the 470 nm light is turned off, the 1186 cm⁻¹ peak, which previously was assigned to trans-O₄⁺, decreases. This experiment was also completed with 30eV Ar⁺ with other parameters held constant (Cu⁻, 0.2% O₃, 10K and 10 sccm) and shows similar results to the 70eV spectra; the 30eV spectra can be found in Figure A7.7 in Appendix A7.

7.3.4 Cu:O₃:CO Experiments: When ions (Cu⁻, and 30eV Ar⁺), (0.05%) O₃ and (0.15%) CO were deposited at 5 sccm and 20K, peaks corresponding to the weakly bound O₃:CO complexes were observed and two broad features at 1733 and 1829 cm⁻¹. The 1733 cm⁻¹ broad peak may correspond to Cu(CO)⁻ with nearby ozone molecules or different cage shapes, which may be causing the broadness. The broad peak at 1829 cm⁻¹ could correspond to Cu(CO)₃⁻, as this is known to be a sharp peak with some broadness underneath it that has been attributed to larger cluster in the literature.^{1,10} There are no obvious peaks in the 800-1000 cm⁻¹ region that would correspond to CuO₃, O₃⁻ or O₄⁻ complexes (Figure A7.8 in Appendix A7). In the 1100-1400 cm⁻¹ region, the cyclic-O₄⁺ doublet may exist; however, the baseline is rather higher and the doublet is not appreciably higher than the baseline, if the cyclic peaks of 1329 and 1331 cm⁻¹ are there (Figure A7.8b). The full spectrum is shown in Figure A7.9 of the Chapter 7 appendix.

When ions (Cu⁻, and 30eV Ar⁺) and 0.5% of O₃ and 0.3% CO were co-deposited at a lower temperature, 10K, and 5 sccm gas flow rate, O₃⁻, O₄⁻ and O₄⁺ complexes (Figure 7.9 a and b) were observed along with a more confusing 1650-2000 cm⁻¹ region.

This region shows possible peaks at 1684 and 1695.8 cm^{-1} , a broad peak at 1734 cm^{-1} with very small peaks at 1727.6, 1730.8, 1733.5, and 1734.1 cm^{-1} on top of the broad feature, and peaks at 1891.1, 1971, and 1973 cm^{-1} were also observed. There may also be a peak at 1717.5 cm^{-1} that is of similar intensity to 1695.8 cm^{-1} ; however, the baseline is noisy and not flat, so all of these peaks could be overruled as background. The 1733.5 and 1891.1 cm^{-1} (possible) peaks are within 1 cm^{-1} of the reported frequencies of $\text{Cu}(\text{CO})^-$ (1733.4 cm^{-1}) and CuCO (1890.7 cm^{-1}); the 1727.6 cm^{-1} is very similar to $(\nu_2+\nu_3)$ O_3 combination band. The difference spectra (Figure A7.10 in Appendix A7) show a decrease in the 1118.5 cm^{-1} peak (trans-O_4^+) with an increase in the 1548 cm^{-1} peak ($\text{H}_2\text{O}:\text{O}_2$), when annealing from 10K up to 15K and 20K, which also was observed in the Cu^- , 0.5% O_3 in Ar experiment with a 2.5 sccm flow rate (deposition at 10K). There also appears to be a decrease in the 1695.8 cm^{-1} and 1733.5 and 1734.4 cm^{-1} , in which the 1730 peaks almost look like a doublet in the 15K-10K difference spectra. However, there is no clear growth of peaks in the region to suggest possible neutralization of the 1733.5 cm^{-1} peak to neutral CuCO (1890.7 cm^{-1}). The difference spectra for the 1700 cm^{-1} region are found in the Chapter 7 appendix (Figure A7.11), as is the full spectrum (Figure A7.12).

When the concentrations of O_3 and CO (0.2% O_3 and 0.2% CO) were very similar and were deposited with Cu^- and Ar^+ (30eV) at 20K and ~ 5 sccm, there is a peak at 797.7 cm^{-1} , which is 1 cm^{-1} higher than a peak assigned to CuO_3 (at 976.77 cm^{-1}) by Andrews and co-workers,⁶ another at 1730.6 cm^{-1} and a broad feature at ~ 1250 cm^{-1} , which has been observed in other experiments when depositing ions and O_3 with (and without) CO . These peaks are shown in Figure 7.10 a-c. The full spectrum is shown in the Chapter 7

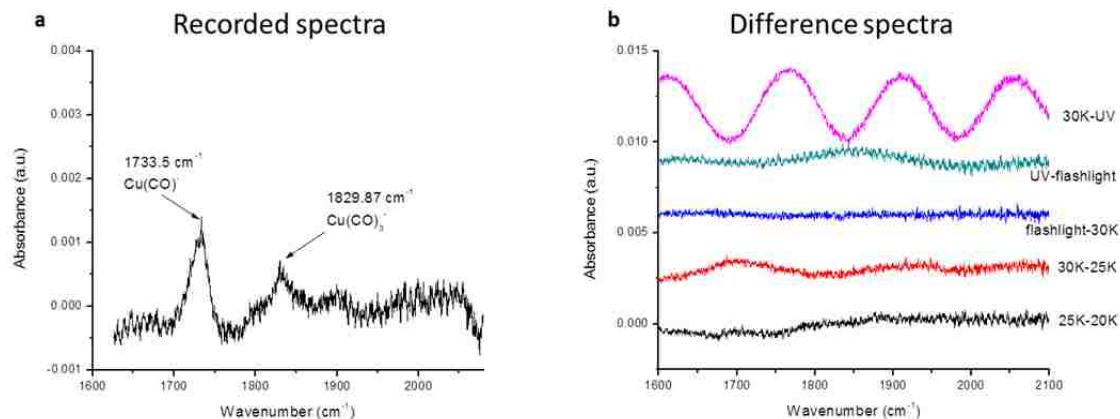


Figure 7.8 a) Recorded spectrum taken at 10K for deposition of Cu⁻, Ar⁺ (30eV), 0.05% O₃ and 0.15% CO in Ar at 20K for 2 hours and b) difference spectra of the 5K annealing and photo-exposure steps. All photo-exposures were completed at 10K. Note that the scales are different in a) and b).

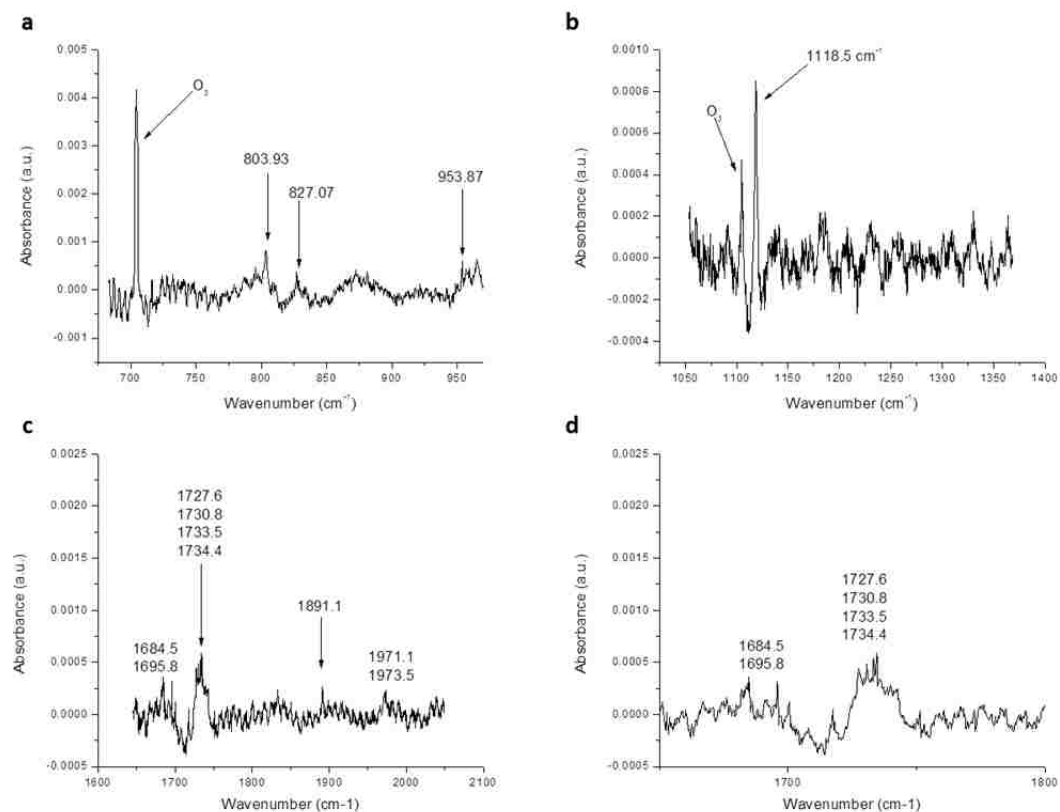


Figure 7.9 a) Region of 700-1000 cm⁻¹ of FTIR spectrum after deposition at 10K of Cu⁻, Ar⁺ (30eV), 0.5% O₃ and 0.3% CO in Ar for 2 hours; b) region of 1050-1400 cm⁻¹; c) region of 1600-2100 cm⁻¹, and d) zoom in on region of 1650-1800 cm⁻¹ to observe the peaks on top of the broad 1734 cm⁻¹ feature. Note that the scales are different in a)-d).

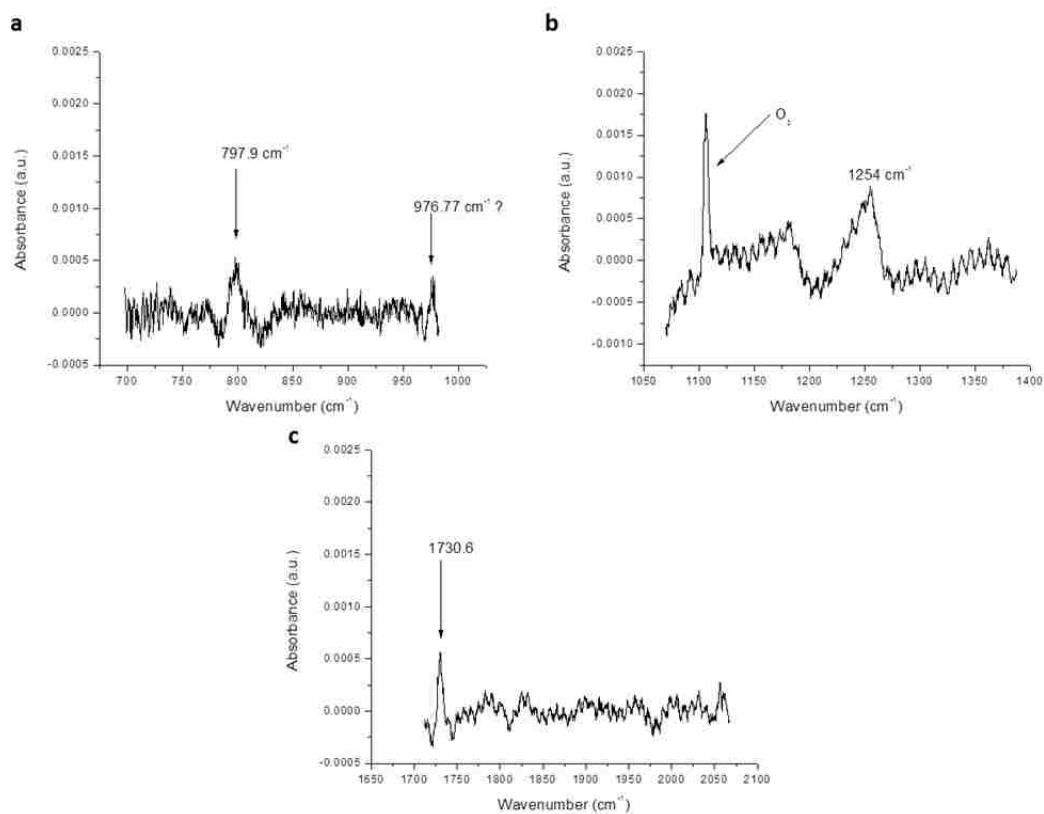


Figure 7.10 a) Region of 700-1000 cm⁻¹ in post-deposition FTIR spectrum after deposition of Cu⁻, Ar⁺ (30eV), 0.2% O₃ and 0.2% CO in Ar at 20K for 2 hours; b) region of 1050-1400 cm⁻¹; c) region of 1650-2100 cm⁻¹. Note that scales are different in a)-c).

appendix, Figure A7.13. No changes were observed with thermal annealing or photo-exposure steps in the difference spectra (Figure A7.14 in Appendix A7).

7.3.5 Peak Comparisons with Cu Computational Work

With the observation of a number of possible peaks that are shifted from literature values for copper ozone, copper oxygen or copper carbonyls, comparisons to calculated binary and ternary complexes can be made in an attempt to better understand the spectra. Calculations of $[\text{CuCO}]^q$, $[\text{CuO}_2]^q$, $[\text{CuO}_3]^q$, $[\text{O}_2\text{CuCO}]^q$ and $[\text{O}_3\text{CuCO}]^q$ ($q=+1,0,-1$) were completed and discussed in Chapter 6. The calculated frequencies of the binary CuCO^q , CuO_2^q , and CuO_3^q complexes can be compared to the experimental frequencies of the respective complexes to determine how much the calculated values are shifted from the experimental. The calculated and experimental frequencies and shifts between these are found in Table A7.2 in the Chapter 7 appendix. These shifts are then applied to the calculated frequencies for CuO_3^- , O_2CuCO^- , and neutral and anionic O_3CuCO complexes, since these complexes have not been reported experimentally in the literature (Table A7.3 and A7.4 in Appendix A7). O_2CuCO (C_{2v}) complex has been previously observed in experiments by Xu and Jiang with 2128.3 cm^{-1} for CO and 1055.3 cm^{-1} for O_2 . For the CuO_3^- (singlet) C_{2v} symmetric complex, the (approximately) expected experimental frequencies should be observed near 786.8 and 716.1 cm^{-1} for symmetric and anti-symmetric O_3 frequencies, respectively. Using the shift for the anti-symmetric stretch (-82.8 cm^{-1}) of CuO_3 is the best estimate for evaluating the shifts of non-symmetric CuO_3 complexes, as well. For the CuO_3^- triplet “out” complex, the expected experimental frequencies are 1080.8 cm^{-1} (for OO bond closer to Cu^-) and 706.2 cm^{-1} for the (exterior OO bond). For the CuO_3^- triplet “in” complex (not C_{2v} symmetric), the

interior OO frequency is expected at 1041.2 cm^{-1} and the exterior is expected at 734 cm^{-1} . For the O_2CuCO^- singlet (C_{2v}) complex, the expected experimental frequency for CO is calculated to be 1851 cm^{-1} and either 688.5 or 818 cm^{-1} for O_2 , depending on the reference CuO_2^- complex of triplet spin state or singlet spin state, respectively. For the O_2CuCO^- triplet complex, the expected experimental frequency for CO could be 1666 cm^{-1} and the O_2 frequency may be 1022.5 or 1152 cm^{-1} , again depending on the triplet or singlet CuO_2^- reference shift. For the O_3CuCO (C_{2v}) “in” complex, the expected experimental CO frequency is 2045 cm^{-1} and the symmetric and anti-symmetric O_3 frequencies are 1007 and 821 cm^{-1} , respectively. The “out” O_3CuCO (neutral) complex has an expected CO frequency of 2060 cm^{-1} and for the interior OO frequency, 564 cm^{-1} is expected, while the exterior OO frequency is expected to be near 1194 cm^{-1} . For O_3CuCO^- singlet (C_{2v}) complex, the expected experimental CO frequency is 1878 cm^{-1} and O_3 symmetric and anti-symmetric frequencies of 811 and 766 cm^{-1} , respectively. For the triplet “in” O_3CuCO^- complex, the expected CO frequency is 1676 cm^{-1} ; interior OO frequency, 655 cm^{-1} , and exterior OO frequency, 1090 cm^{-1} . For the “out” triplet O_3CuCO^- complex, the expected experimental frequency is 1689 cm^{-1} ; interior OO frequency, 497 cm^{-1} , and exterior OO frequency, 1115 cm^{-1} . Finally, for the elongated out O_3CuCO^- triplex complex, the expected experimental CO frequency is 1866 cm^{-1} ; interior OO frequency, 700 cm^{-1} , and exterior OO frequency, 1358 cm^{-1} . The expected experimental frequencies will be compared to the frequencies observed in matrix-isolation experiments of Cu^- , Ar^+ and O^3 and CO, where applicable.

7.4 Discussion:

7.4.1 O₃, CO

Our results are in general agreement with previously report spectra. Raducu *et al.* assign 1041.2 cm⁻¹ to CO:O₃ complex and isolated O₃, but do not explain this assignment, while 1041.3 cm⁻¹ has been previously assigned to isolated O₃.^{2,3} It seems more likely that the 1041.2 cm⁻¹ is isolated O₃ in the “normal” O₃ doublet and the smaller peaks at 1042 and 1043 cm⁻¹ correspond to the weakly bonded O₃:CO complexes, as assigned. We do not see CO₂ formation with UV irradiation, possibly because the UV fiberoptic source is weak; efforts are in progress to design a better way to irradiate the sample with a UV source. One downside to utilizing O₃ and CO in the same gas mix is that the product of their interaction is CO₂; therefore, it is difficult to determine if CO₂ is formed in the bottle or upon deposition of the matrix. We are able to observe the CO:CO₂ complexes at 2143.1 and 2143.4 cm⁻¹, which are different (blue shifted) from those observed by Raducu et al. by ~0.1 cm⁻¹.⁴ Also, the CO:CO₂ complex peaks near CO₂ are more intense than the CO₂ doublet at 2339 and 2345 cm⁻¹, which is somewhat surprising as the CO:CO₂ complexes near CO (2138 cm⁻¹) are very small side peaks at 2143.1 and 2143.4 cm⁻¹. The observation of O₃:CO, (CO)₂, and CO:CO₂ as shoulders and small side peaks to the main CO band, even with 0.125 cm⁻¹ resolution (the highest for our spectrometer) indicates that the CO concentration should be lowered for future studies to better observe and characterize spectra.

7.4.2 Cu, O₃

In the Cu⁻, Ar⁺ (30 eV), and (~0.5%) O₃ experiments at 10K, it was observed that deposition flow rate has significant impact on the observed complexes, since a slower

deposition rate increases the amount of ions per gas molecules. The 2.5 sccm experiment led to formation of a small peak at 802.96 cm^{-1} , assigned to neutral CuO_3 and another peak at 118.5 cm^{-1} , which was assigned to trans-O_4^+ . When the matrix was annealed to up to 20K, the 118.5 cm^{-1} decreased, while a peak at 1548 cm^{-1} increased, which suggests that the O_4^+ complex decomposes into two O_2 molecules that interact with nearby H_2O molecules. Increasing the flow rate to 5 sccm lead to no observation of CuO_3 , but a broad feature at 828.5 cm^{-1} , which is located between two peaks (OCuO or O_2CuO_2) identified by Andrews and co-workers, as discussed above in results. It is possible that the peak at 828 cm^{-1} corresponds to OCuO with a nearby Ar^+ that causes the blue shift in the peak, or this peak could be O_2CuO_2 with a nearby anion (Cu^-) that causes the red shift in the peak to 828 cm^{-1} . However, the difference spectra showed no changes in the 828 cm^{-1} peak as a function of thermal annealing or photo-exposure, which suggests that this peak (and its related complex) is stable. One might expect a complex with a nearby ion to combine upon annealing or photo-exposure. Other similar experiments at 20K also show no formation of CuO_3 complexes, but O_4 ionic complexes have been formed at 10K and 20K deposition temperatures, which suggests that the ozone may be decomposing upon interaction with Cu^- and forming copper oxides and molecular O_2 . Molecular O_2 can interact with other O_2 molecules and the ions in matrix (Cu^- and Ar^+), which could form the O_4^+ and O_4^- complexes. Unfortunately, the range of the current detector (mercury cadmium telluride narrow band with cutoff at 650 cm^{-1} , an MCT A) does not overlap with the vibrational frequencies of copper oxides (anionic or neutral).

When the energy of Ar^+ was increased to 70eV (and deposition time was doubled), O_4^- ionic complexes were more intense and O_3^- was also formed, but no CuO_3 complexes. The O_4^- and O_4^+ complexes display some unique thermally dependent traits in the thermal and photo-exposure steps. The O_4^- peak blue shifts by $\sim 1 \text{ cm}^{-1}$ when heating the sample to 20K; the peak returns to 953.8 cm^{-1} , when the matrix is cooled to 10K. As discussed in results, *trans*- O_4^+ decreases with increasing temperature up to 20K, while peaks at 1310 and 1329/1331 cm^{-1} grow in. Cooling the matrix to 10K again reverses the trends mentioned above and the 1118.5 cm^{-1} (*trans*- O_4^+) peak increases, while 1310 cm^{-1} is lost. The 1329 and 1331 cm^{-1} doublet is retained, which is likely due to an irreversible reaction to form these cyclic- O_4^+ related peaks. With the reversible loss and growth of 1118.5 cm^{-1} and 1310 cm^{-1} in opposite directions, there appears to be a thermal equilibrium that is being probed. This reversibility was identified in an O_2 , Cu^- , and Ar^+ experiment previously in our group, and observation in the O_3 system shows that the oxygen source (O_2 vs. O_3) will not stop the thermal reversibility. The photo-exposure studies also had interesting results, where 1186 cm^{-1} , a *trans*- O_4^+ species grows in under 470 nm light and O_4^- also increases, while 1118.5 cm^{-1} and cyclic- O_4^+ (1329 and 1331 cm^{-1}) decrease. Once the light is turned off, the 1186 cm^{-1} peak decreases, but there is no apparent recovery in the other complexes. All other light exposure steps do not have appreciable effects on these peaks either. These results are somewhat perplexing, especially when compared to the O_2 studies in which the same peaks respond to the flashlight irradiation. Further studies are required on the O_3 system with Ar^+ at different energies (no Cu^-) for better understanding of these results. Also, the “original” 2.5 sccm experiment (10K, Cu^- , 30eV Ar^+) had a concentration of ozone of $\sim 0.5\%$, while the more

recent 10 sccm experiments (10K, Cu^- , 30eV or 70eV Ar^+) had concentrations of ozone of $\sim 0.2\%$; better comparisons could be made with the same or more similar ozone concentrations. Beyond this, more recent work with 10 sccm and the MKS flow controller (and also a Teflon-coated bottle) has significant CO_2 contamination and very depressed levels of ozone, which indicates there is a carbon source in the system.

7.4.3 Cu, O₃, CO

Observation of tiny peaks that correspond to copper carbonyls is very encouraging that it is possible to form copper carbonyls in the presence of different gases at 20K deposition temperature; however, each experiment, whether at 10K or 20K deposition temperature, utilized at least 0.05% CO concentration, which produced the intense CO “parent” peak at 2138 cm^{-1} , but $\text{Cu}(\text{CO})^-$ and $\text{Cu}(\text{CO})_3^-$ were on the order of ~ 0.001 absorbance units. Very tiny peaks and, in some experiments, the lack of copper complexes is not intuitive because deposition of Cu^- , Ar^+ and CO forms $\text{Cu}(\text{CO})_n^q$ ($q=0,-1, n=1-3$) complexes.¹ However, there have also been issues with the co-deposition of O_2 and CO with Cu^- and Ar^+ . The low level of copper-complex formation suggests that the ozone may interfere with the ability of CO and Cu^- to form complexes and also would indicate problems in isolating intermediate complexes of the CO oxidation mechanism.

The lower temperature deposition experiments, at 10K, led to a complex 1650-2000 cm^{-1} region with several peaks on the top of the broad 1734 cm^{-1} peak. The 1733.5 cm^{-1} may correspond to $\text{Cu}(\text{CO})^-$, and other nearby vibrations may be $\text{Cu}(\text{CO})^-$ complexes with a nearby cation, anion, or ozone molecule, or an O_3CuCO^- complex, except no concomitant O_3 peak is observed, unless the peak at 827 cm^{-1} is the O_3 vibration. One observation that goes against this idea is that thermal annealing and

photo-exposure show no obvious changes in the 827 cm^{-1} or 1700 cm^{-1} peak.

Experiments in our group on the anionic copper carbonyls show conversion of the anionic complexes to neutral copper carbonyls with photo-exposure and thermal annealing, depending on the deposition conditions.

When using “higher concentrations” of O_3 and CO (0.2%) co-deposited with ions at 20K, a peak possibly corresponding to CuO_3 was observed and also a peak at 1730.6 cm^{-1} , which is red shifted from the $\text{Cu}(\text{CO})^-$ value by $\sim 3\text{ cm}^{-1}$. The shifting could indicate the formation of a complex of O_3CuCO^- , but there are no changes observed in the difference spectra with thermal annealing and photo-exposure. Based on the neutralization of anionic copper carbonyls when exposed to the flashlight, it would also be reasonable to expect an O_3CuCO^- complex to neutralize, when exposed to light or UV.

Another point of concern in these experiments is that CuO_3 and copper carbonyls were not consistently produced; all of the conditions discussed above were different with respect to concentrations and deposition temperature, which could be the reason for the inconsistencies. When the CO concentration was three times higher than O_3 and deposited at 20K, very small peaks at 1733 cm^{-1} and 1829 cm^{-1} were observed, which correspond to $\text{Cu}(\text{CO})^-$ and $\text{Cu}(\text{CO})_3^-$, respectively. When the concentrations of both gases were higher for deposition at 10K (0.5% O_3 and 0.3% CO in Ar), peaks corresponding to O_3^- , O_4^- and O_4^+ were observed, along with 827 cm^{-1} and several possible peaks in the $1650\text{-}2000\text{ cm}^{-1}$ region with a broad feature at $\sim 1734\text{ cm}^{-1}$ and a number of small peaks were “on top” of the broad feature; the peaks at 1733.5 and 1891.1 cm^{-1} are within 1 cm^{-1} of $\text{Cu}(\text{CO})^-$ and CuCO , respectively. Returning to 20K deposition with very similar concentrations (0.2%) for O_3 and CO , peaks at 797.9 cm^{-1} , 976.77 cm^{-1}

and 1730.6 cm^{-1} were observed, where 797.9 cm^{-1} peak is within $\sim 1\text{ cm}^{-1}$ of a peak related to CuO_3 , as reported by Andrews. Better control of gas concentrations and then a systematic change of the gas concentrations (to unbalanced values in which CO or O_3 is higher than the other) with all other deposition parameters held constant is necessary to better understand the interactions of ozone and CO with Cu^- and Ar^+ .

7.4.4 Peak Comparisons with Cu Computational Work

The comparison of DFT calculated and experimental frequencies is a major goal of this work and thesis to determine if the calculated reaction pathways and complexes are experimentally relevant. The unassigned peaks that were observed in the Cu^- , Ar^+ , O_3 and Cu^- , Ar^+ , O_3 and CO experiments can be compared to the (shifted) calculated frequencies for CuO_3^- , O_2CuCO^- and neutral and anionic O_3CuCO^- complexes (Appendix A7 Tables A7.3 and A7.4). There are peaks, typically broad peaks, observed at 827 or 828 cm^{-1} , which could correspond to O_3CuCO “in” C_{2v} complex, except 828 cm^{-1} is observed in experiments without CO. The calculated (and shifted) CuO_3^- frequencies are blue or red shifted by more than 40 cm^{-1} from the 828 cm^{-1} peak, while the O_3 anti-symmetric stretch of O_3CuCO “in” C_{2v} complex is within 7 cm^{-1} of the 828 cm^{-1} peak. The 827 cm^{-1} peak is found in an experiment with ions, O_3 and CO, where the related CO frequency should be found at $\sim 2045\text{ cm}^{-1}$. There are no unassigned bands (or peaks, in general) in the $2000\text{-}2050\text{ cm}^{-1}$ region, which makes the 827 cm^{-1} assignment less likely; however, there are peaks at 1971 and 1973 cm^{-1} , where one could correspond to a CO frequency, but would indicate that the chosen shift (for CO frequencies) is off by $\sim 70\text{ cm}^{-1}$. The 1684 and 1695 cm^{-1} peaks are similar to the O_3CuCO^- triplet “in” and out” (calculated and shifted) CO frequencies of 1676 and 1689 cm^{-1} , respectively; however,

the OO-related frequencies of the “out” complex are calculated to be near 497 and 1115 cm^{-1} , where 497 cm^{-1} is not observable with our detector and no peak was observed at 1115 cm^{-1} . The calculated (and shifted) OO-related frequencies of triplet “in” O_3CuCO^- complex should be close to 655 and 1090 cm^{-1} , which are not observed in the spectra or at least not above the baseline. For the peaks at 976.77 cm^{-1} and 1730.6 cm^{-1} and the broad feature in one spectrum at 1254 cm^{-1} , there are no calculated (and shifted) frequencies for the aforementioned complexes that are close. While there are some similarities between the (shifted) calculated and experimental frequencies, more experimental work and repeated experiments with the same parameters are necessary for better comparison of calculated and experimental results, along with gaining a better understanding of the O_3 , CO, Cu^- and Ar^+ system.

7.4.5 CO_2 Contamination

Several of the $\text{O}_3:\text{CO}$ experiments (with and without ions) have shown very depressed levels of ozone in the spectra, compared to CO, upon deposition, and the CO_2 peak also tends to be relatively intense in IR spectra. It is possible that ozone is decomposing to form copper oxides in the matrix and (or) decomposing to form O_2 and CO_2 in the bottle, as there was a larger than typical CO_2 peak. Whether we are depositing O_2 from O_3 decomposition in the storage bottle or ozone is decomposing to form O_2 and CuO , the results have shown that O_2 species are in the matrix and appear to be acting as electron scavengers.

A major issue with these results is the ever-present CO_2 in our deposition spectra. While we were able to lower the intensity below that of O_3 for some experiments, CO_2 was always “contaminating” the spectra. Groups who have completed matrix isolation

studies with ozone have stated that some CO₂ is always present in the spectra, but they do not show this region or indicate the intensity for a comparison.^{3,5} This contamination also presents a challenge as the goal of this work is to track CO oxidation, where the major product is CO₂. Contamination with CO₂ makes it more difficult to identify CO oxidation in matrix processes.

7.5 Conclusions

While we have been able to deposit ozone with other gases and observe weakly bound O₃:CO complexes, we have more difficulty in depositing and observing ozone and carbonyl complexes with ions (Cu⁻ and Ar⁺). There have been some observations of small peaks that are related to copper carbonyls, when depositing O₃ and CO with ions. However, oxygen-related complexes (O₃⁻, O₄⁺ and O₄⁻) are observed in greater intensities than copper carbonyl or CuO₃ complexes, when depositing O₃ (with or without CO) and ions. Further, more careful study is necessary to understand what is happening to the ozone in the matrix, along with repetition of experiments with the same parameters; use of a detector that can detect below 650 cm⁻¹ is required to determine if copper oxides are being formed along with the oxygen-related (O₄) complexes.

7.6 Experimental Methods

Experimental details relating to the Cu deposition source and matrix isolation gas deposition system and interface were discussed in Chapter 2. When utilizing the different deposition temperatures, different concentrations of gas mixtures (O₃ and CO in Ar) were made, where the 10K deposition concentrations were between ~0.2% and 0.5% and 20K (and 25K) deposition concentrations were ~0.05% to ~0.15%. The gas deposition flow rates were also altered, depending on the gas metering device; lower flow rates between

~2 and 5 sccm (standard cubic centimeters per minute) were utilized with a regulator and needle valve. Experiments with ~5 sccm (gas) flow rate or lower were completed with a regulator on one liter bottle and needle valve to control the flow throughout the two hour deposition. The approximate rate was determined by flowing argon through an Alicat mass flow controller (on a different deposition line) and recording the pressure in the chamber at certain flow rates (1-10 sccm). The needle valve and regulator settings were dependent on the amount of gas (pressure) in the liter bottle and would require more tuning slowly by hand, while watching the pressure in the chamber, to balance the flow rate to the desired value. A higher flow rate of 10 sccm was used with an MKS flow controller in later experiments for better comparison with “in-house” results, as most other experiments completed with the instrument, but different gas mixtures and delivery system, are done at 10 sccm. Also, a mass flow controller allows one to set and know the desired flow rate consistently. The energy of Ar^+ was also altered between 30 eV and 70 eV; other experiments inside of the group have shown that 70 eV energy (for Ar^+) produced the optimal current (~4-11 nA), but 30 eV is closer to the ionization potential of Ar. All experiments were performed in the dark, based on previous work in the group, in which the gas mixtures (and ions, if in the experimental plan) are deposited onto a KBr window (wedged by 0.5° by Koch Crystal Finishing). After deposition for 2-4 hrs, a spectrum is taken at 10K; the matrix is then thermally annealed to 15, 20, 25 and 30K (for 30 minutes) and the temperature is re-set to 10K after each annealing temperature for “post-annealing” spectra. The matrix is also exposed to light; early experiments used an “ordinary” flashlight and UV (fiberoptic) source and later experiments used a 470 nm (blue light) LED source, a 590 nm (orange) LED source, flashlight, and UV source. The

flashlight spectrum is found in the Chapter 7 appendix, Figure A7.1. Photo-exposure was done at 10K for 5 minutes for the flashlight; 30 minutes for the UV source and 15-30 minutes for the 470 nm and 590 nm LED lights. All spectra were taken at 10K, unless otherwise noted in the text and figure captions. Difference spectra were also generated by subtracting one taken spectrum from another to look at the effects of the annealing and photo-exposure steps, e.g. subtract the post(20K) deposition spectrum from the 25K annealed spectrum. Also found in the Chapter 7 appendix (Figures A7.15-A7.18 and Table A7.5) are the results of experiments with a residual gas analyzer (RGA) to determine the location of CO₂ generation.

7.7 References

- (1) Ludwig, R. M.; Moore, D. T. *J. Chem. Phys.* **2013**, *139*, 244202.
- (2) Brosset, P.; Dahoo, R.; Gauthierroy, B.; Abouaf-Marguin, L.; Lakhlifi, A. *Chem. Phys.* **1993**, *172*, 315-324.
- (3) Raducu, V.; Jasmin, D.; Dahoo, R.; Brosset, P.; Gauthierroy, B.; Abouaf-Marguin, L. *J. Chem. Phys.* **1994**, *101*, 1878-1884.
- (4) Raducu, V.; Jasmin, D.; Dahoo, R.; Brosset, P.; Gauthierroy, B.; Abouafmarguin, L. *J. Chem. Phys.* **1995**, *102*, 9235-9239.
- (5) Tevault, D. E.; Mowery, R. L.; Demarco, R. A.; Smardzewski, R. R. *J. Chem. Phys.* **1981**, *74*, 4342-4346.
- (6) Chertihin, G.; Andrews, L.; Bauschlicher, C. *J. Phys. Chem. A* **1997**, *101*, 4026-4034.
- (7) Thompson, W. E.; Jacox, M. E. *J. Chem. Phys.* **1989**, *91*, 3826-3837.
- (8) Zhou, M.; Hacaloglu, J.; Andrews, L. *J. Chem. Phys.* **1999**, *110*, 9450-9456.
- (9) Cooper, P.; Kjaergaard, H.; Langford, V.; McKinley, A.; Quickenden, T.; Robinson, T.; Schofield, D. *J. Phys. Chem. A* **2005**, *109*, 4274-4279.
- (10) Zhou, M.; Andrews, L. *J. Chem. Phys.* **1999**, *111*, 4548-4557.

Chapter 8. Efforts toward Expanding the Size of Clusters Studied in DFT Calculations: Au_2^q with CO and O_2 (or O_3) ($q = +1, 0, -1$) and Future Work

8.1 Au_2 Introduction

CO oxidation over anionic Au_2 clusters and the interactions of CO and O_2 with these clusters have been studied previously with gas phase experiments and calculations to develop a catalytic cycle, based on the experimental results. While Au_2 anions have been previously studied for CO oxidation (with O_2) and a possible catalytic cycle has been developed,^{1,2} we investigated the Au_2^q ($q = +1, 0, -1$) interactions with CO and O_2 (or O_3) to look for trends in the CO oxidation pathways as a function of size (and charge).

8.2 Results

Binary $[\text{Au}_2\text{CO}]^q$, $[\text{Au}_2\text{O}_2]^q$, and $[\text{Au}_2\text{O}_3]^q$ and ternary complexes of $[\text{O}_2 + \text{Au}_2 + \text{CO}]^q$ and $[\text{O}_3 + \text{Au}_2 + \text{CO}]^q$ have been studied with DFT calculations (B3LYP-SDD/6-311+G(3df)). The binary $[\text{Au}_2\text{CO}]^q$, $[\text{Au}_2\text{O}_2]^q$ complexes are collected into Figure 8.1 and the $[\text{Au}_2\text{O}_3]^q$ complexes are found in Figure 8.2. The ternary $[\text{O}_2\text{Au}_2\text{CO}]^q$ complexes are collected in Figure 8.3. Tables 8.1, 8.2, and 8.3 have the bond lengths, vibrational frequencies and energies for the binary $[\text{Au}_2\text{CO}]^q$, $[\text{Au}_2\text{O}_2]^q$ and ternary $[\text{O}_2\text{Au}_2\text{CO}]^q$ complexes. The ternary $[\text{O}_3\text{Au}_2\text{CO}]^q$ complexes have not been vetted as thoroughly as the O_2 -related Au_2 complexes, nor have pathways been developed (fully) for either oxygen allotrope system. The results presented here are the completed DFT calculations, to this point, for the Au_2^q systems, as shown in Figures 8.2, 8.4 and 8.5 and Tables 8.4 (bond lengths) and 8.5 (energies).

8.2.1 Binary Complexes: Au_2CO , Au_2O_2 , and Au_2O_3

Au_2CO : Au dimer carbonyl complexes have been calculated for the three charge states, +1, 0, -1. The cationic Au_2CO complex is linear, as is the neutral singlet complex (Figure

8. 1 A and B), reminiscent of the linear $[\text{AuCO}]^+$. The Au_2 bond of the cationic complex is similar to Au_2^+ with a CO bond of 1.118 Å; the Au_2 bond of the neutral complex is similar to Au_2 (neutral) and a CO bond of 1.128 Å like free CO and CO frequency of 2190 cm^{-1} . The neutral triplet complex has a non-planar bidentate carbonyl structure; the Au_2 bond length is most similar to Au_2^- (longer than the neutral singlet length by ~ 0.29 Å), and the CO bond is ~ 0.02 Å longer than the neutral singlet; the CO frequency is red shifted by ~ 200 cm^{-1} from the neutral singlet frequency (Tables 8.1 and 8.2). The neutral singlet is stable at -23.33 kcal/mol, while the neutral triplet carbonyl complex is not stable with respect to the reactant asymptote. The anionic (doublet) Au_2CO complex has a bent AuCO angle of 131.9°, which is similar to the AuCO^- structure. The CO bond of 1.178 Å is most similar to CO^- and a related frequency of 1848 cm^{-1} with an Au_2 bond length (2.639 Å) that is shorter than the neutral triplet by 0.21 Å (Tables 8.1 and 8.2).

Au_2O_2 : All Au_2O_2 complexes have bent AuOO angles, reminiscent of the AuO_2^{q} complexes. The cationic Au_2O_2 (doublet) complex has an Au_2 bond of 2.687 Å, similar to Au_2^+ , and OO bond length of 1.202 Å with an AuOO angle of 125.5° and related O_2 frequency. The neutral singlet Au_2O_2 complex has a smaller angle of 124.2° and Au_2 bond shorter than Au_2O_2^+ by ~ 0.12 Å and a longer O_2 bond of 1.222 Å with a red-shifted OO frequency to 1454 cm^{-1} (from Au_2O_2^+ value). The neutral triplet Au_2O_2 complex has a smaller AuOO angle of 121.6°, a slightly longer (than neutral singlet) Au_2 , and OO bonds of 2.571 Å and 1.239 Å, respectively; the OO frequency (1551 cm^{-1}) blue shifts slightly from the neutral singlet (Tables 8.1 and 8.2). The neutral singlet Au_2O_2 complex at 29.17 kcal/mol is not stable with respect to the ground state reactants of Au_2 and O_2 (triplet), while the neutral triplet complex is stable at -0.46 kcal/mol. The anionic

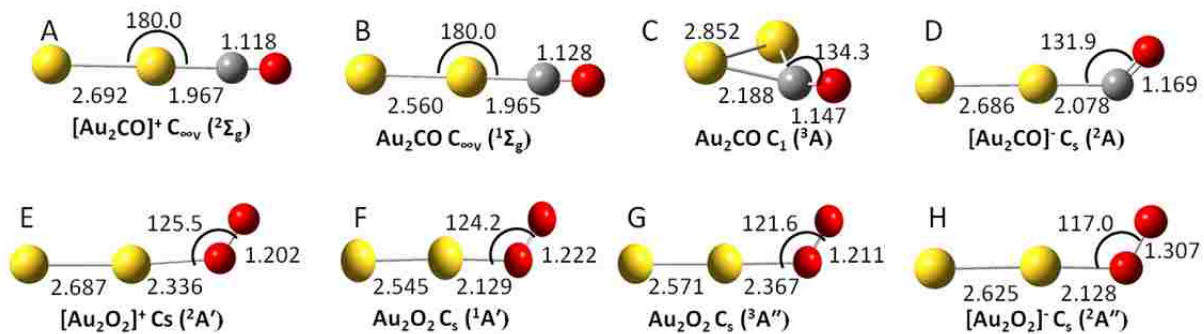


Figure 8.1 B3LYP predicted binary $[\text{Au}_2\text{CO}]^q$ and $[\text{Au}_2\text{O}_2]^q$ ($q=+1, 0, -1$) complexes with bond length (\AA) and angles ($^\circ$).

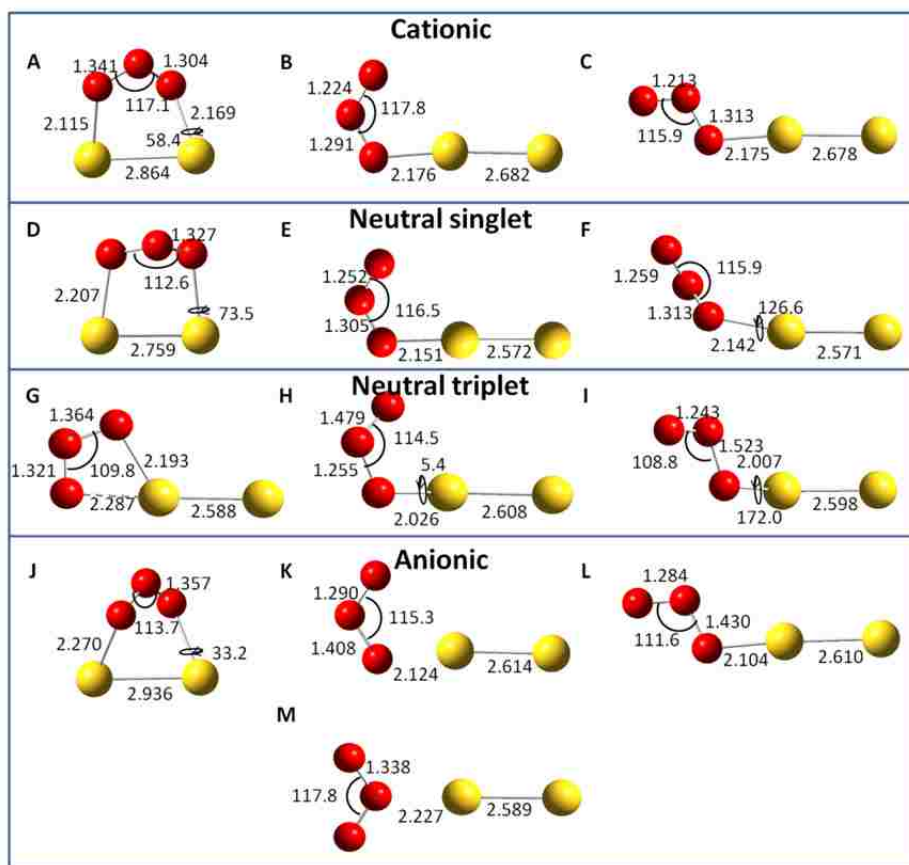


Figure 8.2. B3LYP predicted structures for the binary $[\text{Au}_2\text{O}_3]^q$ complexes with bond lengths (\AA) and angles ($^\circ$), where structures A-C are the cationic (doublet) structures; D-F, neutral singlet; G-I, neutral triplet, and J-M are anionic (doublet) structures.

Table 8.1. B3LYP predicted bond lengths (in Å) for binary $[\text{Au}_2\text{CO}]^q$ and $[\text{Au}_2\text{O}_2]^q$ and ternary $[\text{O}_2\text{Au}_2\text{CO}]^q$ or $[\text{Au}_2\text{COO}_2]^q$ complexes ($q=+1, 0, -1$).

Au ₂ CO bonds			O ₂ Au ₂ CO or Au ₂ (CO)O ₂ bonds					Au ₂ O ₂ bonds				
	Au-C	AuAu	C-O	AuC	C-O	AuAu	AuO	O-O	AuO	Au-Au	O-O	
Separated												
Cationic	1.967	2.692	1.118	1.966	1.118	2.671	2.420	1.198	2.336	2.687	1.202	
Neutral	Singlet	1.956	2.560	1.128	1.974	1.127	2.578	2.167	1.239	2.129	2.545	1.222 ^a
	Triplet	2.188	2.852	1.147	1.960	1.129	2.559	2.794	1.204	2.167	2.571	1.239
Anionic	Doublet	2.047	2.639	1.178	2.038	1.145	2.591	2.165	1.316	2.128	2.625	1.307
“Pre-reactive” (peroxycarbonyl)												
Anionic doublet 180° dihedral				2.047	1.178	2.639		1.245				
Anionic doublet 0° dihedral				2.039	1.179	2.644		1.302				
Reference lengths^b	Au-Au+	2.701	C-O	1.124								
	Au-Au	2.578	C-O ⁺	1.108	O-O	1.203	O-O	1.341	O-O	1.559		
	Au-Au-	2.723	C-O ⁻	1.183	(O ₂)		(O ₂) ⁻		(O ₂) ²⁻			

^aAu₂O₂ singlet is restricted (closed shell) due to high spin contamination in the unrestricted singlet calculation.

^bcalculated at same level of theory: B3LYP/6-311+G(3df) and O₂ reference bond length is from the triplet ground state species.

Table 8.2. B3LYP predicted stretching vibrational frequencies in, cm⁻¹, and intensities (in parenthesis) for binary $[\text{Au}_2\text{CO}]^q$ and $[\text{Au}_2\text{O}_2]^q$ and ternary $[\text{O}_2\text{Au}_2\text{CO}]^q$ or $[\text{Au}_2\text{COO}_2]^q$. Labels A-F correspond to the structures shown in Figure 8.3.

Species		Stretching frequency –cm ⁻¹ (Intensity)			
	Electronic state	Au-C	C-O	Au-O	O-O
$[\text{Au}_2\text{CO}]^+$	² A ₁ (² Σ ⁺)	372 (8.96)	2281 (332.3)		
Au ₂ CO	¹ A ₁ (¹ Σ ⁺)	381 (1.18)	2190 (615.2)		
Au ₂ CO	³ A	267 (1.43)	1993 (628.4)		
$[\text{Au}_2\text{CO}]^-$	² A'	381 (6.56)	1848 (2816.9)		
$[\text{Au}_2\text{O}_2]^+$	² A			218 (2.48)	1596 (27.2)
Au ₂ O ₂	¹ A			361 (3.01)	1454 (468.2)
Au ₂ O ₂	³ A			193 (0.11)	1551 (196.4)
$[\text{Au}_2\text{O}_2]^-$	² A			420 (13.4)	1183 (379.0)
$[\text{O}_2\text{Au}_2\text{CO}]^+$ A	² A	375 (7.50)	2275 (375.4)	101 (0.08)	1580 (184.5)
O ₂ Au ₂ CO B	¹ A	362 (1.14)	2197 (667.9)	333 (12.9)	1382 (676.9)
O ₂ Au ₂ CO C	³ A	377 (0.98)	2188 (661.0)	39 (0.66)	1625 (14.9)
$[\text{O}_2\text{Au}_2\text{CO}]^-$ D	² A	354 (97.1)	2032 (1570.9)	388 (0.89)	1178 (333.0)
$[\text{Au}_2(\text{CO})\text{O}_2]^-$	² A'	683 (8.17)	1840 (349.5)		1016 (5.73)

“out” E		416 (179.9)	
[Au ₂ (CO)O ₂] ⁻	² A''	762 (199)	1857 (526)
“in” F		322 (111)	1214 (64)

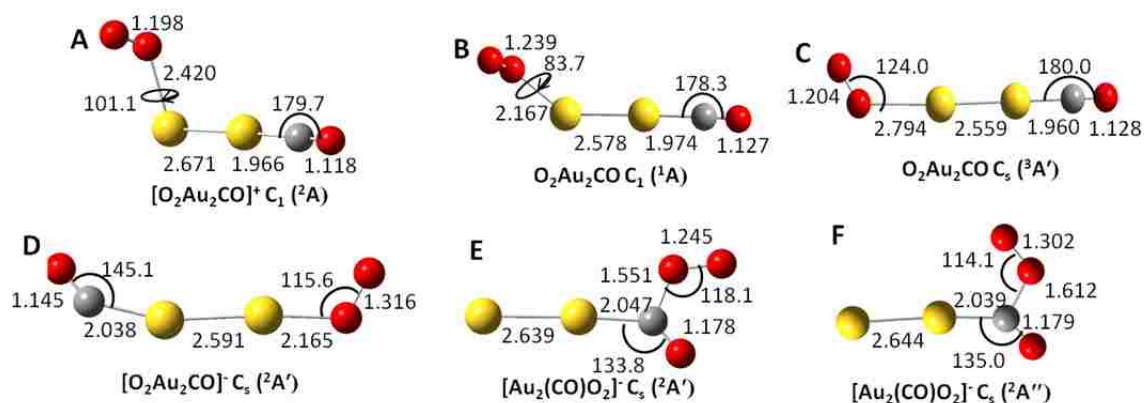


Figure 8.3 B3LYP predicted ternary [O₂Au₂CO]^q (q=+1, 0, -1) complexes with bond length (Å) and angles (°).

Table 8.3. ZPE and BSSE corrected binding energies^a (kcal/mol) for binary [Au₂CO]^q and [Au₂O₂]^q and ternary [O₂Au₂CO]^q or [Au₂COO₂]^q complexes (q=+1, 0, -1) and cooperative binding evaluated for similarly charged complex groups.

	Au ₂ CO	Au ₂ O ₂	O ₂ Au ₂ CO or Au ₂ (CO)O ₂ ^b	Cooperative binding ^{b,c}
Separated				
Cationic	-34.43	-5.68	-39.31	0.81
Neutral	Singlet	-23.33 ^d	29.17 ^e	6.81
	Triplet	26.12	-0.46 ^d	-23.41 ^d
Anionic	-8.76	-65.15	-29.50	44.40
Peroxy carbonyl				
Anionic doublet “out”			-18.70	55.21
Anionic doublet “in”			-31.37 ^d	42.54

^a Computed relative to optimized values of the *ground state* components, with charge (if any) localized on gold center.

^b Parenthetical values computed relative to the energy of O₂ singlet, as shown here: [E_{AuOO} - (E_{Au} + E_{OOsinglet})] or [E_{OOAuCO} - (E_{Au} + E_{CO} + E_{OOsinglet})].

^c Cooperative binding is calculated as the difference between total binding energy of ternary complex and summed binary complexes as shown here: E_{OOAuCO} - E_{AuOO} - E_{AuCO}. The Au₂O₂ energy used in cooperative binding is the ground state triplet. Parenthetical cooperative binding values are calculated in the same fashion, but utilize the parenthetical values of the binary and ternary singlet complexes, where applicable.

^d Lowest energy state per species with the same charge and molecular components.

^e Au₂O₂ singlet was calculated as restricted (closed shell) due to high spin contamination in the unrestricted singlet calculation.

(doublet) Au_2O_2 complex has the smallest AuOO angle of 117.0° , longest OO bond of 1.307 \AA , similar to O_2^- and shorter Au_2 bond at 2.625 \AA with a related OO frequency of 1183 cm^{-1} .

Au_2O_3 : As shown in Figure 8.2, there are several Au_2O_3 isomers in each charge state that are stable with respect to the ground state components; the bond lengths are collected into Table 8.3. There are three stable cationic complexes, bridging (A), O_3 in (B) and O_3 out (C), and an “unstable” Y-like structure complex with an energy of 0.90 kcal/mol . The O_3 in (B) and O_3 out (C) complexes are similar to the O_3 connection to Au in O_3AuCO (separated) complexes, as observed in Figure 8.2. The OO bonds will be described similarly to those in Chapters 5 and 6, where O_α is attached to Au, O_β is the next and O_γ is the last O atom. The bridging complex (8.2 A) is the global minimum of the Au_2O_3^+ complexes with an energy of -25.69 kcal/mol . The Au_2 bond is elongated to 2.864 \AA , and AuO bonds are similar, but not symmetric. The OO bonds are also non-symmetric with lengths of 1.341 \AA and 1.304 \AA , which are most similar to O_3^- . The “ O_3 in” complex (8.2 B) is higher in energy by $\sim 7.5 \text{ kcal/mol}$ with a significantly shorter Au_2 bond, similar AuO bond of 2.176 \AA , and shorter OO bonds by $\sim 0.05 \text{ \AA}$ (or greater) at 1.291 and 1.224 \AA , which are similar to O_3 and O_3^+ , respectively. The third complex, “ O_3 out” (8.2 C), has a similar Au_2 and AuO bond lengths to “ O_3 in” lengths. The $\text{O}_\alpha\text{O}_\beta$ is longer by $\sim 0.02 \text{ \AA}$, while the $\text{O}_\beta\text{O}_\gamma$ is shorter by $\sim 0.01 \text{ \AA}$, where the lengths are similar to O_2^- and O_2 , respectively.

For the neutral singlet state, there are three Au_2O_3 complexes that are stable with respect to the separated components, shown in Figure 8.2 D-F with a bridging structure (D), “ O_3 in” (E), and non-planar “ O_3 out” (F) structure. There is an unstable Au_2O_3

complex at 1.42 kcal/mol, where the Au₂ bond is 4.559 Å and O₃ has “inserted” into the Au₂ bond. The non-planar bridging complex (8.2 D) is the lowest energy structure at -11.56 kcal/mol. The structure has symmetric AuO and OO bonds of 2.207 and 1.327 Å, respectively and an Au₂ bond of 2.759 Å, where the OO bonds are similar to O₃⁻ and Au₂ bond is most similar to Au₂⁻. The O₃ in complex (8.2 E) has a shorter Au₂ and AuO bonds from the bridging complex; the OO bonds are also shortened to non-symmetric values of 1.305 (O_αO_β) and 1.252 Å (O_βO_γ), which are similar to O₃⁻ and O₃, respectively. The energy of the “O₃ in” complex is ~1.10 kcal/mol higher than the bridging complex. The non-planar “O₃ out” complex (8.2 F) is ~3.3 kcal/mol above the “O₃ in” complex, where all bonds are within 0.01 Å of the “O₃ in” lengths.

The neutral triplet state has three stable complexes with bidentate (8.2 G), O₃ in (8.2 H), and non-planar O₃ out (8.2 I) complexes. The asymmetric bidentate complex has an energy of -10.59 kcal/mol; the Au₂ bond is similar to neutral Au₂ and the asymmetric OO bonds are 1.364 Å (O_αO_β) and 1.321 Å (O_βO_γ), which are both most similar to O₃⁻. The non-planar “O₃ in” complex is higher in energy by ~3 kcal/mol, compared to the bidentate complex. This structure has a shortened AuO bond along the Au₂ plane, increased AuO bond (previously 2.193 Å in the bidentate structure), and longer Au₂ bond. The ordering of the O_α to O_γ is altered as the “shorter” AuO bond is different, where O_αO_β bond is now 1.479 Å, like O₃²⁻ and the O_βO_γ bond is 1.255 Å, similar to O₃. The “O₃ out” (non-planar) complex (8.2 I) is slightly higher in energy than the “O₃ in” complex at -7.72 kcal/mol. The structure has an Au₂ bond halfway between the 8.2 G and H lengths and shorter AuO and OO bonds. The O_αO_β bond increases to 1.523 Å, which is longer than the O₃²⁻ bond length.

There are four anionic Au₂O₃ complexes that are stable with respect to the separated components: bridging (8.2 J), “O₃ in” (8.2 K), “O₃ out” (8.2L) and Y-like (8.2 M). The bridging complex has an energy of -13.33 kcal/mol and, like the neutral singlet complex, has symmetric AuO and OO bonds and a significantly elongated Au₂ bond of 2.936 Å, where the OO bonds are 1.357 Å and most similar to O₃⁻. The “O₃ in” complex (8.2 K) is lower in energy by ~46 kcal/mol and has shorter Au₂ and AuO bonds. The OO bonds are non-symmetric with an O_αO_β bond of 1.408 Å and O_βO_γ bond of 1.290 Å, which are similar to O₃⁻ and O₃, respectively. Slightly lower in energy, and the global minimum of the anionic Au₂O₃ complexes at 60.09 kcal/mol, is the “O₃ out” complex (8.2 L); the Au₂, AuO and O_βO_γ bonds decrease slightly, while the O_αO_β bond increases slightly from the “O₃ in” lengths. The final complex is the Y-like structure (8.2 M) with an energy of -38.58 kcal/mol. The Au₂ bond is shorter than the other anionic complexes at 2.589 Å with an AuO bond similar to the bridging complex’s length and symmetric OO bonds of 1.338 Å, which is most similar to O₃⁻.

8.2.2 Ternary Complexes

O₂Au₂CO: For the ternary complexes, there are two types of structures, separated and pre-reactive (or peroxy carbonyl) in Figure 8.3 A-F, which are similar to those discussed in Chapters 3 and 4. For the cationic system, there is only a separated O₂Au₂CO complex with a linear AuCO and bent AuO₂ moieties. The complex looks like an amalgamation of the two binary complexes. The AuCO and OO moieties have similar structural and vibrational frequency data as the respective binary complexes, the Au₂ bond is shorter than the lengths in the binary complexes, and the AuO bond is longer by ~0.1 Å than the binary complex length. The neutral charge state has two structures, both separated, with

one in the singlet and one in the triplet spin state. The neutral singlet separated complex (8.3 B) has a non-planar structure with a linear AuCO and bent AuO₂ moieties, similar to the binary complexes; however, this structure is unstable with respect to the separated components at 6.81 kcal/mol. The structural and frequency data for the Au₂CO moiety remains similar to the binary complex values, where the AuC and Au₂ bonds have increased by $\sim 0.02 \text{ \AA}$. The structural data for the Au₂O₂ moiety is nearly identical to the binary (triplet) complex (Table 8.1), but the OO frequency is blue shifted from the binary value by $\sim 200 \text{ cm}^{-1}$ (Tables 8.2). The neutral triplet complex is planar (8.3 C) with an energy of -23.41 kcal/mol, where the AuCO angle is linear, like the binary complex; the structural and frequency data of the Au₂CO moiety also remains similar to the Au₂CO (singlet) complex. Compared to the triplet Au₂O₂ complex, the AuO bond increases by $\sim 0.6 \text{ \AA}$ and the OO bond decreases by $\sim 0.03 \text{ \AA}$ with a related blue shift in the OO frequency to values very close to “free” O₂.

The anionic class of structures has a separated complex and two pre-reactive (or peroxy carbonyl) complexes, an “out” complex (8.3 E) and “in” complex (8.3 F). The separated complex, with an energy of -29.50 kcal/mol, looks like an amalgamation of the two binary complexes, similar to the occurrence in the cationic and neutral (singlet) ternary complexes. The AuC and OO bonds remain similar to the binary values, while the Au₂, AuO and CO bonds decrease by an average of 0.02 \AA with an accompanying blue shift in the CO frequency. Similar to the Au atom work, the peroxy carbonyl complexes suggest incipient reaction of O₂ with CO, as O₂ is bonded to the carbon atom. For the out complex (8.3 E), the Au₂CO moiety retains the same structural data as the binary complex with a larger blue shift in the AuC frequency. The second CO bond is

1.551 Å and OO bond is 1.245 Å, which remains similar to free O₂, but the OO frequency is 1016 cm⁻¹, which is more similar to O₂⁻. The “out” complex is higher in energy than the separated complex at -18.70 kcal/mol. The “in” complex (8.3 F) is lower in energy than the “out” complex by ~13 kcal/mol and has slightly altered bond lengths from the “out” complex (by less than 0.01 Å) with a slight blue shift in the AuC and CO frequencies. The intermolecular OC bond is longer at 1.612 Å, as is the OO bond at 1.302 Å that is more similar to O⁻ with a blue shifted frequency (from the “out” value) at 1214 cm⁻¹.

O₃AuCO Complexes: So far, there are no separated O₃AuCO⁺ complexes observed in the DFT calculations, but several separated isomers were observed in the neutral singlet and triplet and anionic manifolds. The neutral singlet structures, Figure 8.4 A and B both have (nearly) linear AuCO moieties and bridging O₃ on Au₂ with energies of -41.45 and -41.85 kcal/mol, respectively. In the bridging structures, O_α is attached to the same Au atom (on the “opposite side”) as the carbon atom. In 8.4 A, the AuO₃ dihedral is 84.8° with non-symmetric OO bonds of 1.412 (O_αO_β) and 1.337 (O_βO_γ) Å, which are most similar to O₃²⁻ and O₃, respectively. The Au₂ bond is significantly elongated at 3.114 Å, and the CO bond is similar to free CO with a (nearly) linear AuCO angle (Table 8.4). There are small differences in the bond lengths (<0.04 Å) between the two bridging structures (Figure 8.4 A and B), except the Au₂ bond in B is shorter by 0.065 Å and the AuOOO dihedral angle decreases to 12.0°.

The triplet system has three different separated structures: a bridging structure (8.4 C), “O₃ in and down” structure (8.4 D) and “O₃ out,” non-planar structure (8.4 E).

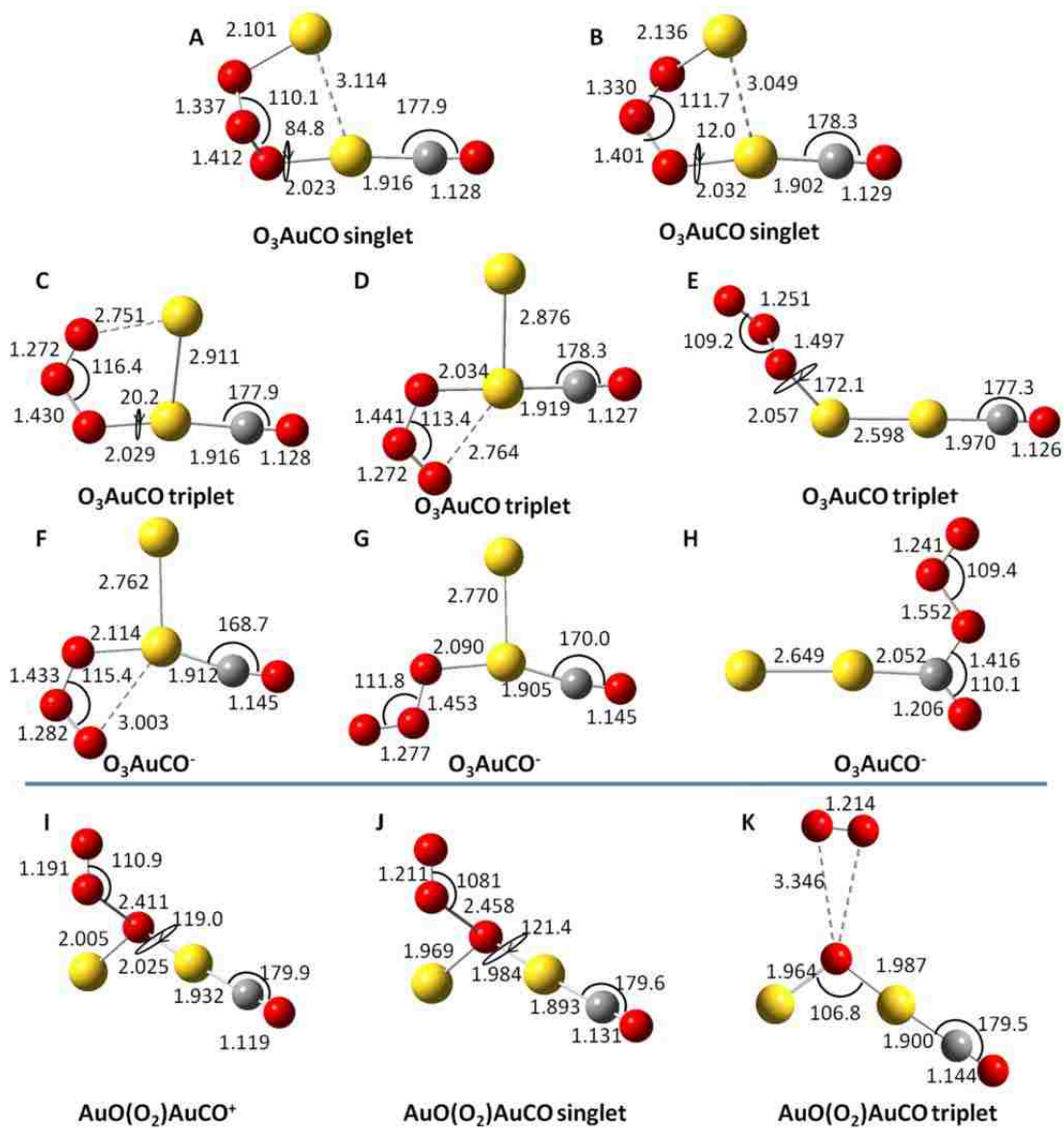


Figure 8.4. B3LYP predicted ternary $[\text{O}_3\text{Au}_2\text{CO}]^q$ ($q=+1, 0, -1$) complexes with bond length (Å) and angles (°), where A-G are separated complexes, H is a “pre-reactive in” (or peroxy carbonyl) complex and I-K are O_3 “insertion” complexes.

Table 8.4. B3PLYP predicted bond lengths (in Å) for binary $[\text{Au}_2\text{CO}]^q$ and $[\text{Au}_2\text{O}_2]^q$ and ternary $[\text{O}_2\text{Au}_2\text{CO}]^q$ or $[\text{Au}_2\text{COO}_2]^q$ complexes ($q=+1, 0, -1$).

		$\text{O}_2\text{Au}_2\text{CO}$ or $\text{Au}_2(\text{CO})\text{O}_2$ bonds						Au_2O_3 bonds				
		AuC	C-O	AuAu	AuO	$\text{O}\alpha\text{O}\beta$	$\text{O}\beta\text{O}\gamma$	AuO	AuAu	$\text{O}\alpha\text{O}\beta$	$\text{O}\beta\text{O}\gamma$	
Cationic		1.932	1.119	3.36	2.005	2.411	1.191	2.115	2.864	1.341	1.304	
					2.025							
								2.176	2.682	1.291	1.224	
								2.175	2.678	1.313	1.213	
Neutral	Singlet	1.916	1.128	3.114	2.023	1.412	1.337	2.207	2.759	1.327	1.327	
					2.101							
			1.902	1.129	3.049	2.032	1.401	1.330	2.151	2.572	1.252	1.305
						2.136						
			1.893	1.131		1.969	2.458	1.211	2.142	2.571	1.249	1.313
						1.984						
	Triplet	1.916	1.128	2.911	2.029	1.430	1.272	2.026	2.608	1.479	1.255	
					2.751							
		1.919	1.127	2.876	2.034	1.441	1.272	2.193	2.588	1.364	1.321	
					2.764							
		1.970	1.126	2.598	2.057	1.497	1.251	2.007	2.598	1.523	1.243	
		1.900	1.144		1.964	3.346	1.214					
					1.987							
Anionic	Doublet	1.912	1.145	2.762	2.114	1.433	1.282	2.270	2.936	1.357	1.357	
					3.003							
			1.905	1.145	2.770	2.090	1.453	1.277	2.124	2.614	1.408	1.290
			2.052	1.206	2.649		1.552	1.241	2.104	2.610	1.430	1.284
			1.416									
								2.227	2.589	1.338	1.338	
Reference lengths^b		C-O	1.124	O-O (O_2)		1.203	O-O (O_3)		1.251			
		C-O ⁺	1.108	O-O (O_2) ⁻		1.341	O-O (O_3) ⁻		1.346			
		C-O ⁻	1.183	O-O (O_2) ²⁻		1.559	O-O (O_3) ²⁻		1.478			

^a Au_2O_2 singlet is restricted (closed shell) due to high spin contamination in the unrestricted singlet calculation.

^bcalculated at same level of theory: B3LYP/6-311+G(3df) and O_2 reference bond length is from the triplet ground state species.

Table 8.5. ZPE and BSSE corrected binding energies^a (kcal/mol) for binary [Au₂CO]^q and [Au₂O₃]^q and ternary [O₃Au₂CO]^q complexes (q=+1, 0, -1) and cooperative binding evaluated for similarly charged complex groups.

		Au ₂ CO	Au ₂ O ₃	O ₂ Au ₃ CO or Au ₂ (CO)O ₃ ^b	Cooperative binding ^{b,c}	
Separated/peroxycarbonyl						
Cationic		-34.43	-25.69 (8.2 A) ^c			
			-18.15 (8.2 B)			
			-15.61 (8.2 C)			
Neutral	Singlet	-23.33 ^d	-11.56 (8.2 D) ^c	-41.45 (8.3 A)	-6.18	
			-10.44 (8.2 E)	-41.85 (8.3 B) ^c	-6.58	
			-8.20 (8.2 F)			
	Triplet	26.12	-10.59 (8.2 G)	-32.77 (8.3 C)	+2.50	
				-7.78 (8.2 H)	-34.22 (8.3 D)	+1.05
				-7.72(8.2 I)	-29.92 (8.3 E)	+5.34
Anionic		-8.76	-13.33 (8.2 J)	-62.79 (8.3 F)	+6.19	
			-59.74 (8.2 K)	-62.11 (8.3 G)	+6.87	
			-60.10 (8.2 L) ^c	-70.92 (8.3 H) ^c	-1.94	
			-38.58 (8.2 M)			
Insertion						
Cationic				-89.29 (8.3 I) ^c	-28.61	
Neutral (singlet)				-32.59 (8.3 J)	+2.68	
Neutral (triplet)				+9.03 (8.3 K)	+44.30	

^a Computed relative to optimized values of the *ground state* components, with charge (if any) localized on gold center.

^b Cooperative binding is calculated as the difference between total binding energy of ternary complex and summed binary complexes as shown here: $E_{\text{OOAuCO}} - E_{\text{AuOO}} - E_{\text{AuCO}}$. The AuO₂ energy used in cooperative binding is the ground state triplet. Parenthetical cooperative binding values are calculated in the same fashion, but utilize the parenthetical values of the binary and ternary singlet complexes, where applicable.

^c Lowest energy state per species with the same charge and molecular components.

Table 8.6. B3LYP predicted stretching vibrational frequencies in cm^{-1} for binary $[\text{Au}_2\text{O}_3]^q$ and ternary $[\text{O}_3\text{Au}_2\text{CO}]^q$. Labels A-I correspond to the structures shown in Figure 8.4.

		$\text{O}_3\text{Au}_2\text{CO}$ or $\text{Au}_2(\text{CO})\text{O}_3$ bonds						Au_2O_3 bonds				
		Fig ID ^a	AuC	CO	AuAu	AuO	$\text{O}\alpha\text{O}\beta$	$\text{O}\beta\text{O}\gamma$	AuO	AuAu	$\text{O}\alpha\text{O}\beta$	$\text{O}\beta\text{O}\gamma$
Cationic		I	1.932	1.119	3.36	2.005	2.411	1.191	2.115	2.864	1.341	1.304
						2.025			2.176	2.682	1.291	1.224
									2.175	2.678	1.313	1.213
Neutral	Singlet	A	1.916	1.128	3.114	2.023	1.412	1.337	2.207	2.759	1.327	1.327
						2.101			2.151	2.572	1.252	1.305
									2.142	2.571	1.249	1.313
	Triplet	C	1.916	1.128	2.911	2.029	1.430	1.272	2.026	2.608	1.479	1.255
						2.751			2.193	2.588	1.364	1.321
									2.007	2.598	1.523	1.243
		K	1.900	1.144	2.598	2.057	1.497	1.251	2.007	2.598	1.523	1.243
						2.764						
Anionic	Doublet	F	1.912	1.145	2.762	2.114	1.433	1.282	2.270	2.936	1.357	1.357
						3.003			2.124	2.614	1.408	1.290
									2.104	2.610	1.430	1.284
									2.227	2.589	1.338	1.338
Reference lengths^b			C-O	1.124	O-O (O_2)	1.203	O-O (O_3)	1.251				
			C-O^+	1.108	$\text{O-O}(\text{O}_2)^-$	1.341	$\text{O-O}(\text{O}_3)^-$	1.346				
			C-O^-	1.183	$\text{O-O}(\text{O}_2)^{2-}$	1.559	$\text{O-O}(\text{O}_3)^{2-}$	1.478				

^aFig. ID labels correspond to the labels in Figure 8.4 for the ternary complexes

^bcalculated at same level of theory: B3LYP/6-311+G(3df) and O_2 reference bond length is from the triplet ground state species.

The bridging and O₃ in and down structures have O_α attached to the same Au atom as carbon, but the O₃ out (non-planar) structure shows O_α attached to a the “first” Au atom, while carbon is attached to the “second” Au atom. The neutral triplet bridging structure (8.4 C) has an energy of -32.77 kcal/mol, which is higher than the neutral singlet complexes, but the structure shares a similar OAuCO moiety with the neutral singlet structure in 8.4 B. The O_αO_β bond is slightly longer at 1.430 Å and AuO_γ is much longer at 2.751 Å. The Au₂ bond is shorter by ~0.14 Å and O_βO_γ is slightly shorter at 1.272 Å, which is similar to O₃ (Table 8.4). The “O₃ in and down” complex (Figure 8.4 D) is a rotamer of C and lower in energy by ~1.5 kcal/mol, where the Au₂OO dihedral angle is now 180° with very similar bond lengths. The Au₂ bond is slightly shorter than the same in C, while the AuO_γ and O_αO_β bonds are slightly longer. Complex 8.4 E is the anionic out non-planar structure, where O_α and carbon are attached to different Au atoms, as stated above, so that it appears an Au atom was inserted into an O₃AuCO complex. This complex is higher in energy than the other neutral complexes at 29.92 kcal/mol. The Au₂ and O_βO_γ bonds shorten to values similar to the neutral lengths (Au₂ and O₃), while the O_αO_β, AuO_α and AuC bonds all increase by 0.02 Å (or greater) and O_αO_β is longer than the O₃²⁻ bond length.

The anionic system has three structures that retain Au, CO and O₃ molecules, which are the O₃ in and down (Figure 8.4 F, similar to D), O₃ out and down (8.4 G), and a “pre-reactive” trioxocarbonyl complex (8.4 H). The anionic “O₃ in and down” complex (8.4 F) shares the same overall structure with the neutral triplet complex (8.4 D), but the AuCO angle is more bent at 168.7°, along with different bond lengths (Table 8.4). This anionic separated complex also has a lower energy than the neutrals at -62.79 kcal/mol. The Au₂

bond of 2.762 Å is similar to Au₂⁻ with a CO bond of 1.145 Å, and two asymmetric OO bonds in O₃ at 1.433 Å (O_αO_β) and 1.282 Å (O_βO_γ), which are similar to O₃²⁻ and O₃, respectively. The “O₃ out and down” structure (Figure 8.4 G) is a rotamer of 8.4 F, where the AuOOO dihedral is now 180°, and is ~0.6 kcal/mol higher in energy. The O_αO_β bond increases by 0.02 Å, while the AuO bond decreases by that amount; the AuC and O_βO_γ bonds decrease slightly and the Au₂ bond and AuCO angle increase slightly. The trioxocarbonyl complex, Figure 8.4 H, is the global minimum for the anionic complexes at -70.92 kcal/mol. The structure has Au₂ bonded to CO and O₃ bonded directly to CO, which suggests an incipient reaction between CO and O₃. The Au₂ bond is shorter than 8.4 G by ~0.1 Å with a similar increase in the AuC bond. The CO bond is 1.206 Å, similar to CO⁻, and the intermolecular OC bond is 1.416 Å. The O_αO_β (bonded to carbon in the case) is the longest of the anionic complexes at 1.552 Å, similar to O₂²⁻, and the O_βO_γ bond is 1.241 Å, which is similar to O₃.

There are also some insertion complexes, where one O atom (of O₃) inserts into the Au₂ bond, which are observed in the cationic and both neutral (singlet and triplet) states. The cationic and neutral singlet (Figure 8.4 I and J) appear similar in the overall structure with AuO₃ dihedrals near 120° and O_αO_β bonds of ~2.4 Å. The cationic complex has a very stable energy of -89.29 kcal/mol; the AuO bonds are ~2.01 Å with a CO bond of 1.119 Å, similar to free CO, and O_βO_γ bond of 1.191 Å, which is shorter than free O₂. The neutral singlet complex is ~10 kcal/mol higher than the separated complexes in energy. The AuO bonds are shorter at 1.969 and 1.984 Å and the AuC bond is shorter by ~0.03 Å. The CO bond is longer at 1.132 Å, still similar to CO, and the OO bond is also longer at 1.211 Å, also similar to free O₂. The neutral triplet

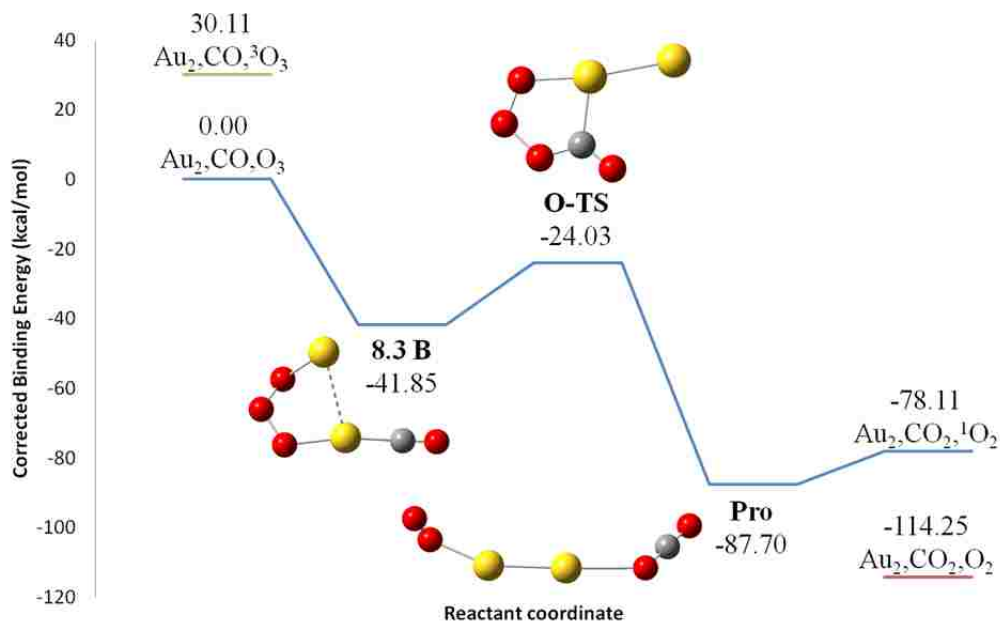


Figure 8.5 Possible oxidation pathway for neutral (singlet) $\text{O}_3\text{Au}_2\text{CO}$ with concerted O_3 molecule. The “reactant-side” minima is 8.3 B, the global minimum for the “separated” $\text{O}_3\text{Au}_2\text{CO}$ (singlet) complexes.

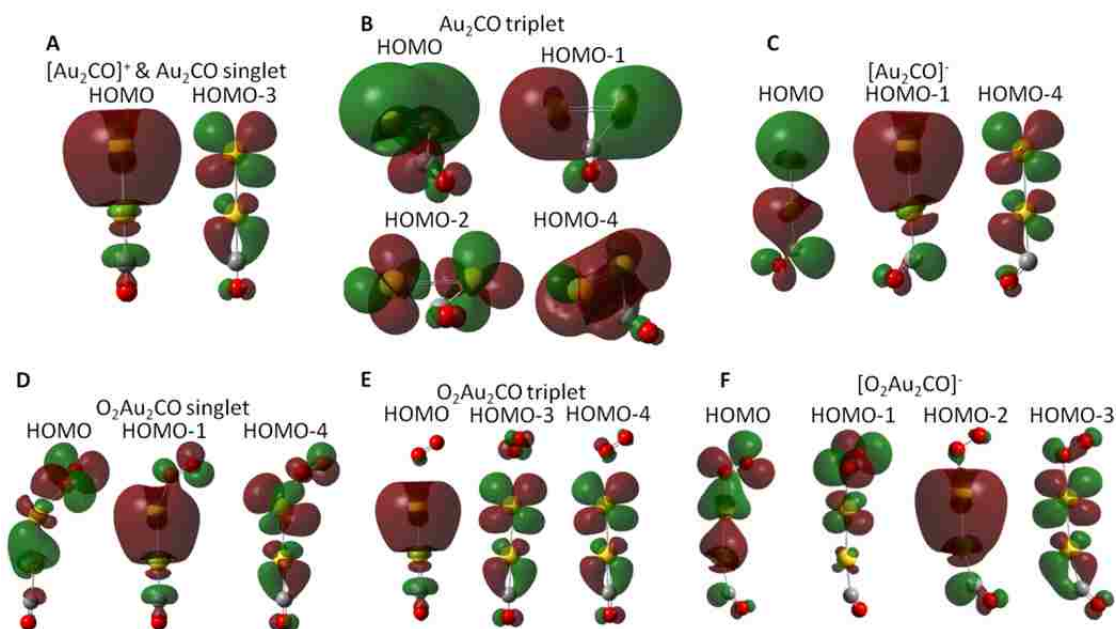


Figure 8.6 Selected higher lying orbitals showing σ -donation and π -backbonding character for binary and ternary complexes: A) $[\text{Au}_2\text{CO}]^+$ (Au_2CO singlet is similar); B) Au_2CO triplet; c) $[\text{Au}_2\text{CO}]^-$; D) $\text{O}_2\text{Au}_2\text{CO}$ singlet (Figure 8.2 B); E) $\text{O}_2\text{Au}_2\text{CO}$ triplet (Figure 8.2 C); F) $[\text{O}_2\text{Au}_2\text{CO}]^-$. For open spin species (B, C, E, F), only the α -spinorbitals are shown.

insertion complex (8.4 K) is unstable with respect to the separated reactants (Au_2 , CO, O_3 singlet) at +9.03 kcal/mol; the complex has a planar structure with a much longer $\text{O}_\alpha\text{O}_\beta$ bond at 3.346 Å, but the AuO and OO bonds are similar to those of the neutral singlet complex (Figure 8.4 J and Table 8.4). The AuC bond is slightly longer and the CO bond is ~ 0.01 Å longer at 1.144 Å.

8.2.3 O_3 Pathway

During the calculations for Au_2 minima with O_3 and CO, a possible transition state was generated with an Au_2COO_3 structure in the neutral singlet state that is reminiscent of the AuCOO_3^q transition states in Chapter 5. From this possible transition state (O-TS), a reaction pathway was developed, as shown in Figure 8.5. The pathway starts from the “separated” global minimum, a bridging $\text{O}_3\text{Au}_2\text{CO}$ complex (Figure 8.3 B) and continues over a barrier of 17.82 kcal, where the AuO_γ bond is broken, O_3 rotates towards CO (behind the Au atom that O_γ was previously attached) and the $\text{Au}_2\text{O}_\alpha\text{O}_\beta$ dihedral moves from 28.5° to 180° . To form the product, the $\text{O}_\alpha\text{O}_\beta$ bond cleaves, O_2 migrates to the second Au atom, the AuC bond is broken and a new AuO bond is formed with the linear OCO moiety. This is a very simple pathway, and not all possible minima and transition states have been investigated at this point. However, this pathway is very similar to the neutral, Au atomic O_3 oxidation pathway, as the barrier is below the reactant asymptote, and the structures look like an extra Au atom was added at each stationary point.

8.3 Discussion

8.3.1 O_2 Systems: There are several similarities across the Au atom and Au dimer systems, where the synergic back-bonding is observed in the Au_2CO^+ and Au_2CO (singlet) molecular orbitals, while the Au_2CO (triplet) and Au_2CO^- complexes have bent

AuCO angles, like the neutral and anionic AuCO binary complexes. For the neutral singlet case, it appears that an additional atom (Au, in this case) is sufficient to form the linear complex, but anionic (doublet) orbitals look very similar to the AuCO⁻ singlet (or O₂AuCO⁻ triplet) orbitals, shown in Chapter 3. Similar to the Au atom systems, the cationic and both spin states for the neutral O₂Au₂CO complexes have linear AuCO moieties, where it appears that the addition of O₂ leads to a neutral singlet-like Au₂CO moiety in the structure and molecular orbitals. The cooperativity of binding values, as evaluated with the binding energies (outlined in Chapter 3), are very different for the Au₂ system, when compared to the Au system with strong cooperativity in forming [O₂+Au^q+CO] complexes. All [O₂Au₂CO]^q complexes have positive cooperative binding values, which suggests anti-cooperativity that is in agreement with experimental results of Wallace and Whetten for Au₂⁻. The cationic and neutral triplet ternary complexes have the lowest anti-cooperativity, while the anionic peroxy carbonyl “out” complex has the highest at +54.97 kcal/mol with the neutral singlet and anionic separated and peroxy carbonyl “in” complexes within ~20 kcal/mol. This anti-cooperativity suggests that the Au₂^q system may be more catalytic than Au^q. Further investigation of the O₂ pathways is necessary to evaluate this idea along with the study of larger Au_n^q clusters to look for an oscillation in cooperative and anti-cooperative interactions between odd and even clusters, respectively, as discussed by Wallace and Whetten.

8.3.2 O₃ Systems: The ozone complexes show similarities to the atomic Au^q systems in the observation of [O₃Au₂CO]^{0,-} “separated” complexes with the linear AuCO moieties (like O₂Au₂CO and the Au atom system), but the lack of cationic separated structures requires more study to verify that none are truly calculated. Also intriguing is the

observation of $\text{AuO}(\text{O}_2)\text{AuCO}$ insertion complexes in the cationic and neutral systems, which also require further investigation. The observation of a possible O_3 oxidation pathway in the $[\text{O}_3+\text{Au}_2+\text{CO}]^0$ system that is reminiscent of the $[\text{O}_3+\text{Au}^q+\text{CO}]$ pathways is encouraging that our goal of identifying trends in the CO oxidation pathways, as a function of size and charge, is possible and that these trends truly exist.

8.4 Future Work

8.4.1 Computational Work: One of the overall goals of the group and this project was to investigate the CO oxidation mechanism as a function of change in size and charge.

The investigation of CO oxidation mechanism as a function of charge were completed for the Au and Cu atoms with charges of -1, 0, and +1; it was discussed that for the O_3 related pathways, additional or subtraction of an electron did not grossly alter the structures and overall pathways observed, while the O_2 pathways had most similarities between the neutral and anionic charge states. These initial results of comparing charges are encouraging that a trend in the reaction mechanism can be determined for CO oxidation over Au (or Cu). However, investigation of larger sizes of Au (or Cu) clusters is needed to further build the knowledge of how CO oxidation proceeds as a function of size. Also, continuing to use the three charge states (+1, 0, -1) offer the ability to track how size affects the charge distributions and, in turn, the how the changes in charge distribution affects the CO oxidation mechanism.

Studies on Au_2^q with CO and O_2 (or O_3) were started to understand the affects of size for the CO oxidation mechanism. This work was started around the same time as the $[\text{O}_3+\text{Au}^q+\text{CO}]$ work was being conducted; unfortunately for the Au_2 work, the observation of $[\text{O}_3\text{AuCO}]^q$ complexes and $\{\text{AuCOO}_3\}^q$ transition states pushed the

“cluster size” work to the side. The best probable place to continue with the “size effects” is with finishing the CO oxidation pathways for O₂ and O₃ systems (with Au₂^q). As shown above, there are some similarities between minima structures found in the Au₂ and Au systems for both oxygen allotropes, along with a shared “O₃ oxidation” transition state between the atom and dimer systems. These results suggest that trends in the reaction pathways may exist over different Au cluster sizes; however, computational studies with the larger sizes are necessary.

Also related to the atom and dimer work, a “cooperativity and anti-cooperativity” trend was observed, where the cooperative binding energies were negative for [O₂+Au^q+CO] systems, while these energies were positive in the [O₂+Au₂^q+CO] system, which matches experimental results of Wallace and Whetten for adsorption of O₂ and CO on Au_n- clusters (n=2-20). Observation of an alternating “cooperative” and “anti-cooperative” binding would be in agreement with experiments and provide additional support for the computational results.

The computational investigation of Cu^q atoms with CO and O₂ (or O₃) was completed to compare the computational results with (current) matrix isolation experiments. Another goal of this project was to compare the computational and experimental vibrational frequencies to see if the predicted complexes are observed in experiments. More experiments, discussed below, are necessary to better evaluate if the computationally predicted complexes are trapped in the matrix isolation experiments, but there were no clear connections between the peaks observed and the expected vibrational frequencies of [O₃CuCO]^q complexes. While completing calculations on the Cu systems, several similarities were identified between the Au and Cu complexes and reaction

pathways for both oxygen allotropes. These similarities indicate that there is periodicity observed in the calculations, at the very least. To complete this column of the periodic table, the interactions of Ag^q, CO and O₂ (or O₃) could be studied to see if the contracted d-shells of Cu and Au are required for the similarities in the pathways discussed in chapters 4-6, or if the s¹ d¹⁰ electron configuration is the important characteristic; this hypothesis would be confirmed if the Ag^q (CO oxidation) pathways for both oxygen allotropes share similar stationary points (and structures) with the Cu and Au systems. Further work can also include investigation of the interactions of water with Au atoms (and clusters), CO, and O₂ (or O₃), as water is thought to increase the activity of metal oxide supported Au nanoparticles.

8.4.2 Experimental Work: In an effort to mitigate the amount of CO₂ transferred from the ozone generation tube to the storage bottle, the ozone generation system can be re-designed with a secondary glass tube. Ozone would still be generated in the current tube as described in chapter, while the second glass tube is chilled with liquid nitrogen. The first (ozone generation tube) would be immersed in an isopentane bath, in an effort to trap CO₂ and not O₃, the valve between the two glass tubes would be opened, and ozone would move into the (colder) liquid nitrogen cooled tube. CO₂ should not flow into the second tube, since it should already be trapped in the isopentane bath tube.

Another effort to reduce CO₂ contamination involves re-design of depositing gases into the chamber by introducing O₃ and CO from two different nozzles. When experiments were completed with O₃ and CO in the same mixture, depressed levels of O₃ (very small intensity) and intense CO and CO₂ bands were typically observed, which indicated that CO was being oxidized by O₃ in the storage bottle and possibly the

stainless steel deposition lines. Co-deposition of ozone and CO mixes from different sources would be possible with the addition of another set of gas deposition lines into the chamber from the O₃ deposition system. The main “CO” deposition and the ozone deposition lines are separated from the respective storage bottles up to the existing deposition nozzle. Separation of the O₃ and CO lines would require addition of a second gas feed-through flange to the chamber, and then “re-routing” the ozone deposition line to that feedthrough. This separation of O₃ and CO until the gases are deposited should cut down on CO₂ contamination. Also, if the amount of CO₂ in the O₃ (only) depositions is decreased to negligible levels or none observed, the observation of CO₂ in the matrix with O₃ and CO co-depositions would indicate that CO is oxidized in the matrix by O₃.

Upon the completion of these changes and if CO₂ contamination is decreased significantly, the experiments of Cu-, O₃ and a counter-ion (Ar⁺ or SF₅⁺) should be repeated at 10K, 15K and 20K deposition temperatures with the concentrations of 0.5-2% for 10K and 0.01-0.05% for 20K, based on experimental by Ryan Ludwig with Cu⁻, Ar⁺ and CO. Consistent concentrations, when deposited at the same temperature, are important and efforts should be made to be more consistent than the experiments discussed in Chapter 7. The gas (deposition) flow rates could be altered between 2-10 sccm to see if the same trend was observed, where a deposition rate of ~2.5 sccm led to formation of CuO₃, but higher flow rates only led to the formation of O₃⁻ and O₄ ionic species, based on previously identified peaks. Another matrix-isolation experiment to complete is deposition of O₃ with Ar⁺ only. Depositing O₃ with Ar⁺ at varying energy values would be advantageous to understand what ozone and oxygen related complexes are formed with different Ar⁺ energies. A similar experiment was completed with O₂ and

Ar^+ , where O_4 ionic complexes were also observed without the presence of Cu^- . Another alteration to experiments would be to change the counter-ion from Ar^+ to SF_5^+ , as preliminary results in the group have shown that SF_5^+ may stop the formation of O_4 ionic complexes.

With the possibility of dual deposition of O_3 and CO , the Cu^- , O_3 , CO and counter-ion (Ar^+ or SF_5^+) should be repeated in a similar way as discussed in the paragraph above with care taken to match the concentrations of O_3 and CO . The concentrations of O_3 and CO could be systematically altered from equivalent values to a higher concentration of CO (or O_3) to look at how the unbalanced concentrations change the observation of peaks in the matrix. From previous experiments, very little to no copper carbonyl peaks, but all previous experiments involved O_3 and CO mixed in the same bottle. Co-deposition could change the intensity of copper carbonyl (or other) peaks.

Finally, more costly alterations include the installation of a MCT(B) detector, which would allow observation of copper oxide region and we could better understand what is happening to Cu^- in the matrix when deposited with O_3 . It is possible that ozone and Cu^- are interacting to form CuO or CuO^- and O_2 , which can form the O_4 ionic complexes. The MCT(A) detector cuts off at 650cm^{-1} and copper oxide vibrations are found in the $620\text{-}640\text{ cm}^{-1}$ region; therefore, we can speculate as to what is happening, but have no experimental evidence. The MCT(B) detector cuts off at 400 cm^{-1} , according to ThermoFisher Scientific, which would work well for copper oxide detection.

It is my hope that with these alterations and more careful ozone experiments, interactions of ozone with Cu^- (and CO and a counter-ion) can be observed with the

formation of CuO_3^- and $\text{O}_3\text{CuCO}^{\ominus}$ complexes and compared to the computationally calculated complexes.

8.5 References

- (1) Wallace, W. T.; Whetten, R. L. *J. Am. Chem. Soc.* **2002**, *124*, 7499-7505.
- (2) Socaciu, L. D.; Hagen, J.; Bernhardt, T. M.; Woste, L.; Heiz, U.; Hakkinen, H.; Landman, U. *J. Am. Chem. Soc.* **2003**, *125*, 10437-10445.

Appendices

A2. Appendix to Chapter 2

A2.1 Gaussian keywords

Optimization keywords: An example optimization input file is shown in Example A2.1.

`opt=tight`: Defines the root mean squared (RMS) force criterion as 1×10^{-5} hartrees/bohr and scales the maximum force and displacement and RMS displacement.

`opt=calcfc`: Indicates that the second derivative of the energy (the force constants) should be calculated at the beginning of the optimization cycle.

`opt=maxcyc=100`: Sets the maximum number of optimization cycles.

`integral=ultrafine`: Defines the grid size (99,590) when evaluating the exchange-correlation energy that is calculated in a grid-based numerical integration step.

`scf=(fermi,xqc,maxconventionalcycles=N)`. The keyword “Fermi” allows for thermal broadening and damping in early iterations of the calculations; `xqc` adds another quadratic convergent SCF procedure if the first-order SCF is not converged. The `cycles` keyword sets the limit for conventional SCF cycles to N during `scf=xqc`.

Counterpoise keywords: An example counterpoise calculation input file is shown in Example A2.2.

`counterpoise=N`: Indicates the number of fragments in the structure. For example, AuCO has two fragments, Au and CO, and `counterpoise=2` would be used. The charge and spin state of the charge states must also be assigned to the fragments and identified in the molecular specification section of the input file.

`scf=tight`: Indicates that tight convergence criteria applies to the SCF cycles. This is also used in population analyses, intrinsic reaction coordinate calculations and ab initio molecular dynamics.

Population analysis keywords: An example population analysis input file is shown in Example A2.3 for Hirshfeld charges and an example for the ChelpG analysis is shown in Example A2.4.

`guess=read`: Instructs the program to read the initial guess from the indicated checkpoint file.

`guess=only`: Used to terminate the calculation after the initial is computed and printed

`pop=full`: Print all orbitals, which is a default with `guess=only` jobs.

In the `pop=` section, NBO, Hirshfeld, or ChelpG is specified; “Hirshfeldee” is typically used in the following calculations to gather interatomic electrostatic interactions, as well. ChelpG calculations also require a “`readradii`” keyword in the `pop=` section to provide an alternate radii for certain elements in the fitting potentials; `readradii` is used with Au (1.90 Å) when calculating ChelpG charges.

Intrinsic Reaction Coordinate (IRC) keywords: An example IRC input file is shown in Example A2.5.

Irc=forward (or reverse): Indicate the direction of the calculation with respect to the transition vector; forward and reverse have no physical, consistent meaning across different calculations with respect to reactant and product, so “reverse” could lead to a reactant and “forward” to product or vice versa.

The IRC calculations need force constants to move from the transition state, so these force constants can be read in from a checkpoint file (guess=read) or the “calcf” keyword can be utilized for the force constants to be calculated from the input geometry specifications. The step size, in units of 0.01 bohr (in Gaussian 09) can also be indicated in the input file, where 10 is the default. Through many IRC calculations, we have found that stepsize=25 works best for the forward and reverse IRC calculations and larger steps (25 and greater) typically work better than smaller (< 25). The number of points to be considered can also be defined, where 10 is the default, but a larger value is better to verify that the IRC calculation is not stopping due to in-sufficient number of steps; therefore, maxpoints=50 are used, as “extra” points will not hamper the calculation. The maximum number of cycles per step can also be specified, where the default is again 20; maxcyc=50 is used to increase the likelihood of a successful transit toward a minimum. Similar to the geometry optimization calculations, the “tight” and “integral=ultrafine” keywords are utilized in these DFT calculations.

Atom-centered Density Matrix Propagation (Ab initio molecular dynamics)

keywords: An example optimization input file is shown in Example A2.6.

The fictitious electron mass, which ensures that little energy is transferred between the electrons and nuclei, is set at default to 0.1 amu (keyword electronmass=N, $\lfloor N/10000 \rfloor$, default N=1000). The nuclear kinetic energy is set to 0.1 hartrees as a default, but can be changes with keyword NKE=N in microhartrees.

stepsize=n (500): $n \cdot 0.0001$ fs provides the true size of the time step.

maxpoints= (number): The default number of maximum points is 100, but can be overridden; 5000 points have been utilized for these calculations.

A2.2 Input File Examples

Example A2.1. Geometry optimization input, where the first line is the checkpoint file name, the second line is the input line, the next line with text is the “title” for comments on the file, the following section is the molecular specification section that gives the charge and spin state and Cartesian coordinates of each atom, and the final section is the basis set specification, when utilizing more than one basis set.

```
%chk=C:\G09W\Angie\Au monomer\B3LYP\Au neutral\Au CO\DONE\AU CO  
DOUBLET SDD-6311+G3Dfb3lyp ultrafineopt+freqtrue.chk  
#p opt=(calcfc,tight,maxcyc=200) freq ub3lyp/genecp guess=read integral=ultrafine
```

```
Au CO try 3 opt b3lyp in gauss 09
```

```
0 2  
Au      0.00000000  0.39067100  0.00000000  
C       0.32936000 -1.65198600  0.00000000  
O      -0.24702000 -2.61888600  0.00000000
```

```
C O 0  
6-311+G(3df)  
****
```

```
Au 0  
SDD  
****
```

```
Au 0  
SDD
```

Example A2.2. Counterpoise correction input, where much of the file is similar to the geometry optimization input, except the charge and spin of each fragment is indicated next to the overall charge and spin and the “fragments” are identified with each atom in the molecular specification file.

```
%chk=C:\G09W\Angie\Au monomer\B3LYP\Au neutral\Au CO\DONE\AU CO  
DOUBLET SDD-6311+G3Dfb3lyp ultrafineopt+freqtruecp2spe.chk  
#p ub3lyp/genecp integral=ultrafine scf=tight counterpoise=2
```

```
Au CO try 3 opt b3lyp in gauss 09
```

```
0 2 0 2 0 1
```

Au(Fragment=1)	0.00000000	0.39062500	0.00000000
C(Fragment=2)	0.32704500	-1.64248800	0.00000000
O(Fragment=2)	-0.24528400	-2.62556000	0.00000000

```
C O 0
```

```
6-311+G(3df)
```

```
****
```

```
Au 0
```

```
SDD
```

```
****
```

```
Au 0
```

```
SDD
```

Example A2.3. Population analysis input for Hirshfeld charges, where much of the file is similar to the geometry optimization input, except there are different keywords in the input section.

```
%chk=C:\G09W\Angie\Au monomer\B3LYP\Au neutral\Au CO\DONE\AU CO  
DOUBLET SDD-6311+G3Dfb3lyp ultrafineopt+freqtruehirshee.chk  
#p ub3lyp/genecp guess=(read,only) integral=ultrafine scf=tight density=current  
pop=(full,hirshfeldee)
```

```
Au CO try 3 opt b3lyp in gauss 09
```

```
0 2  
Au      0.00000000  0.39062500  0.00000000  
C       0.32704500 -1.64248800  0.00000000  
O      -0.24528400 -2.62556000  0.00000000
```

```
C O 0  
6-311+G(3df)  
****  
Au 0  
SDD  
****
```

```
Au 0  
SDD
```

Example A2.4. Population analysis input for ChelpG charges, where much of the file is similar to the Hirshfeld input, except there are different keywords in the population section and the radius for the Au atom is found after the basis set specification section.

```
%chk=C:\G09W\Angie\Au monomer\B3LYP\Au neutral\Au CO\DONE\AU CO  
DOUBLET SDD-6311+G3Dfb3lyp chelpg.chk  
#p ub3lyp/genecp guess=(read,only) integral=ultrafine scf=tight  
pop=(full,chelpg,readradii)
```

```
Au CO try 3 opt b3lyp in gauss 09
```

```
0 2  
Au          0.00000000  0.39062500  0.00000000  
C           0.32704500 -1.64248800  0.00000000  
O          -0.24528400 -2.62556000  0.00000000
```

```
C O 0  
6-311+G(3df)  
****
```

```
Au 0  
SDD  
****
```

```
Au 0  
SDD
```

```
Au 1.90
```

Example A2.5. Intrinsic reaction coordinates (IRC) input for a “forward” path following, where much of the file is similar to the geometry optimization input, except there are different keywords in the input section.

```
%chk=H:\O2IRC\ircqst3OmgdoubOCuCO2b3lypsdd6-311+G3df.chk  
#p irc=(forward,maxpoints=50,calcfc,maxcyc=50,stepsize=25) ub3lyp/genecp  
integral=ultrafine scf=tight
```

Title Card Required

```
0 2  
C      -1.37537800  -0.47518300  0.00001300  
O      -2.47312000  -0.70217500  -0.00000400  
O       2.04077600  -0.79311300  0.00000900  
O      -0.50348000  1.54187100  0.00000700  
Cu       0.54271900  0.08546300  -0.00000600
```

```
-C -O 0  
6-311+G(3df)  
****  
-Cu -Au -Ag 0  
SDD  
****
```

```
-Cu -Au -Ag 0  
SDD
```

Example A2.6. Ab initio molecular dynamics (Atom-centered Density Matrix Propagation), where much of the file is similar to the geometry optimization input, except there are different keywords in the input section and an additional line between the molecular specification section and the basis set specification section.

```
%chk=H:\ADMP nearTSOAUCO2DOUB B3LYP6-
31+Gdnke19123pts5000defEmass.chk
#p ub3lyp/genecp admp=(stepsize=500,maxpoints=5000,nke=19123) integral=ultrafine
scf=tight
```

TSOAUCO2DOUB.B3LYP6-31+Gdstep500points4500EMass5000, which was 25fs

```
0 2
Au      0.00000000  0.62123000  0.00000000
C       0.56576900 -1.66256900  0.00000000
O       1.70818000 -1.94335600  0.00000000
O      -1.21502826 -0.62316373  0.01399518
O      -0.57483800 -2.14559900  0.00000000
```

```
C O 0
6-31+G(d)
****
Au 0
SDD
****
```

```
Au 0
SDD
```


A3. Appendix to Chapter 3.

A3.1 Tables and Figures in support of text.

Table A3.1. Geometry and stretching frequencies for reference atoms/molecules, Au^q, CO^q and O₂^q calculated at the levels of B3LYP/SDD for Au and B3LYP/6-311+G(3df) for C, O atoms.

Species	Geometry		Stretching Frequency (Intensity)			
	Symmetry	Electronic State	r _{C-O} (Å)	r _{O-O} (Å)	C-O in cm ⁻¹	O-O in cm ⁻¹
Au ⁺	O _h	¹ A _{1g}				
Au	O _h	² A _{1g}				
Au ⁻	O _h	¹ A _{1g}				
CO	C _{∞v}	¹ Σ	1.124		2217 (79.8)	
CO ⁺	C _{∞v}	² Σ	1.108		2300 (12.8)	
CO ⁻	C _{∞v}	¹ Σ	1.183		1665 (623.5)	
O ₂	D _{∞h}	¹ Σ _g		1.203		1634 (0)
O ₂	D _{∞h}	³ Σ _g		1.203		1645 (0)
O ₂ ⁻	D _{∞h}	² Σ _g		1.341		1181 (0)
O ₂ ²⁻	D _{∞h}	¹ Σ _g		1.559		703 (0)

Table A3.2. Raw energy, ZPE correction and corrected energy for reference atoms/molecules, Au^q, CO^q, and O₂^q calculated at the levels of B3LYP/SDD for Au and B3LYP/6-311+G(3df) for C, O atoms.

Species	Symmetry	Electronic State	Raw Energy (hartrees)	ZPE Correction (hartrees)	ZPE Corrected Energy (hartrees)
Au ⁺	O _h	¹ A _{1g}	-135.4084733		-135.408473
Au	O _h	² A _{1g}	-135.7555015		-135.755501
Au ⁻	O _h	¹ A _{1g}	-135.8371439		-135.837144
CO	C _{∞v}	¹ Σ	-113.3567921	0.005051	-113.351741
CO ⁺	C _{∞v}	² Σ	-112.8358525	0.005239	-112.830613
CO ⁻	C _{∞v}	¹ Σ	-113.3121897	0.003793	-113.308397
O ₂	D _{∞h}	¹ Σ _g	-150.3181537	0.003722	-150.314432
O ₂	D _{∞h}	³ Σ _g	-150.3794861	0.003747	-150.375739
O ₂ ⁻	D _{∞h}	² Σ _g	-150.3975189	0.002691	-150.394828
O ₂ ²⁻	D _{∞h}	¹ Σ _g	-150.1380483	0.001602	-150.136446

Table A3.3. Bond lengths (in Å) and angles (in °) and stretching frequencies (cm⁻¹) of [AuO₂]^q and [OAuO]^q (q=0,-1) complexes calculated at the level of B3LYP-SDD/6-311+G(3df).

Species	Geometry				Stretching Frequency (Intensity)			
	Symmetry	Electronic State	r _{Au-O}	r _{O-O}	<OAuO or <AuOO	sym Au-O	anti-sym Au-O	O-O
AuO₂	C _s	² A''	2.347	1.223	120		74 (9.36)	1444 (563.8)
AuO₂	C _{2v}	⁴ B ₁	5.080	1.203	83		12 (0)	1645 (0.01)
OAuO	D _{∞h}	² Π _g	1.789		180	798 (0)	879 (30.3)	
OAuO	D _{∞h}	⁴ Σ _g	1.910		180	615 (0)	568 (20.9)	
[AuO₂]⁻	C _s	¹ A''	2.173	1.304	118		173 (0.11)	1144 (718.4)
[AuO₂]⁻	C _s	³ A''	3.115	1.233	125		35 (0.22)	1387 (1969.3)
OAuO⁻	D _{∞h}	¹ Δ _g	1.911		180	518 (0)	637 (61.6)	
OAuO⁻	D _{∞h}	³ Σ _{g⁻}	1.866		180	697 (0)	741 (85.0)	

Table A3.4. Raw energies and corrected energies with BSSE and ZPE corrections of optimized [AuO₂]^q and [OAuO]^q (q=0,-1) at the level of B3LYP-SDD/6-311+G(3df).

Species	Symmetry	Electronic State	Raw Energy (hartrees)	BSSE Correction (hartrees)	ZPE Correction (hartrees)	Corrected Energy (hartrees)
AuO₂	C _s	² A''	-286.1359488	0.00039739	0.004118	-286.131433
AuO₂	C _{2v}	⁴ B ₁	-286.1343995	0.00006874	0.003808	-286.130523
OAuO	D _{∞h}	² Π _g	-286.0825659	0.00170492	0.004618	-286.076243
OAuO	D _{∞h}	⁴ Σ _g	-286.0989203	0.00160864	0.003389	-286.093923
[AuO₂]⁻	C _s	¹ A''	-286.1951936	0.00047195	0.003887	-286.190835
[AuO₂]⁻	C _s	³ A''	-286.2218261	0.00022273	0.003587	-286.218016
OAuO⁻	D _{∞h}	¹ Δ _g	-286.2322574	0.00158702	0.003503	-286.227167
OAuO⁻	D _{∞h}	³ Σ _{g⁻}	-286.2393439	0.00162054	0.004174	-286.233549

Table A3.5. Hirshfeld charges per fragment calculated from the Hirshfeld population analysis of $[\text{AuO}_2]^q$ and $[\text{OAuO}]^q$ ($q=0,-1$) complexes calculated with B3LYP-SDD/6-311+G(3df).

		q_{Au}	q_{O}	q_{O_2}
AuO₂	Doublet	0.000		0.000 (+0.029) ^a
AuO₂	Quartet	0.000		0.000 (0.000)
OAuO	Doublet	0.357	-0.178 -0.178	
OAuO	Quartet	0.207	-0.103 -0.103	
[AuO₂]⁻	Singlet	-0.340		-0.654 (-0.146)
[AuO₂]⁻	Triplet	-0.157		-0.834 (-0.064)
OAuO-	Singlet	-0.175	-0.412 -0.412	
OAuO-	Triplet	-0.142	-0.428 -0.428	

^aValue in parenthesis denote the charge on the atom(s) attached to the Au atom center.

Table A3.6. Raw energies and corrected energies with BSSE and ZPE corrections of optimized binary and ternary complexes^{a,b} for B3LYP-SDD/6-311+G(3df).

Species	Symm.	Elec. state	Raw Energy (hartrees)	BSSE Correction (hartrees)	ZPE Correction (hartrees)	Corrected Energy (hartrees)
[AuCO]⁺	$C_{\infty v}$	1A_1 ($^1\Sigma^+$)	-248.8402310	0.00079779	0.007551	-248.831882
AuCO	C_s	$^2A'$	-249.1256097	0.00039389	0.006038	-249.119178
[AuCO]⁻	C_s	$^1A'$	-249.1964776	0.00013209	0.005305	-249.191040
[AuO₂]⁺	C_s	$^3A''$	-285.8078127	0.00165083	0.004501	-285.801661
AuO₂	C_s	$^2A''$	-286.1359488	0.00039739	0.004118	-286.131433
AuO₂	C_{2v}	4B_1	-286.1343995	0.00006873	0.003808	-286.130523
[AuO₂]^{-c}	C_s	$^1A''$	-286.1951936	0.00047195	0.003887	-286.190835
[AuO₂]⁻	C_s	$^3A''$	-286.2218261	0.00022273	0.003587	-286.218016
[O₂AuCO]⁺ A	C_s	$^3A''$	-399.2473448	0.00054012	0.012830	-399.233975
O₂AuCO B	C_s	$^2A''$	-399.5449983	0.00150283	0.012602	-399.530893
Au(CO)O₂ E	C_s	$^2A''$	-399.511226	0.00184242	0.013467	-399.495917
Au(CO)O₂ 3.4 E	C_s	$^2A''$	-399.5080901	0.00188132	0.013485	-399.492724
Au(CO)O₂ 3.4 A	C_s	$^2A''$	-399.5052349	0.00059087	0.010003	-399.494641
[O₂AuCO]⁻ C	C_{2v}	1A_2	-399.5966330	0.00200699	0.012074	-399.582552
[Au(CO)O₂]⁻ F	C_s	$^1A''$	-399.6074061	0.00233213	0.013444	-399.591630
[Au(CO)O₂]⁻ 3.4 F	C_s	$^1A''$	-399.6075074	0.00221827	0.013456	-399.591833
[Au(CO)O₂]⁻ 3.4 B	C_1	1A	-399.5579809	0.00233213	0.009985	-399.545664
[O₂AuCO]⁻ D	C_s	$^3A''$	-399.5937385	0.00111093	0.010388	-399.582240
[Au(CO)O₂]⁻ 3.4 C	C_1	3A	-399.5827960	0.00065639	0.009458	-399.572682
[Au(CO)O₂]⁻ 3.4 D	C_s	$^3A''$	-399.5829858	0.00055627	0.009351	-399.573079

^a Lowest energy state for species of the same charge and molecular components are in **bold**.

^b Labels A-D correspond to the structures shown in Figure 3.3. Labels 3.4 A-F correspond to structures in supporting information Figure 3.4.

^c [AuO₂]⁻ singlet is restricted (closed shell) due to high spin contamination in the unrestricted singlet calculation.

Table A3.7. Calculated stretching vibrational frequencies in cm⁻¹ and intensities (in parentheses) of optimized long range and pre-reactive rotamer ternary complexes for B3LYP-SDD/6-311+G(3df).

Species	Stretching Frequency – cm ⁻¹ (Intensity)				
	Electronic State	Au-C	C-O	Au-O	O-O
long range					
Au(CO)O ₂ A ^a	² A''	350 (4.47)	2089 (715.9) 38 (2.65)		1571 (232.9)
[Au(CO)O ₂] ⁻ B	¹ A	167 (1.17)	2082 (476.4)	401 (18.5)	1123 (584.5)
[Au(CO)O ₂] ⁻ C	³ A	285 (7.77)	1997 (749.8)	45 (0.09)	1281 (1493.3)
[Au(CO)O ₂] ⁻ D	³ A''	95 (5.99)	1984 (431.7) 317 (15.7)		1393 (3808.5)
pre-reactive rotamers					
Au(CO)O ₂ E	² A''	853 (209.3)	1904 (345.2) 623 (82.8)		1106 (1.06)
[Au(CO)O ₂] ⁻ F	¹ A'	786 (233.5)	1802 (366.3) 1095 (300.8)		746 (105.8)

^a Labels A-F correspond to the structures shown in Figure 3.4.

Table A3.8. ZPE and BSSE corrected binding energies^a for long range and pre-reactive rotamer ternary complexes calculated with the B3LYP-SDD/6-311+G(3df) in kcal/mol and cooperative binding evaluated as a function of like charges.

		O ₂ AuCO or Au(CO)O ₂ ^b	cooperative binding ^{b,c}
Long Range			
Neutral	Doublet	-7.21 A ^d	0.40
	Singlet	11.90 (-26.57) B	16.47 (-0.59)
Anionic	Triplet	-5.06 C	-0.48
	Triplet	-5.31 D	-0.73
Pre-reactive Rotamers			
Neutral	Doublet	-6.11 E	1.50
Anionic	Singlet	-17.07 (-55.54) F	-12.50 (-29.56)

^a Computed relative to optimized values of the **ground state** components, with charge (if any) localized on gold center.

^b Parenthetical values computed relative to the energy of O₂ singlet, as shown here: [E_{AuOO-} - (E_{Au-} + E_{OOsinglet})] or [E_{OOAuCO-} - (E_{Au} + E_{CO} + E_{OOsinglet})].

^c Cooperative binding is calculated as the difference between total binding energy of ternary complex and summed binary complexes as shown here: E_{OOAuCO} - E_{AuOO} - E_{AuCO}. The AuO₂ energy used in cooperative binding is the ground state triplet. Parenthetical cooperative binding

values are calculated in the same fashion, but utilize the parenthetical values of the binary and ternary singlet complexes, where applicable.

^d Labels A-F correspond to the structures shown in Figure 3.4.

Table A3.9. Calculated bond lengths (in Å) for long range and pre-reactive rotamer ternary complexes at the level of B3LYP-SDD/6-311+G(3df).

		O₂AuCO or Au(CO)O₂				
		Au-C bond	C-O bond	Au-O bond	O-O bond	
Long Range						
Neutral	Doublet	2.065	1.136 2.964	3.157	1.209 A	
Anionic	Singlet	2.824	1.138	2.194	1.309 B	
	Triplet	2.467	1.148	3.064	1.235 C	
	Triplet	2.375	1.149 2.908		1.235 D	
Pre-reactive Rotamers						
Neutral	Doublet	2.007	1.169 1.466		1.315 E	
Anionic	Singlet	2.096	1.193 1.282		1.472 F	
Reference Lengths^b	C-O	1.124				
	C-O ⁺	1.108	O-O	1.203	O-O	1.341
	C-O ⁻	1.183	(O ₂)		(O ₂) ⁻	(O ₂) ²⁻

^a Labels A-F correspond to the structures shown in Figure 3.4.

^bcalculated at same level of theory: B3LYP/6-311+G(3df) and O₂ reference bond length is from the triplet ground state species.

Table A3.10. Calculated shifts in vibrational frequencies (in cm⁻¹) of optimized (long range and pre-reactive rotamer ternary complexes^a in B3LYP-SDD/6-311+G(3df).

		O₂AuCO or Au(CO)O₂	
		CO Frequency (in cm⁻¹)	O₂ Frequency (in cm⁻¹)
Long Range			
Neutral	Doublet	-127.96	-74.21 A
Anionic	Singlet	-134.76	-521.94 B
	Triplet	-219.99	-264.06 C
	Triplet	-233.1	-251.94 D
Pre-reactive Rotamers			
Neutral	Doublet	-313.37	-539.28 E
Anionic	Singlet	-415.44	-898.30 F
reference frequencies^b		CO – 2217	O ₂ – 1645
		CO ⁺ – 2300	O ₂ ⁻ – 1181
		CO ⁻ – 1665	O ₂ ²⁻ – 703

^aLabels A-F correspond to the structures shown in Figure 3.4.

^bcalculated at same level of theory: B3LYP/6-311+G(3df) and O₂ reference frequency is the triplet ground state

Table A3.11. Hirshfeld charges per fragment^a calculated from the Hirshfeld population analysis for long range and pre-reactive rotamer ternary complexes.

		O₂AuCO or Au(CO)O₂		
		q _{Au}	q _{CO}	q _{O₂}
Long Range				
Neutral	Doublet	-0.046	+0.061 (0.155)	-0.014 A ^b (-0.014)
Anionic	Singlet	-0.427	-0.109 (+0.063)	-0.460 B (-0.160)
	Triplet	-0.613	-0.157 (+0.033)	-0.224 C (-0.083)
	Triplet	-0.604	-0.137 (+0.050)	-0.252 D (-0.151)
Pre-reactive Rotamers				
Neutral	Doublet	+0.096	-0.003 (+0.179)	-0.092 E
Anionic	Singlet	-0.283	-0.104 (+0.166)	-0.611 F

^aThe charge value in parentheses denotes the charge on the atom(s) in an intermolecular bond.

^b Labels A-F correspond to the structures shown in Figure 3.4.

Table A3.12. Atomic charges per fragment^a calculated from the natural bond order (NBO) population analysis for neutral and anionic separated and pre-reactive ternary complexes^{b,c} using B3LYP/SDD/6-311+G(3df).

		AuCO		O₂AuCO or Au(CO)O₂			AuO₂	
		q _{Au}	q _{CO}	q _{Au}	q _{CO}	q _{O₂}	q _{Au}	q _{O₂}
Separated								
Cationic ^d		+0.792	+0.208 (+0.471)	+0.630	+0.254 (+0.526)	+0.117 A (-0.097)	+0.922	+0.078 (-0.115)
Neutral	Doublet	+0.038	-0.038 (+0.398)	+0.467	+0.139 (+0.516)	-0.606 B (-0.395)	+0.145	-0.145 (-0.037)
	Quartet						-0.002	+0.002 (+0.001)
Anionic	Singlet	-0.881	-0.119 (+0.440)	+0.401	-0.211 (+0.337)	-1.190 C (-0.595)	-0.310	-0.690 ^e (-0.306)
	Triplet			+0.147	-0.425 (+0.159)	-0.721 D (-0.398)	-0.768	-0.232 (-0.062)
Pre-reactive								
Neutral (doublet)				+0.223	+0.082 (+0.576)	-0.306 E		
Anionic (singlet)				-0.139	+0.072 (+0.703)	-0.934 F		

^a The charge value in parentheses denotes the charge on the atom(s) in an intermolecular bond.

^b Labels A-F correspond to the structures shown in Figure 3.3.

^c Lowest energy state for species of the same charge and molecular components are in **bold**.

^d [AuCO]⁺ has a singlet ground state and other cationic complexes have triplet ground states.

^e [AuO₂]⁻ singlet was calculated as restricted (closed shell) due to high spin contamination in the unrestricted singlet calculation.

Table A3.13. Charges per fragment^a calculated from the CHELPG^b population analysis of atomic charges for cationic, neutral and anionic binary and ternary complexes^{c,d} calculated with B3LYP-SDD/6-311+G(3df).

		AuCO		O₂AuCO or Au(CO)O₂			AuO₂	
		q _{Au}	q _{CO}	q _{Au}	q _{CO}	q _{O2}	q _{Au}	q _{O2}
Separated								
Cationic^e		+0.845	+0.155 (-0.014)	+0.367	+0.339	+0.295 A (+0.148)	+0.843	+0.157 (-0.020)
Neutral	Doublet	-0.066	+0.066 (+0.220)	+0.200	+0.174 (+0.289)	-0.374 B (-0.167)	+0.067	-0.067 (-0.008)
	Quartet							
Anionic	Singlet	-0.841	-0.159 (+0.026)	+0.051	-0.189 (+0.131)	-0.863 C (-0.431)	-0.484	-0.516 ^f (-0.099)
	Triplet			+0.028	-0.415 (-0.098)	-0.613 D (-0.269)	-0.747	-0.262 (+0.009)
Pre-reactive								
Neutral (doublet)				0.243	-0.108 (+0.190)	-0.135 E		
Anionic (singlet)				-0.222	-0.013	-0.765 F (+0.624)		

^a The charge value in parentheses denotes the charge on the atom in an intermolecular bond.

^b Read radius of 1.90 Å used for Au.

^c Labels A-F correspond to the structures shown in Figure 3.3.

^d Lowest energy state for species of the same charge and molecular components are in **bold**.

^e [AuCO]⁺ has a singlet ground state and other cationic complexes have triplet ground states.

^f [AuO₂]⁻ singlet was calculated as restricted (closed shell) due to high spin contamination in the unrestricted singlet calculation.

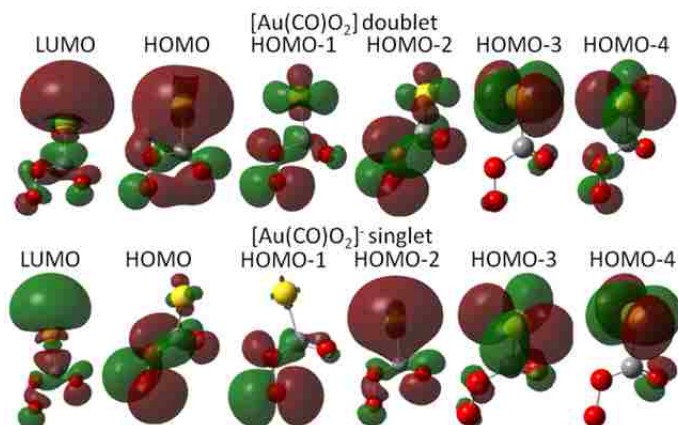


Figure A3.1. Five highest occupied molecular orbitals and LUMO of “pre-reactive rotamer complexes,” $\text{Au}(\text{CO})\text{O}_2$ (Fig. 3.4 E) and $[\text{Au}(\text{CO})\text{O}_2]^-$ singlet (Fig. 3.4 F). $\text{Au}(\text{CO})\text{O}_2$ β -spinorbitals are not shown, but are similar to the (shown) α -spinorbitals, except that the LUMO- β is the same structure as HOMO-2 α (shown in figure). Note that for both series, all orbitals feature a node in the “breaking” bond (O-O), and a bonding interaction in the “forming” bond (2nd C-O bond).

A3.2 Comparison of B3LYP, mPW1PW91, B3PW91:

We investigated the effect of hybrid DFT functionals on the structural data (bond lengths and angles), frequencies and binding energies (for the binary and ternary complexes) and compared the results across the hybrid DFT functionals of B3LYP, mPW1PW91 and B3PW91 (and also mPW1LYP, a mixture of the (modified) Perdew-Wang exchange and LYP correlation functionals). Originally, complexes were calculated with the mPW1PW91 functional and then recalculated in B3LYP, which is a well-known and very popular functional, especially in the Au complex literature. When differences in some of the complexes were observed between these two functionals, B3PW91 was added and mPW1LYP was added later to try and understand if certain exchange or correlation functionals were responsible for anomalous bonds/structures. To start, the “simple” molecules of CO^q and O_2^q were tested across these functionals and the bond lengths and frequencies are shown in Table A3.14 for the mixed basis set of SDD/6-311+G(2d),

where q ranges from +1 to -2, but the +1 charge is applied to CO and not O₂ and the -2 charge is applied to O₂, not CO. For the CO ^{q} molecules, the bond lengths are within 0.005 Å and the frequencies are different by less than 30 cm⁻¹, while the O₂ ^{q} data has greater difference in the bond lengths, with differences in values up to 0.033 Å in the O₂²⁻ molecule, and frequencies are different by a maximum of 73 cm⁻¹. These results show that these functionals are relatively robust and can be used to verify agreement in the general shape of the calculated complexes or identify anomalies in the calculated structures as a function of the different functionals. Furthermore, these functionals were used in calculations for the binary [AuCO] ^{q} and [AuO₂] ^{q} and ternary [O₂AuCO] ^{q} ($q = +1, 0, -1$) complexes, where the bond lengths are shown in Tables A3.15 and A3.16, frequencies in Table A3.17 and binding energies in Table A3.18. The functionals are grouped together in terms of each complex from the binary [AuCO]⁺ complex to ternary [O₂AuCO]⁻ triplet complex, as this is the easiest way to compare the functionals for the various structural and energetic data. The binary and ternary complexes show greater differences in the bond lengths than was observed in the molecular data (CO and O₂). Similar to the CO molecular data above, the CO bond lengths in the binary and ternary complexes are within approximately 0.01 Å with the largest differences existing in the AuCO⁻ (singlet) complex and the related anomalies will be discussed later. The Au-C bond lengths have an average difference of 0.05 Å across the four functionals for binary and ternary complexes, where the maximum difference of 0.82 Å (in AuCO⁻) is not included in the average. For the OO bond lengths in the binary and ternary complexes, the average difference is ~0.02 Å, which is similar to the O₂ molecular data discussed above. For the AuO bonds, the average difference is ~0.03 Å, with respect to the four

functionals, but similar to Au-C, there are anomalies that appear in the Au-O bonds, specifically the binary AuO₂ doublet and AuO₂⁻ singlet complexes, which will be discussed below. Other generalities can be observed in the bonds in terms of the functionals, such as the observation that Au-C and Au-O bonds are, generally, longer in the B3LYP and mPW1LYP functionals than the other two functionals by approximately 0.025 Å, except in AuCO⁻ and AuO₂ doublet (discussed below).

For AuCO⁻, the B3LYP and mPW1LYP functionals have shorter CO bonds than those in B3PW91 and mPW1PW91 by 0.022 Å. This anomaly for AuCO⁻ continues in the Au-C bond, where B3LYP and mPW1LYP have unusually long bonds of 2.945 and 3.218 Å, respectively, where the maximum difference in the AuC bond (compared to the other two functionals) is 0.82 Å. The AuO₂ doublet has a maximum difference of 0.65 Å and AuO₂⁻ singlet has a maximum difference of 0.33 Å, but the “anomalous” functionals are different in each case. For the neutral complex, mPW1PW91 and mPW1LYP have significantly longer Au-O bonds than B3PW91 and B3LYP, while the anionic complex has longer Au-O bonds in mPW1PW91 and B3LYP than the other two functionals. However, the “anomalous” AuO₂⁻ singlet bond lengths, 2.379 and 2.497 Å are reasonably similar to the other two functionals (2.165 and 2.170 Å). As the original focus of the DFT “comparison” work was comparing mPW1PW91 to B3LYP, the similarity of the Au-O bonds (in these functionals) gave credibility to the idea that the AuO₂⁻ singlet complex was not a “problem” complex that needed further study with LanL2DZ or higher level theory, such as CCSD(T). For AuO₂, mPW1PW91 has the longest AuO bond at 3.042 Å and mPW1LYP is also longer at 2.761 Å, while B3LYP and B3PW91 are both close to 2.4 Å for AuO. This anomaly initially indicated that the modified

Perdew-Wang exchange and one HF exchange term may be responsible for anomalies, but the AuC anomaly occurs in B3LYP and mPW1LYP, which would indicate that the issue may be related to the LYP correlation term. Further investigation into the literature indicated that AuCO⁻ was known to be difficult to calculate accurately.

The frequencies were also calculated and compared across the four functionals. Similar to the bond lengths, the AuCO⁻ and AuO₂ complexes have broad frequency distributions for the functionals, which span 176 cm⁻¹ (for CO) and 226 cm⁻¹ (for OO), respectively. The Au-C and Au-O frequencies of these complexes also have broad distributions of 139 cm⁻¹ and 153 cm⁻¹, respectively. AuO₂⁻ singlet also has a fairly broad distribution of frequencies of 114 cm⁻¹ for OO and 222 cm⁻¹ for Au-O; however, the mPW1LYP frequency of Au-O is ~ 75 cm⁻¹ lower than the closest value (247 cm⁻¹ in B3LYP), which is very odd as mPW1LYP had a shorter Au-O bond than B3LYP and mPW1PW91. If the anomalous frequencies are ignored, the average difference of the Au-C frequencies (across all functionals and complexes) is 30 cm⁻¹; Au-O, 15 cm⁻¹; CO, 37 cm⁻¹, and O₂, 63 cm⁻¹. The average differences are greater than the CO and O₂ molecular data, but are still close enough to identify anomalous species and indicate that the DFT functionals are relatively robust for calculating transition metal complexes with carbon and oxygen containing ligands. These DFT calculations, specifically B3LYP, were utilized for the complexes discussed in chapter 3. The B3LYP results were also calculated with the double-hybrid DFT functional, B2PLYP, and second order Moller-Plesset perturbation theory (MP2), to ensure that the complexes and structural data were not artifacts of DFT calculations. Major differences between the B3LYP results and

B2PLYP results will be discussed as they appear throughout the chapters, since very few structures showed differences between these two types of calculations.

The $[\text{AuCO}]^-$ singlet structural and frequency data were further investigated to look for trends as a function of different hybrid DFT functionals and basis sets for Au (SDD or LanL2DZ) and CO (varying Pople basis set sizes shown in Table A3.18). General trends exist within the same functional (different basis sets), but there is no single general trend across all functionals, other than the observation that B3PW91 and mPW1PW91 typically have shorter AuC bonds and (mostly) longer CO bonds than B3LYP values (across all basis sets). For B3LYP/SDD, the AuC bonds increase by $\sim 0.15 \text{ \AA}$, while the CO bonds decrease with increasing Pople basis set size; the CO frequencies are in agreement and increase (blue shift) with increasing basis set size. These general trends also occur in LanL2DZ (for B3LYP); however, the AuC bond decreases slightly ($\sim 0.03 \text{ \AA}$) from 6-311+G(2d) to 6-311+G(3df) basis set. With the mPW1PW91 functional and both Au basis sets, the AuC and CO bonds are close to $\sim 2.4 \text{ \AA}$ and $\sim 1.15 \text{ \AA}$ across the various Pople basis sets, respectively, where the LanL2DZ/6-311+G(3df) results has the shortest bond length, of its Pople basis sets, at 2.371 \AA . Comparatively, the results for SDD indicate the shortest AuC bond length (2.422 \AA) in 6-31+G(d), 6-311+G(2d) and 6-311+G(3df). B3PW91 data, for both Au basis sets and across the Pople basis sets, have AuC and CO bonds in the 2.4 \AA and 1.16 \AA ranges, where the shortest AuC bonds in both Au basis sets are observed in the 6-311+G(3df) basis set. In both mPW1PW91 and B3PW91, the AuC and CO bonds do not have a clear trend of increasing or decreasing as a function of Pople basis set size, which is also reflected in the CO frequencies. It is interesting that the mPW1PW91 and B3PW91 functionals have

similar AuC and CO bond lengths (and frequencies), which suggests that the correlation energy portion of the functional has significant impact on the calculation result.

However, calculations with another LYP correlation energy functional would be necessary to better understand the influence of the correlation energy portion of the functional.

In B3LYP and both Au basis sets, the AuO length increases with increasing Pople basis set size up to 6-311+G(2d) and then drops for the 6-311+G(3df) basis set with the shortest distance of 2.347 Å, but all Pople basis sets are in the 2.3-2.5 Å range for AuO. In a similar trend, the OO bond (for the SDD data points) shortens with increasing Pople size up to 6-311+G(2d), which is the shortest distance of 1.198 Å, while the OO bond increases slightly in the 6-311+G(3df) basis set (to 1.223 Å). The LanL2DZ data points indicate that 6-311+G(d) has the shortest OO bond at 1.219 Å, but all of the OO bonds are around 1.22 Å. The mPW1PW91 functional has the longest AuO bonds of these tested functionals with values between 2.7 and 3.1 Å, which are generally longer than the B3LYP values by 0.4 Å. In the SDD data, the AuO bond length increase with increasing Pople basis set size and 6-311+G(3df) has the longest bond at 3.074 Å, while the OO bond has no clear trend in bond length changes, but 6-311+G(3df) has the shortest OO bond at 1.193 Å. For mPW1PW91/LanL2DZ data, there are no clear trends in the AuO and OO bond lengths, where the AuO bond is shortest in 6-311+G(2d) at 2.834 Å (longest in 6-311+G(3df) at 3.103 Å) and the OO bond is shortest in 6-311+G(3df) at 1.193 Å. For B3PW91, the SDD and LanL2DZ data are similar and more like B3LYP in lengths than mPW1PW91, where the shortest AuO bonds are observed in the 6-311+G(3df) results at 2.315 and 2.258 Å and the longest Au bonds are in 6-311+G(2d) at 2.433 and

2.490 Å, respectively. For the OO bond, SDD data has the shortest bond in the 6-31+G(d) basis set (1.208 Å) and 6-311+G(2d) was the longest at 1.226 Å. Comparatively, the LanL2DZ data has the shortest bond in the 6-311+G(d) basis set at 1.210 Å and the longest bond at 6-31+G(d) at 1.222 Å. As pointed out above, B3LYP and B3PW91 AuO bond length data are more similar with bond lengths near 2.4 Å, while mPW1PW91 grossly overestimates the AuO bond at 2.7-3.1 Å. These results suggest that the exchange/Hartree Fock portions of the functional are affecting AuO more than the correlation portion; however, studies with another mPW1 functional are needed for better comparison. AuCO and AuO₂ have two different functional-related trends for the metal-ligand bonds, where B3LYP overestimates the AuC bond greatly for AuCO-, while mPW1PW91 greatly overestimates the AuO bond for AuO₂. For the Au basis sets, it is not clear as to whether SDD or LanL2DZ is “better” for the calculations, as both appeared to perform well in these results and tended to have similar results.

Table A3.14. Calculated geometry and stretching vibrational frequencies of optimized CO and O₂ reference species for **B3PW91**, mPW1PW91, *B3LYP* and mPW1LYP-SDD/6-311+G(2d).

Species	Geometry	Frequency (stretching)	Species	Geometry	Frequency (stretching)
CO singlet	r _{C-O}	C-O	O ₂ triplet	r _{O-O}	OO
	1.125	2219		1.202	1670
	1.123	2240		1.197	1702
CO ⁺ doublet	<i>1.128</i>	<i>2211</i>	O ₂ ⁻ doublet	<i>1.206</i>	<i>1629</i>
	<u>1.124</u>	<u>2228</u>		<u>1.205</u>	<u>1650</u>
	1.108	2314		1.335	1214
CO ⁻ doublet	1.106	2339	O ₂ ²⁻ singlet	1.329	1240
	<i>1.109</i>	<i>2295</i>		<i>1.346</i>	<i>1176</i>
	<u>1.107</u>	<u>2315</u>		<u>1.343</u>	<u>1191</u>
CO ⁻ doublet	1.182	1669	O ₂ ²⁻ singlet	1.543	728
	1.181	1669		1.533	749
	<i>1.185</i>	<i>1651</i>		<i>1.566</i>	<i>694</i>
	<u>1.185</u>	<u>1649</u>		<u>1.562</u>	<u>706</u>

B3LYP results shown in bold, *B3PW91* results are in italics and mPWLYP are underlined.

Table A3.15. Calculated bond lengths (in Å) for binary and ternary complexes with **B3PW91**, mPW1PW91, *B3LYP*, & mPW1LYP^a-SDD/6-311+G(2d).

		AuCO		O ₂ AuCO			AuO ₂	
		Au-C bond	C-O bond	Au-C bond	C-O bond	Au-O bond	O-O bond	O-O bond
Cationic (triplet) ^b		1.942	1.115	1.934	1.116	2.189	1.204	2.286
		1.946	1.112	1.934	1.113	2.188	1.199	2.294
		<i>1.966</i>	<i>1.115</i>	<i>1.954</i>	<i>1.116</i>	<i>2.205</i>	<i>1.211</i>	<i>2.310</i>
		<u>1.977</u>	<u>1.113</u>	<u>1.961</u>	<u>1.114</u>	<u>2.210</u>	<u>1.208</u>	<u>2.324</u>
Neutral (doublet)		2.028	1.139	1.903	1.127	2.019	1.318	2.396
		2.030	1.136	1.902	1.124	2.014	1.314	2.396
		<i>2.069</i>	<i>1.139</i>	<i>1.922</i>	<i>1.127</i>	<i>2.031</i>	<i>1.328</i>	<i>2.402</i>
		<u>2.085</u>	<u>1.135</u>	<u>1.926</u>	<u>1.125</u>	<u>2.029</u>	<u>1.327</u>	<u>2.761</u>
Anionic Singlet		2.398	1.156	1.836	1.163	1.939^c	1.486	2.165
		2.422	1.152	1.830	1.159	1.934	1.478	2.379
		2.945	<i>1.141</i>	<i>1.904</i>	<i>1.168</i>	<i>1.955</i>	<i>1.503</i>	<i>2.497</i>
		3.218	<u>1.134</u>	<u>1.851</u>	<u>1.159</u>	<u>1.954</u>	<u>1.499</u>	<u>2.190</u>
				2.006	1.183	2.149	1.317	3.037
Anionic Triplet				2.000	1.181	2.135	1.313	3.036
				<i>2.033</i>	<i>1.183</i>	<i>2.174</i>	<i>1.326</i>	<i>3.027</i>
				<u>2.033</u>	<u>1.181</u>	<u>2.165</u>	<u>1.325</u>	<u>3.037</u>

^a **B3LYP** results shown in bold, *B3PW91* results are in italics and mPWLYP are underlined.

^b [AuCO]⁺ is singlet; other cationic complexes are triplets

^c Perpendicular distance to O-O bond center in C_{2v} complex.

Table A3.16. Calculated stretching vibrational frequencies (in cm^{-1}) and intensities of optimized binary complexes for **B3PW91**, mPW1PW91, *B3LYP*, and mPW1LYP^a-SDD/6-311+G(2d).

Species		Stretching frequency $-\text{cm}^{-1}$ (Intensity)			
	Electronic state	Au-C	C-O	Au-O	O-O
[AuCO] ⁺	¹ A ₁ (¹ Σ ⁺)	399 (14.0)	2318 (204.6)		
		<u>397 (13.7)</u>	<u>2343 (207.0)</u>		
		<i>379 (12.5)</i>	<i>2306 (194.2)</i>		
		<u>370 (11.6)</u>	<u>2327 (192.9)</u>		
AuCO	² A'	380 (6.4)	2081 (852.9)		
		<u>374 (7.2)</u>	<u>2105 (902.4)</u>		
		<i>343 (6.4)</i>	<i>2071 (816.6)</i>		
		<u>325 (7.7)</u>	<u>2092 (844.4)</u>		
[AuCO] ^{-b}	¹ A'	319 (8.7)	1945 (1016.5)		
		<u>313 (8.5)</u>	<u>1975 (1015.2)</u>		
		<i>225^b (6.6)</i>	<i>2057^b (681.7)</i>		
		<u>180^b (5.37)</u>	<u>2121^b (496.1)</u>		
[AuO ₂] ⁺	³ A''			261 (1.0)	1602 (37.4)
				<u>255 (1.9)</u>	<u>1639 (22.7)</u>
				<i>251 (1.1)</i>	<i>1563 (36.4)</i>
				<u>243 (2.0)</u>	<u>1590 (21.3)</u>
AuO ₂ ^b	² A''			271 (5.1)	1496 (489.2)
				<u>119^b (0.04)</u>	<u>1674^b (35.3)</u>
				<i>272 (5.8)</i>	<i>1448 (511.2)</i>
				<u>171 (0.42)</u>	<u>1581 (149.9)</u>
[AuO ₂] ⁻	¹ A'			396 (18.7)	1178 (697.2)
				<u>275 (3.8)</u>	<u>1241 (1081.7)</u>
				<i>247 (4.0)</i>	<i>1266 (1114.4)</i>
				<u>174 (0.12)</u>	<u>1152 (789.9)</u>
[AuO ₂] ^{-b}	³ A''			161 (3.7)	1410 (1890.8)
				<u>160 (5.5)</u>	<u>1436 (2237.0)</u>
				<i>161 (3.4)</i>	<i>1363 (1821.4)</i>
				<u>159 (4.7)</u>	<u>1380 (2143.4)</u>

^a *B3LYP* values shown in italics; **B3PW91** values are shown in bold, and mPWLYP values are underlined.

^b Anomalously long bond lengths and different frequencies when compared to other functionals.

Table A3.17. Calculated stretching vibrational frequencies (in cm^{-1}) and intensities of optimized ternary complexes for **B3PW91**, mPW1PW91, *B3LYP*, and mPW1LYP^a-SDD/6-311+G(2d).

Species		Stretching frequency $-\text{cm}^{-1}$ (Intensity)			
	Electronic state	Au-C	C-O	Au-O	O-O
[O ₂ AuCO] ⁺	³ A''	420 (21.3)	2313 (307.6)	303 (2.2)	1613 (7.8)
		419 (20.2)	2337 (306.2)	304 (3.0)	1647 (9.7)
		<i>402 (18.9)</i>	<i>2302 (293.6)</i>	<i>298 (2.4)</i>	<i>1574 (7.1)</i>
		<u>397 (16.9)</u>	<u>2322 (287.5)</u>	<u>298 (3.3)</u>	<u>1599 (8.9)</u>
O ₂ AuCO	² A''	454 (5.3)	2224 (563.7)	543 (8.6)	1187 (10.7)
		456 (6.2)	2250 (555.7)	549 (10.6)	1210 (7.1)
		<i>434 (4.0)</i>	<i>2211 (545.1)</i>	<i>533 (9.0)</i>	<i>1152 (10.5)</i>
		<u>431 (3.7)</u>	<u>2234 (533.0)</u>	<u>536 (11.0)</u>	<u>1166 (7.1)</u>
[O ₂ AuCO] ⁻	¹ A ₂	557 (22.1)	2019 (1227.1)	460 (56.6)	858 (179.0)
		562 (22.3)	2042 (1269.5)	466 (60.5)	874 (192.9)
		<i>540 (20.2)</i>	<i>2001 (1261.2)</i>	<i>445 (54.1)</i>	<i>826 (181.0)</i>
		<u>539 (20.0)</u>	<u>2019 (1310.1)</u>	<u>448 (56.9)</u>	<u>833 (195.4)</u>
[O ₂ AuCO] ^{-b}	³ A''	485 (10.4)	1831 (689.0)	385 (5.0)	1202 (43.9)
		493 (9.3)	1850 (685.5)	396 (8.8)	1230 (24.5)
		<i>465 (10.4)</i>	<i>1816 (729.0)</i>	<i>364 (5.3)</i>	<i>1163 (55.3)</i>
		<u>468 (9.6)</u>	<u>1828 (746.1)</u>	<u>372 (10.3)</u>	<u>1182 (32.5)</u>

^a*B3LYP* values shown in italics; **B3PW91** values are shown in bold, and mPW1LYP values are underlined.

Table A3.18. Comparison of the trends in geometry and stretching frequency for hybrid DFT functionals of B3LYP, mPW1PW91 and B3PW91, Au basis sets of SDD and LanL2DZ and varying levels of Pople basis sets for C and O atoms – 6-31+G(d), 6-311+G(d), 6-311+G(2d), 6-311+G(3df) – for the anomalous [AuCO]⁻ singlet complex.

[AuCO] ⁻ singlet							
Functional	Au basis set	C,O basis set	r _{Au-C} (Å)	r _{C-O} (Å)	∠AuCO (°)	v _{Au-C} (cm ⁻¹)	v _{C-O} (cm ⁻¹)
B3LYP	SDD	6-31+Gd	2.812	1.156	112	30	2023
B3LYP	LanL2DZ	6-31+Gd	2.642	1.161	113	55	1985
mPW1PW91	SDD	6-31+Gd	2.422	1.152	115	101	1975
mPW1PW91	LanL2DZ	6-31+Gd	2.442	1.163	115	110	1974
B3PW91	SDD	6-31+Gd	2.402	1.168	116	105	1942
B3PW91	LanL2DZ	6-31+Gd	2.430	1.167	115	113	1947
B3LYP	SDD	6-311+Gd	2.915	1.144	111	55	2049
B3LYP	LanL2DZ	6-311+Gd	2.694	1.149	113	54	2003
mPW1PW91	SDD	6-311+Gd	2.452	1.154	115	94	1981
mPW1PW91	LanL2DZ	6-311+Gd	2.452	1.154	114	109	1980
B3PW91	SDD	6-311+Gd	2.425	1.158	115	101	1951
B3PW91	LanL2DZ	6-311+Gd	2.440	1.158	115	112	1954
B3LYP	SDD	6-311+G(2d)	2.945	1.140	111	55	2057
B3LYP	LanL2DZ	6-311+G(2d)	2.748	1.146	112	41	2017
mPW1PW91	SDD	6-311+G(2d)	2.422	1.152	116	98	1975
mPW1PW91	LanL2DZ	6-311+G(2d)	2.412	1.153	115	98	1970
B3PW91	SDD	6-311+G(2d)	2.398	1.156	115	102	1945
B3PW91	LanL2DZ	6-311+G(2d)	2.398	1.157	115	100	1944
B3LYP	SDD	6-311+G(3df)	2.996	1.138	110	42	2075
B3LYP	LanL2DZ	6-311+G(3df)	2.715	1.145	112	40	2020
mPW1PW91	SDD	6-311+G(3df)	2.422	1.151	115	96	1984
mPW1PW91	LanL2DZ	6-311+G(3df)	2.371	1.153	116	104	1967
B3PW91	SDD	6-311+G(3df)	2.398	1.155	116	100	1955
B3PW91	LanL2DZ	6-311+G(3df)	2.358	1.157	116	109	1942

Table A3.19. Comparison of the trends in geometry and stretching frequency for hybrid DFT functionals of B3LYP, mPW1PW91 and B3PW91, Au basis sets of SDD and LanL2DZ and varying levels of Pople basis sets for C and O atoms – 6-31+G(d), 6-311+G(d), 6-311+G(2d), 6-311+G(3df) – for the anomalous [AuO₂]⁻ singlet complex.

AuO ₂ doublet							
Functional	Au basis set	O basis set	r _{Au-O} (Å)	r _{O-O} (Å)	∠AuOO (°)	ν _{Au-O} (cm ⁻¹)	ν _{O-O} (cm ⁻¹)
B3LYP	SDD	6-31+Gd	2.369	1.236	120	74	1444
B3LYP	LanL2DZ	6-31+Gd	2.430	1.231	119	73	1477
mPW1PW91	SDD	6-31+Gd	2.739	1.208	121	51	1648
mPW1PW91	LanL2DZ	6-31+Gd	3.075	1.204	121	44	1693
B3PW91	SDD	6-31+Gd	2.360	1.208	119	67	1492
B3PW91	LanL2DZ	6-31+Gd	2.438	1.222	119	69	1531
B3LYP	SDD	6-311+Gd	2.435	1.222	121	82	1459
B3LYP	LanL2DZ	6-311+Gd	2.479	1.219	120	72	1483
mPW1PW91	SDD	6-311+Gd	2.756	1.198	122	52	1644
mPW1PW91	LanL2DZ	6-311+Gd	3.092	1.195	122	45	1687
B3PW91	SDD	6-311+Gd	2.4334	1.213	121	77	1511
B3PW91	LanL2DZ	6-311+Gd	2.490	1.210	120	64	1538
B3LYP	SDD	6-311+G(2d)	2.402	1.198	120	69	1433
B3LYP	LanL2DZ	6-311+G(2d)	2.368	1.222	119	69	1480
mPW1PW91	SDD	6-311+G(2d)	3.042	1.218	121	40	1674
mPW1PW91	LanL2DZ	6-311+G(2d)	2.834	1.200	121	13	1651
B3PW91	SDD	6-311+G(2d)	2.396	1.218	120	63	1496
B3PW91	LanL2DZ	6-311+G(2d)	2.478	1.213	119	63	1533
B3LYP	SDD	6-311+G(3df)	2.347	1.223	120	74	1444
B3LYP	LanL2DZ	6-311+G(3df)	2.303	1.225	119	76	1433
mPW1PW91	SDD	6-311+G(3df)	3.074	1.193	121	41	1694
mPW1PW91	LanL2DZ	6-311+G(3df)	3.103	1.193	121	43	1698
B3PW91	SDD	6-311+G(3df)					
B3PW91	LanL2DZ	6-311+G(3d)	2.258	1.219	119	101	1465

A4. Appendix to Chapter 4.

Table A4.1. Hirshfeld charges per fragment^a calculated from the Hirshfeld population analysis for reactant-side (minima) complexes^b (q=+1, 0, -1) calculated using B3LYP-SDD/6-311+G(3df).

O₂AuCO or Au(CO)O₂					
Charge	Spin	Name	q_{Au}	q_{CO}	q_{O2}
Separated					
Neutral	Doublet	Sep	+0.153	+0.162 (+0.214)	-0.314 (-0.133)
Anionic	Singlet	Sep	-0.071	-0.191 (0.029)	-0.736 (-0.368)
Pre-reactive					
Neutral	Doublet	Pre ₁	+0.083	-0.007 (+0.175)	-0.075
	In				
	Out	Pre ₂	+0.194	+0.023 (+0.336)	-0.217
Anionic	Singlet	Pre ₁	-0.266	-0.172 (+0.142)	-0.560
	In				
	Out	Pre ₂	-0.334	+0.202 (+0.753)	-0.867

^a The charge value in parentheses denotes the charge on the atom involved in an intermolecular bond with Au.

^b Labels Sep, Pre₁, Pre₂ correspond to Figures 4.1 and 4.2.

Table A4.2. Hirshfeld charges per fragment calculated from the Hirshfeld population analysis for reactant-side transition states^a calculated with the B3LYP-SDD/6-311+G(3df).

	Name	q_{Au}	q_{CO}	q_{O2}	q_{CO2}	q_O
Transitions between sep and pre minima						
{AuCOO₂}	TS ₁	+0.040	+0.061 (+0.172) ^b	-0.101 (-0.055)		
{AuCOO₂}⁻	TS ₁	-0.398	-0.126 (+0.071)	-0.473 (-0.191)		
Low barrier transition between pre-reactive minima						
AuCOO₂	LB ₁	+0.100	+0.019 (+0.187)	-0.119		
AuCOO₂⁻ singlet	LB ₁	-0.321	-0.073 (+0.182)	-0.602		

^a Labels correspond to Figures 4.1 and 4.2.

^b Value in parenthesis denote the charge on the atom(s) attached to the Au atom center.

Table A4.3. Hirshfeld charges per fragment calculated from the Hirshfeld population analysis for major transition states^a calculated with the B3LYP-SDD/6-311+G(3df).

	Name	q _{Au}	q _{co}	q _{o2}	q _{co2}	q _o
{AuCO₂O} in	In-TS	+0.107	+0.093 (+0.270) ^b	-0.199		
{AuCO₂O} out	Out-TS	+0.117	+0.035 (+0.224)	-0.152		
{Au(CO₂)O} in	In-TS	-0.348	-0.273 (+0.203)	-0.373		
{Au(CO₂)O} out	Out-TS	-0.659			+0.079 (+0.312)	-0.416

^a Labels correspond to Figures 4.1 and 4.2.

^b Value in parenthesis denote the charge on the atom(s) attached to the Au atom center.

Table A4.4. Hirshfeld charges per fragment calculated from the Hirshfeld population analysis for low barrier and post-reactive transition states^a calculated with the B3LYP-SDD/6-311+G(3df).

	Name	q _{Au}	q _{co}	q _{o2}	q _{co2}	q _o
OAuCO₂	LB ₂	+0.165			+0.011 (-0.175) ^b	-0.175
AuO-CO₂	TS ₂	+0.117			-0.040	-0.076
AuO-CO₂	TS ₃	+0.279			-0.181	-0.097
OAuCO₂⁻ singlet	TS ₂	-0.415			-0.062 (+0.325)	-0.519

^a Labels correspond to Figures 4.1 and 4.2.

^b Value in parenthesis denote the charge on the atom(s) attached to the Au atom center.

Table A4.5. Hirshfeld charges per fragment calculated from the Hirshfeld population analysis for ternary post-reactive and product complexes^a calculated with the B3LYP-SDD/6-311+G(3df).

		q _{Au}	q _{co2}	q _o	q _{co3}
AuOCO₂	AR ₁	+0.189	-0.034	-0.155	
AuCO₃	Pro ₁	+0.350			-0.350 (-0.180)
AuCO₃⁻ singlet	Pro ₁	-0.142			-0.856 (-0.208)
OAuCO₂	Pro ₂	0.018	0.205 (+0.405)	-0.223	
OAuCO₂⁻ singlet	Pro ₂	-0.112	-0.370 (+0.163)	-0.515	

^a Labels correspond to Figures 4.1 and 4.2.

^b Value in parenthesis denotes the charge on the atom(s) attached to the Au atom center.

Detailed results of changes along pathways: The neutral system is described first and the anionic singlet section headings will be in *bold and italics*. The neutral system also has an additional set of post-reactive structures, which will be discussed after the product characteristics.

Sep: The separated complex, Sep, has been described previously and is the neutral (reactant side) global minimum at -30.07 kcal/mol, but is not the global minimum for the (reactant side) minima of the anionic singlet charge state (-11.25 kcal/mol). The complex is formed from the separated reactants and is the structure from which the pathway begins on the discussed reaction coordinate.

TS₁: A transition state (TS₁) between the separated complex and pre-reactive “in” complex has been identified that is 24.86 kcal/mol above Sep on the neutral pathway, but below the reactant asymptote (-5.21 kcal/mol). TS₁ is relatively similar in appearance to the previously described pre-reactive complex, Pre₁, as the O₂ moiety has rotated around Au to form a long intermolecular O-C bond. This transition state has been previously identified by Fan et al. and their reported structural and energetic data (-5.7 kcal/mol with respect to the reactant asymptote) are in agreement with these calculations. {} With respect to Sep, there are large increases in the Au-O and Au-C bonds and slight increases in CO and O-O to 1.138 Å (similar to free CO) and 1.236 Å (like free O₂), respectively. The transition state has an intermolecular O-C bond of 2.111 Å and the AuCO angle decreases from 180° to 145°. The vibrational frequency of CO (2089 cm⁻¹) red shifts slightly and remains similar to CO, while OO frequency (1377 cm⁻¹) blue shifts closer to “free” O₂. The electrostatic potential (ESP) is mapped onto the isodensity surfaces to visualize charge distribution throughout the complex; the ESP surfaces are shown in

context of the reaction pathways for both charge states and are shown in Figures 4.3 (neutral) and 4.4 (anionic singlet). Compared to Sep, the electrostatic potential surface (ESP) of TS_1 , shown in Figure 4.3, has a well-distributed charge on the complex (less polarized appearance), where there is a slight positive charge on AuCO (approximately half the amount of Sep moiety), and slight negative charge on O_2 (approximately one-third of that on the Sep moiety).

TS₁, transition state between Sep and Pre₁: This (anionic) structure resides at +11.14 kcal/mol above the reactant asymptote, and 22.39 kcal/mol above Sep, with an increase in the AuC and AuO bonds and decrease in the AuCO bond from 180° . The CO bond decreases by 0.016 Å (1.146 Å, like “free” CO) and OO also decreases by 0.183 Å (1.312 Å, like “ O_2^- ”). The CO frequency blue shifts slightly (by 9 cm^{-1}) to 2014 cm^{-1} and ν_{OO} also blue shifts by 275 cm^{-1} to 1114 cm^{-1} , which is similar to the superoxide frequency. In the ESP surface, negative character remains on the O_2 moiety, but less than in the Sep species; positive character remains on the AuCO moiety, but again less than in Sep.

Pre₁/Pre₂: From TS_1 , Pre_1 is formed where this complex has been previously described in greater detail than the pre-reactive “out” structure (Pre_2), where the Pre_2 structural data, energy (-6.11 kcal/mol) and molecular orbitals were also included in Chapter 3. Pre_2 is a rotamer of Pre_1 with an AuCOO dihedral of 180° (shown in Figure 4.1), and is formed from Pre_1 over a small rotational barrier (LB_1) of 6.79 kcal/mol. Compared to Pre_1 , the Au-C bond of Pre_2 is shorter by 0.01 Å and the intermolecular O-C bond is also shorter by 0.03 Å at 1.466 Å. The CO bond of 1.169 Å is similar to Pre_1 and “free” CO; the O-O bond of 1.315 Å is similar to O_2^- (superoxide) and longer than Pre_1 by $\sim 0.015\text{ Å}$. The vibrational frequency of CO (1904 cm^{-1}) is between frequencies of CO and CO^- , like

Pre₁, while the OO frequency (1106 cm⁻¹) is red-shifted beyond O₂⁻ and lower than the Pre₁ frequency. The ESP surface, in Figure 4.3, shows positive character residing on the Au atom, with negative character on the dangling O atom.

Pre₂: The pre-reactive “out” minimum, shown in Figure 4.2, lies at -17.07 kcal/mol, which is 0.12 kcal/mol lower than Pre₁ and is characterized by the AuCOO dihedral of 180°, like the neutral structure. Pre₂ can be formed from Pre₁ over a rotational barrier of 9.53 kcal/mol from the Pre₁ structure (-7.42 kcal/mol below reactant asymptote) between the pre-reactive minima with small changes in the CO (-0.014 Å to 1.191 Å) and O-O bonds (+0.055 Å to 1.502 Å) bonds and concomitant changes in the vibrational frequencies with a blue shift of 82 cm⁻¹ for CO and red shift of 125 cm⁻¹ for O₂.

Compared to the “in” minimum, AuC bond is slightly longer by 0.021 Å and the OO bond increases by 0.025 Å to 1.472 Å, which is most similar to O₂²⁻. The CO-related bonds decrease by ~0.015 Å, where CO is 1.193 Å and similar to CO⁻ and the intermolecular O-C is 1.282 Å. The CO frequency blue shifts by 83 cm⁻¹ to 1802 cm⁻¹ and remains similar to CO⁻, while the OO frequency red shifts by 137 cm⁻¹ to 1095 cm⁻¹, which remains more similar to O₂⁻. The ESP surface (Fig 4.4) shows positive character on Au and strong negative character on the O₂ moiety, similar to Pre₁.

In-TS transition state from Pre₁ to products: As discussed above, the pathway splits into two possible pathways from Pre₁ (Fig. 4.1). With 17.51 kcal/mol of energy, the “In” pathway can continue from Pre₁ over the In-TS transition state (+9.39 kcal/mol above reactant asymptote), where the structure has an elongated O-O bond of 1.667 Å and shortened Au-O bond. The transition state was previously described on the pathway by Fan et al. with the relative energy from Pre₁ to In-TS of 19.7 kcal/mol. Fan et al. indicate

the energy of this transition state is only 4.9 kcal/mol above the reactant asymptote, while these calculations indicate an energy of +9.39 kcal/mol; however, this may be a result of the different methods utilized in the two studies. The Au-C bond increases, as does CO to 1.176 Å, similar to CO⁻, while the intermolecular O-C bond decreases to 1.239 Å. The CO frequency blue shifts slightly (1904 cm⁻¹), remaining similar to CO⁻, and the intermolecular CO has a large blue shift to 1131 cm⁻¹. The ESP surface (Fig. 4.3) shows positive charge localized on the Au atom and negative character on the separating O atom.

In-TS, transition state from Pre₁ to products: From Pre₁, the anionic singlet pathway (Fig. 4.2) can continue over a barrier of 9.60 kcal/mol above reactant asymptote (26.5 kcal/mol above Pre₁), which corresponds to a structurally distinct, In-TS, transition state. From Pre₁, the AuC and OO bonds show large increases in bond lengths, where O-O increases by 0.417 Å to 1.864 Å, which is longer than the O₂²⁻ length. The intermolecular OC bond decreases slightly by 0.08 Å to 1.222 Å, which is similar to CO₂⁻ and the CO bond is 1.202 Å, which also is similar to CO₂⁻. The CO frequency blue shifts by 122 cm⁻¹ to 1841 cm⁻¹ and the intermolecular OC bond blue shifts by 33 cm⁻¹ to 1160 cm⁻¹, where these two frequencies are most similar to the symmetric and anti-symmetric CO₂⁻ values. The ESP surface (Fig. 4.4) is similar to LB₁, where the negative character remains on the O₂ moiety with a majority of the negative character on the separating O atom and a slight positive charge on Au.

Out-TS: Similar to the existence of “in” and “out” pre-reactive complexes, there is an “out” transition state (Out-TS in Fig. 4.1), which is, in simple terms, an elongated version of the Pre₂ minimum. This transition state resides on the “Out” pathway after Pre₂ and is

higher in energy than Pre_2 by 22.63 kcal/mol (+16.52 kcal/mol above reactant asymptote). The Au-C bond increases significantly, as does the OO bond to 1.781 Å, which is longer than previous complexes. The CO bond increases slightly to 1.175 Å, similar to CO^- , while the intermolecular OC bond decreases to 1.262 Å, and a new (2.570 Å) Au-O bond is formed. The CO frequency (1940 cm^{-1}) is similar to that of In-TS (between CO and CO^-); the intermolecular OC frequency is 1088 cm^{-1} and red shifted from the In-TS value by $\sim 40\text{ cm}^{-1}$. The ESP surface (Fig 4.3) is similar to In-TS, as positive character resides on the Au-C bond and the “dangling O atom” has negative character.

Out-TS, transition state from Pre_2 to products: From Pre_2 , a structurally distinct transition state, Out-TS (Fig 4.2), can be reached with 20.32 kcal/mol (from Pre_2) or +3.25 kcal/mol above the reactant asymptote, which is mainly characterized by the elongation of the AuC and OO bonds. The OO bond is 1.701 Å (with an increase of 0.23 Å from Pre_2) and suggests cleavage of the OO bond as this is longer than the O_2^{2-} length. The Au-C bond also greatly increases by $\sim 0.9\text{ Å}$, while the CO bonds decrease by 0.04 Å for CO (to 1.154 Å, which is most similar to CO_2) and 0.08 Å for the intermolecular OC bond (to 1.204 Å, similar to CO_2^-). Also, a new long OC bond forms at 1.985 Å. The CO species have formed symmetric and anti-symmetric CO_2 stretches of 1243 and 2266 cm^{-1} , respectively, which are similar to the CO_2^- symmetric stretch and CO_2 anti-symmetric stretch. The new, long CO bond has a corresponding frequency of 317 cm^{-1} and the elongated OO bond has a red shift of 372 cm^{-1} to 374 cm^{-1} , where both of these frequencies are very low and are in agreement with the (elongated) bond lengths. The

ESP surface (Fig. 4.4) shows a very diffuse charge across the entire complex, which is different from the rest of the surfaces along the anionic singlet pathways.

Pro₁ (AuCO₃): A product minimum with a carbonate-like structure of AuCO, Pro₁, can be formed from the “Out” or “In” pathways (Fig. 4.1). Formation of Pro₁ from Out-TS occurs via translation of the dangling O atom to form the third C-O bond, along with breaking the Au-C bond and formation of two symmetric Au-O bonds. From In-TS, the neutral system reaches Pro₁ via a post-reactive minima and low barrier transition state, while IRC calculations on the anionic singlet indicate formation of Pro₁ directly from In-TS. The neutral PRO₁ complex has an energy of -56.40 kcal/mol and C_{2v} symmetric structure. The symmetric Au-O bonds are 2.216 Å and the related CO bonds are 1.301 Å, which are longer than CO₃⁻. The third “dangling” CO bond is 1.226 Å with a frequency of 1436 cm⁻¹, which is similar to CO₂⁻. The symmetric CO bonds form symmetric and anti-symmetric stretches of 1010 and 1292 cm⁻¹, respectively, and are similar to the related stretches of CO₃⁻. The ESP surface (Fig. 4.3) shows negative character on the CO₃ moiety with the strongest character on “dangling” CO bond and positive character residing on the Au atom.

Pro₁, AuCO₃⁻ carbonate-like product: Unlike the neutral AuCO₃ structure, AuCO₃⁻ singlet (Fig. 4.2) does not have a C_{2v} symmetric structure; instead, Au is connected to CO₃ via one O atom with another “long range” AuO bond of 3.037 Å. Therefore, the structural data is different, but the charge distribution is similar to the neutral structure, where anionic character is located on CO₃ and positive character on Au, as observed in the ESP surface in Figure 4. Also unique to the anionic singlet, PRO₁ is the global minimum of the product complexes at -78.87 kcal/mol. The carbonate-like product can

be formed from either In-TS or Out-TS transition state, based on IRC calculations and resides at -78.87 kcal/mol; however, the formation of Pro₁ will be discussed from Out-TS as this step is easy to conceptualize. The Au-C bond is broken and the Au-O bond shortens by 0.9 Å to 2.020 Å. The “original” CO bond increases by 0.08 Å to 1.233 Å and the 2nd CO bond increases by 0.19 Å to 1.397 Å (most similar to “free” CO₃), while the new CO bond decreases significantly by 0.74 Å to 1.250 Å, where the two ~1.24 Å bonds are similar to CO₃⁻. The two CO bonds in the 1.23-1.25 Å range form symmetric and anti-symmetric CO₂ frequencies of 1264 and 1684 cm⁻¹, respectively, which are similar to CO₂⁻. The longer OC bond, which is connected to Au, has a very low frequency of 835 cm⁻¹, which is in agreement with the elongated CO bond. The ESP surface (Fig. 4.4) shows a strong positive character on Au with negative character on the CO₃ moiety.

TS₃⁰: There is a transition state between the AuCO₃ (PRO₁) and OAuCO₂ (PRO₂) minima, which is TS₃ in the neutral system and TS₂ in the anionic singlet system. The neutral TS₃ species (Fig. 4.1) is higher than PRO₁ by 19.48 kcal/mol (-36.92 kcal/mol below reactant asymptote) and no longer has a planar, symmetric AuCO₃ structure, as CO₂ is being formed and separating from AuO with an elongated O-C bond.

Two of the CO bonds (1.178 and 1.207 Å) have shortened to values similar to free CO₂ and CO₂⁺, while the third CO bond is elongated greatly to 1.694 Å, indicating the probable location for cleavage of CO₂ from AuO. Only one AuO bond remains in this transition state structure and is shortened by ~0.3 Å to 1.980 Å. The two shorter CO bonds have formed symmetric and anti-symmetric vibrational stretches of 2030 and 1262 cm⁻¹, which are similar to those of free CO₂. The ESP surface (Fig. 4.3) shows positive

character on the Au atom and negative character on all three O atoms, which is similar to the Pro₁ ESP surface.

Anionic singlet TS₂: While Pro₁ is the most stable product, the desired OAuCO₂⁻ (singlet) product can also be formed over a barrier of ~26 kcal/mol (Fig. 4.2 TS₂: -52.90 kcal/mol below reactant asymptote). From Pro₁, one C-O bond is broken; CO₂ becomes nearly linear (175.1°), rotates away from AuO, but remains attached to Au via long Au-C and Au-O bonds (3.519 and 3.667 Å, respectively). Both CO bond lengths (1.158 and 1.162 Å) have decreased by ~0.08 Å from Pro₁ and are similar to “free” CO₂, and AuO also decreases to 1.900 Å. The vibrational frequencies are in agreement with the bond lengths, where the CO₂ frequencies (1367 and 2399 cm⁻¹) have blue shifted, with respect to AuCO₃⁻, to values similar to free CO₂. The ESP surface (Fig. 4.4) shows strong negative character on O atom and positive character on CO₂.

Pro₂: The desired product (Pro₂ in Fig 4.1) of the oxidation pathways, OAuCO₂, is the global minimum of the neutral pathway at -60.36 kcal/mol and can be formed from In-TS or Out-TS pathways. On the In-TS pathway, Pro can be formed directly from In-TS or over a small barrier of ~0.5 kcal/mol from a post-reactive, Lewis acid-base stabilized complex (AR₁). From the Out-TS pathway (and also In-TS), the product can be formed from Pro₁ over a barrier of 19.48 kcal/mol above Pro₁ by breaking one O-C bond and rotation of AuO away from CO₂. The Pro₂ structure is constructed of AuO and linear CO₂ moieties, where CO₂ is attached to Au through an O atom. This minimum was also observed by Fan et al., where their energy (relative to the reactant asymptote) of 69.5 kcal/mol is within 10 kcal/mol of the Pro₂ energy of 60.36 kcal/mol calculated in these studies. The Pro₂ energy relative to In-TS is 69.75 kcal/mol, while the similar relative

energy calculated by Fan *et al.* was 74.4 kcal/mol, which may again be due to the different methods utilized. The AuO bond is 1.917 Å, which is shortened from In-TS and Pro₁ (AuCO₃), while the AuO bond of CO₂ is longer at 2.247 Å. The CO bonds are 1.149 and 1.169 Å for the exterior and interior (closest to Au) bonds, respectively, which are similar to CO₂ and CO₂⁺, respectively. The CO₂ moiety has formed symmetric and anti-symmetric vibrational stretches of 1375 and 2425 cm⁻¹, respectively, which are within 11 cm⁻¹ of free CO₂. The ESP surface (Fig 4.3) shows negative character on the AuO moiety with positive character on CO₂, where most of that positive character is on the carbon atom.

Pro₂, OAuCO₂⁻: The desired product, OAuCO₂⁻ (singlet) in Fig 4.2, can be formed directly from In-TS or from Pro₁ via TS₂. Pro₂ resides at -61.98 kcal/mol, which is ~17 kcal/mol above Pro₁. The product is an AuO moiety with a bent CO₂ bonded to Au via the carbon atom. From In-TS and TS₂, the AuC bond decreases to 2.090 Å, as does the AuO bond to 1.860 Å. The CO bonds of CO₂ are 1.194 and 1.237 Å, which are most similar to CO₂⁻ and have symmetric and anti-symmetric frequencies of 1207 cm⁻¹ and 1934 cm⁻¹, respectively, which are most similar to CO₂⁻ and are in agreement with the bond lengths. The ESP surface (Fig. 4.4) shows negative character on the AuO moiety and little negative charge to a slightly positive charge on the CO₂ moiety.

Neutral post-reactive minima and transition states: AR₁: The products, Pro₁ and Pro₂, can be accessed directly from In-TS and Out-TS, or the In-TS transition state can lead to the formation of a different post-reactive minimum, AR₁ in Fig. 4.1. AR₁ is a long-range AuO-CO₂ complex at -52.17 kcal/mol, which is higher in energy than both Pro₁ and Pro₂. The bonds of CO₂ are matched at 1.159 Å, which is similar to “free” CO₂, with the long

range O-C bond of 2.926 Å and an AuO bond of 1.928 Å. The frequencies of 1373 and 2406 cm⁻¹ (symmetric and anti-symmetric, respectively) are also very similar to free CO₂ with the long OC bond frequency of 76 cm⁻¹. The ESP surface (Fig. 4.3) shows positive character on the Au atom and slight negative character on the O atom with a (seemingly) neutral CO₂ moiety.

TS₂: From AR₁, the higher barrier transition state at 15.78 kcal/mol, TS₂ in Fig. 4.1, will lead to the formation of Pro₁, the carbonate-like complex. The TS₂ complex has the same energy as TS₃ and also shares most of the same structural and frequency data, but has a different direction for the AuOCO dihedrals. The long OC bond decreases by 1.232 Å (to 1.694 Å), while the CO bonds (of CO₂) increase by 0.02Å (to 1.178 Å) and 0.05Å (to 1.207 Å), which are similar to CO₂⁺ and CO₂⁻, respectively. The CO₂ frequencies red shift by 376 cm⁻¹ for the symmetric stretch to 2030 cm⁻¹ and by 111 cm⁻¹ to 1262 cm⁻¹ for the anti-symmetric stretch, but remain most similar to CO₂ values. The ESP surface (Fig 4.3) shows positive character on the Au atom and negative character on the O atoms.

LB₂: There is another barrier that can be crossed from AR₁, which is LB₂ in Fig. 4.1, and leads to the formation of Pro₂. LB₂ is only 0.55 kcal/mol above AR₁, which is a very small energetic barrier to cross. The CO₂ moiety has rotated back into the plane and is forming a “new” Au-O bond of 3.521 Å. The CO₂ bonds have shifted away, slightly, from the 1.159Å values, but still remain very similar to free CO₂ and there is no change in the AuO bond. The CO₂ frequencies become even closer to the “free CO₂” frequencies at 2413 and 1374 cm⁻¹ for the anti-symmetric and symmetric stretches, respectively. The ESP surface (Fig. 4.3) shows slight positive charge on Au, slight negative on the O atom and a neutral CO₂ moiety.

Detailed discussion: TS_1 : The structural changes that occur in TS (from Sep), which includes reduction of the AuCO angle and rotation of O₂ around Au cause the loss of the strong charge transfer into O₂ and Dewar-Chatt-Duncanson-like bonding of AuCO. The positive character resides on Au, which was previously on CO in separated complex, and there is less negative character on the O₂ moiety, since structural data indicates a “free” O₂-like moiety. The orbitals attempt to retain the Dewar-Chatt-Duncanson-like bonding, where the HOMO, HOMO-2 show evidence for σ and π bonding interactions; however, movement of O₂ and decrease in the AuCO angle leads to a less than ideal overlap of AuCO orbitals and removes the easy charge transferability observed in the separated structures. TS_1 seems to be a versatile transition state as it connects Sep and Pre₁ on the same reaction coordinate, and also matches the transition state calculated by Fan et al. for an incipient reaction of AuCO and O₂, as their previous minimum to this transition state is a more elongated AuCO---O₂ complex. Also, as this barrier is below the reactant asymptote, it is possible for the Sep minimum to be “skipped over” with enough energy in the system (i.e. non energy-dissipative conditions).

Pre_2 : Similar to the Pre₁ rotamer, Pre₂ has an OCOO conjugated π -system, which is observed in the HOMO-2 orbital of the neutral frontier orbitals, and is slightly higher in energy than Pre₁. The higher energy of Pre₂ can be understood as a lack of Au-O stabilization, since the O atom dangles below OCO. Both Pre₁ and Pre₂ (neutral) complexes have positive Au atoms and negative charge spread across the conjugated π -systems, but Pre₁ has possible additional stabilization from interactions of Au-O. The energy differences of the anionic singlet pre-reactive complexes will be discussed in charge dependent trends.

In-TS: The In-TS transition state involves elongation of the O-O bond that is longer than previous complexes, indicating progress towards cleavage of the bond. There is discrepancy between the CO bond length and vibrational frequency; however, the bond length change is less than 0.01 Å and the intermolecular O-C bond is shortening in preparation of forming CO₂, which could account for the blue shifted frequency. The ESP surface appears less polarized in TS₁ than Pre₁ and the positive charge is residing on the Au-C bond to possibly neutralize the negative charge residing on the separating O atom. The barrier of +9.39 kcal/mol (above reactant asymptote) is in general agreement with previous work. As discussed earlier, the In-TS transition state has been identified by Fan et al, but their energy, +4.9 kcal/mol is approximately half of what we calculated, while the energies relative to the previous minimum are within ~2 kcal/mol (Fan et al. is 19.7 kcal/mol; this work, 17.5 kcal/mol). The differences may span from the utilization of different methods for energy calculations, but general agreement in structure and energy barriers are encouraging that the calculations are valid.

Out-TS: The Out-TS structure suggests formation of a planar, AuCO₃ (carbonate-like) structure as the next minimum, since the carbonate structure would be the easiest to form from this structure. With the elongated O-O bond, the negative character remains on the dangling O atom, while some of the positive character spreads onto the carbon atom. The In-TS and Out-TS structures show similarities in the AuCO moieties, which could be called “rotamers,” as they are formed from the pre-reactive, nearly iso-energetic, rotamers and retain similarities in the elongation of the OO bond and AuCO moiety. The neutral In-TS structure is lower in energy than Out-TS, possibly due to the extra

stabilization offered by the interaction of the separating O atom with Au, similar to that described in Pre_1/Pre_2 .

Pro₁: The $AuCO_3$ structural data and ESP surface indicate probable charge transfer into the CO_3 sub-unit, especially the dangling CO, where the negative character of CO_3 induces the positive charge on the Au atom. The HOMO-3 orbital of the neutral system may also help explain the ESP surface, where the “wrap-around” orbitals from the dangling O atom to the upper two O atoms would match the negative charge residing on the O atoms. *Pro₁* and *Pro₂* will be discussed more in charge dependent trends.

TS₃ (neutral)/TS₂ (anionic singlet): Both charge states show clear indication of CO_2 separating from AuO with a lengthened (or broken) “third” CO bond and structural data similarities to free CO_2 . Charge transfer still occurs in this transition state, where both charge states have negative charge on O atom(s) and positive character on Au in the neutral complex (CO_2 -anionic singlet).

Pro₂: The structural data and ESP surface of the neutral $O Au CO_2$ complex indicates probable charge transfer induced by the O atom. The oxygen atom is known to be electron-withdrawing and can pull electron density from the Au atom and induces the positive character on CO_2 . Comparatively, the anionic singlet structure shows strong negative character on the O atom (-0.515) with less negative character on CO_2 (-0.370), indicating that the molecule spreads the anionic charge across the entire complex, but more is retained by the O atom.

A5. Appendix to Chapter 5.

Table A5.1. ZPE and BSSE corrected binding energies^a for cationic, neutral and anionic binary and ternary complexes^{b,c} calculated with the B3LYP-SDD/6-311+G(3df) in kcal/mol and cooperative binding evaluated as a function of like charges.

		AuCO	AuO ₃	O ₃ AuCO ^{c,d}	Cooperative Binding ^{c,d}
Cationic	Singlet	-44.97	-27.22	-76.68	-4.49
			-24.48	-75.68	-3.67
	Triplet		-20.86 (-50.16)	-60.80 (-89.47)	11.39 (5.67)
			-15.11 (-44.51)	-68.95 (-97.49)	3.24 (-2.35)
Neutral	Doublet	-7.49	-26.32	-71.76	-37.95
			-24.12	-70.19	-36.38
Anionic	Singlet	-1.35	-29.05	-63.42	-28.83
				-52.97	-18.38
	Triplet		-33.23 (-62.34)	-51.72 (-80.53)	-17.13 (-16.84)
			-32.09 (-61.22)	-52.29 (-81.09)	-17.70 (-17.40)
				-77.34 (-105.74)	-42.75 (-42.05)

^a Computed relative to optimized values of the **ground state** (lowest energy) fragments, with charge (if any) localized on gold center.

^b Lowest energy state per species with the same charge and molecular components are in **bold**.

^c Parenthetical values computed relative to the energy of O₃ triplet, as shown here: [E_{AuO₃} - (E_{Au} + E_{O₃triplet})] or [E_{O₃AuCO} - (E_{Au} + E_{CO} + E_{O₃triplet})].

^d Cooperative binding is calculated as the difference between total binding energy of ternary complex and summed binary complexes as shown here: E_{O₃AuCO} - E_{AuOO} - E_{AuCO}. The AuO₃ energy used in cooperative binding is the ground state singlet for cationic states (ground state triplet for anionic states). Parenthetical cooperative binding values are calculated in the same fashion, but utilize the parenthetical values of the binary and ternary triplet complexes, where applicable.

Table A5.2. Bond lengths (in Å) of low barrier (LB) reactant-side transition state of [O₃+Au+CO]_q^a complexes, q=(+1,0,-1), calculated with B3LYP-SDD/6-311+G(3df).

Charge	Spin	Name	{O ₃ AuCO} ^a transition states				
			Au-C bond	C-O bond	Au-O _α ^b bond	O _α -O _β bond	O _β -O _γ bond
Cationic	Singlet	¹ LB ⁺	1.941	1.116	2.112	1.323	1.207
	Triplet	³ LB ₁ ⁺	1.970	1.115	2.026	1.576	1.216
Neutral	Doublet	² LB ₁ ⁰	1.900	1.128	1.992	1.502	1.252
Anionic	Singlet	¹ LB ₁ ⁻	1.881	1.150	1.924	1.724	1.293
	Triplet	³ LB ₁ ⁻	1.990	1.182	2.117	1.445	1.283
		³ LB ₂ ⁻	1.949	1.175	2.014	1.614	1.257

^a O₃ in structure is listed first and O₃ out structure is listed second per charge/spin state.

^b O_α, O_β, and O_γ refer to the order of oxygen atoms, where O_α is the closest to (or attached to) Au.

Table A5.3. Vibrational frequencies (in cm^{-1}) of the low barrier (LB) reactant-side transition state of $[\text{O}_3+\text{Au}+\text{CO}]q^a$ complexes, $q=(+1,0,-1)$, calculated with B3LYP-SDD/6-311+G(3df).

O₃AuCO									
Charge	Spin	Name	Au-C	C-O	Au-O	O _{α} - O _{β} ^a	O _{β} -O _{γ}	O ₃ sym	O ₃ anti
Cationic	Singlet	¹ LB ⁺	409	2297	347	958	1383		
	Triplet	³ LB ₁ ⁺	382	2304	370				
Neutral	Doublet	² LB ₁ ⁰	451	2128	568			1048	822
Anionic	Singlet	¹ LB ₁ ⁻	473	2054	632		1157		
	Triplet	³ LB ₁ ⁻	486	1832	378	697	1191		
		³ LB ₂ ⁻	462	1872	663		1284		

^a O _{α} , O _{β} , and O _{γ} refer to the order of oxygen atoms, where O _{α} is the closest to (or attached to) Au.

Table A5.4. Bond lengths (in Å) for low barrier, post-reactive transition state, $\{\text{O}_2\text{AuO}-\text{CO}\}^q$, complexes, $q=(+1,0,-1)$, calculated with B3LYP-SDD/6-311+G(3df).

{O₂AuO-CO}q transition states								
Charge	Spin	Name	C-O bond	Au-O _{x} ^{a,b} bond	O _{α} -O _{β} bond	O _{β} -O _{γ} bond		
Cationic	Triplet	³ LB ⁺	1.126	2.129		1.245		
			1.778	1.963				
Neutral	Doublet	² LB ₂ ⁰	1.159	4.106	1.226			
			1.159	2.322				
			² LB ₃ ⁰	1.127			1.925	1.232
Anionic	Singlet	¹ LB ₂ ⁻	2.147	2.054		1.297		
			1.143	1.879				
			2.068	1.971				
	Triplet	³ LB ₃ ⁻	1.142	1.927		1.319		
			2.047	2.045				
			³ LB ₄ ⁻	1.203			2.089	1.315
			1.274	2.047				
³ LB ₅ ⁻	1.203	2.220		1.314				
	1.268	2.068						

^a O _{α} , O _{β} , and O _{γ} refer to the order of oxygen atoms, where O _{α} is the closest to (or attached to) Au.

^b AuOCO bond length is listed first and AuO₂ bond length is second.

Table A5.5. Vibrational frequencies (in cm^{-1}) for low barrier (LB) post-reactive transition states, $\{\text{O}_2\text{O}_\alpha\text{AuCO}\}^q$ transition state complexes, $q=(+1,0,-1)$, calculated with B3LYP-SDD/6-311+G(3df).

Charge	Spin	Name	CO	AuO ^a	O _{α} -O _{β} ^b	O _{β} -O _{γ}	CO ₂ sym	CO ₂ anti			
Cationic	Triplet	³ LB ⁺	2152	532		1557					
				318							
Neutral	Doublet	² LB ₂ ⁰		14	1374		1426	2413			
				83							
Anionic	Singlet	¹ LB ₂ ⁻	2049	586		1362					
				350							
	Triplet	³ LB ₃ ⁻	2053	604		1097					
				426							
				285					1177	1208	1752
				478							
³ LB ₅ ⁻			374		1176	1215	1773				
			541								

^a AuO _{α} vibrational frequency is listed first and AuO _{β} is second.

^b O _{α} , O _{β} , and O _{γ} refer to the order of oxygen atoms, where O _{α} is the closest to (or attached to) Au.

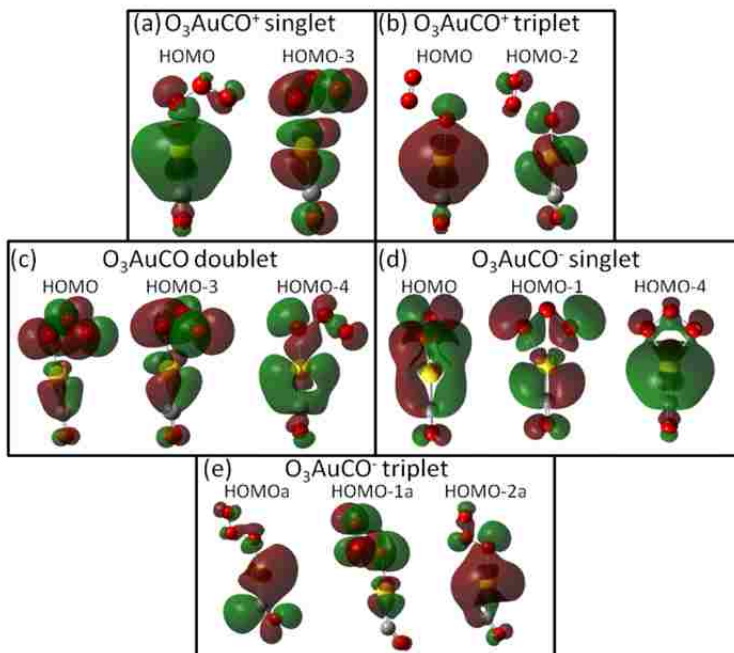


Figure A5.1. Selected (higher lying) molecular orbitals showing σ -donation and π -backbonding character (or lack thereof in anionic triplet) in cationic singlet (a) and triplet (b), neutral (c), anionic singlet (d), and anionic triplet (e) O_3AuCO^q minima.

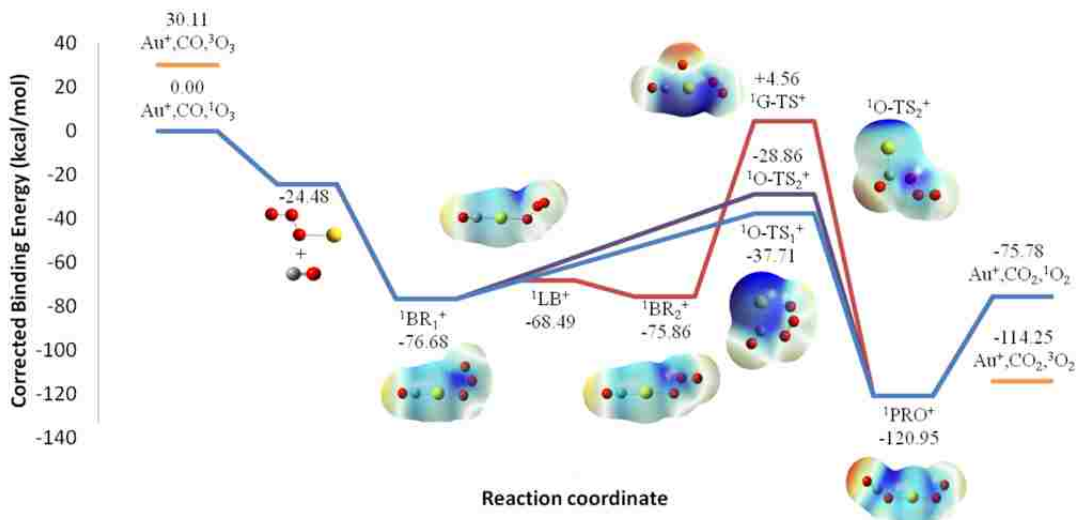


Figure A5.2. Cationic singlet reaction profiles with electrostatic potentials mapped on B3LYP total electron density isosurfaces (density=0.0004) for each complex. The O3 oxidation processes are shown with blue (O-TS1) and purple (O-TS) lines; AuO oxidation pathway is represented by red lines. The color map spans a range of 0.1 in each case with red (blue) as most negative (positive). The charges for cationic complexes are mapped over +0.10 to +0.20. Note that color intensities are also mapped to the values, such that colors near the ends of the range appear brightest, while those in the center appear transparent.

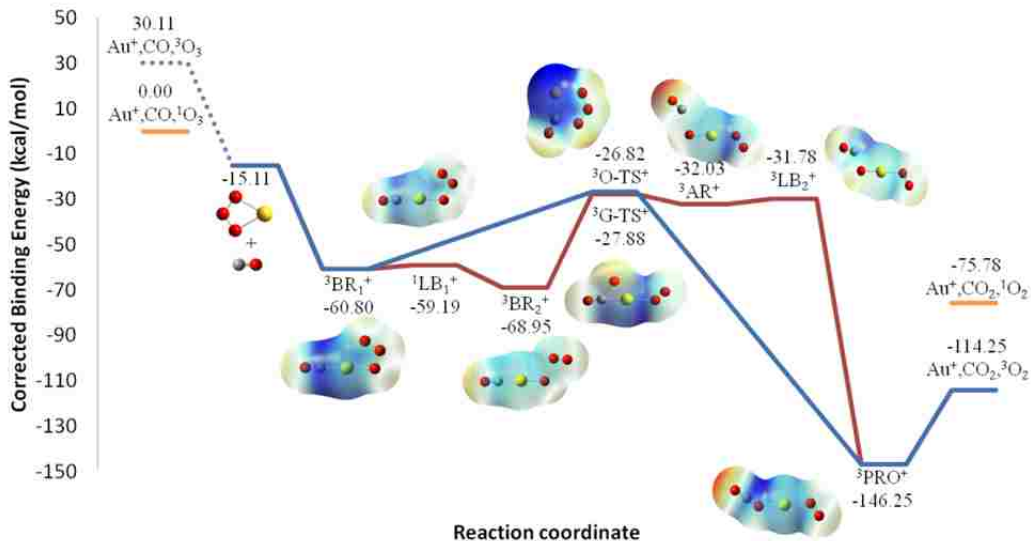


Figure A5.3. The cationic triplet pathway(s) are shown with electrostatic potentials mapped on B3LYP total electron density isosurfaces (density=0.0004) for each complex. The O3 oxidation process is shown with the blue line; AuO oxidation pathway is represented by red lines. The color map spans a range of 0.1 in each case with red (blue) as most negative (positive). The charges for cationic complexes are mapped over +0.10 to +0.20. Note that color intensities are also mapped to the values, such that colors near the ends of the range appear brightest, while those in the center appear transparent.

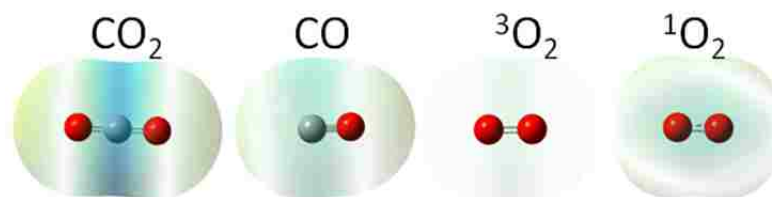


Figure A5.4. CO₂, CO, ³O₂ and ¹O₂ molecules with electrostatic potential mapped on to the total electron density and referenced to the neutral range of -0.05 to +0.05.

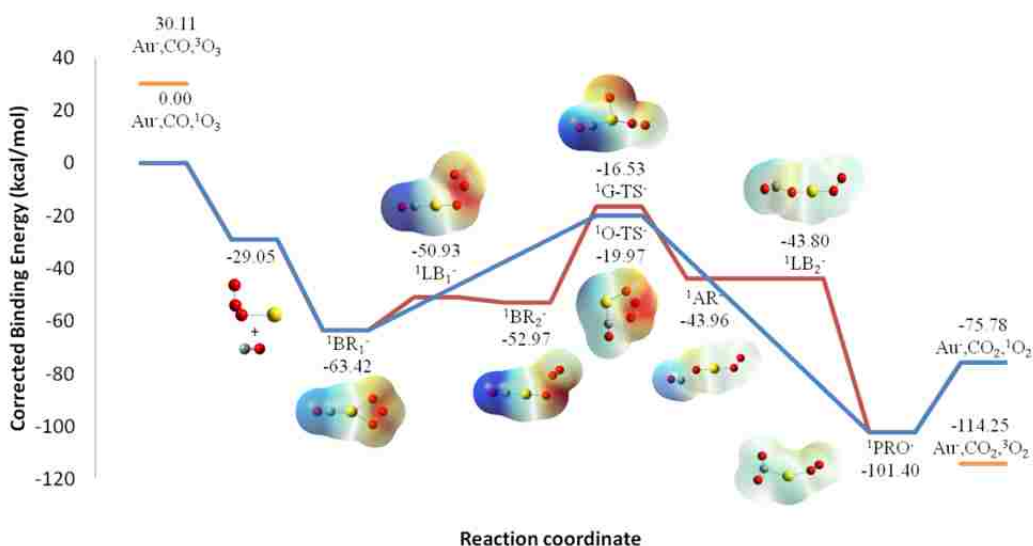


Figure A5.5. Anionic singlet reaction profiles are shown with electrostatic potentials mapped on B3LYP total electron density isosurfaces (density=0.0004) for each complex on the O₃ oxidation (blue line) and AuO oxidation (red line) pathways. The color map spans a range of 0.1 in each case with red (blue) as most negative (positive). The charges for cationic complexes are mapped over -0.20 to -0.10. Note that color intensities are also mapped to the values, such that colors near the ends of the range appear brightest, while those in the center appear transparent.

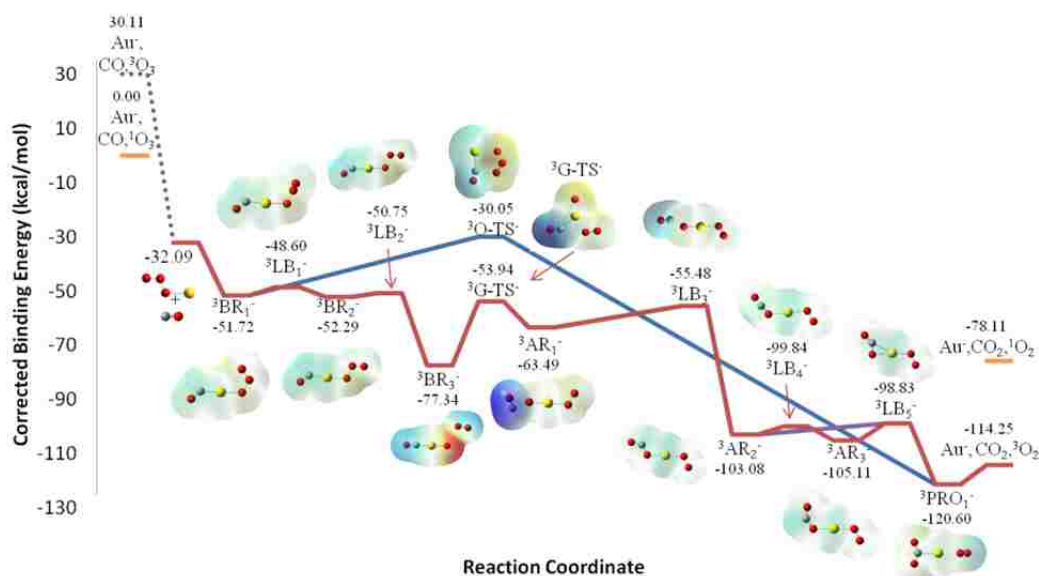


Figure A5.6. Anionic triplet reaction profiles are shown with electrostatic potentials mapped on B3LYP total electron density isosurfaces (density=0.0004) for each complex on the O₃ oxidation (blue line) and AuO oxidation (red and purple lines) pathways. The color map spans a range of 0.1 in each case with red (blue) as most negative (positive). The charges for cationic complexes are mapped over -0.20 to -0.10. Note that color intensities are also mapped to the values, such that colors near the ends of the range appear brightest, while those in the center appear transparent. The Cu) oxidation pathway splits after structure AR₂, where the purple line goes directly to LB₅ and the red line continues over LB₄ to the AR₃ minimum and then over LB₅ to the PRO.

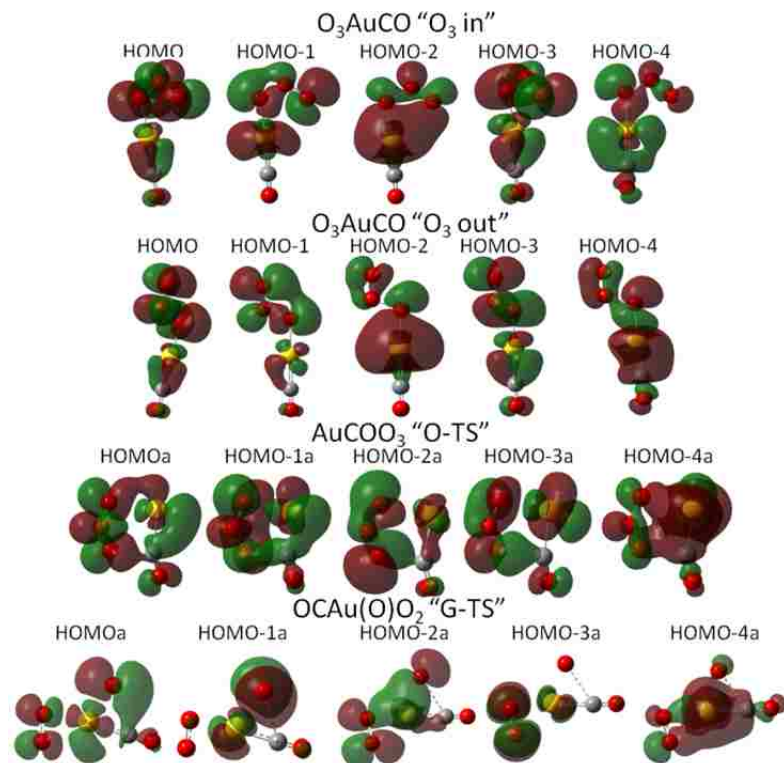


Figure A5.7. Five highest molecular orbitals of the main minima and transition states of the neutral pathway for Au, CO, and O₃. The β -spin orbitals are not shown, but are similar to the (shown) α -spin orbitals, except that in the G-TS system the β -LUMO matches the α -HOMO-3 and indicates HOMO-3 as the singly occupied orbital.

Detailed description of the neutral (and other charge states, as noted) pathways:

(BR): The minima near the reactants are referred to as the “separated” complexes, [O₃AuCO]^q and denoted as BR in the figures for “before reaction.” These structures also are reminiscent of the [O₂AuCO]^q separated minima that have been discussed in previous papers, but have an additional O atom. {{3520 Smith,Angela N. 2012}} As previously mentioned, these minima are further defined by the direction of the AuOOO dihedral angle with respect to CO, where the “O₃ in” structure (BR₁) has a dihedral of 0° with O₃ rotated towards CO and is the global minimum at -71.76 kcal/mol, while “O₃ out” (BR₂) has a 180° dihedral and is less than 2 kcal/mol higher in energy at -70.19 kcal/mol. Both minima have a very noticeable linear AuCO orientation, which is different from the bent

orientation of the binary AuCO species; {{3520 Smith,Angela N. 2012}} the AuC and CO bond lengths (and frequencies) are also similar for both BR complexes, where the CO lengths (1.127 Å) remain close to “free” CO. Both isomers have broken symmetry with respect to the bonds of O₃, and the major differences between BR₁ and BR₂ appear in the AuO₃ sub-unit. BR₁ has a difference in O-O bonds by 0.16 Å (O_αO_β is 1.433 Å; O_βO_γ, 1.273 Å), where O_αO_β is similar to O₃⁻ and O_βO_γ is similar to O₃. The vibrational frequency of O_βO_γ, 1229 cm⁻¹, is comparable to a combination of the free O₃ symmetric and anti-symmetric frequencies, while the O_αO_β is much lower at 729 cm⁻¹ and similar to O₂²⁻. Compared to BR₁, the AuO bond of BR₂ is shortened by 0.04 Å and O_βO_γ is shortened by 0.03 Å to 1.244 Å and remains similar to “free” O₃. The O_αO_β bond increases by 0.08 Å to 1.513 Å, which is comparable to O₂²⁻; the difference between these two O-O bonds is 0.27 Å, almost twice the difference for BR₁. The vibrational frequency trend is similar to the structural data with a frequency of 594 cm⁻¹ for O_αO_β, which is red shifted by 135 cm⁻¹ from BR₁ and lower than O₂²⁻, and 1308 cm⁻¹ for O_βO_γ, which is blue shifted by 80 cm⁻¹ from BR₁ and similar to the free O₃ symmetric frequency. the significant changes in bond lengths and vibrational frequencies (from the “free” CO and O₃ molecules) and large stabilization energies for BR₁ and BR₂ suggests that large cooperativity, which is observed in the cooperative binding values of -37.95 and -36.38 kcal/mol, respectively.

The electrostatic potential surfaces (ESPs) help to visualize the charge distribution in each complex and can be used to interpret charge transfer throughout the complexes and how the charge distributions change along the reaction pathways. For these separated complexes, the ESP surfaces are analyzed to understand how connectivity and orientation

affect the charge distributions. Both separated surfaces show strong positive character on CO and negative character on the O₃ moiety, where O_α has slightly more negative character than O_γ.

Other charge states: The cationic (singlet and triplet) and anionic singlet reactant-side complexes have linear AuCO angles, while anionic triplet BR₁ and BR₂ have bent AuCO angles. Anionic singlet BR₁ has retained the O₃ symmetric structure with an overall C_{2v} symmetry, where the structural data indicates an O₃⁻-like species, but formation of BR₂ involves the significant elongation of O_αO_β to 2.017 Å and rotation of AuOOO dihedral to 90°, so that the complex is non-planar. Also, the cationic triplet BR₂ displays a long O_αO_β and much shorter O_βO_γ (1.166 Å); however, this elongation is an artifact of B3LYP, since the B2PLYP calculations show the O_αO_β bond to be 1.369 Å (O_βO_γ, 1.330 Å), which is in better agreement with the other charge states. Similar to the neutral reactant-side complexes, the anionic singlet complexes show strong positive character on CO and negative character on the O₃ moieties, where the elongated O_αO_β bond leads to stronger negative character on O_α. In contrast, the cationic singlet and triplet and anionic triplet ESP surfaces show well distributed charge across the entire complex. The global minimum of the reactant side complexes differ as a function of spin state and certain charge states have more separated energies. The cationic singlet, anionic triplet and neutral (doublet) reactant-side complexes are within 2 kcal/mol, while the cationic triplet complexes are separated by 8 kcal/mol and anionic singlet complexes are separated by 11 kcal/mol with BR₁ as the reactant-side global minimum; BR₁ is also the global minimum (of the reactant side) for the cationic singlet and neutral doublet, while the cationic triplet has the “O₃ out” (BR₂) complexes as its reactant-side global minimum. Similar to the

neutral BR complexes, the anionic singlet and triplet BR complexes also have large cooperativity of binding and large stabilization energies for binding both CO and O₃ to the Au atom (or anion). For cationic singlet BR₁ and BR₂ structures, there is little cooperative binding (-4.49 and -3.67 kcal/mol), which is similar to the cationic O₂AuCO cooperative binding. Comparatively, the cationic triplet BR complexes display anti-cooperativity with positive values of 11.39 kcal/mol for BR₁ and 3.24 kcal/mol for BR₂, while slight cooperativity of binding is observed when calculating BR₂ (cooperativity) with respect to O₃ triplet.

Additionally, the anionic triplet system has a third reactant-side complex, BR₃, which is lower than BR₁/BR₂ by ~25 kcal/mol and the reactant-side global minimum, with a linear AuCO angle, significantly elongated O_αO_β bond of 2.709 Å, and strong negative character on O_α in ESP surface. The linear AuCO is similar to all other BR₁ and BR₂ complexes (except anionic triplet), while the elongated O_αO_β is reminiscent of the anionic singlet BR₂ structure.

For all charge states, there are low barrier, LB, transition states between the reactant-side complexes (BR₁ and BR₂ and BR₃ for the anionic triplet) with barriers generally smaller than 10 kcal/mol. These LB₁ transition states can be described, typically, as rotational barriers from the “in” to “out” structures, except the cationic triplet, anionic singlet and LB₂ of anionic triplet transition states involve elongation of the O_αO_β bond, instead of dihedral rotation.

“Major” transition states: The ozone system has two major transition states involved in the pathways to forming the O₂AuCO₂ product from the separated O₃AuCO complexes, which have distinct structures. The energetically favored transition state for

neutral system is O-TS and involves a geometry that suggests an incipient reaction of O₃ with neutral AuCO. The other transition state, G-TS, is rather different with a structure that looks like the “separated” O₂AuCO complex, previously described in the literature, with an “extra” oxygen atom bonded to one side of Au and forming an angle of ~90° for OAuC.

O₃ oxidation transition state (O-TS): The O-TS structure appears to be the result of O₃ rotating around Au, from BR₁, to form an intermolecular bond between O_γ and carbon. Also, this structure is reminiscent of the previously described “pre-reactive, in” structure of AuCOO₂,³⁵²⁰ Smith, Angela N. 2012} but O-TS has an additional oxygen atom to form O₃. This O-TS transition state resides at -23.91 kcal/mol below the reactant asymptote and 47.85 kcal/mol above BR₁. The Au-O_α bond remains intact with an increase to 2.307 Å, the AuC and CO bonds also lengthen by 0.13 Å to 2.031 Å and 0.02 Å to 1.135 Å, respectively, where CO remains similar to free CO, and the AuCO angle decreases from 180° to 159.2°. The O_βO_γ bond also increases to 1.338 Å, while O_αO_β bond decreases to 1.359 Å, which makes both similar to O₃⁻. The changes in O-O bond lengths bring the two bonds within 0.02 Å of each other, which re-establishes the symmetry of O₃ as observed with vibrational frequencies. The CO frequency red shifts slightly and remains similar to free CO; the O₃ vibrational frequencies (symmetric stretch is 1048 cm⁻¹; anti-symmetric, 821 cm⁻¹) are also similar to O₃⁻ (1068 and 896 cm⁻¹), which are in agreement with the bond lengths. The ESP surface shows retention of negative character on the O₃ moiety, which is distributed more evenly across O_α and O_γ than in BR₁, while positive character has migrated onto the Au atom from CO.

Other charge states: O-TS (O-TS₂): In the O₃ oxidation transition state (O-TS), only the cationic triplet structure is planar; all other charge states are non-planar. Similar to the neutral O-TS, the anionic triplet system also re-forms a symmetric O₃ moiety, while the other charge states have non-symmetric O₃ moieties, where the anionic singlet structure moves from the symmetric (C_{2v}) O₃ moiety in BR₁ to a non-symmetric moiety in O-TS. Unique to the cationic singlet is a second O-TS transition state with a COOO dihedral of 180°, where there is no longer Au-O interaction; this species is ~ 9 kcal/mol higher in energy than O-TS₁, but resides below the reactant asymptote.

AuO oxidation transition state (G-TS): The general structure of the G-TS transition state involves a linear AuCO with O₂ on the opposite side of Au with the “migrating” oxygen atom “on top,” of the Au atom (attached 90° from CO and O₂). This structure is visually similar to the previously reported O₂AuCO structure with an additional O atom bonded to the Au atom. {{3520 Smith,Angela N. 2012}} This transition state also exists below the reactant asymptote at -21.95 kcal/mol and is 48.24 kcal/mol higher than BR₂. Compared to BR₂, the O_α-O_β bond has been broken and new Au-O_β and (long) O_α-C bonds are formed. The Au-C bond increases by 0.065 Å to 1.966 Å, as does AuO_α (2.052 Å), and O_βO_γ increases to 1.286 Å, which is similar to O₂⁻. The CO bond decreases slightly by 0.006 Å to 1.122 Å and remains similar to free CO with retention of the linear AuCO. The CO frequency blue shifts slightly and remains similar to “free” CO, while O_βO_γ (1234 cm⁻¹) is red shifted closer to O₂⁻, in agreement with the bond lengths. The ESP surface has positive character remaining on AuCO, negative character on the (migrating) O_α atom, and slight negative character on O₂.

Other charge states G-TS: Similar to the neutral G-TS transition state, the cationic singlet and anionic triplet states also have planar structures, while the cationic triplet and anionic singlet states have non-planar structures. Unlike all other transition states, the cationic singlet G-TS is 4.56 kcal/mol above the reactant asymptote, which is also higher in energy than both of its O-TS transition states. The cationic and anionic triplet states have G-TS transition states as the lower energy pathways, while the cationic and anionic singlet(s) and neutral doublet states have O-TS as the lower energy pathways.

5.3. 3 Post-reactive species and low barrier transition states: The neutral system has post-reactive minima and (low barrier) transition states for the O-TS and G-TS pathways, prior to the formation of the O_2AuCO_2 product, where the minima and transition states are discussed below. The other charge states, except the cationic singlet, also have post-reactive minima and transition states in the G-TS pathways and will be discussed after the neutral minima and transition states in the cationic and anionic reaction pathways.

Post-reactive minimum on O-TS pathway, AR₁: From the O-TS transition state, the $O_\alpha O_\beta$ and AuC bonds are broken, the second CO bond shortens to form CO_2 and CO_2 moves away from AuO_2 , which leads to long bonds forming between Au, CO_2 and O_2 (Au-O is 3.737 Å; Au-O -of CO_2 -, 3.142 Å). This minima (AR₁) resides at -114.34 kcal/mol and appears to be a Lewis acid-base stabilized complex with the long bonds between Au, CO_2 and O_2 . The structural and frequency data and ESP surface of the CO_2 (1.160 and 1.158 Å; 1374 and 2413 cm^{-1}) and O_2 (1.230 Å, 1403 cm^{-1}) moieties are similar to free CO_2 and O_2 , respectively.

Post-reactive transition state on O-TS pathway, LB₂: From AR₁, the pathway can continue over a very small barrier (0.01 kcal/mol) where the CO_2 moiety is moving away

from AuO₂. Both Au-O bonds increase, where the bond between CO₂ and Au increases significantly by 0.37 Å to 4.106 Å and AuO of O₂ only increases by 0.03 Å to 2.322 Å, while CO₂ and O₂ moieties remain similar to their respective “free” molecules in the structural data. The ESP surface is similar to the AR1 ESP surface, where CO₂ and O₂ moieties are similar to the free CO₂ and O₂ ESP surfaces, observed in Figure S4 and have a mostly neutral character. From this transition state, CO₂ rotates further from O₂ and the Au-O bond shortens to form the O₂AuCO₂ product.

Post-reactive minimum on G-TS pathway, AR₂: From the G-TS transition, a post-reactive minimum is found at -31.65 kcal/mol (~10 kcal/mol below G-TS), where the Au-C bond has been broken and a long intermolecular O-C bond is forming. The AuO₂ and OAuO angles increase from 85.1° and 114.6° in G-TS to 126.5° and 174.6° in AR₂, respectively, and the intermolecular OC bond increases by 0.37 Å, while the CO bond remains like free CO. Both AuO_α and AuO_β bonds decrease by 0.15 and 0.08 Å to 1.902 and 2.041 Å, respectively; the O₂ bond also decreases by 0.05 Å to 1.237 Å which is most similar to free O₂. The vibrational frequency of CO red shifts slightly (by 25 cm⁻¹) and remains like free CO, while the O₂ frequency blue shifts (by 90 cm⁻¹) to 1180 cm⁻¹, which is only one wavenumber lower than the O₂⁻ frequency. The ESP surface has a well distributed charge with a negative charge on O_α and nearly equivalent positive charge on Au (with very slight positive character on CO and O₂).

Other charge states: In other charge states, post-reactive species are only observed on the G-TS pathway; therefore, these post-reactive complexes are identified as AR or AR₁ (for anionic triplet), except the cationic singlet has no post-reactive complexes. The structure described in the neutral system is similar across the charge (and spin) states with

post-reactive complexes, where there is an OAuCO--CO structure with a long intermolecular OC bond. Like the neutral structure, the cationic triplet structure is planar, while the anionic (singlet and triplet) structures are non-planar. The anionic triplet state is the only charge state to have an “extended” post-reactive pathway with several post-reactive complexes and transition states, which has been previously identified by Castleman and colleagues as the reaction pathway for $\text{OAuO}_2^- + \text{CO}$. For AR_2 of the anionic triplet pathway (from LB_3), the OC bond is further shortened to form the CO_2 moiety for a complex of $\text{O}_2\text{AuCO}_2^-$ (triplet) with an AuOCO dihedral of 180° . From the anionic triplet LB_4 , the AuOCO dihedral rotates to 0° , where OCO faces “in” towards Au, and forms AR_3 .

Post-reactive transition state on G-TS pathway, LB_3 : From AR_2 , the LB_3 transition state (-29.38 kcal/mol) is reached with 2.27 kcal/mol, where the intermolecular OC bond decreases significantly (by 0.648 Å to 2.147 Å) in preparation of forming the product. The CO bond remains similar to free CO and the O_2 bond decreases very slightly to 1.232 Å, which remains similar to free O_2 , while the AuO_α and AuO_β bonds increase by 0.02 and 0.013 Å to 1.925 and 2.054 Å, respectively. The CO frequency red shift slightly (36 cm^{-1}) to 2180 cm^{-1} and remains similar to CO, while O_2 blue shifts slightly (38 cm^{-1}) to 1362 cm^{-1} , which remains closer to O_2^- . The ESP surface, similar to AR_2 , has a well distributed charge with negative character on O_α and positive character on Au (with a slight positive character on CO and slight negative on O_2).

Other charge states: In other charge states, post-reactive, low barrier transition states, denoted as LB_x ($x=2-5$), are only observed on the G-TS pathway, except the cationic singlet has no post-reactive complexes. For the cationic triplet and anionic singlet LB_2

and anionic triplet LB₃ transition states, the intermolecular OC bond is significantly shortened from the immediately previous post-reactive minimum (AR/AR₁), similar to the neutral system. As mentioned above, the anionic triplet state is the only charge state to have an “extended” post-reactive pathway. From AR₂, the LB₄ transition state involves rotation of the AuCO₂ dihedral to ~90° (out of plane). The LB₅ barrier can be crossed from two post-reactive minima, AR₂ (barrier of 4.24 kcal/mol) or AR₃ (barrier of 6.28 kcal/mol). From AR₂, the AuO_α bond shortens, the AuOC angle decreases, and a new AuC bond forms, in preparation of forming the final O₂AuCO₂ product that has an Au-C bond. From AR₃, the AuO_α bond shortens, the AuOC angle decreases, and a new AuC bond forms with rotation of the AuOCO angle back to ~180°.

5.3.4 Product (PRO): The product, O₂AuCO₂, can be directly formed from either “main” transition state (O-TS or G-TS) or from post-reactive complexes and low barrier transition states. Formation of the product involves the shortening of the “newly formed” O-C bond (from either transition state) and breaking of the Au-C bond. In the neutral structure, the O₂ moiety is bonded to Au opposite of CO₂ and the linear OCO sub-unit is attached via an Au-O bond. The CO₂ bonds are 1.151 Å and 1.168 Å; the shorter OC bond is the exterior bond and similar to “free” CO₂, while the longer (interior) O-C bond is similar to CO₂⁺ length. The AuO_α and O_αO_β bonds decrease, where O_αO_β is now 1.273 Å, between “free” O₂ and O₂⁻ bond lengths. The vibrational frequencies clearly show formation of CO₂ as there are CO₂ symmetric and anti-symmetric stretches (1366 and 2409 cm⁻¹, respectively), which are similar to “free” CO₂, and the O₂ frequency of 1219 cm⁻¹ is similar to O₂⁻. The ESP surface shows negative character on O₂ with a

strong positive character on CO₂, especially the carbon atom, which is reminiscent of the charge profile on the CO sub-unit of BR₁.

Other charge states PRO: The products can be divided and discussed based on connectivity of CO₂ to Au, as all structures have bent AuO₂ angles. The cationic and neutral products have attachment of CO₂ to Au via an O atom, while the anionic products have connection via the carbon atom. The cationic and neutral products also have linear CO₂ moieties with the interior OC bond similar to CO₂⁺ and exterior OC bond closer to “free” CO₂ bond lengths, while the vibrational frequencies are similar to free CO₂. The anionic complexes have bent CO₂ moieties and non-planar structures (anionic singlet: CAuOO dihedral of 85.7°; anionic triplet: CAuOO dihedral of 180°) with structural data that are most similar to CO₂⁻. The anionic singlet, similar to the neutral product, has superoxo-like O₂ (O₂⁻), based on the structural data; the anionic triplet has disagreement in structural data, where the bond length is similar to free O₂, but the vibrational frequency is indicative of a superoxo (O₂⁻) or peroxo-like (O₂²⁻) sub-unit. Other than the neutral product, the ESP surfaces show well-distributed charge for cationic and anionic charge states.

A6. Appendix to Chapter 6.

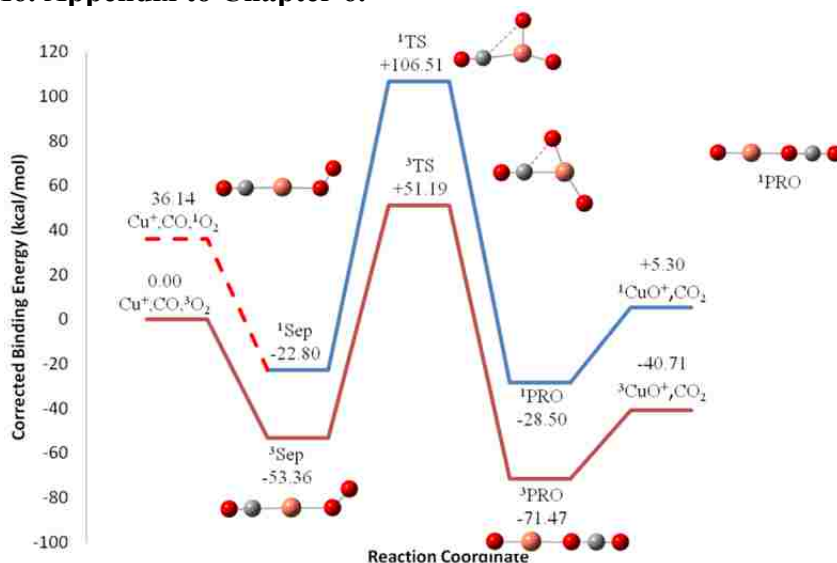


Figure A6.1. The cationic singlet pathway, shown in blue, shows the formation of the singlet separated complex and the Cu oxidation transition state (^1TS) that is ~ 128 kcal/mol higher than the Sep species; this pathway continues to the OCuCO_2^+ singlet product (^1PRO). The dashed red line indicates the instability of the starting components with singlet O_2 . The red line is the cationic triplet pathway, which shows the formation of the triplet separated complex (^3Sep).

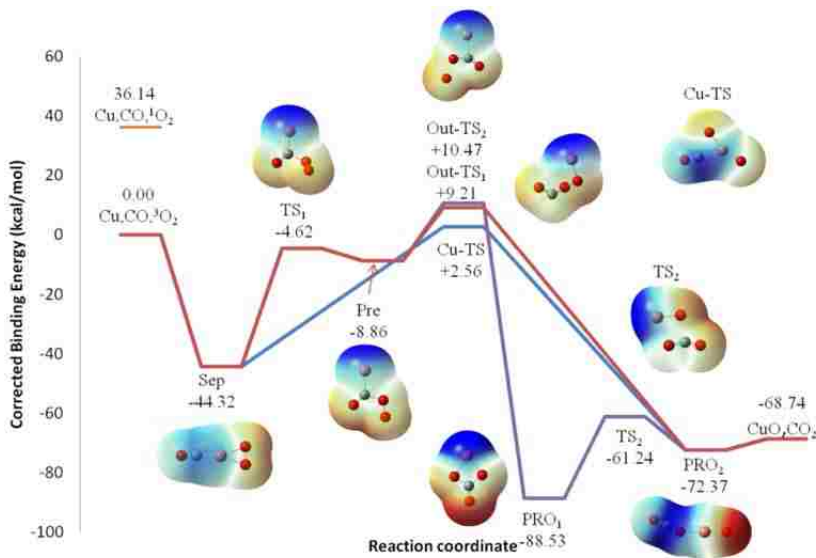


Figure A6.2. The reaction pathway(s) for the neutral doublet state is shown for $[\text{O}_2+\text{Cu}+\text{CO}]^0$, where each position is now represented by the respective electrostatic potential (ESP) mapped on to the total electron density isosurface (density = 0.0004). The color map spans a range of 0.1 with red (blue) as most negative (positive) from -0.05 to +0.05. The main minima and transition states that are described above in the text are in bold.

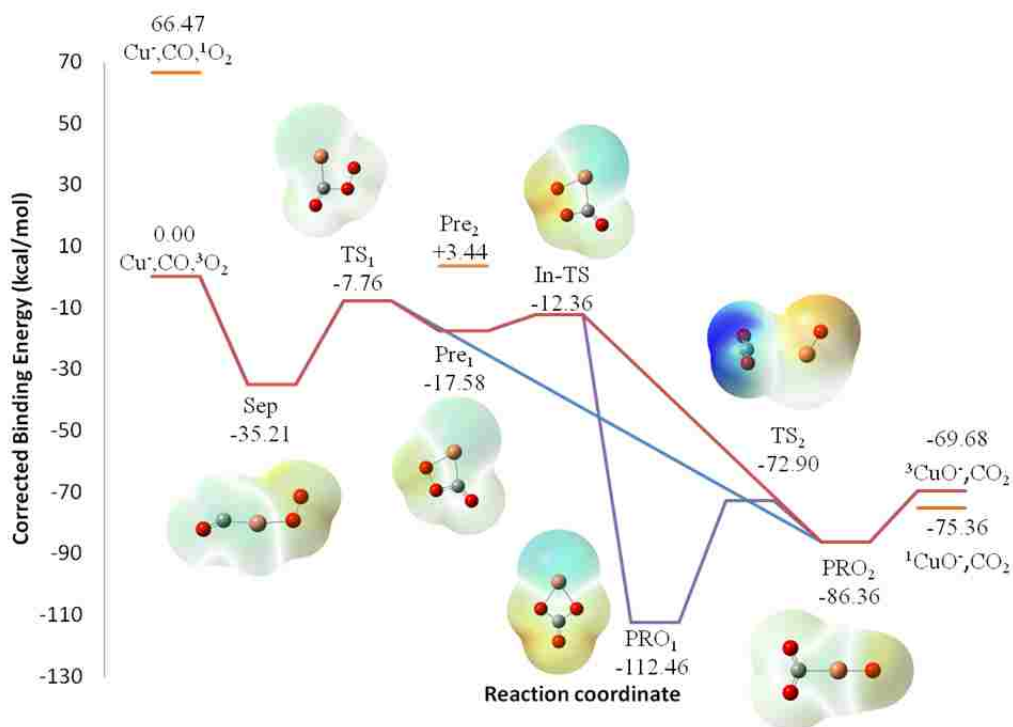


Figure A6.3. The reaction pathway(s) for the anionic triplet state is shown for $[O_2+Cu+CO]^-$, where each position is now represented by the respective electrostatic potential (ESP) mapped on to the total electron density isosurface (density = 0.0004). The color map spans a range of 0.1 with red (blue) as most negative (positive) from -0.2 to -0.1. The main minima and transition states that are described above in the text are in bold.

Table A6.1 Bond lengths (in Å) of low barrier (LB) transition state of $[O_3+Cu+CO]^{q-}$ complexes, $q=(+1,0,-1)$, calculated with B3LYP-SDD/6-311+G(3df).

$\{O_3CuCO\}^q$ Transition States							
Charge	Spin	Name	Cu-C bond	C-O bond	Cu-O_α bond^b	O_α-O_β bond	O_β-O_γ bond
Cationic	Singlet	$^1LB^+$	1.867	1.115	1.895	1.314	1.211
	Triplet	$^3LB_1^+$	1.917	1.113	1.806	1.599	1.212
Neutral	Doublet	$^2LB_1^0$	1.797	1.126	1.807	1.484	1.258
	Triplet	$^3LB_1^-$	1.827	1.181	1.869	1.451	1.283
		$^3LB_2^-$	1.797	1.173	1.804	1.609	1.259

^a O_3 in structure is listed first and O_3 out structure is listed second per charge/spin state.

^b O_α , O_β , and O_γ refer to the order of oxygen atoms, where O_α is the closest to (or attached to) Au.

Table A6.2 Vibrational frequencies (in cm^{-1}) of the low barrier (LB) transition state of $[\text{O}_3+\text{Cu}+\text{CO}]q^a$ complexes, $q=(+1,0,-1)$, calculated with B3LYP-SDD/6-311+G(3df).

O_3CuCO Low Barrier Transition States							
Charge	Spin	Name	Cu-C	C-O	Cu-O	$\text{O}_\alpha\text{-O}_\beta^a$	$\text{O}_\beta\text{-O}_\gamma$
Cationic	Singlet	$^1\text{LB}^+$	411	2306	323	991	1369
	Triplet	$^3\text{LB}_1^+$	334	2321	425	592	1402
Neutral	Doublet	$^2\text{LB}_1^0$	417	2222	626	699	1253
	Triplet	$^3\text{LB}_1^-$	391	1845	515	675	1189
		$^3\text{LB}_2^-$	475	1891	682		1271

^a O_α , O_β , and O_γ refer to the order of oxygen atoms, where O_α is the closest to (or attached to) Au.

Table A6.3 Bond lengths (in Å) for the post-reactive minima, $[\text{O}_2\text{CuOCO}]^q$ or $[\text{CuO}_2\text{CO}_2]^q$, complexes, $q=(+1,0,-1)$, calculated with B3LYP-SDD/6-311+G(3df).

Charge	Spin	Name	C-O bond	$\text{Cu-O}_x^{a,b}$ bond	$\text{O}_\beta\text{-O}_\gamma$ bond
Anionic	Singlet	$^1\text{AR}_1^-$	1.207	1.886	1.333
			1.257	1.858	
	Triplet	$^1\text{AR}_2^-$	1.207	1.864	1.333
			1.272	1.851	
		$^3\text{AR}_1^-$	1.207	1.887	1.332
			1.257	1.859	
$^3\text{AR}_2^-$	1.207	1.864	1.333		
	1.273	1.850			

^a O_α , O_β , and O_γ refer to the order of oxygen atoms, where O_α is the closest to (or attached to) Au.

^b AuO_α bond length is listed first and AuO_β bond length is second.

Table A6.4 Vibrational frequencies (in cm^{-1}) for post-reactive minima, $[\text{O}_2\text{CuOCO}]^q$ or CuO_2CO_2 , $q=(+1,0,-1)$, calculated with B3LYP-SDD/6-311+G(3df).

Charge	Spin	Name	CO	$\text{CuO}_x^{a,b}$	$\text{O}_\beta\text{-O}_\gamma$
Anionic	Singlet	$^1\text{AR}_1^-$	1776		1172
			1256		
	Triplet	$^1\text{AR}_2^-$	1743		1174
			1259		
		$^3\text{AR}_1^-$	1777		1170
			1254		
$^3\text{AR}_2^-$	1743		1174		
	1258				

^a AuO_α vibrational frequency is listed first and AuO_β is second.

^b O_α , O_β , and O_γ refer to the order of oxygen atoms, where O_α is the closest to (or attached to) Au.

Table A6.5 Bond lengths (in Å) for low barrier, post-reactive transition state, $\{\text{O}_2\text{CuO-CO}\}^q$, complexes, $q=(+1,0,-1)$, calculated with B3LYP-SDD/6-311+G(3df).

Charge	Spin	Name	Cu-C bond	C-O bond	Cu-O _x ^{a,b} bond	O _β -O _γ bond	
Anionic	Singlet	¹ LB ₁ ⁻		1.177	1.956	1.411	
				1.199	1.792		
			¹ LB ₂ ⁻	2.792	1.170		1.344
		Triplet	³ LB ₃ ⁻		1.174	1.847	
				1.207	1.862	1.332	
				1.265	1.853		
				1.206	1.939	1.333	
			³ LB ₄ ⁻		1.274	1.867	

a O_α, O_β, and O_γ refer to the order of oxygen atoms, where O_α is the closest to (or attached to) Au.
b AuOCO bond length is listed first and AuO₂ bond length is second.

Table A6.6 Vibrational frequencies (in cm⁻¹) for low barrier (LB) post-reactive transition states, $\{\text{O}_2\text{OCuCO}\}^q$ transition state complexes, $q=(+1,0,-1)$, calculated with B3LYP-SDD/6-311+G(3df).

Charge	Spin	Name	CuC	CO	CuO ^a	O _β -O _γ	CO ₂ sym	CO ₂ anti	
Anionic	Singlet	¹ LB ₁ ⁻			594	908	1207	2131	
					486		1293	2272	
	Triplet	³ LB ₃ ⁻			1756	391			
					1253	527			
				³ LB ₄ ⁻	113	1754	503		
						1207			

a AuO_α vibrational frequency is listed first and AuO_β is second.

b O_α, O_β, and O_γ refer to the order of oxygen atoms, where O_α is the closest to (or attached to) Au.

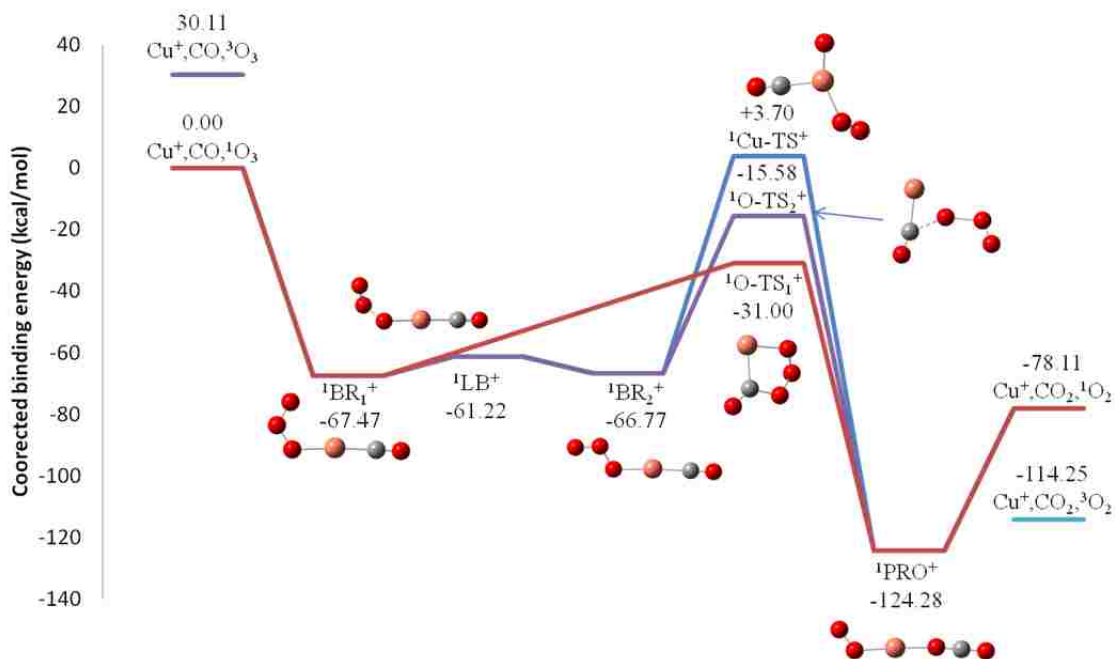


Figure A6.4 The reaction pathways for the cationic singlet state for Cu^+ , CO and O_3 are shown, where the red and purple lines represent the two O_3 oxidation pathways, ${}^1\text{O-TS}_1^+$ & ${}^1\text{O-TS}_2^+$ and blue line represents the CuO oxidation pathway, ${}^1\text{Cu-TS}^+$.

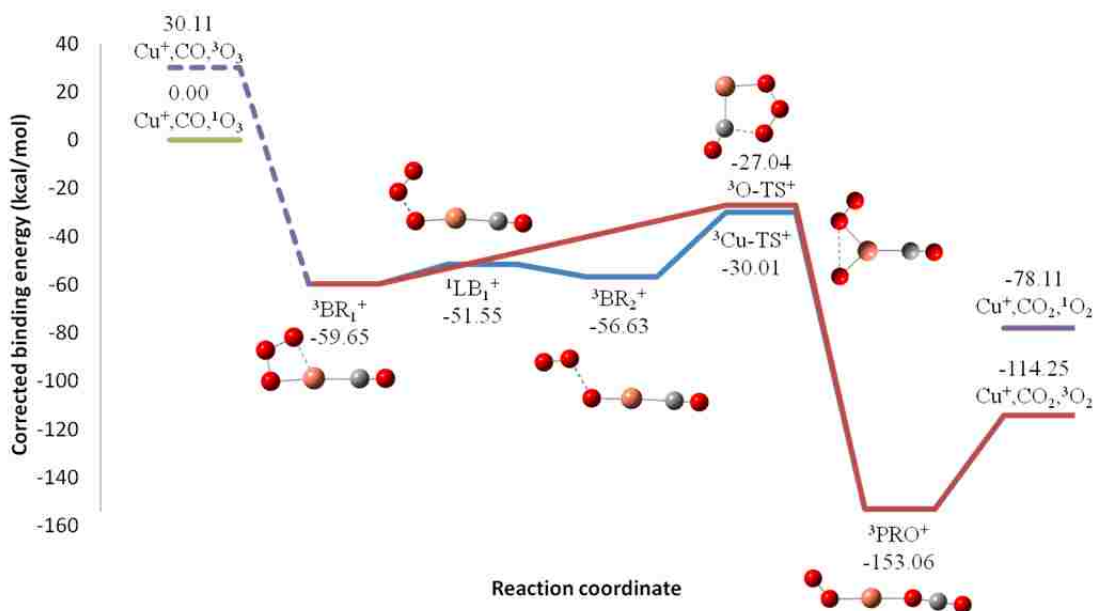


Figure A6.5 The reaction pathways for the cationic triplet states are shown, where ${}^3\text{Cu-TS}^+$ (blue line) represents the CuO pathway and ${}^3\text{O-TS}^+$ (red line) represents the O_3 pathway.

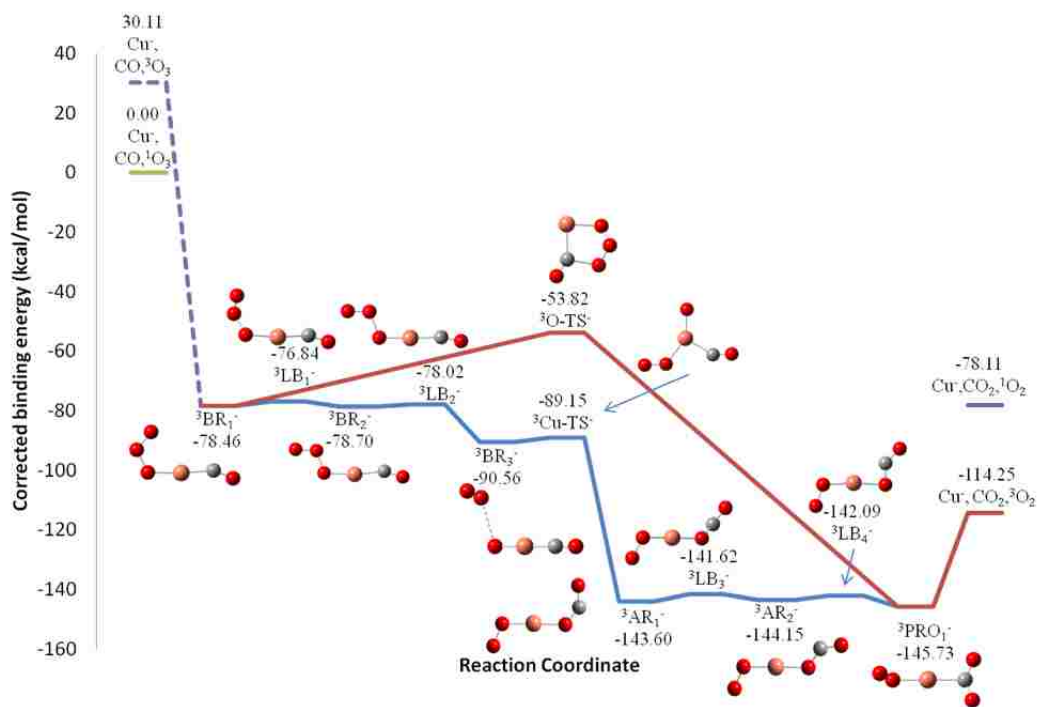


Figure A6.6 The reaction pathway(s) for the anionic triplet state is shown for Cu-, CO and O₃. The dotted purple line shows the reactants with triplet ozone and indicates its instability. The red line shows the O₃ oxidation pathway and the blue line represents the CuO pathway.

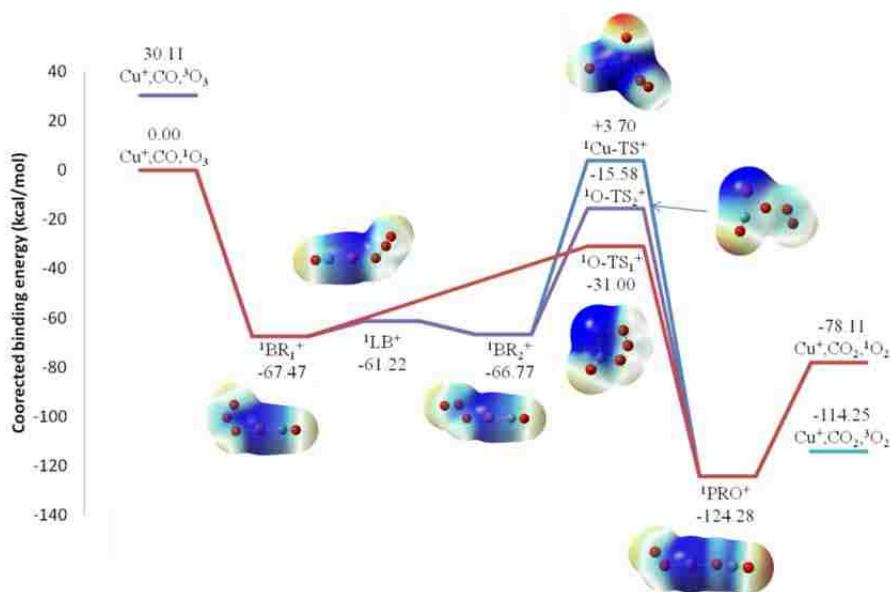


Figure A6.7. Cationic singlet reaction profiles with electrostatic potentials mapped on B3LYP total electron density isosurfaces (density=0.0004) for each complex. The O₃ oxidation processes are shown with red (O-TS₁) and purple (O-TS₂) lines; CuO oxidation pathway is represented by blue lines. The color map spans a range of 0.1 in each case with red (blue) as most negative (positive). The charges for cationic complexes are

mapped over +0.10 to +0.20. Note that color intensities are also mapped to the values, such that colors near the ends of the range appear brightest, while those in the center appear transparent.

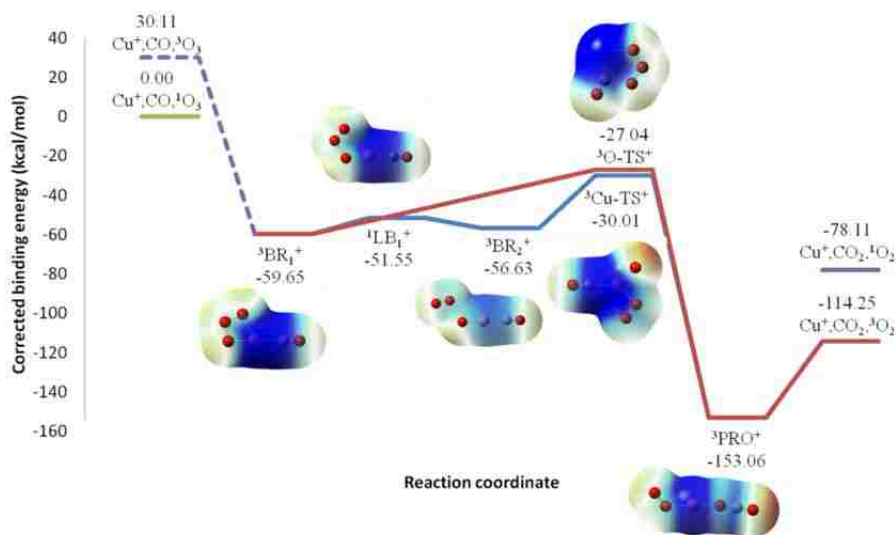


Figure A6.8. The cationic triplet pathway(s) are shown with electrostatic potentials mapped on B3LYP total electron density isosurfaces (density=0.0004) for each complex. The O₃ oxidation process is shown with the red line; CuO oxidation pathway is represented by blue line. The color map spans a range of 0.1 in each case with red (blue) as most negative (positive). The charges for cationic complexes are mapped over +0.10 to +0.20. Note that color intensities are also mapped to the values, such that colors near the ends of the range appear brightest, while those in the center appear transparent.

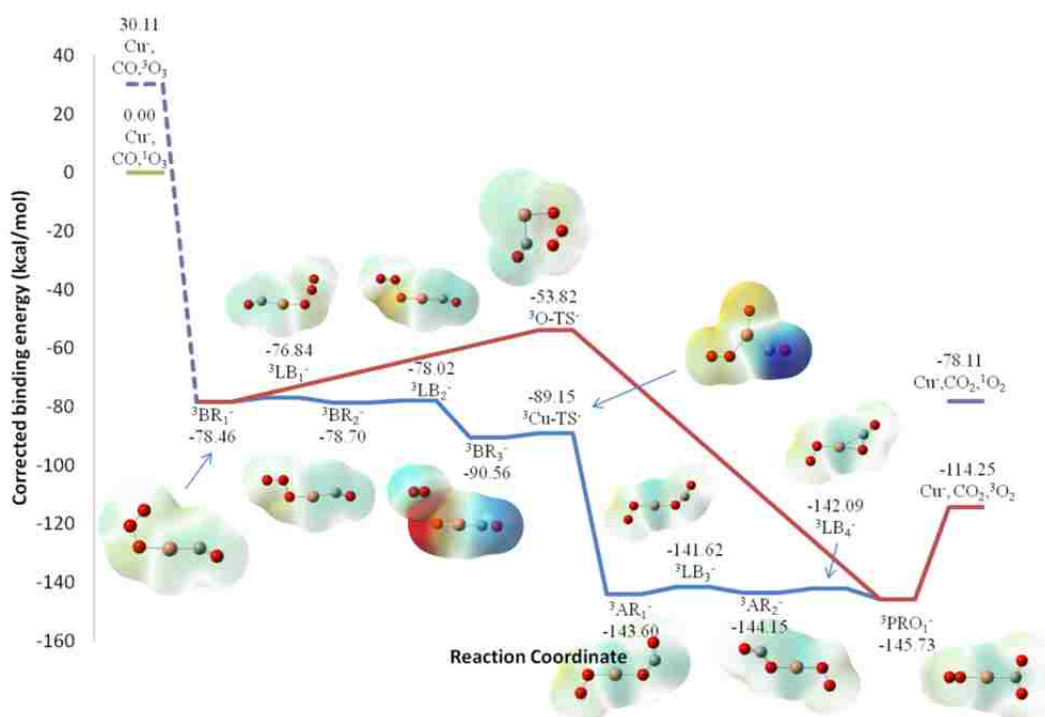


Figure A6.9. Anionic triplet reaction profiles are shown with electrostatic potentials mapped on B3LYP total electron density isosurfaces (density=0.0004) for each complex on the O₃ oxidation (red line) and CuO oxidation (blue lines) pathways. The color map spans a range of 0.1 in each case with red (blue) as most negative (positive). The charges for cationic complexes are mapped over -0.20 to -0.10. Note that color intensities are also mapped to the values, such that colors near the ends of the range appear brightest, while those in the center appear transparent.

A7. Appendix to Chapter 7.

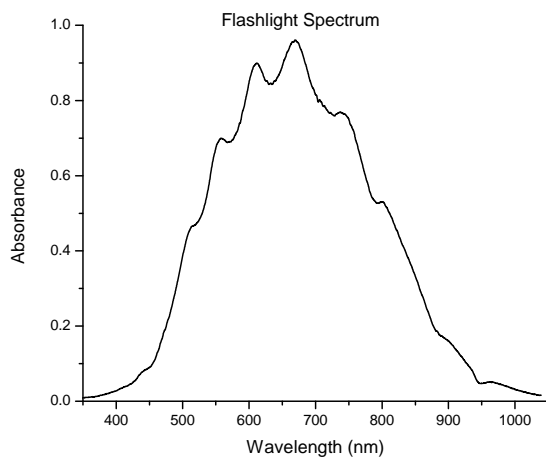


Figure A7.1 The spectrum of the light produced by an ordinary flashlight is shown, which is largely in the visible range ($\sim 400\text{-}800\text{ cm}^{-1}$) and into the infrared region.

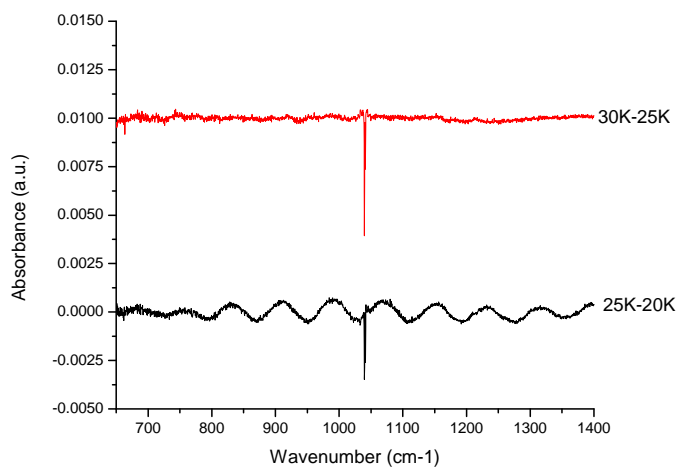


Figure A7.2 Difference spectra for the O₃ in Ar only experiment, where difference spectra for the thermal annealing steps show decreases in the main O₃ peak with shifts into the O₃ dimer band at 1035 cm^{-1} .

Table A7.1 Integrated areas of the O₃ peaks in the 20K deposited spectra and difference spectra (25K-20K) and the O₃:CO recorded and difference spectra.

Experiment	Peak	Peak area	Difference spectrum peak area
20K 0.05% O ₃ in Ar	O ₃ (1030-1050 cm ⁻¹) ¹⁾	0.1227	-0.0075
20K 0.06% O ₃ , 0.14% CO in Ar	O ₃ (1030-1050 cm ⁻¹)	0.0279	0.0044
	CO (2120-2160 cm ⁻¹) ¹⁾	4.3257	0.00422

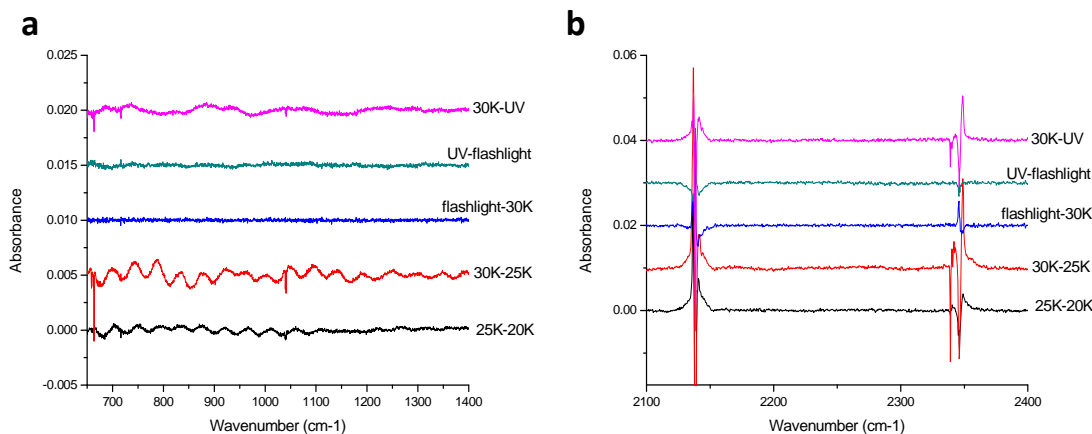


Figure A7.3 Difference spectra of the 5K annealing and photo-exposure steps for the O₃:CO experiment, where each spectrum is taken at 10K for a 0.06% O₃ and 0.14% CO in Ar mixture after 20K deposition for 2 hours at ~5 sccm (resolution of 0.5 cm⁻¹). . a) Difference spectra between 600-1400 cm⁻¹ to show the differences around the O₃ peak. b) Difference spectra for the region of 2100-2400 cm⁻¹ to show the thermal and photo-exposure changes in and around the CO and CO₂ peaks.

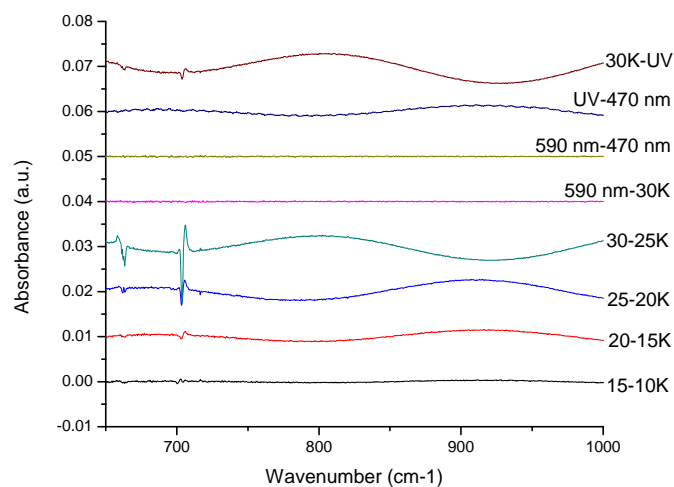


Figure A7.4 Difference spectra of the 5K annealing and photo-exposure steps for the deposition of Cu^- , Ar^+ (30V), 0.5% O_3 in Ar at 10K for 2 hours at ~ 5 sccm (resolution of 0.5 cm^{-1}). Difference spectra, between $600\text{-}1000 \text{ cm}^{-1}$, show that there are no changes observed for the 828.5 cm^{-1} (broad) peak. The shifts in the frequencies at $\sim 663 \text{ cm}^{-1}$ (CO_2 bend) and 704 cm^{-1} (O_3 bend) have been observed in other experiments without ions.

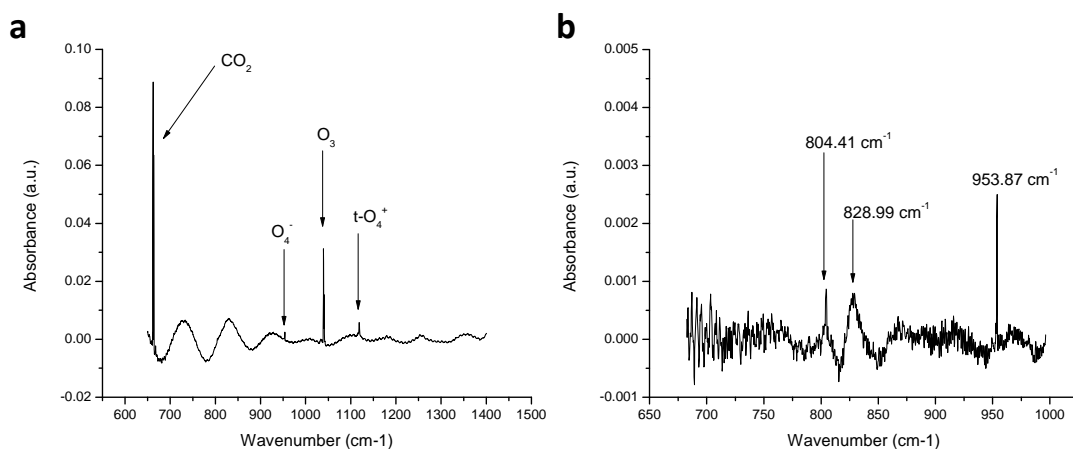


Figure A7.5 a) Spectrum ($600\text{-}1400 \text{ cm}^{-1}$) of the deposited matrix taken at 10K for Cu^- , Ar^+ (70eV) co-deposited with 0.2% O_3 in Ar mixture at 10 sccm and 10K for 4 hours (resolution of 0.5 cm^{-1}). The sine wave observed is etaloning due to the matrix b) Focus on the $700\text{-}1000 \text{ cm}^{-1}$ region, where O_3^- and O_4^- peaks are observed along with a peak at 828.99 cm^{-1} . Note that all spectra are on different wavenumber and absorbance scales.

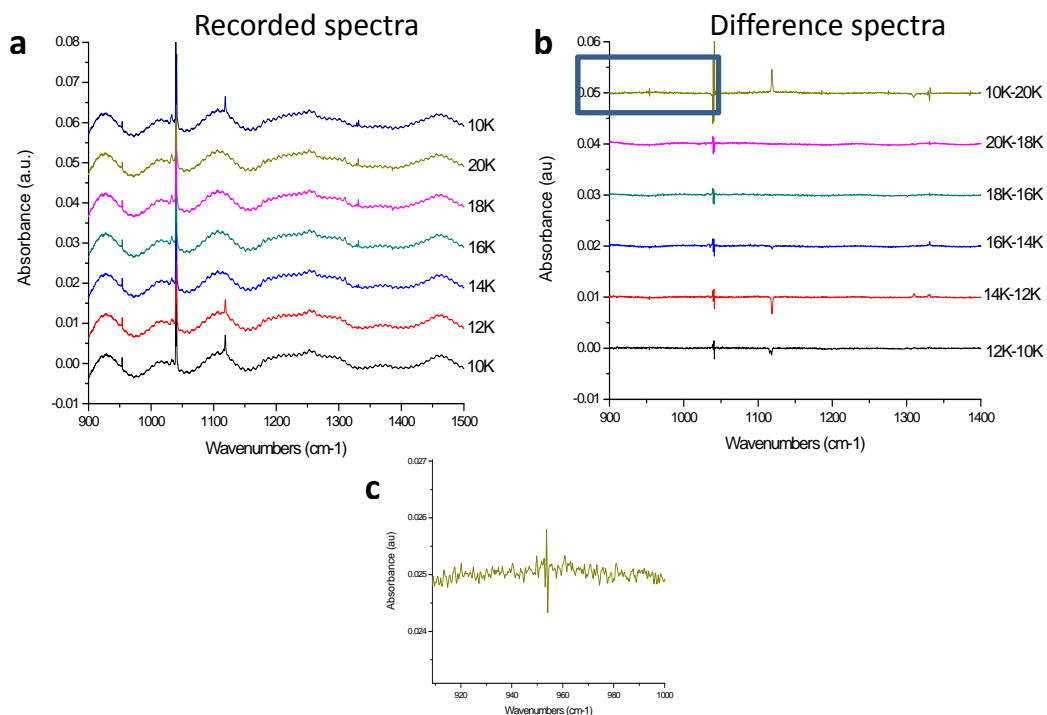


Figure A7.6 a) Recorded and b) difference spectra of the 2K annealing steps for deposition of Cu^- , Ar^+ (70eV), 0.2% O_3 at 10K and 10 sccm between 900 and 1500 cm^{-1} . Spectra were taken at temperature listed to the right of the spectra. The box in b) is highlighted in c) that focuses on the region of 900-1000 cm^{-1} , which shows the shift in the O_4^- peak. The observed shifting in the O_3 peak around 1040 cm^{-1} matches those observed in “no ions” experiments.

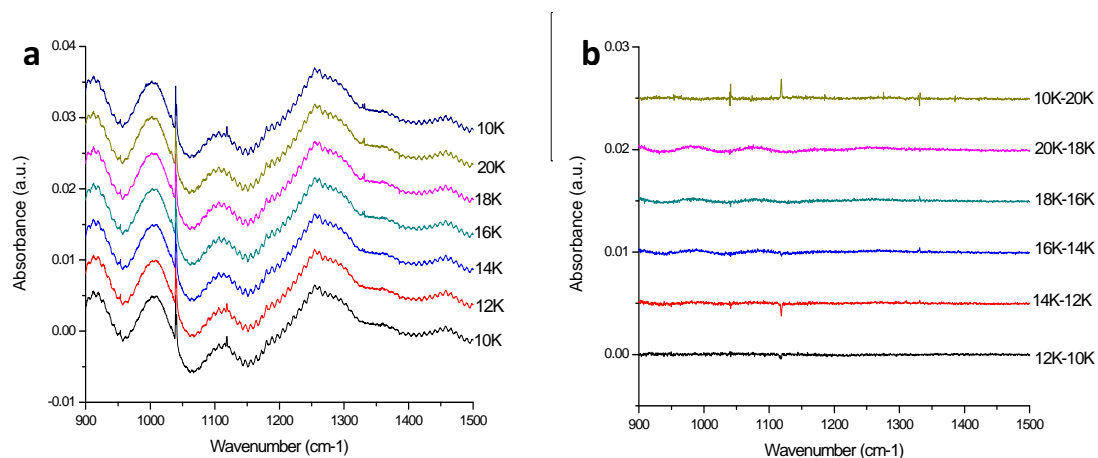


Figure A7.7 a) Recorded and b) difference spectra of the 2K annealing steps for deposition of Cu^- , Ar^+ (30eV), 0.2% O_3 in Ar at 10K and 10 sccm for 4 hours. Spectra were taken at temperature listed to the right of the spectra. In a), the sine wave observed between 900 and 1100 cm^{-1} is etaloning. In b), the differences between the annealing steps are shown.

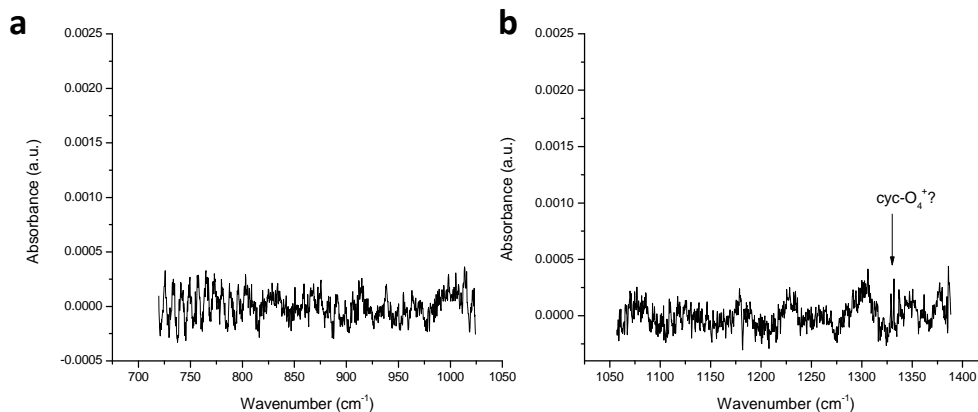


Figure A7.8 Recorded spectrum of a) 700-1000 cm^{-1} and b) 1100-1400 cm^{-1} regions that are taken at 10K after deposition at 20K for Cu^- , Ar^+ (30eV), 0.05% O_3 and 0.15% CO in Ar deposited at 20K and ~ 5 sccm for 2 hours. Note that the scales are different in a) and b). Possible cyclic- O_4^+ doublet (1329/1331 cm^{-1}) in b), but it is difficult to distinguish from the baseline.

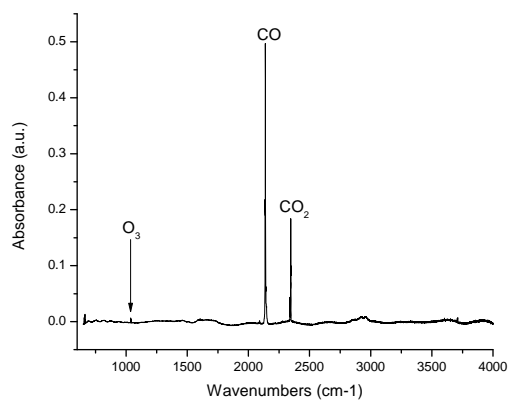


Figure A7.9 Full spectrum (650-4000 cm^{-1}) taken at 10K after deposition at 20K for Cu^- , Ar^+ (30eV), 0.05% O_3 and 0.15% CO in Ar deposited at 20K and ~ 5 sccm for 2 hours.

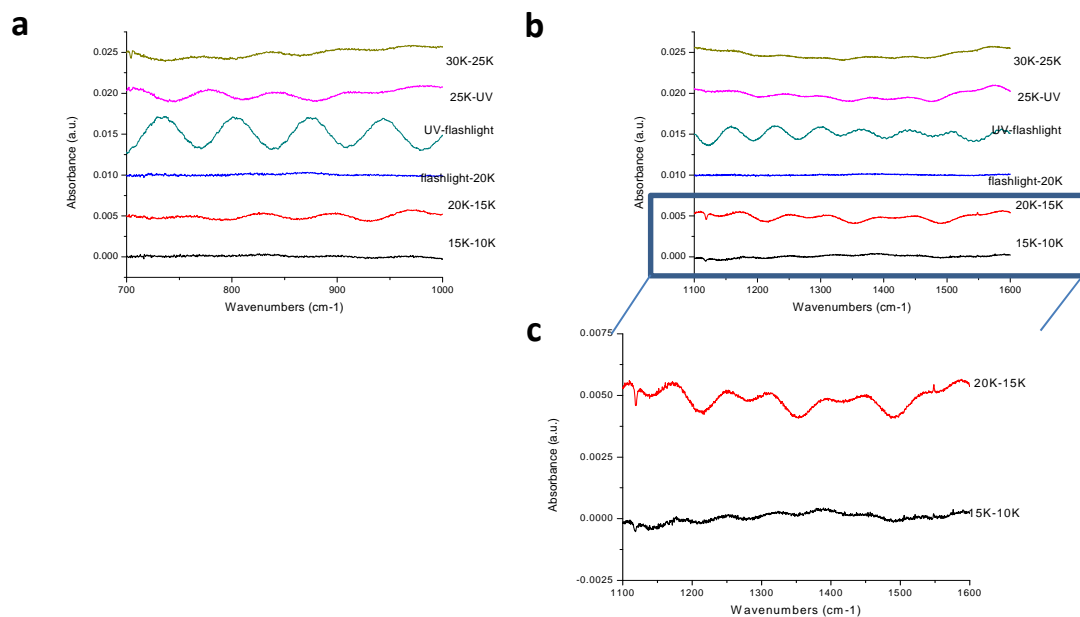


Figure A7.10 Difference spectra of Cu^- and Ar^+ (30eV) co-deposition with 0.5% O_3 and 0.3% CO in Ar mixture at ~ 5 sccm at 10K for 2 hours (resolution of 0.5 cm^{-1}). a) Region of $700\text{-}1000 \text{ cm}^{-1}$ of all difference; b) region of $1100\text{-}1600 \text{ cm}^{-1}$ in the difference spectra. The box in b) is highlighted in c) that focuses on the 15-10K and 20-15K difference. Note that the scales are different in a), b) and c).

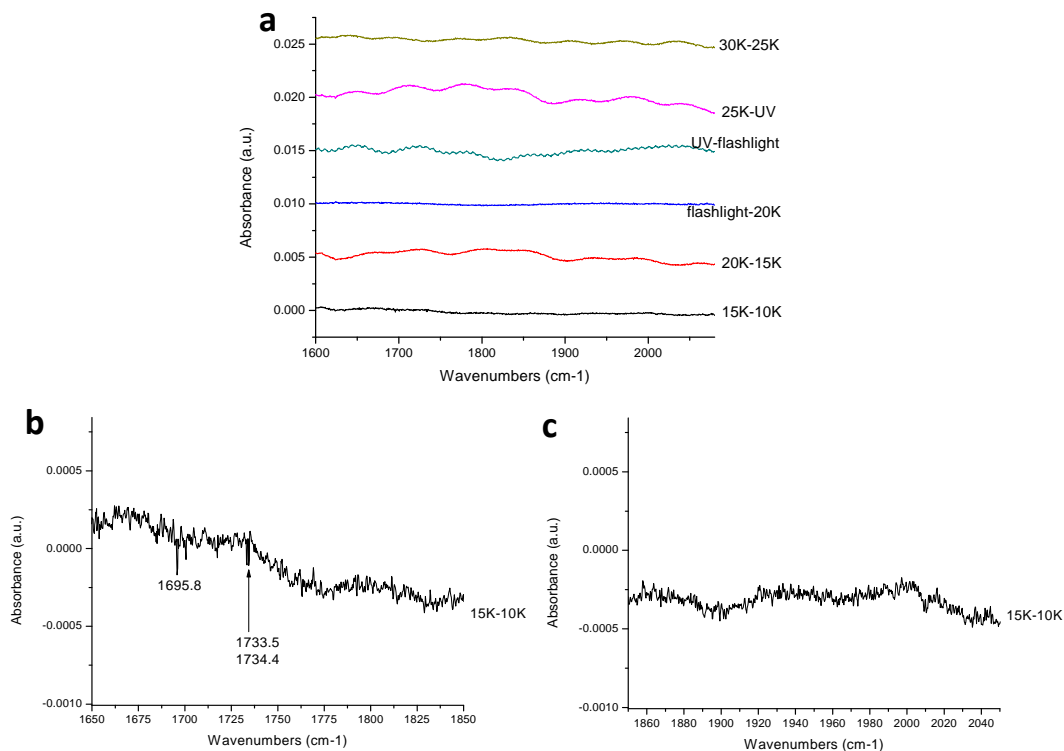


Figure A7.11 Difference spectra of Cu^- and Ar^+ (30eV) co-deposited with 0.5% O_3 and 0.3% CO in Ar mixture at ~ 5 sccm at 10K for 2 hours (resolution of 0.5 cm^{-1}). a) Region of $1600\text{-}2080 \text{ cm}^{-1}$ of all difference spectra to look for changes in this region; b) zoom in on the 15K-10K difference spectrum ($1650\text{-}1850 \text{ cm}^{-1}$) to look for changes in the several peaks observed in that zone. c) zoom in on the 15K-10K difference spectrum ($1850\text{-}2050 \text{ cm}^{-1}$) to look for any increases in neutral copper carbonyl related peaks. Note that the scales are different in a), b) and c).

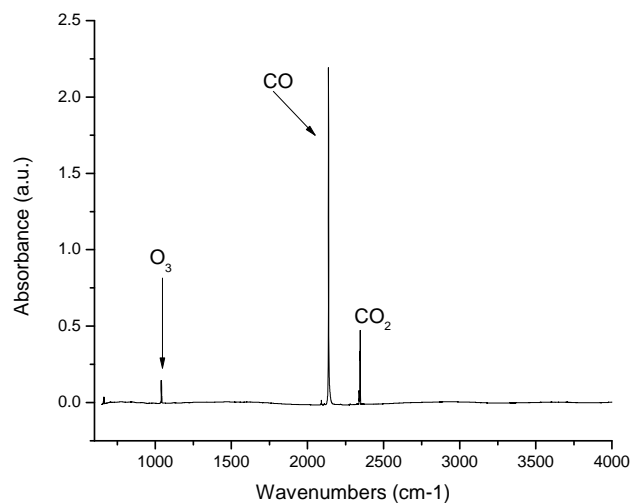


Figure A7.12 Full spectrum (650-4000 cm^{-1}) taken at 10K after deposition at 10K of Cu^- , Ar^+ (30eV), 0.5% O_3 and 0.3% CO in Ar deposited at ~ 5 sccm for 2 hours.

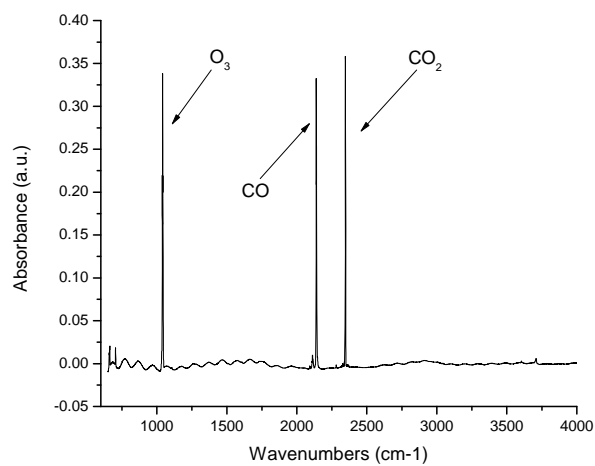


Figure A7.13 Full spectrum (650-4000 cm^{-1}) taken at 10K after deposition at 20K of Cu^- , Ar^+ (30eV), 0.2% O_3 and 0.2% CO in Ar at ~ 5 sccm for 2 hours.

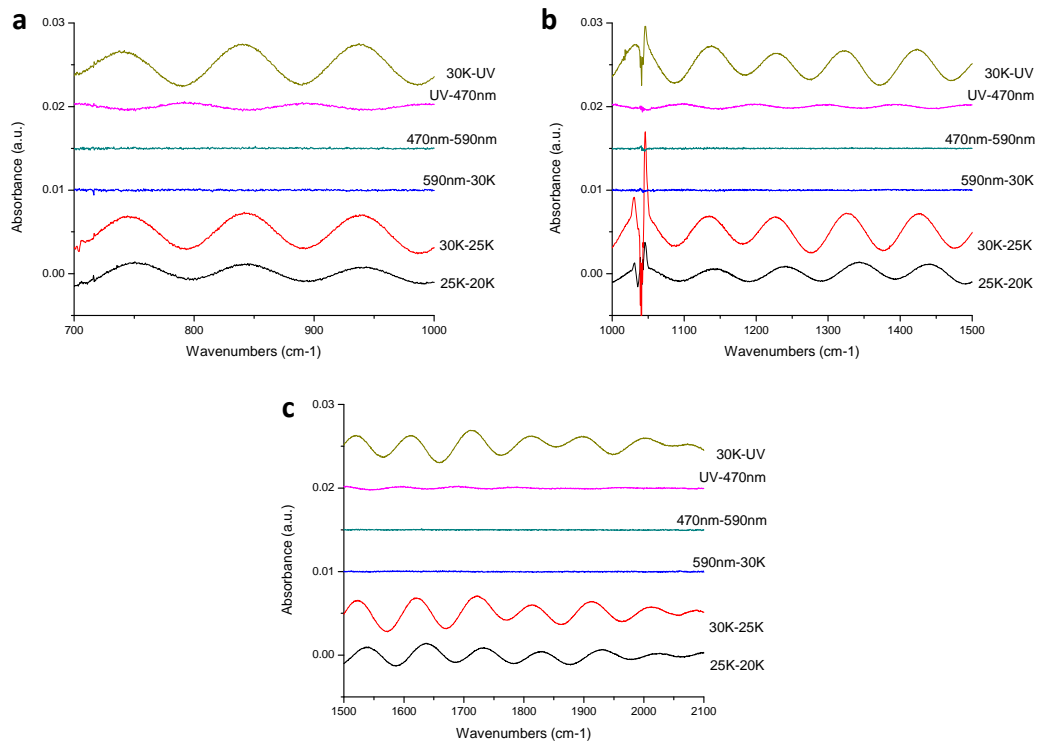


Figure A7.14 Difference spectra of Cu^- and Ar^+ (30eV) co-deposited with 0.2% O_3 and 0.2% CO in Ar mixture at ~ 5 sccm at 20K for 2 hours (resolution of 0.5 cm^{-1}) a) Region of $700\text{-}1000 \text{ cm}^{-1}$ of the difference spectra; b) region of $1000\text{-}1500 \text{ cm}^{-1}$ of the difference spectra; c) region of $1500\text{-}2100 \text{ cm}^{-1}$ of the difference spectra. The shifts in the O_3 peak is expected and observed in experiments without ions. Note that the scales are different in a)-c).

Table A7.2 The DFT calculated and experimental frequencies used to calculate the shifts for the binary complexes. These shifts are then used in calculating the probable experimental frequencies for the (unknown) ternary complexes.

Complex	Calculated freq. (cm ⁻¹)	Experimental freq. (cm ⁻¹)	Difference/shift between calc. and experimental values (cm ⁻¹)
CuCO	2050	1890.7 ¹	-159.3
CuCO⁻	1894	1733.4 ¹	-160.6
CuO₂⁺	1585	1544.7 ²	-40.3
CuO₂	1201	1089 ²	-112
CuO₂⁻ (singlet)	1021		-12
CuO₂⁻ (triplet)	1151	1009.5 ²	-141.5
CuO₃	(anti-sym) 885.5	802.7 ²	-82.8

Table A7.3 The DFT calculated ternary complex frequencies of CuO₃⁻, the shift used (from Table A7.2), and expected experimental frequency from applying the shift to the calculated frequency.

Complex & Frequency identity	Calculated frequency (cm ⁻¹)	Shift used (cm ⁻¹)	Expected experimental frequency (cm ⁻¹)
CuO₃⁻ singlet (O₃ anti-sym stretch)	798.9	82.8	716.1
CuO₃⁻ singlet (O₃ sym stretch)	869.6	82.8	786.8
CuO₃⁻ triplet “out” interior OO	1163.6	82.8	1080.8
CuO₃⁻ triplet “out” exterior OO	789	82.8	706.2
CuO₃⁻ triplet “in” interior OO	1124.2	82.8	1041.4
CuO₃⁻ triplet “in” exterior OO	816.8	82.8	734

Table A7.4 The DFT calculated ternary complex frequencies of O_3CuCO , O_3CuCO^- , and O_2CuCO^- , the shift used (from Table A7.2), and expected experimental frequency from applying the shift to the calculated frequency.

Complex & Frequency identity	Calculated frequency (cm^{-1})	Shift used (cm^{-1})	Expected experimental frequency (cm^{-1})
O_3CuCO “in” C_{2v} (CO)	2205	160	2045
O_3CuCO “in” C_{2v} O_3 sym stretch	1090	82.8	1007.2
O_3CuCO “in” C_{2v} O_3 anti-sym. stretch	904	82.8	821.2
O_3CuCO “out” (CO)	2220	160	2060
O_3CuCO “out” interior OO	647	82.8	564
O_3CuCO “out” exterior OO	1277	82.8	1194.2
O_3CuCO^- singlet C_{2v} (CO)	2038	160	1878
O_3CuCO^- singlet C_{2v} O_3 sym stretch	894	82.8	811.2
O_3CuCO^- singlet C_{2v} O_3 anti-sym. stretch	849	82.8	766.2
O_3CuCO^- triplet “in” CO	1835	160	1676
O_3CuCO^- triplet “in” interior OO bond	738	82.8	655.2
O_3CuCO^- triplet “in” exterior OO bond	1173	82.8	1090.2
O_3CuCO^- triplet “out” CO	1849	160	1689
O_3CuCO^- triplet “out” interior OO bond	580	82.8	497.2
O_3CuCO^- triplet “out” exterior OO bond	1198	82.8	1115.2
O_3CuCO^- triplet “elongated out” CO	2026	160	1866
O_3CuCO^- triplet “elongated out” interior OO bond	783	82.8	700.2
O_3CuCO^- triplet “elongated out” exterior OO bond	1441	82.8	1358.2
O_2CuCO^- singlet CO	2011	160	1851
O_2CuCO^- singlet O_2	830	141.5 (12)	688.5 (818)
O_2CuCO^- triplet CO	1826	160	1666
O_2CuCO^- triplet O_2	1164	141.5 (12)	1022.5 (1152)

RGA studies of ozone to identify CO₂ contamination source

During initial ozone in argon experiments (no ions), strong carbon dioxide (CO₂) peaks were observed, indicating that there was significant contamination from either ozone cleaning the stainless steel bottle and lines or leaks in the fittings in the lines. The fittings were tested using a helium leak test with the RGA. At each fitting, the exterior of the fitting was exposed to a flow of helium; if the RGA responded with an increase in the helium peaks, specifically mass 4 peak, the fitting was leaking and was tightened until the mass 4 peak decreased to the baseline value. This was performed across the entire ozone system (deposition lines, bottle, and generation system) to remove leaks as a possible CO₂ source. Next, solvent-liquid nitrogen baths were investigated to determine if these could assist in decreasing the CO₂; the isopentane (2-methylbutane) and liquid nitrogen bath was selected as the most probable to work, since the bath temperature (113K) is approximately half the boiling point of CO₂ (216 K), but higher than the freezing point of ozone (81 K). To test the most likely origin of CO₂, I completed a series RGA experiments with the isopentane baths on the generation tube and deposition line trap with the following combinations: A) No isopentane baths, B) isopentane bath on generation tube, C) isopentane bath on deposition trap, and D) isopentane baths on both tube and trap. For example, if the generation tube is the main (or only) source of CO₂, the isopentane bath on that tube should lead to no CO₂, or very little, observed in the RGA. With no isopentane baths, a small amount of CO₂ is observed at 5 minutes of “deposition” into the chamber at room temperature and the amount of CO₂ and O₃ increase as the time increases to 30 minutes, as shown in Figure 2.3. Shown in Figure 2.4 are the 5, 15 and 30 min spectra taken at these intervals of ozone deposition into the

chamber with an isopentane bath on the generation tube. Similar to experiment A, the ozone peak increases with the increase in time, while CO₂ actually decreases slightly. For the isopentane bath on the trap only (experiment C), the mass spectra for times of 5, 15 and 30 minutes of gas deposition are shown in Figure 2.5, where the CO₂ peak remains at the same intensity through 30 minutes and O₃ peak increases with more time up to 30 minutes. Finally with isopentane baths on both the tube and trap, the results are shown in Figure 2.6 and CO₂ is very small, as is O₃ (almost hidden in the baseline), but each of these peaks are steady at approximately the same value through the entire 30 minute experiment. As can be seen in all of the experiments, there is a very significant peak at mass 28, which can correspond to either CO or N₂, where CO is most likely a fragment of CO₂. Also, the mass 32 peak is also significant, which matches O₂, and is most likely a fragment of ozone. There is also a peak at mass 14 throughout all experiments, which corresponds to nitrogen atom (N), which would indicate the existence of leak in the system. However, the ozone lines were helium leak checked prior to this experiment, so any leak would be from another section of the gas rack system. After this experiment, a leak was discovered near the O₂ source bottle and was removed, which is the probable source of nitrogen, and possibly portions of CO₂ and O₂ peaks, in these mass spectra. Table 2.6 shows the maximum pressure of CO₂ and ozone during each of these four RGA experiments. In experiments A and B, the CO₂ peaks are very similar, which indicates that the tube is unlikely to be the source (or major source) of CO₂. It is interesting to note that the ozone peak in B is approximately 1/3 that of A, which may be due to the isopentane bath being too cold and trapping some ozone, or less ozone was generated in that cycle. Comparing the C and D experiments, the amount of CO₂ is

approximately a magnitude smaller than the same peaks in A and B, which indicates that ozone is likely to be formed in the bottle and stainless steel lines. It is possible that ozone is oxidizing the carbon in the stainless steel to produce CO_2 . The O_3 peaks of C and D are also much smaller than A and B; therefore, the isopentane baths on the trap were probably too cold and trapping some of the ozone as well.

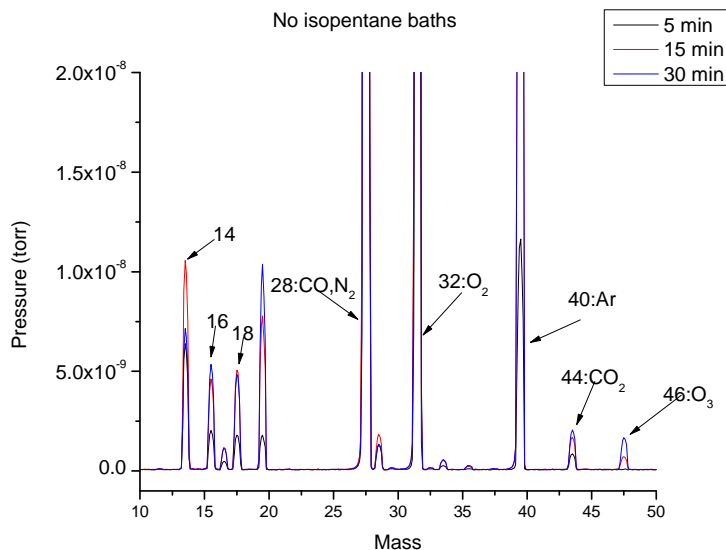


Figure A7.15 Mass spectrum from RGA of ozone with no isopentane baths in the system. Gas was introduced into the chamber at a flow rate of ~ 1 sccm through a needle valve at room temperature, as the experiment was performed before a flow controller was installed. Large argon peak is likely due to the background pressure of lines and bottle at 100 millitorr when moving ozone into the bottle. Deposition lines were at 25 millitorr before “depositing” ozone into the chamber; ozone was in the bottle for 15 minutes before deposition.

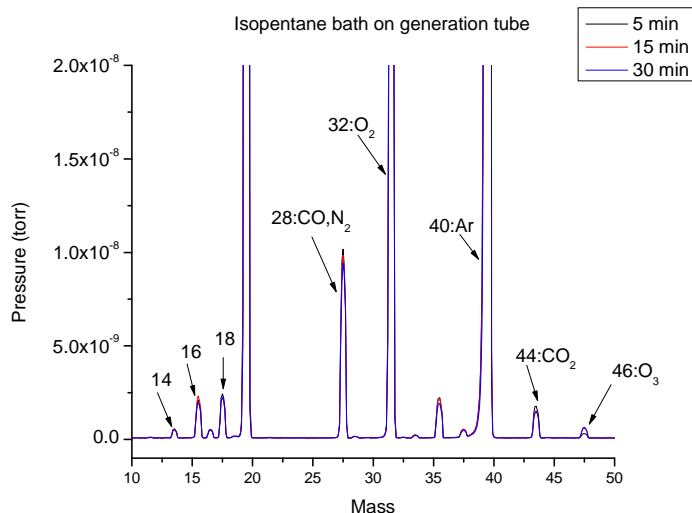


Figure A7.16 Mass spectrum from RGA of ozone with an isopentane bath on the generation tube. Gas was introduced into the chamber at a flow rate of ~ 1 sccm through a needle valve at room temperature, as the experiment was performed before a flow controller was installed. The large argon peak is likely due to the background pressure of lines and bottle at 150 millitorr when moving ozone into the bottle. Deposition lines were at 150 millitorr before “depositing” ozone into the chamber; ozone was in the bottle for 90 minutes before deposition.

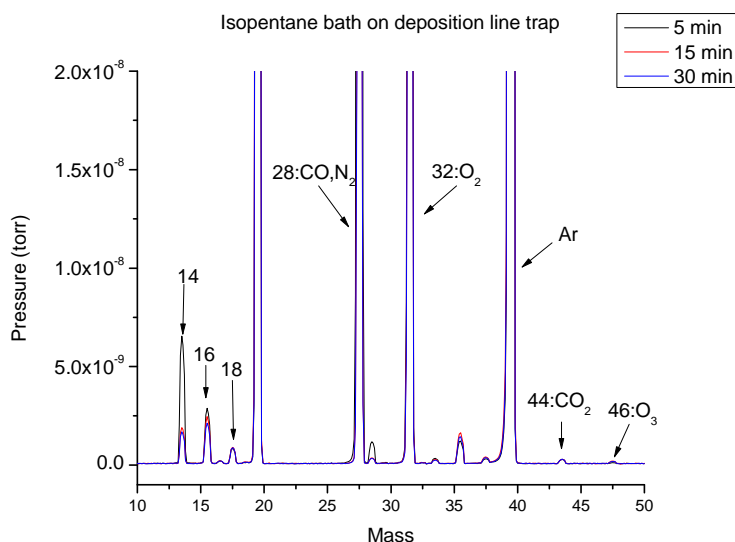


Figure A7.17 Mass spectrum from RGA of ozone with an isopentane bath on the deposition line trap. Gas was introduced into the chamber at a flow rate of ~ 1 sccm through a needle valve at room temperature, as the experiment was performed before a flow controller was installed. The large argon peak is likely due to the background pressure of lines and bottle at 90 millitorr when moving ozone into the bottle. Deposition lines were at 180 millitorr before “depositing” ozone into the chamber; ozone was in the bottle for 30 minutes before deposition.

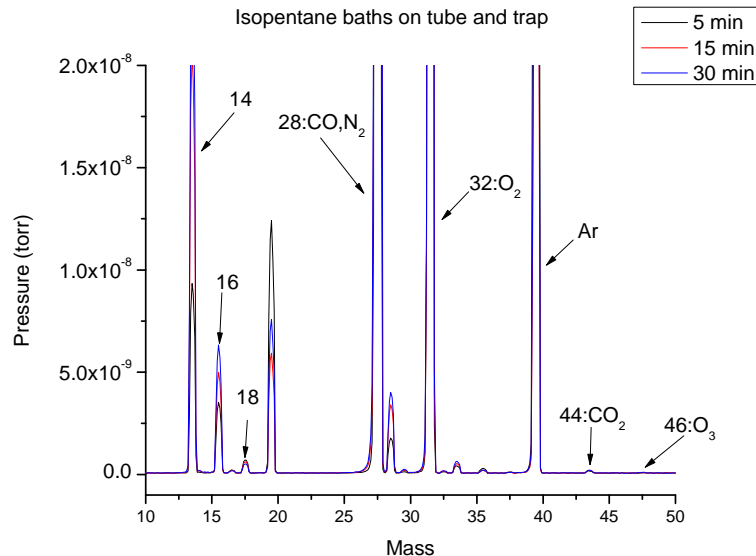


Figure A7.18 Mass spectrum from RGA of ozone with isopentane baths on the generation tube and deposition line trap. Gas was introduced into the chamber at a flow rate of ~ 1 sccm through a needle valve at room temperature, as the experiment was performed before a flow controller was installed. The large argon peak is likely due to the background pressure of lines and bottle at 330 millitorr when moving ozone into the bottle. Deposition lines were at 64 millitorr before “depositing” ozone into the chamber; ozone was in the bottle for ~ 20 minutes before deposition.

Table A7.5 Pressures of CO₂ and O₃ in torr in the four RGA experiments.

RGA experiment name	Pressure (torr) CO ₂ (mass 44 peak)	Pressure (torr) O ₃ (mass 48 peak)
A: No isopentane baths	2.0×10^{-9}	1.7×10^{-9}
B: Isopentane bath on tube	1.78×10^{-9}	6.5×10^{-10}
C: Isopentane bath on trap	3.0×10^{-10}	2.0×10^{-10}
D: Isopentane bath on both	2.14×10^{-10}	1.1×10^{-10}

A7 References

- (1) Zhou, M.; Andrews, L. *J. Chem. Phys.* **1999**, *111*, 4548-4557.
- (2) Chertihin, G.; Andrews, L.; Bauschlicher, C. *J. Phys. Chem. A* **1997**, *101*, 4026-4034.

Angela N. Smith

Smithan05@gmail.com

Work Address:

Department of Chemistry
Lehigh University
6 E. Packer Ave.
Bethlehem, PA 18015

Home Address:

8510 Putnam Ct
Breinigsville, PA 18031
(814) 934-6163

EDUCATION

Lehigh University

Ph.D., Physical Chemistry

Advisor: David T. Moore, Ph.D.

Thesis: Experimental and theoretical investigation of CO oxidation over unsupported Au nanoparticles

Honors:

Chemistry Department Fellowship

Sigma Xi GIAR grant recipient

University Research Fellowship

Bethlehem, PA

Summer 2014 (expected)

May 2013-May 2014

March 2013

August 2009-August 2010

Juniata College

B.S., Chemistry

Overall GPA: 3.55

Academic Honors:

Dean's List (multiple semesters)

Analytical Chemistry Award

Cora and Dean van Ellis scholarship (merit scholarship)

Huntingdon, PA

May 2009

May 2008

May 2008

EXPERIENCE

Lehigh University

Research Assistant

Bethlehem, PA

Fall 2009-present

- Worked in a team to investigate interactions of carbon monoxide (CO) and oxygen species with metal atoms utilizing matrix isolation techniques to determine CO oxidation mechanism
- Worked individually to design and incorporate small scale ozone generator into vacuum system
- Identified cooperative binding and charge transfer in interactions of oxygen species and CO with Au atoms via density functional theory calculations to understand CO oxidation mechanism
- Calculated probable reaction pathways for CO oxidation with oxygen allotropes (O₂ and ozone) catalyzed by Au and Cu atoms and observed periodicity between Au and Cu pathways

Teaching Assistant

Fall 2012-Spring 2013

Fall 2010-Spring 2011

- Asked to provide opinion of student performance and execution of experiments
- Only TA asked to review and provide input to edit and improve physical chemistry manual
- Influenced decision on teaching materials used in physical chemistry classes

Lehigh University

Bethlehem, PA

Research Intern

Summer 2009

- Worked in a team to determine how parameters of a nanoclusters source affect the energy (birth potential) of copper clusters and optimize the ion pathway for cluster deposition

Research Intern

Summer 2008

- Undergraduate student working on project to determine exchange rates of self-assembled monolayers (SAMs) on gold with thiolalkyl salts

Juniata College

Huntingdon, PA

Tutor in Calculus and Organic Chemistry

Fall 2008-Spring 2009

Physical Chemistry Teaching Assistant

Spring 2009, Spring 2006

- Recognized as a freshman to instruct upperclassmen in lab setting and returned as a senior

Organic Chemistry Teaching Assistant

Spring 2007

- Gave short lectures on experiments and mechanistic details in support of professor.
- Assisted students during characterization and micro-scale syntheses of methyl salicylate and Cyalume.

Research Intern (LECO Corporation)

May 2006-August 2007

- Worked in a team on development of computer simulation program for 2D-GC instrument
- Conducted GC-MS and 2D-GC experiments on Restek standard mixtures for retention indices

PRESENTATIONS & PUBLICATIONS

- **Smith, Angela N.;** Gressick, Allison; Schettler, Paul D. (2008, March). "GCxGC simulator calibration." Poster at 235th ACS National Conference, New Orleans, LA.
- **Smith, Angela N.;** Schettler, Paul D.; Dorman, Frank; Gardner, Suzanne; Bloom, Anna; Federle, Sarah. (2009, March). "Predicting the ability of GC stationary phase designs to separate isomers." Poster at 237th ACS National Conference, Salt Lake City, UT.

- **Smith, Angela N.;** Hunter, Alex D.; Moore, D. T. (2010, August). "Using calculated vibrational shifts to map cooperative effects in CO oxidation on Au atoms." Poster at Gordon Research Conference: Vibrational Spectroscopy, Biddeford, ME.
- **Smith, Angela N.;** Hunter, Alex D.; Moore, D. T. (2011, August). "Using calculated vibrational shifts to map cooperative effects in CO oxidation on Au atoms and dimers." Poster at 242nd ACS national conference, Denver, CO.
- **Smith, Angela N.;** Moore, D. T. "Charge-dependent Trends in Structures and Vibrational Frequencies of [CO-Au-O₂]^q (q=-1,0,+1) Complexes: Evidence for Cooperative Interactions." *J. Phys. Chem. A*, **2012**, *116* (37), 9370–9381.
- **Smith, Angela N.;** Moore, D.T. (2012, August). "Theoretical investigation of Au^q (q=+1,0,-1), CO and ozone interactions for reaction pathways of CO oxidation." Poster at Gordon Research Conference: Vibrational Spectroscopy, Biddeford, ME.
- **Smith, Angela N.;** Moore, D.T. (2012, August). "Theoretical investigation of Au^q (q=+1,0,-1), CO and ozone interactions for potential reaction intermediates of CO oxidation in matrix isolation studies." 244th ACS national conference, Philadelphia, PA.
- **Smith, Angela N.;** Moore, D.T. (2013, September). "Understanding reaction profiles of CO oxidation with ozone and Au^q atoms (q=-1,0,+1) utilizing DFT calculations and AIMD." Oral presentation at 246th ACS national conference, Indianapolis, IN.
- **Smith, Angela N.;** Moore, D.T. "Observation of carbonate formation in DFT calculations for CO oxidation pathways with neutral and anionic Au atoms, CO and O₂ complexes" (*In preparation*).
- **Smith, Angela N.;** Moore, D.T. "Understanding the reaction pathways for CO oxidation utilizing Au^q (q=0,-1), CO and ozone" (*In preparation*).

PROFESSIONAL AFFILIATIONS & ACTIVITIES

National Association of Parliamentarians	<i>June 2004-present</i>
American Chemical Society	<i>October 2007-present</i>
<i>Gamma Sigma Epsilon</i> (Chemistry Honor Society)	<i>March 2008-present</i>
Coldwater Crossing HOA architectural committee member	<i>Fall 2009-Fall 2012</i>
Really Terrible Orchestra	<i>June 2012-present</i>
Sigma Xi (Scientific Research Society)	<i>May 2013-present</i>
Association for Women in Science	<i>November 2013-present</i>
Lehigh Valley local section of ACS secretary	<i>Elected for 2014.</i>